

HIGH IMPACT STRENGTH POLYMERS HAVING NOVEL NANO-STRUCTURES
PRODUCED VIA REACTIVE EXTRUSION

By

NATHAN FRASER TORTORELLA

A DISSERTATION PRESENTED TO THE GRADUATE SCHOOL
OF THE UNIVERSITY OF FLORIDA IN PARTIAL FULFILLMENT
OF THE REQUIREMENTS FOR THE DEGREE OF
DOCTOR OF PHILOSOPHY

UNIVERSITY OF FLORIDA

2005

Copyright 2005

by

Nathan Fraser Tortorella

This dissertation is dedicated to my wife, Michelle, and my daughter, Katelynn.

ACKNOWLEDGMENTS

I would like to thank my advisor and mentor, Professor Charles L. Beatty. He fostered my creativity and desire to succeed over the last several years and the KISS principle is forever instilled in me. My committee members have been an invaluable resource to me, namely Drs. Jack Mecholsky, Abbas Zaman, Hassan El-Shall, and Ken Wagener. Their guidance on both a personal and professional level helped me succeed as a graduate student. Funding for this research was graciously provided by Proctor and Gamble. Chuck Yeazell and colleagues at P&G were extremely helpful in furthering the development of this new material.

My wife Michelle has been unwavering in support, love, and understanding and our beautiful daughter Katelynn is an inspiration. Stevan and Donna, my parents, and Harry and Carol, Michelle's parents, deserve to be recognized for their encouragement and love through thick and thin. I would like to thank my sisters, Stevany, Emily, and Danica, for being there when I needed a quick laugh or to relax.

Many people have helped me throughout the years to eventually complete the dissertation. In the Beatty research group, Ajit Bhaskar, Dr. Kunal Shah, and Xiosong Huang were outstanding friends and colleagues. Thanks go to Mike Tollon for the SEM pictures, Dr. Valentine Craciun for XRD, Dr. Laurie Gower and her students for optical microscopy, James Leonard in the Wagener research group for GPC, and Phil McCartney at Virginia Tech for TEM photos. Dr. Tony Brennan, Dr. Clay Bohn, Dr. Leslie Wilson, and Michelle Carman were extremely helpful in training and support on several

instruments in the polymer characterization lab. Lastly, I would like to acknowledge the staff in the Materials Science and Engineering Department for their help and dedication over the last eight years.

TABLE OF CONTENTS

	<u>page</u>
ACKNOWLEDGMENTS	iv
LIST OF TABLES	x
LIST OF FIGURES	xiii
ABSTRACT	xxi
CHAPTER	
1 GENERAL INTRODUCTION	1
1.1 Introduction.....	1
1.2 Chapter Summaries.....	4
2 BACKGROUND AND LITERATURE REVIEW	6
2.1 Polymers of Interest.....	6
2.1.1 Isotactic Polypropylene	6
2.1.2 Ethylene-1-Octene Copolymer	7
2.2 Processing.....	9
2.2.1 Reactive Twin Screw Extrusion	9
2.2.2 Morphology Development in an Extruder – Dispersive and Dissipative Mixing.....	11
2.2.3 Melting and Droplet Breakup Mechanisms.....	13
2.2.4 Morphology Development Dependency on Rate of Reaction.....	16
2.2.5 Viscosity and Reaction Effects on Morphology Development	18
2.3 Toughening of Polymers.....	19
2.3.1 Origins of Polymer Toughening.....	19
2.3.2 Elastomer/Rubber Toughened Blends.....	20
2.4 Free Radical Reactions	23
2.4.1 Initiator Decomposition.....	23
2.4.2 What Happens After Peroxide Decomposition?.....	26
2.4.3 Polymerization.....	26
2.4.4 Copolymerization	28
2.4.5 Multifunctional Monomer	30
2.4.6 Hydrogen Abstraction	31

2.4.7 Polyethylene Crosslinking Reactions	32
2.4.8 Degradation of Polypropylene.....	33
2.5 Previous Efforts to Reduce/Prevent Degradation of Polypropylene	35
2.5.1 Free Radical Grafting of Polymers.....	35
2.5.2 Solid State Grafting	36
2.5.3 Reactions in the Polymer Melt	37
2.5.4 Fundamentals of Free Radical Grafting	39
2.5.5 Melt Grafting Monomers onto Polyolefins	41
2.6 Melt Grafting and <i>In-situ</i> Compatibilization	43
2.7 Conclusions.....	47
3 PHYSICAL BLENDING OF AN IMPACT MODIFIER WITH POLYPROPYLENE.....	48
3.1 Introduction.....	48
3.2 Experimental.....	48
3.2.1 Materials	48
3.2.2 Methods	48
3.2.2.1 Processing.....	48
3.2.2.2 Mechanical properties	50
3.2.2.3 Morphology	51
3.2.2.4 Thermal analysis and rheology	52
3.3 Results and Discussion	53
3.3.1 Mechanical and Rheological Properties	53
3.3.2 Morphology	59
3.3.3 Viscoelasticity	62
3.3.4 Crystallinity	68
3.4 Conclusions.....	72
4 TOUGHENED POLYPROPYLENE BASED ALLOYS	74
4.1 Introduction.....	74
4.2 Experimental.....	74
4.2.1 Materials	74
4.2.2 Methods	76
4.2.2.1 Processing.....	76
4.2.2.2 Mechanical properties	77
4.2.2.3 Morphological characterization.....	78
4.2.2.4 Chemical composition and molecular structure	81
4.2.2.5 Thermal analysis and rheology	82
4.3 Results and Discussion	84
4.3.1 Notched Izod Impact Analysis	86
4.3.2 Stress-Strain Behavior.....	91
4.3.3 Grafting onto Polyolefins	97
4.3.4 Morphology	101
4.3.5 Possible Crosslinking of the System	111
4.3.6 Rheological Properties.....	112
4.3.7 Crystallinity and Crystallization.....	116

4.3.8	Viscoelasticity	138
4.4	Conclusions.....	145
5	THE EFFECT OF PROCESSING CONDITIONS ON ALLOY PROPERTIES	147
5.1	Introduction.....	147
5.2	Experimental.....	147
5.2.1	Materials.....	147
5.2.2	Methods.....	149
5.2.2.1	Processing.....	149
5.2.2.2	Mechanical properties	150
5.2.2.3	Chemical composition.....	151
5.2.2.4	Rheology	152
5.3	Results and Discussion	152
5.3.1	Effect of Processing Temperature	152
5.3.2	Effect of Screw Speed	155
5.3.3	Effect of Initiator Concentration	158
5.3.4	Effect of Multifunctional Monomer Concentration	160
5.3.5	Effect of Styrene Concentration with DEGDA as Multifunctional Monomer.....	163
5.3.6	Effect of Styrene Concentration with TMPTA as Multifunctional Monomer.....	165
5.4	Conclusions.....	167
6	CONTROLLING ALLOY PERFORMANCE BY VARYING ELASTOMER PROPERTIES.....	168
6.1	Introduction.....	168
6.2	Experimental.....	168
6.2.1	Materials.....	168
6.2.2	Methods.....	170
6.2.2.1	Processing.....	170
6.2.2.2	Mechanical properties	171
6.2.2.3	Chemical composition and molecular structure	172
6.2.2.4	Thermal analysis and rheology	174
6.3	Results and Discussion	174
6.3.1	Effect of Elastomer Density on Alloy Performance.....	174
6.3.1.1	Physical blends.....	175
6.3.1.2	Alloys	183
6.3.2	Effect of Elastomer Molecular Weight on Alloy Performance.....	190
6.3.2.1	Physical blends.....	193
6.3.2.2	Alloys	200
6.3.3	Supercritical CO ₂ as a Possible Route to Improve Grafting Efficiency ...	210
6.4	Conclusions.....	211

7	REACTIVE EXTRUSION OF HIGH DENSITY POLYETHYLENE	213
	7.1 Introduction.....	213
	7.2 Experimental.....	213
	7.2.1 Materials.....	213
	7.2.2 Methods.....	215
	7.2.2.1 Processing.....	215
	7.2.2.2 Mechanical properties	216
	7.2.2.3 Design of experiments.....	217
	7.3 Results and Discussion	218
	7.3.1 Mechanical Properties	218
	7.3.2 Design of Experiments Results	221
	7.3.2.1 Impact strength.....	221
	7.3.2.2 Elastic modulus	225
	7.3.2.3 Yield strength	228
	7.3.2.4 Elongation at break.....	231
	7.4 Conclusions.....	234
8	CONCLUSIONS AND FUTURE WORK.....	236
	8.1 Summary and Conclusions.....	236
	8.2 Future Work.....	240
APPENDIX		
A	CALIBRATION CURVE FOR ABSOLUTE STYRENE CONCENTRATIONS IN REACTIVE BLENDS.....	244
B	STRESS-STRAIN GRAPHS AND STATISTICS.....	246
C	FTIR GRAPHS.....	256
D	IMAGE ANALYSIS	262
E	ALIASED TERMS FROM CHAPTER 7	265
	LIST OF REFERENCES.....	266
	BIOGRAPHICAL SKETCH	288

LIST OF TABLES

<u>Table</u>	<u>page</u>
2-1 The mechanisms of main reactions in the grafting process.....	23
2-2 Characteristics of Lupersol 101.....	24
2-3 Half life of Lupersol 101 based on temperature.....	25
2-4 Typical free radical kinetic values in solution.	27
2-5 Copolymerization constants for styrene and ethyl acrylate monomers.....	29
2-6 Structural and physical information about the monomers of interest.	29
3-1 ENGAGE® product data table.....	49
3-2 DSC consecutive heating/cooling cycles	53
3-3 Image analysis averages taken from etched SEM images of PP:8407 physical blends. At least three images were analyzed from Figures 3(a) thru (e), with data compiled in Appendix D.	61
3-4 DSC endothermic data comparing pure PP and 8407 to physical blends of PP and 8407. Standard deviation for pure PP is from an average of four samples.	70
3-5 DSC exothermic data comparing pure PP to 90:10_0, 90:10_A, and 90:10_B. An average of 3 runs were performed on 90:10_B.	72
4-1 ENGAGE® product data table.....	75
4-2 Structures of reactive materials of interest.....	75
4-3 PLM consecutive heating/cooling cycles.....	81
4-4 DSC consecutive heating/cooling cycles	83
4-5 Identification of formulations.....	86
4-6 Image analysis of etched SEM surfaces of several blends and alloys. This information is gathered from Appendix D, Figure 4-16, and Figure 3-5. Ligament thickness is calculated using the number average diameter.	102

4-7	Melt behavior of PP, PP-8407 physical blends, and PP-8407 alloys.....	115
4-8	DSC endothermic data comparing pure PP to 90:10_0, 90:10_A, and 90:10_B. An average of three runs were performed on 90:10_B.....	127
4-9	DSC exothermic data comparing pure PP to 90:10_0, 90:10_A, and 90:10_B.....	131
5-1	ENGAGE® product data table.....	148
5-2	Structures of reactive materials of interest.....	148
5-3	Three different temperature profiles for the extrusion of 80:20_C.....	152
5-4	Stress-strain behavior of 80:20_C as a function of temperature.....	154
5-5	Screw speed relationship to residence time.....	156
5-6	Stress-strain behavior of 80:20_C as a function of screw speed.....	158
5-7	Stress-strain behavior of PP:8407 alloys at a ratio of 90:10 as a function of initiator concentration.....	160
5-8	Stress-strain behavior of PP:8407 alloys at a ratio of 90:10 as a function of multifunctional monomer concentration.....	163
5-9	Stress-strain performance of PP:8407 alloys at a ratio of 90:10 as a function of styrene concentration.....	165
6-1	ENGAGE® product data table.....	169
6-2	Structures of reactive materials of interest.....	170
6-3	DSC consecutive heating/cooling cycles.....	174
6-4	Identification of Formulations in relation to Figure 6-2.....	175
6-5	Stress-strain data of 8407_0, 8401_0, and 8402_0.....	177
6-6	DSC endothermic data of 8407_0, 8401_0, and 8402_0.....	179
6-7	DSC exothermic data of 8407_0, 8401_0, and 8402_0.....	181
6-8	Stress-strain data of PP:ENGAGE alloys as a function of elastomer density.....	186
6-9	DSC endothermic data of 8407_A, 8407_B, 8402_A, and 8402_B.....	188
6-10	DSC exothermic data of 8407_A, 8407_B, 8402_A, and 8402_B.....	188
6-11	DSC endothermic data of 002_0, 8407_0, 8200_0, and 8842_0.....	197

6-12 DSC exothermic data of 002_0, 8407_0, 8200_0, and 8842_0	199
6-13 Stress-strain behavior of 002_B, 8407_B, 8200_B, and 8842_B.	205
6-14 DSC endothermic data of 8407_A, 8407_B, 8842_A, and 8842_B	208
6-15 DSC exothermic data of 8407_A, 8407_B, and 8842_A, and 8842_B.....	209
7-1 ENGAGE® product data table.....	214
7-2 Structures of reactive materials of interest.....	214
7-3 Factors of interest, coded variables, and levels for the impact modification of HDPE	217
7-4 Basic fractional factorial design using coded variables from Table 7-3.	218
7-5 Impact strength, elastic modulus, yield stress, and elongation at break results from the fractional factorial design created for the modification of HDPE.....	220
7-6 Analysis of variance table (partial sum of squares) for impact strength.	223
7-7 Analysis of variance table (partial sum of squares) for elastic modulus.....	226
7-8 Analysis of variance table (partial sum of squares) for yield stress.....	230
7-9 Analysis of variance table (partial sum of squares) for elongation at break.	232
B-1 Actual stress-strain values with standard deviations from figures in both Chapter 3 and Chapter 4.	246
B-2 Stress-strain properties of PP:ENGAGE blends and alloys as a function of elastomer melt flow index.	253
E-1 Aliased terms from the fractional factorial design given in Chapter 7	265

LIST OF FIGURES

<u>Figure</u>	<u>page</u>
2-1 The phase inversion mechanism proposed by Shih.	14
2-2 Morphology development of binary polymer blends proposed by Scott and Macosko.	15
2-3 Chemical structure of Lupersol 101	24
2-4 Schematic of H abstraction from PP and subsequent β -chain scission.	34
3-1 Schematic drawing of the reactive twin screw extruder and a common temperature profile.	50
3-2 Effect elastomer concentration on room temperature notched impact strength and melt flow index.	54
3-3 Stress-strain behavior of PP:8407 physical blends	56
3-4 Stress-strain properties of PP-8407 blends as a function of elastomer content.	57
3-5 SEM images of etched, cryo-fractured surfaces of PP:8407 physical blends as a function of elastomer concentration. (a) Virgin PP at 2,000X, (b) 95:5_0 at 10,000X, (c) 90:10_0 at 10,000X, (d) 80:20_0 at 10,000X, and (e) 70:30_0 at 2,500X. The bar markers for (a) and (e) = 10 μ m, and for (b), (c), and (d) = 1 μ m. 60	60
3-6 Storage modulus vs. temperature for PP:8407 Blends	63
3-7 Tan δ vs. temperature for PP:8407 blends from -120°C to 120°C. Insert represents Tan δ vs. temperature from -60°C to 60°C.	65
3-8 Loss modulus vs. temperature for PP:8407 physical blends	68
3-9 DSC melting endotherm of both pure PP and 8407 as well as blends of the two polymers.	69
3-10 Percent crystallinity of the physical blends and pure PP as a function of PP concentration.	70
3-11 DSC cooling exotherm of both pure PP and 8407 as well as blends of the two polymers.	71

4-1	Schematic drawing of the reactive twin screw extruder and a common temperature profile.	77
4-2	FTIR image of PP:polyisoprene reactive blend.	85
4-3	Representation of sample reference code.....	85
4-4	Room temperature notched Izod impact strength of PP blends and alloys. Reference material is virgin PP at 0.99 ft-lbs/in.	87
4-5	Izod Impact test specimens post-fracture. Left– Pure PP, Middle – 90:10_0, Right – 90:10_B.	88
4-6	SEM image showing the tip of an arrested crack from a room temperature notched Izod impact test of 90:10_0. Insert is a magnified image of crack tip.	89
4-7	SEM image showing the tip of an arrested crack from a room temperature notched Izod impact test of 90:10_B.	90
4-8	SEM image of 80:20_C (left) and Pure PP (right) fractured at room temperature without etching. Each image is located at the center of the impact bar, with magnification = 2,000X and marker bar = 10µm.	91
4-9	Stress-strain properties of 95:5 alloys compared to the 95:5 physical blend.	92
4-10	Stress-strain properties of 90:10 alloys as compared to the 90:10 physical blend...93	
4-11	Stress-strain properties of 80:20 alloys as compared to the 80:20 physical blend...93	
4-12	Stress-strain properties of 70:30 alloys as compared to the 70:30 physical blend...94	
4-13	FTIR image of a typical PP:8407 alloy containing styrene and multifunctional acrylate	98
4-14	Styrene grafting efficiency at various 8407 concentrations both with and without multifunctional monomer.	99
4-15	Molecular weight averages for pure 8407 and three grafted 8407 materials.	101
4-16	SEM images of (a) 95:5_B at 10,000X, (b) 90:10_B at 10,000X, (c) 80:20_B at 10,000X, and (d) 70:30_B at 5,000X. Each bar marker = 1µm.	103
4-17	Matrix ligament thickness of PP blends and alloys as a function of volume % of 8407.....	105
4-18	Room temperature notched Izod impact strength as a function of matrix ligament thickness for blends and alloys at various volume % 8407.....	105

4-19	TEM bright field images of (a) virgin PP and (b) 90:10_0 stained with RuO ₄ at a magnification of 63,500X. Bar marker on insert = 100nm.	107
4-20	TEM image of 90:10_A at 63,500X. All marker bars = 100nm.	108
4-21	TEM image of 90:10_B at 63,500X. All marker bars = 100nm.	109
4-22	TEM images of 80:20_A (left) and 80:20_B (right) at 63,500X.	110
4-23	TGA graphical comparison of a physical blend (90:10_0) and alloy (90:10_B)...	112
4-24	Melt flow index of physical blends and alloys as a function of 8407 content.	114
4-25	XRD pattern of pure PP, 90:10_0, 90:10_A, and 90:10_B.	118
4-26	Alignment of lamellae within spherulites of α -PP (left) and β -PP (right) from reference 278.	121
4-27	Etched lamellar morphology of isotactic polypropylene of well defined spherulite at 15kX magnification (a), bar marker = 2 μ m and periphery of a spherulite at 20kX magnification (b), bar marker = 2 μ m.	123
4-28	Etched lamellar morphology of 90:10_0 at 10.5kX magnification, with the bar marker = 5 μ m.	124
4-29	Etched lamellar morphology of 90:10_0 at 20kX magnification, with the bar marker = 2 μ m.	125
4-30	DSC heating traces of a physical blend (90:10_0) and alloys (90:10_A and 90:10_B).	126
4-31	DSC heating traces of a physical blend (80:20_0) and alloys (80:20_A, 80:20_B, and 80:20_C without styrene).	129
4-32	DSC cooling traces of a physical blend (90:10_0) and alloys (90:10_A and 90:10_B).	130
4-33	Polarized optical images of virgin PP cooled from the melt. (a) = 115.5°C at 50X, (b) = 113.5°C at 50X, (c) = 110°C at 50X, and (d) = 25°C at 20X magnification.	133
4-34	Polarized optical images of 90:10_0 cooled from the melt. (a) = 118°C at 50X, (b) = 114.5°C at 50X, (c) = 105°C at 50X, and (d) = 25°C at 20X magnification. A bubble (artifact) appears in the lower left hand of (b) and (c) and along the edges of (d).	134
4-35	Polarized optical images of 90:10_A cooled from the melt. (a) = 128°C at 50X, (b) = 124°C at 50X, (c) = 122°C at 50X, and (d) = 25°C at 20X magnification.	135

4-36	Polarized optical images of 90:10_B cooled from the melt. (a) = 135°C at 50X, (b) = 133°C at 50X, (c) = 130°C at 50X, and (d) = 25°C at 20X magnification.....	137
4-37	Storage modulus (E') and Tanδ comparison of 95:5_0 and 95:5_B as a function of temperature.....	139
4-38	Storage modulus (E') and Tanδ comparison of 90:10_0, 90:10_A, and 90:10_B as a function of temperature.....	140
4-39	Tanδ comparison of 90:10_0, 90:10_A, and 90:10_B between -50°C and 60°C to show a magnified graph of β ₈₄₀₇ and β _{PP}	141
4-40	Storage modulus (E') and Tanδ comparison of 80:20_0 and 80:20_B as a function of temperature.....	143
4-41	Storage modulus (E') and Tanδ comparison of 70:30_0 and 70:30_B as a function of temperature.....	144
5-1	Schematic drawing of the reactive twin screw extruder and a common temperature profile.....	149
5-2	Effect of extruder barrel temperature on room temperature impact strength, melt flow index, and grafting efficiency of 80:20_C.....	153
5-3	Impact strength, MFI, and grafting efficiency of 80:20_C as a function of screw speed.....	157
5-4	Impact strength, MFI, and grafting efficiency of 90:10_B as a function of initiator concentration.....	159
5-5	Notched impact strength, melt flow index, and grafting efficiency of PP:8407 alloys at a ratio of 90:10 as a function of multifunctional monomer concentration.....	161
5-6	Notched impact strength, melt flow index, and grafting efficiency of PP:8407 alloys at a ratio of 90:10 as a function of styrene monomer concentration.....	164
5-7	Notched impact strength, melt flow index, and grafting efficiency of PP:8407 alloys at a ratio of 80:20 as a function of styrene concentration.....	166
6-1	Schematic drawing of the reactive twin screw extruder and a common temperature profile.....	171
6-2	Representation of sample reference code.....	175
6-3	Impact strength, melt flow index, and melting temperature of physical blends as a function of the density of the copolymer.....	176

6-4	Digital images of room temperature fractured Izod impact bars as a function of elastomer density in the physical blends. From left to right: 8407_0, 8401_0, 8402_0.....	177
6-5	Stress-strain performance of PP/elastomer physical blends as a function of elastomer density.....	178
6-6	DSC melting endotherm of 8407_0, 8401_0, and 8402_0.....	179
6-7	DSC cooling exotherm of PP/elastomer physical blends as a function of elastomer density. Insert is for the temperature range of 20 to 100°C.....	180
6-8	Dynamic mechanical analysis of 8407_0, 8401_0, and 8407_0. Insert is a magnified graph from -60°C to 60°C of the β relaxation of PE.....	182
6-9	Room temperature impact strength, melt flow index, and grafting efficiency of 8407_B, 8401_B, and 8402_B.....	183
6-10	Room temperature impact strength, melt flow index, and grafting efficiency of 8407_C, 8401_C, and 8402_C.....	185
6-11	DSC melting endotherms of 8407_A, 8407_B, 8402_A, and 8402_B ranging from 60°C to 180°C. Insert is a magnified graph of the α melting peak of PP.....	187
6-12	DSC cooling exotherms of PP/elastomer physical blends as a function of elastomer density. Insert is for the temperature range of 20 to 100°C.....	189
6-13	Dynamic Mechanical Analysis comparison of (a) 8402_0 and 8402_B, (b) 8401_0 and 8401_B, and (c) 8407_0 and 8407_B.....	190
6-14	Molecular weight averages of the polyolefin elastomers of interest, ranked according to their melt flow index.....	192
6-15	Polydispersity (molecular weight distribution) of the polyolefin elastomers of interest.....	193
6-16	MFI and room temperature notched Izod impact strength of 8842_0 (highest molecular weight), 8200_0, 8407_0, and 002_0 (lowest molecular weight).....	194
6-17	Stress-strain performance of physical blends as a function of MFI of the copolymer.....	196
6-18	DSC melting endotherms of 002_0, 8407_0, 8200_0 and 8842_0.....	198
6-19	DSC crystallization exotherms of 002_0, 8407_0, 8200_0, and 8842_0.....	199
6-20	Impact Strength and melt flow index of 8842_A, 8200_A, 8407_A, and 002_A.....	201
6-21	Izod impact strength and melt flow index of 8842_C, 8200_C, 8407_C, and 002_C.....	202

6-22	Izod impact strength and melt flow index of 8842_B, 8200_B, 8407_B, and 002_B.	203
6-23	Dynamic mechanical behavior (E' and $\tan\delta$) of various alloys and blends. (a) 002_0 vs. 002_B, (b) 8407_0 vs. 8407_B, (c) 8200_0 vs. 8200_B, and (d) 8842_0 vs. 8842_B.	206
6-24	DSC melting endotherm of 8407_A, 8407_B, 8842_A, and 8842_B.	208
6-25	DSC crystallization exotherm of 8407_A, 8407_B, 8842_A, and 8842_B.	209
6-26	Effect of supercritical carbon dioxide at 1500 psi on the grafting efficiency of 8842_B. Injection was in zone 3.	211
7-1	Schematic drawing of the reactive twin screw extruder and a common temperature profile.	215
7-2	Half normal plot showing, in coded variables, the most significant effects on impact strength. A = initiator concentration and C = concentration of 8842.	222
7-3	Normal plot of residuals (a) and outliers (b) show the diagnostic results of the model for impact strength.	224
7-4	Cube graph of the effect of % initiator, 8842 content, and % styrene on impact strength at constant screw speed, % DEGDA, and temperature.	225
7-5	Half normal plot showing, in coded variables, the most significant effects on elastic modulus.	226
7-6	Normal plot of residuals (a) and outliers (b) show the diagnostic results of the model for elastic modulus.	227
7-7	Cube graph of the effect of % initiator, 8842 content, and % styrene on elastic modulus at constant screw speed, % DEGDA, and temperature.	228
7-8	Half normal plot showing, in coded variables, the most significant effects.	229
7-9	Normal plot of residuals (a) and outliers (b) show the diagnostic results of the model for yield stress.	230
7-10	Cube graph of the effect of % initiator, 8842 content, and % styrene on yield stress at constant screw speed, % DEGDA, and temperature.	231
7-11	Half normal plot showing, in coded variables, the most significant effects.	232
7-12	Normal plot of residuals (a) and outliers (b) show the diagnostic results of the model for elastic modulus.	233
7-13	Cube graph of the effect of % initiator, 8842 content, and % styrene on elongation at break at constant % styrene, % DEGDA, and temperature.	234

8-1	Schematic drawing of the likely free radical initiated processes during the reactive extrusion of PP, 8407, initiator, styrene, and multifunctional monomer.	237
8-2	Interpretation of the effect of <i>in-situ</i> grafted polymeric chains at the PP-elastomer interface (blue circles = elastomer domains, black lines = grafted polymers). The physical blend (left) has no grafting and the alloy (right) has a high degree of grafting.	239
B-1	Stress-strain graph comparison of 95:5 (PP:8407) physical blend and alloys.	247
B-2	Stress-strain graph comparison of 90:10 (PP:8407) physical blend and alloys.	247
B-3	Stress-strain graph comparison of 80:20 (PP:8407) physical blend and alloys.	248
B-4	Stress-strain graph comparison of 70:30 (PP:8407) physical blend and alloys.	248
B-5	Stress-strain graph comparison of the effect of extruder barrel temperature in relation to 5-2 and Table 5-4. 1= low temperature, 2=middle temperature, 3=high temperature.	249
B-6	Stress-strain graph comparison of the effect of extruder screw speed in relation to Table 5-6.	249
B-7	Stress-strain graph comparison of the effect of initiator concentration in relation to Table 5-7.	250
B-8	Stress-strain graph comparison of the effect of DEGDA concentration in relation to Table 5-8.	250
B-9	Stress-strain graph comparison of the effect of styrene concentration in relation to Table 5-9.	251
B-10	Stress-strain graph comparison of the effect of elastomer density in relation to Figure 6-5 and Table 6-5.	251
B-11	Stress-strain graph comparison of the effect of elastomer density in relation to Table 6-8.	252
B-12	Stress-strain graph comparison of the effect of elastomer density in relation to Table 6-8.	252
B-13	Stress-strain graph comparison of the effect of elastomer density in relation to Table 6-8.	253
B-14	Stress-strain graph of physical blends of ENGAGE elastomers with PP as a function of elastomer melt flow index	254
B-15	Stress-strain graph comparison of the effect of elastomer MFI.....	254

B-16	Stress-strain graph comparison of the effect of elastomer MFI.....	255
C-1	FTIR graph comparison of 95:5_0, 95:5_A, 95:5_B, and 95:5_C.....	256
C-2	FTIR graph comparison of 90:10_0, 90:10_A, 90:10_B, and 90:10_C.....	257
C-3	FTIR graph comparison of 80:20_0, 80:20_A, 80:20_B, and 80:20_C.....	257
C-4	FTIR graph comparison of 70:30_0, 70:30_A, 70:30_B, and 70:30_C.....	258
C-5	FTIR graphs from Chapter 5 (Figure 5-2) of alloys processed at varying temperatures. 1 = low barrel temperature, 2 = middle barrel temperature, 3 = high barrel temperature.	258
C-6	FTIR graphs from Chapter 5 (Figure 5-3) of alloys processed at varying screw speeds.	259
C-7	FTIR graphs from Chapter 5 (Figure 5-4) of alloys processed at varying concentration of initiator.	259
C-8	FTIR graphs from Chapter 5 (Figure 5-5) of alloys processed at varying concentration of multifunctional monomer.	260
C-9	FTIR graphs from Chapter 5 (Figure 5-6) of alloys processed at varying concentration of styrene, with DEGDA as multifunctional monomer.	260
C-10	FTIR graphs from Chapter 5 (Figure 5-7) of alloys processed at varying concentration of styrene, with TMPTA as multifunctional monomer.	261
D-1	Histogram of average particle diameters for (a) 70:30_0 and (b) 70:30_B.	262
D-2	Histograms of particle roundness for (a) 70:30_0 and (b) 70:30_B.	262
D-3	Histogram of average particle diameters for (a) 80:20_0 and (b) 80:20_B.	263
D-4	Histograms of particle roundness for (a) 80:20_0 and (b) 80:20_B.	263
D-5	Histogram of average particle diameters for (a) 90:10_0 and (b) 90:10_B.	263
D-6	Histograms of particle roundness for (a) 90:10_0 and (b) 90:10_B.	264
D-7	Histogram of average particle diameters for (a) 95:5_0 and (b) 95:5_B.	264
D-8	Histograms of particle roundness for (a) 95:5_0 and (b) 95:5_B.	264

Abstract of Dissertation Presented to the Graduate School
of the University of Florida in Partial Fulfillment of the
Requirements for the Degree of Doctor of Philosophy

HIGH IMPACT STRENGTH POLYMERS HAVING NOVEL NANO-STRUCTURES
PRODUCED VIA REACTIVE EXTRUSION

By

Nathan Fraser Tortorella

December 2005

Chair: Charles L. Beatty

Major Department: Materials Science and Engineering

A major focus of scientists and engineers over the last century has been to increase the impact strength and therefore reduce the brittleness of materials. By altering and adding energy absorption mechanisms, brittle failure can be averted. Isotactic polypropylene (PP) is the focus of this dissertation because it is an extremely low cost, high volume, versatile plastic but behaves in a brittle manner at or below room temperature or in a notched state. Early work on impact modification of polypropylene focused on blending energy-absorbing low density elastomers and rubbers. These binary blends all had a common problem – an increase in impact strength was paralleled by a significant decrease in both elastic modulus and yield stress.

Reactive extrusion processing has allowed the *in-situ* compatibilization of isotactic polypropylene and metallocene-catalyzed ethylene-octene copolymers (EOCs). This process involves combining both the comonomer and vector fluid approaches to grafting polyolefins. Styrene monomer and a multifunctional acrylate monomer undergo

peroxide-induced copolymerization and grafting in the presence of both PP and EOC.

This results in a phase separated alloy with an impact strength over 13 times that of pure polypropylene and double that of the physical blend. There is also a significant improvement in stress-strain performance when comparing the alloys to physical blend counterparts.

Many researchers have categorized the necessary components to toughening polypropylene as pertaining to the amorphous phase. The alloys described in this dissertation meet the criteria put forth by these researchers, namely low density, crystallinity, and modulus of the elastomer phase, sub-micron particle diameter, close inter-particle distance, and a high degree of entanglements of both the PP matrix phase and EOC minor phase. But many people neglect to study the crystalline state of impact modified PP in conjunction with the amorphous phase. This work shows that the typical 10-100 μm diameter spherulitic structures found in pure PP are not present in the alloys. In fact, the spherulites are less than a micron in diameter, are uniformly distributed throughout the sample, and crystallize at much higher temperatures. SEM images, when coupled with DSC and XRD, reveal the presence of a high number of small lamellar crystals composed of a unique highly dense cross-hatched structure. Thus, impact strength and stiffness can be simultaneously improved by controlling the size and cross-hatch density of the lamellar crystals and applying phase transformation toughening concepts.

CHAPTER 1 GENERAL INTRODUCTION

1.1 Introduction

The field of materials science and engineering has emerged as a premier discipline which encompasses the development, synthesis, and processing of new materials. Calister describes materials science as investigating the relationships that exist between the structures and properties of materials, whereas materials engineering is based upon designing or engineering the structure of a material to produce a predetermined set of properties [1]. The structure-processing-properties relationship holds true for the creation of all advanced materials, with polymers, metals, ceramics, and electronic materials as the core classes. Polymers are the focus of the dissertation, which are essentially organic macromolecules chemically based on carbon, hydrogen, and other nonmetallic elements.

Polymer blending is an economic process to create a material with a balance of properties that would otherwise not be possible [2-12]. If a material can be generated that will lower the cost while maintaining or improving performance of a particular product then the manufacturer must use it to remain competitive. Many engineering resins may lack chemical resistance, impact toughness, flame retardancy, high temperature performance, or weatherability, which can be solved via blending with other engineering or commodity plastics. The development of a new blend or compound from existing materials is generally more rapid than that of an entirely new polymer.

Polymer blends can be characterized by their phase behavior as being either miscible or immiscible (immiscible blends having multiple amorphous phases) [10, 12-

14]. A blend's mechanical, thermal, and rheological properties, amongst others, depend strongly on its state of miscibility. Nearly all polymer pairs are immiscible, forming two-phased systems in which the interface is a source of weakness. Polymer-polymer immiscibility is a direct consequence of the high molecular weights of the polymer molecules. Blending two polymers is not thermodynamically favorable because the mixing of a relatively low number of molecules leads to a positive enthalpy of mixing and low entropy of mixing [8, 15-18].

By simply blending two immiscible polymers, the resulting material has improved properties but usually at the expense of another property. For example, adding rubbery or elastomeric particles to a polypropylene (PP) matrix increases impact strength but sacrifices yield strength and elastic modulus [19-24]. Previous routes to toughen PP have their drawbacks, such as the migration phenomenon with plasticizers and costly in-reactor copolymerization of ethylene and propylene. In order to overcome these problems, many researchers have found that by controlling the size and distribution of the rubber particles, cohesive strength of the elastomer, the degree of physical entanglements in the system, and interfacial adhesion between the rubber and the matrix, all properties are vastly improved over the original blend.

Physically blending an elastomer with a brittle semicrystalline polymer is not sufficient for overall property improvement, so a reactive extrusion process (compatibilization) is often applied to create novel polymeric alloys. The term alloy has been defined by the *Polymer Technology Dictionary* as a composition, or blend, which is based on two or more polymers, the properties of which are significantly better than would be expected from a simple blend [25]. The system is typically phase separated

with a certain degree of chemical bonding or grafting between phases. Compatibilizers are sometimes used to control the adhesion aspect of these blends, which therefore results in finer dispersed phase morphology, uniform distribution of domains, better processability, enhanced mechanical properties, and increased thermal stability. They effectively act as high molecular weight surfactants by locating at the interface between the immiscible polymers [12, 14, 26-40].

Compatibilizers are traditionally thought of as block or graft copolymers which contain functional groups that may or may not react with the polymers present in the blend. Three drawbacks of these pre-made copolymers are that they are expensive, unstable upon annealing, and can cause a substantial increase in viscosity during processing [41]. The effectiveness of these materials are also diffusion dependent and may not entirely wet the interface of the dispersed domain [31, 42, 43].

In-situ compatibilization is a process in which a fine dispersion of a minor phase can be generated quickly by reactive extrusion. This process involves using liquid reactants, such as functional monomers, to locate at the interface between immiscible polymers and subsequently polymerize. The purpose is to graft the monomers onto both polymers in a binary blend and create what is believed to be a network-like bridge between the phases. The ultimate product has enhanced mechanical properties, better processability, and a unique morphology.

This dissertation focuses on the *in-situ* compatibilization of two phases – the isotactic polypropylene matrix and an ethylene-1-octene copolymer (otherwise known as linear low density polyethylene) minor phase. PP is known to behave in a brittle manner at or below room temperature and in a notched state, thus limiting its use in blow molded

bottles, for example. The elastomeric copolymer, which has a glass transition temperature well below room temperature, will act as the impact modifier for polypropylene and contains a fully saturated backbone which limits environmental degradation. But addition of elastomer alone compromises both stress-strain performance and processability of the blend. The *in-situ* compatibilization technique established by previous researchers has been applied to this system, and drastic improvements in all macro-scale properties have been achieved.

In order to understand this dissertation, one must be versed in processing of polymers, polymer blends and toughening of polymers, solid state and melt free radical grafting of polymers, and free radical polymerization. This is a very complex process, not only because of the number of components and variables, but because of the dependency on both the rate of reaction and rate of morphology development. The following six chapters describe various aspects of this unique polymeric alloy.

1.2 Chapter Summaries

Chapter 2 is a background/review of much of the research that has explored the complex issues involved in reactive extrusion. The description includes the polymers of interest (i.e., isotactic polypropylene and ethylene-1-octene copolymers), the type of processing equipment involved, how the morphology of polymer blends develop in an extruder, toughening brittle semicrystalline thermoplastics, many characteristics of free radical polymerization and free radical induced grafting of polyolefins, and how all of these aspects tie in to create novel *in-situ* compatibilized polymers.

A fundamental study of the physical blends of a certain grade of copolymer with polypropylene is undertaken in Chapter 3. Little research has been conducted on using low molecular weight ethylene-octene copolymers to toughen polypropylene, but this

chapter proves that these new copolymers are effective PP modifiers up to a certain concentration. Many concepts and characterization techniques are introduced and explained in detail so as to aid in analysis of results gathered in following chapters.

A complete picture of the mechanisms of toughening in several alloyed systems is described in Chapter 4. This includes defining the effect of elastomer content on mechanical, chemical, rheological, and morphological properties of alloys. A comparison is made between physical blends and alloys containing various levels of liquid reactants. The crystalline as well as amorphous states are described in detail, with both contributing to the overall performance of the alloys.

In Chapter 5, the actual processing characteristics of the alloys are elaborated upon. Extruder screw speed and barrel temperature are directly tied into alloy performance. The effects of varying reactant concentrations are also systematically studied.

Chapter 6 delves deeper into the effect of elastomer molar mass and crystallinity on the behavior of both the physical blends and alloys. It explains many aspects of alloy behavior that would not have otherwise been possible.

For Chapter 7, a design of experiments has been conducted to see the effect of this *in-situ* compatibilization technique on high density polyethylene's impact strength and stress strain behavior. High density polyethylene is a high volume commodity plastic and modification to a high impact polymer is the goal. This chapter is followed by a concluding chapter with future research possibilities along with appendices and references.

CHAPTER 2 BACKGROUND AND LITERATURE REVIEW

2.1 Polymers of Interest

2.1.1 Isotactic Polypropylene

Isotactic polypropylene (PP) combines low price with attractive performance; e.g., heat distortion temperature $> 100^{\circ}\text{C}$, strength, stiffness, corrosion resistance, and versatility in applications, ranging from automotive moldings to films and textile fibers [44-47]. PP is a semi-crystalline thermoplastic so its properties are strongly dependent on molecular weight and defect distributions, which in turn affect both rheology and crystallinity. Most end-use properties of PP homopolymers, such as stiffness, hardness, and high temperature mechanical properties, are positively influenced by their overall crystallinity, whereas impact strength and elongation are negatively influenced.

A major factor in the profitability of PP is the availability of low-cost propylene monomer. There are two main sources of the monomer: co-production with ethylene or separation from gasoline cracker streams in a petroleum refinery. When polymerizing PP, three requirements are always present: its chain must be linear (monomer always adds to the chain end), regiospecific (monomer is always added in head-to-tail manner), and stereospecific (monomer always adds in the same stereo arrangement, or same side of chain) [46]. In 1954 Giulio Natta polymerized propylene by means of a modified Ziegler catalyst and obtained a blend of isotactic and atactic polypropylene [45b, 45c]. For his pioneering invention, he and Karl Ziegler received the Nobel Prize for chemistry in 1963. The present day polymerization process medium can be either liquid or gaseous

propylene or an inert hydrocarbon such as hexane. The process can be either bulk or gas phase or a combination of both. Most polyolefin manufacturing processes presently utilize heterogeneous Ziegler-Natta catalysts. Because these catalysts have more than one type of active site, they produce PP with a broad molecular weight distribution (MWD) and non-uniform stereoregularity.

Isotactic polypropylene is such a versatile plastic that its applications are innumerable [45]. Some markets include fibers, carpet and upholstery, films, medical devices, automotive (under the hood, exterior, interior), containers, construction, nonwoven fabrics, appliances, and transportation. The resistance of PP to chemicals is well documented and one of the principal reasons automobile batteries are made of PP. Having a HDT above 100°C allows use with hot aqueous liquids, including steam-sterilized medical goods. The processability of PP also makes it attractive. These methods include extrusion, oriented and melt blown fibers, biaxially oriented film, blown film, sheet, thermoforming, profiles and pipe, wire and cable coating, injection molding, extrusion and injection blow molding, and compression molding.

2.1.2 Ethylene-1-Octene Copolymer

Dupont Dow Elastomers produce and license novel ethylene-1-octene copolymers with the tradename ENGAGE® via INSITE® technology, which allows extraordinary control over polymer structure, properties, and rheology [48-52]. They use a relatively new single-site metallocene catalyst to polymerize a wide variety of bulky monomers, including linear α -olefins. In contrast to Zeigler Natta (Z-N) catalysts, they yield polymers which incorporate higher levels of the α -olefin to achieve lower polymer density or crystallinity, and a uniform comonomer distribution with a polydispersity of about two [45a, 53, 54]. The microstructural uniformity from metallocene catalysts

allows greater dimensional stability, higher impact resistance, greater toughness at low temperatures, and higher resistance to environmental stress cracking [49]. The ability to incorporate higher levels of comonomer has allowed densities of the copolymers to reach 0.87 g/cm³, previously unattainable by Z-N catalysts. The development of new metallocene catalyst generations has bridged the gap between rubber and thermoplastic technology [44].

These materials exhibit an enormous span of rheological, mechanical, and thermal properties [48, 55, 56]. They have excellent low temperature properties, clarity and crack resistance. Their superior UV, ozone and weather resistance are primary advantages over other impact modifiers such as EPDM (ethylene-propylene-diene monomer), EPR (ethylene-propylene rubber), and SBS (styrene-butadiene-styrene).

In a comparison of elastomers, an EOC had a melting temperature 10°C higher than EPDM of similar crystallinity and molecular weight [57]. A more homogeneous distribution of crystal morphology is apparent for the copolymers, with the more defect-ridden EPDM providing less mechanical integrity. The maximum strength and extensibility of the ethylene-octene copolymer are greater than EPDM even though the EOC is lower in molecular weight.

An extensive study of several ethylene- α -olefin copolymers was conducted by Bensason et al. [52] who classified these novel materials into four types: Type 1 copolymers are those with densities less than 0.89 g/cm³ and show a low degree of crystallinity, low melting temperature, and the absence of cooling rate effects. Spherulites are nonexistent and the granular, nonlamellar morphology suggest that the crystalline regions should be described as fringed micelles. Type 2 copolymers range in density

from 0.91 – 0.9 g/cm³ and form poorly developed, unbanded spherulites containing both bundled and lamellar crystals. Type 3 materials (0.93 – 0.91 g/cm³) form smaller spherulites with thinner lamellae than HDPE homopolymer. Although the branches restrict crystallization to an extent, the ethylene sequences are long enough to crystallize in the lamellae. The fourth type has a density of 0.93 g/cm³ or greater and exhibits lamellar morphology with well-developed spherulites. Lamellar thickness is strongly related to the kinetics of crystallization because of the lack of long chain branching.

Over the last decade, much effort has been put forth to understand the crystalline morphology and crystallization processes of these copolymers. A common consensus is that as the concentration or length of comonomer increases, crystallinity decreases [28, 48-52, 58-64]. The introduction of more comonomeric units hinders the chain regularity necessary for crystallization to take place [56, 57]. There is a distortion of the crystalline lattices with an increase of 1-octene content but even at very low density (0.882 g/cm³), certain amounts of lamellar crystal is still present [60]. The melting enthalpy is reduced with increasing 1-octene content in the copolymer. Melting temperature was shown by DSC to be inversely proportional to comonomer content [51]. Reorganization of polymer chains occurs at room temperature for copolymers having a comonomer content higher than 2.1 mol% of 1-octene [61] but this seems less likely for very high comonomer contents because during annealing the branches would have to be drawn through crystals [65].

2.2 Processing

2.2.1 Reactive Twin Screw Extrusion

Polymer processing in a twin screw extruder has been developed since the 1930s and 40s, with several varieties offering numerous advantages over the other [2-4, 31, 66].

Twin screw extrusion (TSE) has been shown to be a versatile, cost effective method to produce a uniform, optimized polymer based product. An ideal compounder will have a uniform shear and elongational stress field, flexible control over uniform temperature, pressure and residence time, compatibility for homogenization of liquids with large differences in rheological properties, efficient homogenization before degradation, and flexibility for change in mixing parameters. TSE's are useful because of the ease of feeding materials, excellent dispersive and distributive mixing, temperature control, control over residence time distribution, reaction under pressure, continuous processing, unreacted monomer and byproduct removal, post-reaction modification, and viscous melt discharge. Most of the mixing is achieved with kneading paddles.

The main geometrical features that distinguish twin screw extruders are the sense of rotation and the degree of intermeshing. Twin screw extruders whose screws rotate in the same direction are co-rotating. The intermeshing twin screw extruder is self-wiping in nature and helps to minimize the very long residence time tail frequently found with extruders. They give a relatively uniform shear rate distribution and because the feed rate is independent of screw speed, high screw speeds are possible (500 rpm) with correspondingly high throughput rates. With this high speed, small sized equipment can achieve high melting and mixing capacities. Two drawbacks are the cost to purchase and maintain and a metered feeding device is needed in starve feeding mode. APV- Baker Perkins is the manufacturer of our extruder, with some unique features being a clam shell barrel, greater free volume, and barrel valves.

The first developments in the use of extruders as reactors were made about 60 years ago and melt phase modification of polymers has been done for over 35 years. Reactive

extrusion (REX) refers to the deliberate use of chemical reactions during continuous extrusion of polymers and/or polymerizable monomers [4, 31, 67-69]. Reactions have been performed on molten polymers, on liquefied monomers, or on polymers dissolved, suspended in, or plasticized by solvent. The types of chemical reactions that have been performed by reactive extrusion include bulk polymerization, graft reaction, interchain copolymer formation, coupling/crosslinking reactions, controlled degradation, and functionalization/functional group modification. The attainment of proper mixing is undoubtedly the single most important consideration when specifying or designing an extruder-reactor. Chemical reaction is a molecular event, so proper mixing in reactive extrusion means mixing at the molecular level and maximizing the interface between dispersed phases and the matrix [4, 31, 70-72].

Polyolefins have proven to be preferred substrates for reactive extrusion experiments largely due to their ready availability, low cost, and commercial applications. The advantages of synthesizing graft copolymers by reactive extrusion as opposed to alternating technologies include little or no use of solvents, simple product isolation, short reaction times, continuous process, and relatively low infrastructure costs [68]. The ability of an extruder to handle materials having high viscosities without any solvents results in a dramatic raw material cost reduction, no solvent recovery equipment, an ready-to-use products [73]. Some potential disadvantages or difficulties are the need to achieve intimate mixing of reactants and substrates, high reaction temperatures necessary to form a polymer melt, and polymer degradation or crosslinking.

2.2.2 Morphology Development in an Extruder – Dispersive and Dissipative Mixing

The performance of extruded materials is determined, amongst others, by the final morphology and dispersion [74, 75]. For blends and alloys, the morphology depends on

the composition, rheological and physical characteristics of the components, relative compatibility, and the nature and intensity of the mixing. When purely compounding two plastics, they go through dispersive as well as distributive mixing stages [3, 31, 32, 76, 77]. Dispersive mixing is the breaking up of clumps or aggregates of solids into the ultimate particulate size, or of immiscible polymers into the desired domain size. It is dependent upon shear and elongational stress and is achieved by shearing the particulate matter under high stress usually by kneading disks. In distributive mixing, spatial uniformity of all components throughout the mixture is desired. This is best achieved by frequent reorientation of flow elements under strain, including dividing, stretching, distorting, and/or reorienting the flow. Mixing performance is known to decrease with increasing viscosity [72].

The most significant evolution of morphology occurs in the initial melting zone of the extruder. During the initial stages of blending, the elastic behavior is most important but the viscous and interfacial behavior of the components in a system is undoubtedly important in the later stages of mixing. The maximum shear stress, accompanied with frictional and extensional forces, is usually generated at the melting zone of the extruder and imparts a high degree of mixing [13, 31, 32, 60, 78, 79]. The melting mechanism arises from the dissipation of the energy created by interparticle friction, rather than by friction against the barrel wall or by heat transfer through the barrel wall [3, 75]. The rate of melting controls the rate of reaction and morphology development [31]. Each polymeric component changes into very small particles as droplets within a very short time and distance (0.1-10 seconds and a few millimeters). A thermoplastic is dispersed in

the rubber phase with the plastic pellet size reduced from 3 mm to 5-20 μm , then to approx 1 μm with eventual coalescence [31, 78, 79].

2.2.3 Melting and Droplet Breakup Mechanisms

As the solid begins to melt, the feed mixture may go through its most viscous stage, that of a highly filled slurry or paste of unmelted solids in just-melted resin [3, 32, 75, 80-82]. Often the minor phase softens first and will coat particles of the major phase, which will delay its melting [13]. Transformation of a solid pellet involves three steps: melting/plastification of the pellet, deformation/stretching of the molten polymer, and formation of fine particles which may be subject to coalescence [31].

Several theories have been formulated which describe the process of melting and morphology development [32, 75, 78, 81, 83]. The first to model this behavior was Shih [78, 79] with the phase inversion mechanism. He found that polymer blends go through a number of sequential physical changes before being combined into a cohesive mixture to minimize free energy. For semicrystalline polymer/rubber mixtures, plastic pieces are initially torn from the pellet surfaces and form a mixture with drawn out layers of rubber. A lower melting or softening polymer dispersed into a higher melting polymer of major phase volume follows a 4-stage inversion mechanism as shown in Figure 2-1: A. The rubber forms a continuous phase closely packed pellets are suspended in it; B. Plastic pellets break up layer by layer as the pellet surfaces begin to soften, shear, and pull off from the unmelted solid core and are dispersed in the rubber phase; C. In the region of maximum torque (0.7 μm particles), an abrupt phase inversion occurs due to coalescence

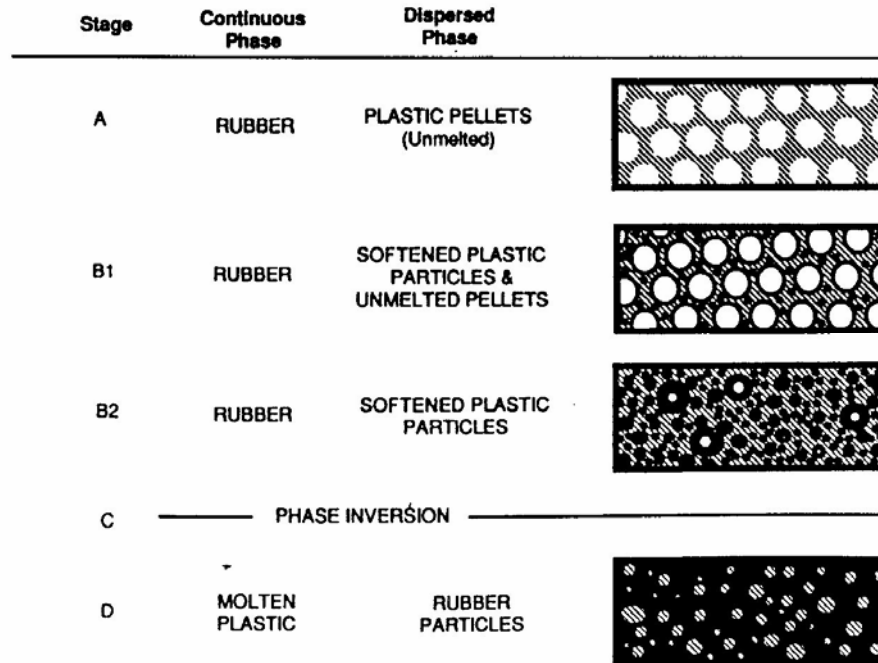


Figure 2-1: The phase inversion mechanism proposed by Shih.

of molten plastic particles and finely divided rubber droplets are formed in a continuous plastic matrix; D. The final stage is a viscoelastic fluid matrix with finely divided rubber droplets suspended in it followed by a continued decrease in torque.

Although the onset of phase inversion is abrupt, the completion of the phase inversion during phase C is not instantaneous. A small amount of the high melting polymer remains trapped in the rubber phase at the end of the mixing cycle. During the phase inversion, the mixture morphology changes from a continuous rubber phase with a very high concentration of high melting particles (80%) to a continuous molten plastic phase with a smaller amount of dispersed rubber particles (20%). The overall viscosity is expected to drop significantly, simply from the change in dispersed phase concentration.

Sundararaj [32] and Scott and Macosko [83] proposed a droplet breakup and coalescence theory for morphology development (Figure 2-2). An initial mechanism of droplet breakup involves the formation of sheets or ribbons of the dispersed phase in the

matrix, which are drawn out of a large mass of the dispersed phase. The pellet breakup is primarily controlled by the rate of deformation and subsequent relaxation of the pellet phase. As the relaxation time of the pellet decreases (more elastic behavior), it becomes more difficult to create a sheet. Owing to the effects of flow and interfacial tension, these sheets are unstable and holes begin to form in them. A high stress level followed by a lower stress level is required to achieve efficient mixing [84]. In the high stress level, the dispersed phase is stretched and extended into shapes, which undergo instabilities and break up upon entering the low stress level.

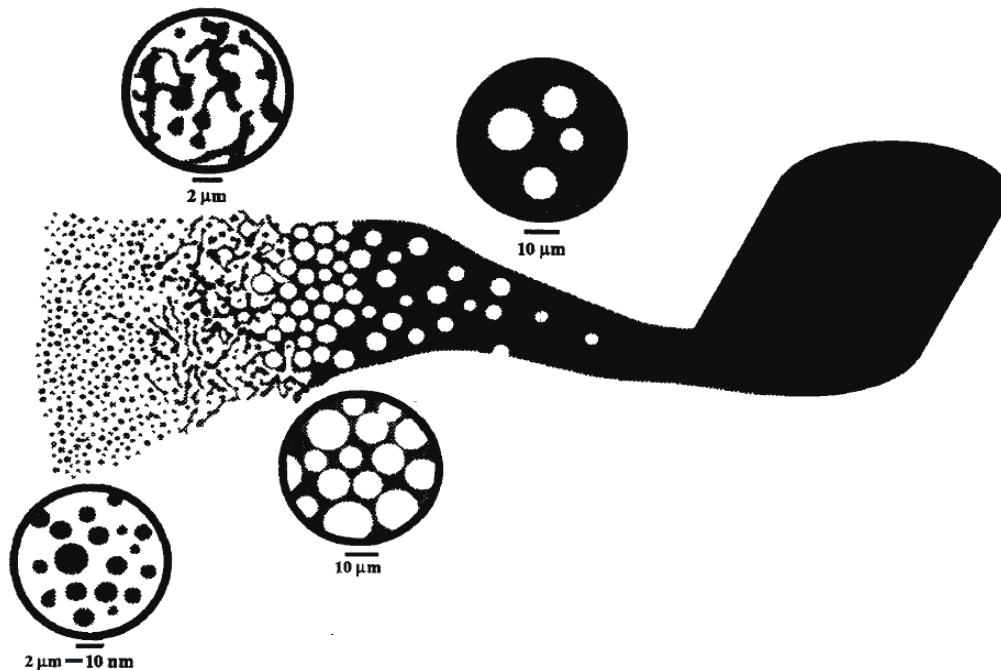


Figure 2-2: Morphology development of binary polymer blends proposed by Scott and Macosko.

As the sheet grows, the holes are filled with the matrix phase, which surrounds the sheet on either side. When the holes in the sheet or ribbon attain a sufficient size and concentration, a fragile lace structure is formed, which begins to break apart into irregularly shaped pieces of a wide distribution in size. These pieces are approximately

the diameter of the particles generated in the blend at long mixing times. The irregular pieces continue to break down until all of the particles become nearly spherical.

This proposed mechanism results in the generation of very small particles at very short timescales. As a piece of dispersed phase undergoes this deformation mechanism, many very small particles may be generated very quickly. As the mixing time proceeds, a greater proportion of dispersed phase is cycled through this mechanism.

2.2.4 Morphology Development Dependency on Rate of Reaction

Typically, small minor phase drops less than 1 micron are desired. If the dispersed phase is dilute, this is relatively easy but at dispersed phase concentrations greater than 1%, collisions between drops occur and domain size increases due to coalescence [13, 32, 42, 78, 79]. Also, the particle size distribution broadens at higher concentrations. Coalescence of the dispersed domains has been shown to be dramatically reduced (up to 30%) by bonding at the interface [32, 42, 85, 86]. Reaction increases the effective interfacial tension and both delays and intensifies the phase inversion process. The morphology development of the reactive system parallels its non-reactive counterpart, but the final number average particle size is two orders of magnitude smaller. Steric stabilization of the dispersed phase is more important than interfacial tension decrease [32, 87-89]. When the blend is reactive, very high concentrations of the major phase can exist as the dispersed phase for longer periods of time before phase inversion occurs. If the particles are not monodisperse and are not perfect spheres, then much higher concentrations (>74%) of the dispersed phase are possible [32].

One can imagine that when the major phase envelops the minor phase, small particles of the major phase generated during melting will be trapped inside the minor

phase. If the system is reactive, then the occluded domains will be stabilized and will not be able to coalesce with the matrix [32].

During reactive extrusion, a time scale will exist for both the morphology development and reaction. Polymeric alloys all have one thing in common – the rate of melting dictates when the reaction will begin [13, 31, 32, 42]. For these systems, reaction occurs almost immediately after the melting of the polymers. There is a fine balance between the time for morphology generation and reaction time, so the ratio must be manipulated to obtain the best processing conditions and optimum morphologies. When compounding all components together, the benefits of co-melting are realized by good dispersion of the materials and a greater probability of locating reactive ingredients at the interfaces to facilitate grafting/bonding [27, 90]. If liquid reactants are added downstream after melting has occurred, dispersion is difficult due to the highly viscous molten polymer which will lead to polymerization rather than grafting onto the polymer.

The flow in an extruder promotes the reaction in two ways: First, it either breaks or deforms the suspended droplets and increases the interfacial area available for the reaction. Second, the flow convectively increases the mass transport to supply fresh reactants to the reaction [71]. The improved reaction rate by back and forth flow can be attributed to more efficient production of new interfacial area [72].

Many studies have shown that the majority of reaction occurs in the melting zone. For monomer grafting onto polypropylene, the conversion can be up to 70% of the final value upon melting [91]. The level of styrene grafting onto a polyolefin can be 85% after the materials pass through a kneading block zone [92]. Another study has shown that free radical grafting of a monomer onto PE or PP has already gone to completion just

after the kneading block [90]. Machado et al. found that regardless of the type of polyolefin, the majority of grafting reaction occurred in the melting zone of the extruder [93]. They also found that higher grafting yields exist for lower viscosity polymers, possibly due to the melting phenomenon. Grafting may actually occur below the melting temperature of the polymer because of significant levels of peroxide decomposition [94, 95].

Diffusion of reactants is not the most important issue for an alloyed system because if the reaction rate is fast, the size of the dispersed phase will be very small [42]. A good compatibilizing chemistry has to be fast enough compared with the rate of interfacial area generation so that once the interface is created, it is stabilized quickly by a layer of copolymer so as to minimize coalescence [31]. The shearing or extensional flow experienced by the high molecular weight polymers creates a very large interfacial area, thus reducing the need for long range diffusion and facilitating reaction at the interface.

2.2.5 Viscosity and Reaction Effects on Morphology Development

When two immiscible polymers are blended, one phase is mechanically dispersed inside the other. The size and shape of the dispersed phase depend on several processing parameters including rheology, interfacial properties, and composition [31, 32, 96].

Viscosity ratio and surface tension between the major and minor phases play important roles in determining droplet size [31, 39, 69, 75, 82]. With the viscoelastic fluids generally encountered in polymer processing, the lower the elastic nature of dispersed phase, the lower the matrix stresses required to break up and stabilize them. Taylor was the first to theoretically describe droplet breakup and formation while suspended in another liquid medium [97, 98]. When the rate of distortion of the fluid or the radius of the drop is great enough, the drops tend to break up. For a very small

viscosity ratio ($\eta_{\text{Drop}}/\eta_{\text{Matrix}}$), the drop remains coherent in spite of the fact that it gets very long and narrow. The act of bursting is always an elongation to a threadlike form followed by degeneration into drops which are of the order of $1/100^{\text{th}}$ of the size of the original drop. A low viscosity minor phase will break up into small droplets early in the extrusion process [32, 76, 96] but beyond a minimum viscosity coalescence is favored [39].

2.3 Toughening of Polymers

2.3.1 Origins of Polymer Toughening

Polymer toughness, or the property of resisting fracture by absorbing and dissipating energy, is a highly sought after characteristic of a material or product. It depends on many parameters including temperature, pressure, deformation rate, shape of specimen, and type of load, aside from material properties like molecular weight, polydispersity, chain packing, chain entanglements, crystallinity, heterogeneity, etc. Brittle fracture occurs at high strain rates, low temperatures, and in thick sections because each restricts the extent of the yield zone. Plastic deformation itself is a complex phenomenon and involves both crystalline and amorphous phases [99]. Energy is absorbed within the sample by viscoelastic deformation of the polymer chains, and finally by the creation of new surface areas [100].

Fracture resistance in rubber toughened polymers is generally attributed to three major mechanisms that absorb or dissipate energy as cracks advance through polymers chains: rubber cavitation [29, 99, 101-105], matrix crazing [28, 106, 107], and/or shear yielding [5, 8, 12, 101, 103, 105, 106, 108, 109] with chain breakage accompanying the failure of polymers. Impact resistance has also been correlated with the presence of a secondary transition at least 50°C below the testing temperature [100, 105, 107]. The

speed of the impact test effectively raises the temperature of this secondary transition by 50°C (time/temperature equivalent); therefore, secondary transitions occurring near the test temperature at low frequency are effectively shifted into the glassy region at testing frequency. Below its T_g , a rubber particle will not cavitate and will therefore behave in a brittle manner. Secondary transitions must be associated with motion of the polymer backbone (glass transition temperature), not pendant side chain groups, for them to be effective at improving impact resistance.

When a toughened polymer blend is subjected to a uniaxial stress, the localized stress experienced by the matrix material in the vicinity of a rubber particle will be magnified by the local stress concentration factor. The initial cavitation of a rubber particle relieves the triaxial stress existing at a crack tip and enhances localized yielding in the matrix, thus avoiding a brittle catastrophic failure of this material. If the applied stress is increased further, the crack tip may be bridged by the stretching rubber particle, provided there is sufficient adhesion between the rubber and the matrix and that the particle can stretch sufficiently rapidly in terms of the speed of the crack advance. For this reason, it is desirable that the rubber should have as low a T_g as possible, while allowing the rubber to fibrillate and maintain a degree of structural integrity in response to impact loading [12]. Conventional wisdom states that for toughening polymers, the rubber droplets must be at least as large as the cracks they are trying to stop, putting the minimum size at several hundred angstroms to 300-500 nm [100].

2.3.2 Elastomer/Rubber Toughened Blends

A fundamental understanding of how rubber particles affect the creep response of polymers is described by the Eyring theory, which states that energy barriers at the molecular level control the macroscopic rates of flow [110]. This is a fundamental

property which depends on rubber composition, volume fraction of dispersed phase, rubber particle size and distribution, and rubber-matrix interfacial interactions [2, 3, 8, 9, 22, 28, 69, 107, 111-115].

Toughness is the greatest at an optimum rubber particle size for polymers that dissipate fracture energy mainly by matrix crazing (PS and PMMA) [70, 116]. But for semicrystalline polymers, close interparticle distance is just as important as small particle size and high interfacial adhesion [5, 21, 69, 113, 116-118]. A critical interparticle distance (matrix ligament) exists below which a material behaves in a ductile manner and above which behaves in a brittle manner [69, 103, 113, 119-124]. Ligament thickness is an inherent property of the polymer and is independent of rubber volume fraction or particle size. At large separation distances, the stress field in the matrix is simply a superposition of those around isolated particles, and the polymer blend will remain brittle. However, when the particle surfaces are sufficiently close, the stress field is no longer simply additive, and the fields around the particles will interact. This will result in enhanced matrix yielding, and a transition to tough behavior [119]. Even if rubber particles are chemically bound to the matrix, a polymer blend will still be brittle if the interparticle distance or particle size is greater than a critical value.

Bartczak [125] and Muratoglu et al. [126] expanded upon the matrix ligament theory and revealed that a layer of anisotropic crystalline material having a lower plastic resistance than the bulk surrounds the dispersed particles. Van Dommelen et al. have actually modeled this behavior and show that this unique layer is a highly efficient method for toughening semicrystalline polymers by altering matrix craze formation, reducing principal stresses, and inducing extensive matrix shearing [115].

In general, the critical particle size for toughening decreases with increasing ductility of the matrix polymer. For a Nylon 6,6-rubber blend, it was found that if rubber particles are large, a greater amount of rubber is needed to achieve toughening and vice versa [119]. Chou et al. showed that rubber particles narrowly distributed around 0.5 to 1 micron in size are effective for toughening PP [103]. A large number of small rubber particles are preferred when toughening PP because they are more efficient at promoting shear yielding and crazing throughout the matrix [22, 69, 127]. Also, a bimodal distribution of rubber gives a good balance of toughness and stiffness in PP [23].

If rubber is well bonded to the matrix, stresses can become redistributed between phases subsequent to yielding, so that the plastic zone is just as capable of resisting crack extension as the homopolymer. The effect of poor matrix-rubber bonding is a weaker plastic zone, thus canceling out the benefits to be derived from a reduction in yield stress. Good rubber-matrix adhesion and small particle size are necessary criterion for screening rubbers to toughen PP and increase impact strength [19, 22, 110, 128]. Blends with very small particle size have a relatively high cavitation stress, which results in a high yield stress of the blend [104].

A final contribution to toughening semicrystalline polymers is from stress-induced phase transformations [129]. If changes in crystallinity take place during deformation, energy will be absorbed by melting or released by crystallization. A comparison can be made of the softening effects due to a rise in temperature to those associated with an isothermal reduction in crystallinity. Adiabatic heating of polymers fractured at high deformation rates is common [21, 130, 131] and influences the melting/recrystallization process which in turn affects plastic deformation [21, 129-135].

In summary, for optimum impact strength improvement in PP/elastomer blends, the following conditions must be satisfied [136]:

1. Elastomer particles are finely and uniformly distributed in the PP matrix,
2. The modulus of the elastomer is much less than that of the PP,
3. The crystallinity of the elastomer is low,
4. A certain degree of interfacial adhesion is present between the elastomer particles and the PP matrix,
5. The cohesive strength of the elastomer is large,
6. A certain degree of entanglement of high MW polymer chains is present in the PP matrix.

2.4 Free Radical Reactions

The free radical grafting process is very complex and not completely understood.

The following table lists the most likely reactions to be encountered while grafting monomers onto polyolefin substrates.

Table 2-1: The mechanisms of main reactions in the grafting process.

Initiator Decomposition	$R'OOR' \longrightarrow 2R'O\cdot$
Hydrogen Abstraction	$R'O\cdot + P \longrightarrow R'OH + P\cdot$
β -Chain Scission (PP phase)	$P\cdot \longrightarrow P_1\cdot + P_2\cdot$
Crosslinking (PE phase)	$P\cdot + P\cdot \longrightarrow P-P$
Graft Initiation	$P\cdot + M \longrightarrow PM\cdot$
Graft Propagation	$PM_n\cdot + M \longrightarrow PM_{n+1}\cdot$
Homopolymerization	$R'O\cdot + M \longrightarrow R'OH + M_n\cdot$
Termination by Recoupling	$PM_{n+1}\cdot + M_n\cdot \longrightarrow PM_m$

2.4.1 Initiator Decomposition

Previous research has shown that a peroxide initiator is necessary to create enough free radicals to graft monomers onto polyolefin substrates which may be due to the presence of stabilizers in the polymer resin [4, 7, 90, 94, 137-143]. Initiator

decomposition is known to be the rate limiting step for hydrogen abstraction [92]. Dialkyl peroxides are the initiators of choice because they are amongst the most stable of all commercially available organic peroxides and the free radicals generated from decomposition have a variety of uses [144]. 2,5-dimethyl-2,5-di-(t-butylperoxy) hexane (tradename Lupersol 101) is often used to degrade polypropylene, crosslink various types of polyethylenes, and graft monomers onto these polyolefins because of its efficiency [73, 92, 94, 147, 148]. Figure 2-3 gives the chemical structure while Table 2-2 lists characteristics of the peroxide.

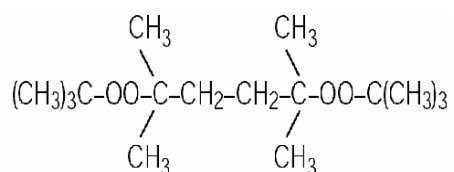


Figure 2-3: Chemical structure of Lupersol 101

Table 2-2: Characteristics of Lupersol 101 [145, 146].

Molar Mass (g/mol)	290.44
Peroxide content (%)	91-93
Oxygen content (%)	10.03-10.25
Physical form	Liquid
Melting point (°C)	8
Boiling Point (°C)	249
Specific gravity (cm ³ at °C)	0.865 @ 25°C
Viscosity (mPa.s) @ 20°C	6.52
Typical Decomposition products in inert media: methane, ethane, ethylene, acetone, t-butyl alcohol. Lupersol 101 is considered a suitable food additive.	

The half life of a peroxide is very important, defined as the time it takes for one half of a given quantity of peroxide in dilute solution to decompose at a given temperature. The melt free radical grafting rate is dictated by peroxide efficiency, or half life [138, 146]. One has to keep in mind that the half life of Lupersol 101 in molten LDPE is reported to be 2-3 times longer than in organic solvents [4, 90, 94]. A similar

result is found when peroxide decomposition is in the solid (glassy) state of a polymer [149]. The low reactivity of polymers compared to model compounds is attributed to several factors, including the lower concentration of tertiary C-H reaction sites, coiled conformations, and high viscosity [150, 138].

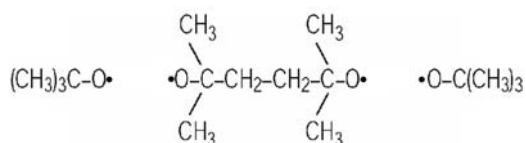
Conventional wisdom shows that half life time should be about 5 times that of the residence time of the polymers [68, 92]. If the half life is too long, the initiator may not be completely utilized. A short half life may increase the crosslinking of radical-radical combination or grafting yield may be limited by the rate of monomer diffusion to the site of reaction, especially a heterogeneous melt. Other work has shown that no grafting occurs after consumption of the initiator (as estimated by half life) [151]. Half life is calculated as $\tau_{1/2} = 0.693/k_d$, where $k_d = Ae^{-E_a/RT}$, E_a is the activation energy, R is the universal gas constant, T = temperature (K), and A is an integration constant [146].

Table 2-3 is a manufacturer's generated list of estimated half lives for Lupersol 101 at various temperatures.

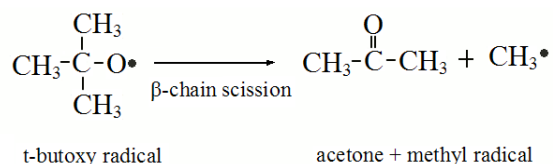
Table 2-3: Half life of Lupersol 101 based on temperature

Temp (°C)	165	190	210	230
Half life (seconds)	280 (4.7 minutes)	28	5.4	1.2

The mechanism of free radical production from Lupersol 101 involves a primary and secondary reaction, with decomposition of each group independent of each other [68]. Upon addition of heat, this peroxide decomposes homolytically into 4 alkoxy radicals at a bond dissociation energy of about 36 kcal/mol [145, 152, 153]:



A secondary reaction can occur in which the tertiary alkoxy radicals can undergo further fragmentation (e.g. β -scission) to form ketones and alkyl radicals:



The extent of reaction at a given position is proportional to the amount of peroxide initiator that has decomposed at that position. In regions of high temperature, the peroxide reacts more rapidly, inducing a concentration gradient that drives additional peroxide to diffuse into the hot region and react. The faster the initiator is consumed, the less time it has to diffuse to other portions of the channel and react [154].

2.4.2 What Happens After Peroxide Decomposition?

A radical produced by either primary or secondary reactions can abstract a hydrogen (from the polymer backbone) or add to a double bond (vinyl monomer). The secondary reaction is strongly temperature dependent, more so than abstraction or addition [68, 155]. So with an increase in temperature, there is an increase in the number of methyl radicals, which attack bonds in a much more random nature than t-butoxy radicals and usually add to vinyl monomers rather than abstract hydrogen atoms from the polymer [156]. Methyl radicals add to styrene some three orders of magnitude faster than the model compound 2,2,4 trimethylpentane [68].

2.4.3 Polymerization

The feasibility of radical polymerization of a monomer depends primarily on the polarity and size of the substituents on the double bond and the tendency to chain transfer [153, 157-160]. The reactivity of the monomer is influenced by two factors:

1. The stability of the monomer toward addition of a free radical

2. The stability of the monomer radical thus formed (more important).

Monomers with less resonance stabilization represent much higher energy states. The order of reactivity of the radicals is the reverse of that for monomers; i.e., styrene monomer is more likely than methyl acrylate to consume a radical but addition of styrene monomer to a polymerizing chain is 100 times slower than methyl acrylate [153, 161]. A larger propagation rate constant will lead to higher molecular weight. Resonance stabilization depresses the activity of the radical. Low activation energies are indicative of a greater decrease in energy from reactants to products [157, 162, 163]. Table 2-4 gives typical activation energies for several aspects of free radical polymerization in solution [146].

Propagation is bimolecular and its rate is independent of chain length. The initial chain formed rapidly produces a high molecular weight polymer [146]. A monomer's ceiling temperature is defined as the temperature above which monomer cannot be converted into long chain polymer. A relatively low ceiling temperature is suggested for grafting single monomer units onto polymers or to limit homopolymerization. For styrene and acrylate-based monomers whose ceiling temperatures are well above polypropylene extrusion processing temperatures, depropagation or "unzipping" of the chain is not a concern.

Table 2-4: Typical free radical kinetic values in solution.

Type of Reaction	Activation Energy (kcal/mol)
Initiator Decomposition	30-50
Initiation	5-7
Propagation	4-10
Chain Transfer	10-20
Termination	0-6
Less stable π -bond \rightarrow more stable σ -bond: -12 to -23.9kcal/mol: exothermic	

During free radical polymerization [164, 165] and graft copolymerization [166, 167] bimolecular termination is still energetically favorable but the macroradicals are large with slow diffusion, so termination will be almost exclusively diffusion controlled. The rate constant of termination for styrene is inversely proportional to the viscosity of the medium over a thousand fold range of viscosity.

Chain transfer may occur, defined as the termination of one macroradical to produce another macroradical which serves as a branch point. The new free radical produced may or may not be initiate another polymer chain formation, depending on its activity. Styrene is more to likely add monomer than undergo chain transfer to either polypropylene or polystyrene [162a]

Styrene monomer (Table 2-6) is an aromatic hydrocarbon which, under normal conditions, is a clear, colorless, flammable liquid. It is a versatile material, the derivatives of which are styrene-based polymers. Styrene is one of the few vinyl monomers that undergo rapid thermal polymerization [168, 169].

2.4.4 Copolymerization

When studying the copolymerization of two monomers, their reactivity ratios result from a combination of steric, resonance, and polar effects [153, 159, 160].

- Steric effects: bulky substituents decrease reactivity in radical polymerizations.
- Resonance: If a radical can be stabilized by resonance, it is more likely to form (monomer is more reactive). However, resonance stabilization of the radical also makes the radical less reactive towards propagation.
- Polar effects: A monomer with an electron-withdrawing substituents is more likely to react (cross-propagate) with a monomer having an electron-donating substituent than it is to self-react. So, ethyl acrylate will want to add styrene monomer units over other ethyl acrylate units.

Two monomers can either undergo self-polymerization or copolymerization. The terms r_1 and r_2 are reactivity ratios, and define the relative tendencies to self-propagate or cross-propagate. If $r_1 > 1$, then monomer 1 tends to self-propagate, whereas if $r_1 < 1$, copolymerization is preferred. In Q-e schemes, Q is a measure of monomer reactivity (resonance stabilization), and e relates to monomer polarity. Q values increase with increasing resonance stabilization, while e values become less negative as groups attached to the double bond become more electron attracting. Table 2-5 gives Q and e values [162c] and reactivity ratios [162b] for styrene and ethyl acrylate, while Table 2-6 gives basic information on the three monomers of interest.

Table 2-5: Copolymerization constants for styrene and ethyl acrylate monomers.

Monomer (r)	Q value	e value	reactivity ratio
Styrene (r_2)	1.00	-0.8	0.699
Ethyl acrylate (r_1)	0.41	0.55	0.139

Because $r_1 * r_2$ deviates from unity and since e is much different for the monomers, alternating copolymerization will exist [161]. The reactivity ratio of styrene does not change with temperature but ethyl acrylate can be strongly affected. The higher the temperature, the more ethyl acrylate units will be incorporated into the copolymer [170]. The initiator has no significant effect on the reactivity ratio values. For two monomers far apart on the polarity series, the rate of copolymerization is often much higher than for either monomer alone [160].

Table 2-6: Structural and physical information about the monomers of interest.

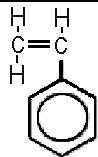
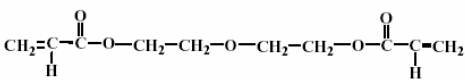
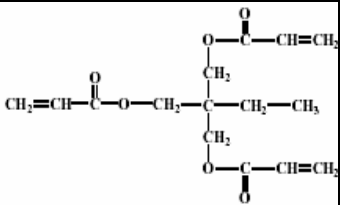
Monomer	Styrene	Diethyleneglycol diacrylate (DEGDA)	Trimethylolpropane Triacrylate (TMPTA)
Structure			

Table 2-6 Continued

Functionality	1	2	3
Molar Mass (g/mol)	104	214	296
Viscosity @ 25°C (cps)	0.76	12	106

2.4.5 Multifunctional Monomer

The random nature of free radical polymerization processes likely results in the assemblage of units in an irregularly patterned structure. Nonlinear polymers are obtained from monomers at least some of which possess a functionality exceeding two. Gelation can be avoided in nonlinear polymerization by limiting the extent of reaction or using small proportions of reactants [161].

In a study which compared homo- and co-polymerizing multifunctional monomers, Diffusion of the monomer played a significant role in bond conversion. As the composition of the crosslinker is increased, the maximum double bond conversion decreases due to diffusional limitations to the polymerization process [163, 171]. The acrylate copolymers are more homogeneous than methacrylate copolymers [163]. When comparing di-functional vs. tri-functional monomers, the concentration of crosslinking double bonds is 43% higher for tri- due to higher functionality per monomer [172]. For neat monomers, the maximum polymerization rate for di-functional is twice that of tri-functional.

A survey of multifunctional acrylates was conducted to assess the effect of monomer rank (number of atoms between acrylate functionalities), size of functional group, and number of functional groups [171]. As the rank increased, the conversion of

double bonds increased from 74.5% to 84.2%. This was explained by the increased mobility in the double bonds in the latter part of the reaction. Activation energy and rate of polymerization decreases as the number of alkyl groups increases [173]. The opposite trend was observed for increasing bulkiness of pendant functional group and increasing functionality of the monomers. The increase in the number of double bonds of the monomer did not necessarily increase the possible crosslinking concentration. Acrylates reacted faster and had higher enthalpy of polymerization than methacrylates. The monomers with smaller pendant groups and lower functionality exhibited higher rate constants during polymerization due to increased diffusivity of the monomer and pendant double bonds in the reacting gel. The reactive pendant group could introduce hindrance, reduce the reactivity of the double bonds and reduce the conversion.

2.4.6 Hydrogen Abstraction

The specificity of hydrogen abstraction depends on an array of steric, polar, and stereoelectronic factors, including bond dissociation energies and kinetic effects [68, 140, 150, 152, 174-178]. The lower the bond dissociation energy, the more stable the radical and therefore the more reactive. Alkyl radical stability increases in the order primary (1°) < secondary (2°) < tertiary (3°) < allyl \approx benzyl. Barriers for tertiary, secondary, and primary radical formation are 10, 11.5, and 12.2 kcal/mol, respectively, which indicates an order of magnitude difference in kinetics between tertiary and primary formation [155, 156]. For isotactic polypropylene at 130°C, the relative reactivity of CH:CH₂:CH₃ groups with benzoyl peroxide as initiator is 50:10:1 (reactivities per H atom) [68]. Another study showed that the PP macroradical actually forms a mixture of primary, secondary, and tertiary free radicals (1:14:18) [179]. Abstraction from the tertiary C-H position for a PP model accounts for two-thirds of the total product distribution [150].

In modeling polyethylene, secondary radicals were seen but there was no evidence of signals from primary radicals [156]. As previously stated, methyl radical formation begins to dominate at high temperatures. At 200°C, CH:CH₃ hydrogen abstraction for methyl radicals is 8:1 and CH₂:CH₃ is 3:1. At 200°C, CH:CH₃ hydrogen abstraction for t-butoxy radicals is 6:1, and CH₂:CH₃ is 5:1 [68, 180]. It is possible that, if secondary or primary radicals are produced, they may be transformed into the more stable tertiary radicals by subsequent inter- or intra-molecular abstraction reactions [68].

When comparing polymers, bulky side groups can also reduce the reactivity of the substrate [151, 181-183]. For grafting branched polyethylenes, tertiary-hydrogen atoms are three to four times more reactive than secondary hydrogen atoms [155]. The introduction of a branch leads to the replacement of 4 secondary hydrogen atoms by one tertiary and three relatively unreactive primary H atoms.

For an ethylene-octene copolymer with 10% octene, the site of grafting is 12:1 for secondary:tertiary [150]. Therefore, a greater number of secondary groups results in predominant grafting at these points offsetting the greater reactivity of the tertiary C-H reaction sites. As the octene content of the copolymer changes to 5%, the ratio of secondary to tertiary sites changes to 22:1.

2.4.7 Polyethylene Crosslinking Reactions

Polyethylene will crosslink in the presence of free radicals because of the long lived macroradical present after hydrogen abstraction. Cross-termination of PE has a high rate constant [155]. ENGAGE® polyolefin elastomers have been found to form an insoluble gel only above 0.3 wt% initiator [184]. It is now known that the highest molecular weight fractions of polyethylene will be consumed first and a higher amount of crosslinking agent shifts the distribution towards lower molecular weights [149, 185].

The low MW fraction is believed to act as grafted pendant chains in the presence of longer polymer chains. The network formed within the low MW fraction consists mainly of chemical crosslinks, whereas high MW material comprises both physical entanglements and chemical crosslinks. Trapped entanglements generate the major part of the crosslinking points at low peroxide concentrations, especially in HDPE. At high number average molecular weight values, dense networks are easily created with only a small amount of chemical crosslinks, as the probability of entanglement formation is very high.

The presence of polyfunctional monomers greatly increases the efficiency of polyethylene crosslinking [186]. The degree of crosslinking levels off rapidly at 3% monomer, but monofunctional monomers such as styrene, methyl methacrylate, and vinyl acetate were observed to have no effect on PE crosslinking.

Yang et al. desired to reduce crosslinking when trying to graft glycidyl methacrylate onto polyethylene and used several inhibitors and monomers to do so [187]. They found that the chain transfer agent/inhibitor p-benzoquinone gave an acceptable grafting degree with minimal crosslinking. Styrene monomer, on the other hand, gave an unusually high gel content along with grafting degree.

2.4.8 Degradation of Polypropylene

Chain scission is the most energetically and kinetically favorable process after hydrogen abstraction from the β position on the PP backbone. Disproportionation, another term for β -chain scission, results in a saturated product and an unsaturated molecule, depicted in Figure 2-4 [137, 153, 188]. This degradation discolors the plastic, reduces crystallinity, compromises mechanical strength, and lowers the viscosity and melt strength [189, 190]. But some authors have shown that peroxide addition can

narrow the molecular weight distribution and eliminate the high molecular weight tail of polypropylene to facilitate processing [73, 189, 191-194].

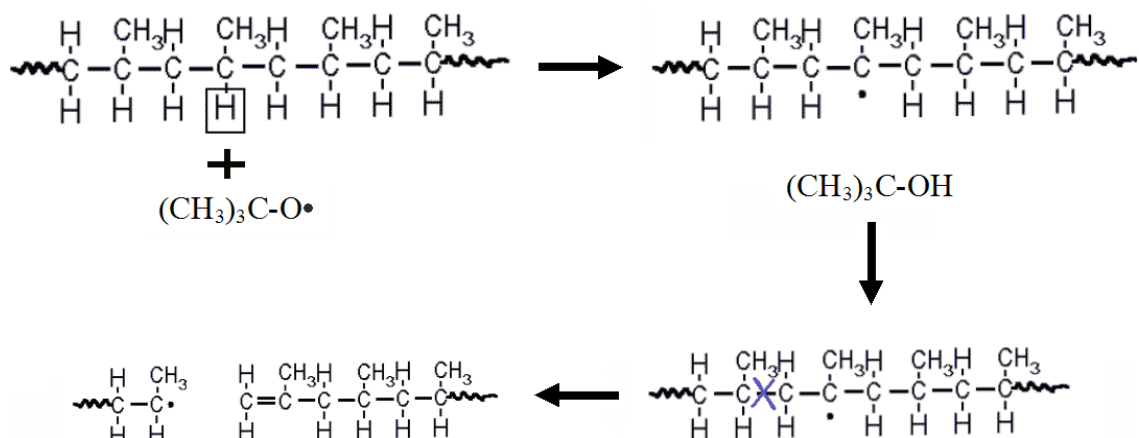


Figure 2-4: Schematic of H abstraction from PP and subsequent β -chain scission.

The degree of chain scission is found to be proportional to the initiator level. Each reaction occurs randomly, leading to random chain scission. Under typical extrusion processing temperatures and low levels of peroxide, the backbone radical center is highly unstable and undergoes β -chain scission almost immediately after H abstraction. The activation energy for β -chain scission has been reported to be between 29.6-32 kcal/mol but the relative rate is a function of temperature [137, 179]. Bimolecular termination, which is highly diffusion controlled, may be negligible because of the low concentration and short lifetime of the backbone radical [152, 154, 195]. The scission occurs randomly along the chains and higher MW chains have a greater number of bonds, so longer chains will experience β -scission preferentially [152, 154]. The number average molecular weight is inversely proportional to the degree of chain scission, which in turn is linear with respect to the amount of initiator [194].

2.5 Previous Efforts to Reduce/Prevent Degradation of Polypropylene

2.5.1 Free Radical Grafting of Polymers

Numerous processes of grafting monomers onto polymer backbones exist, with free radical melt, solution, and solid state grafting common practice [7, 68, 90, 91, 138, 148, 155, 177, 179, 190, 196-199]. Gamma [200] and UV [201, 202] radiation as well as ozonation to produce hydroperoxide functionalities on PP [203, 204] are also interesting grafting methods. The goal of each process is to achieve a high grafting yield and a low incidence of side reactions, which require that the radical sites on the backbone are efficiently transformed to graft sites [68, 205].

This dissertation revolves around free radical grafting of polyolefins via peroxide decomposition. All reactions are done primarily in the melt state rather than in solution for several reasons. In the past, solvents would dissolve the polymer and high graft yields ensued, but solvents had to be distilled for separation, and the grafted copolymer had to be dried of solvent before use. Not to mention the high solvent loadings needed which makes the process expensive and poses environmental issues [7, 206].

The idea of grafting monomers onto polyolefin backbones is not new and several patents have been issued over past several decades. The original purpose was to impart polarity, resistance to degradation, and improved adhesion [199, 207-211]. The monomer(s) and initiator mixture can be either mixed with polymer before melting or added to the melt above 120°C. Grafting is done continuously in a reactor that provides intimate contact between the components (i.e. extrusion) with devolatilization prior to exiting the die. Typically, the reactive components are a peroxide or azo initiator (at 0.1-0.7 wt%) to create the free radicals and a monomer (at 0.5-5 wt%) with a functionality

that can further react. A low molecular weight product with a sharp increase in flow rate is common.

2.5.2 Solid State Grafting

There may be some solid state (surface) grafting for a reactive extrusion process when all materials are added at once into the extruder [94, 95, 143, 212]. For grafting below the surface, initiator decomposition rate may be of secondary importance to monomer diffusion. But during extrusion, monomer and initiator may become trapped into small pockets of molten polymer which are then broken as the melt is sheared. Diffusion of liquid reactants into the amorphous region (not crystalline [213]) may occur. The coalescent state of the monomer droplet facilitates an increased rate of polymerization but also homopolymer formation [172, 178]. The grafting yield of PP as a solid particle is much lower compared to in the melt even though the amount of β -chain scission is three orders of magnitude less. For grafting at 120°C (solid state), melt flow index is over 100 times greater than at that 220°C (molten state) [7, 180].

High melt strength polypropylene has been created by absorbing styrene and butadiene and subsequently polymerizing to produce a branched alloy with enhanced strain hardening, melt strength, and drawability [179]. This branched architecture can also be created by irradiation of PP with a difunctional monomer [214]. Higher functionality monomers were not as effective at crosslinking PP and caused the formation of an undesirable gel. Shorter chain monomers are better than longer chain monomers for improving melt strength and an acrylate-based functionality was better than methacrylate at the same molecular weight because the reactivity of acrylate monomer is higher than methacrylate [215].

2.5.3 Reactions in the Polymer Melt

In order to minimize side reactions, the radicals formed on the polyolefin backbone must be trapped as soon as they are formed [68]. Some monomers are more effective than others, which may be due to relative solubility of the monomers in polyolefin melt or inherent reactivity of monomer. By increasing grafting yields, degradation and side reactions such as homopolymerization will decrease. This strategy involves choosing a monomer combination such that the primary monomer has a high reactivity towards free radicals and can effectively trap radicals on the polyolefin backbone and the secondary monomer facilitates this grafting process by creating branch sites or speed up the polymerization process of the primary monomer. The higher grafting yields are attributed to:

- Longer chain grafts - rates of copolymerization of electron donor acceptor pairs are greater than for homopolymerization.
- More grafting sites - more efficient trapping of radical sites on polymer backbone.

A straightforward method to crosslink PP was to simply add an excess amount of peroxide initiator to induce addition reactions of fragmented chains [216-219].

Generation of free radicals on PP leads to degradation because of the low stability of macroradicals on the tertiary carbon. Crosslinking efficiency is low due to the fragmentation of a large portion of macroradicals. Decrease of crosslinking efficiency occurs with increasing temperature because the rate of fragmentation increases (a higher energy process) compared to recombination. The rate of fragmentation depends primarily on temperature while the rate of recombination depends on both initiator concentration and the rate of its decay. The activation energy of recombination is close to zero while the energy of fragmentation is greater than 29 kcal/mol.

Another, more effective method to crosslink PP is to use a polyfunctional monomer. The idea is based on two assumptions: the double bonds of the monomer will react with tertiary PP macroradicals to suppress fragmentation and the double bonds of the monomer will increase the number of crosslinks between PP chains [68, 114, 180, 190]. Formation of stable radicals after addition of PP radicals is the most important role of the monomer double bonds and is a very effective free radical trap. The contribution of a few long polymer chains can drastically affect the elongational viscosity by increasing the degree of chain entanglement in PP and creating chains 2-3 times bigger than can be formed by intermolecular combination [215].

Ludwig and Moore found that peroxide initiated grafting of a hexafunctional coupling agent can reduce chain scission of PP dramatically [220]. The high tail end of the molecular weight distribution increased and was attributed to the formation of PP crosslinks through the coupling agent. Notched Izod impact strength and tensile strength improved with the coupling agent. The decrease in the degradation of PP is due to the primary radicals reacting preferentially with multifunctional monomer [190].

A branched PP was created by the use of a polyfunctional acrylate monomer (trimethylolpropane triacrylate), a peroxide initiator, and an iniferter compound [221]. The iniferter acts as a free radical initiator, chain transfer agent, and chain terminator and was found to facilitate the long chain branching from TMPTA. The iniferter also prevented gel formation and homopolymerization of the TMPTA, both of which are deleterious to the ultimate properties of the grafted PP. Several authors have tried to crosslink isotactic polypropylene in order to improve the melt extensibility and

mechanical properties but also to reduce chain scission while grafting functional monomers.

Normally, thermal degradation of PP during its processing can be avoided by adding thermal stabilizers (antioxidants). However, this kind of stabilizing mechanism cannot be applied to the grafting process because the stabilizer eliminates the free radicals, which initiate grafting. The major purpose of crosslinking is to both enhance the mechanical properties of grafted PP and increase its melt viscosity, which may facilitate its dispersion into other phases during melt blending [7, 222].

Monomers alone do not necessarily reduce degradation of polypropylene, but some studies have shown that styrene grafting can cause cross-termination and increase branching of the copolymer [92, 94]. Styrene-GMA copolymerization and grafting can create long chain branching of PP macromolecules [94]. The resulting structure of grafted PS materials is more likely a highly branched, entangled network, as opposed to a crosslinked network. The entangled chain ends behave as temporary junctions. Although rheological testing revealed a gel point, soxhlet extraction with xylene yielded no insoluble material.

2.5.4 Fundamentals of Free Radical Grafting

The proposed chemical mechanisms for free radical grafting reactions onto polymers include initiation, propagation, transfer, and termination [94]. These are the same reactions for free radical polymerization [154, 158, 159]. Once the initiator decomposes and primary radicals are generated, they must diffuse away from each other. A concern when dealing with a highly viscous system is that two primary free radicals recombine to yield an inactive species, known as the cage effect. If it breaks free of the cage, it may abstract a hydrogen atom from the polymer backbone, creating potential free

radical grafting sites. Most of the functional monomers used for graft modification are capable of homopolymerizing, which generally enhances the ability of the monomer to graft onto the polymer [138]. Termination of the free radicals is either by kinetically identical combination or disproportionation, which is negligible for primary radicals. Chain transfer is not a likely source for grafting sites onto the polymer backbone [141]. In fact, the rate of propagation in melt grafting is over 35 times that of chain transfer [92]. The activation energy for grafting is slightly higher than initiator decomposition, which is the rate determining step of the reaction [223].

Few studies have probed free radical reactions under the conditions likely to be encountered in melt phase polymer reactions. These involve relatively high temperatures, relatively high pressures, and media of relatively high viscosity [68, 138, 181]. As homopolymer is produced, there is some phase separation; the monomer that is trapped in the homopolymer phase cannot graft onto the polymer, resulting in a lower degree of grafting and grafting efficiency than the model system. Homopolymerization does compete successfully with the grafting reactions in model systems [111].

The kinetics and mechanism of grafting onto a saturated polymer (like polybutadiene) is the same as homopolymerization in solution regardless of whether the polybutadiene is present [179]. Both free and grafted chains are in the same environment and presumed to grow at equivalent rates [139-142, 224, 225]. Styrene homopolymerization readily competes with grafting but if benzyl acrylate is used in place of styrene, grafting is severely reduced. This is attributed to the fact that the benzyl acrylate monomer is much less reactive than styrene and the rather inactive polybutadiene macroradical cannot compete for benzyl acrylate monomer [140]. The grafting of styrene

and homopolymerization is 10 times that of a monomer which tends to graft as single units because of styrene's high ceiling temperature [92].

When grafting polypropylene, the ratio of tertiary to secondary to primary grafting sites in neat solution is 5.6:1.5:1, respectively, and 3.9:0.3:1 in benzene, respectively [150]. This study suggests that the position of t-butoxy radical initiated grafting in LLDPE and PP is most likely different, with LLDPE grafting mainly at the secondary sites.

2.5.5 Melt Grafting Monomers onto Polyolefins

Gaylord and Mishra have found that free radical based functionalization of polypropylene results in random attachment of the functional group in conjunction with degradation of PP by β -chain scission [226]. In fact, some authors have found that when grafting monomers onto PP, the majority of the grafts are formed after chain scission [68, 94, 180].

Doney and Salsman were successful in patenting a reactive extrusion process for creating block copolymers of isotactic polypropylene in the presence of an alkenically unsaturated polar monomer and a peroxide initiator [227]. Polypropylene is first preferentially degraded via β -chain scission by peroxide-derived free radicals. This is followed by addition of a peroxide/monomer mixture to the degraded chains which therefore link up PP chains to form block and graft copolymers with tailored hydrophilicity.

When grafting acrylate functional monomers onto polyolefins, their ceiling temperatures are typically above 400°C and homopolymerization will occur alongside grafting. Methacrylate monomers, on the other hand have ceiling temperatures approximately 200°C and tend to graft as very short chain branches with limited

homopolymerization. The initiator derived primary radicals have a relatively low reactivity towards the acrylated monomer and preferentially abstract hydrogen atoms from the hydrocarbon substrate. Addition of the monomer to the resulting polyolefin radical has a rate constant four orders of magnitude faster than homopolymerization. On the other hand, styrene undergoes more rapid addition to hydrocarbon radicals [156].

Over the years, several routes have been developed to improve the grafting efficiency of functional monomers. One early process used toluene as an interfacial agent [207]. The graft yield increased for two reasons: improved solubility of the monomer in the solvent and more surface area by swelling the surface of the polymer. The main type of PP grafting proposed at elevated temperatures is β -scission followed by graft initiation on one of the chain fragments [94]. The use of a multifunctional monomer greatly reduced the extent of degradation but did not seem to improve the grafting yield of GMA [7].

Hu et al. were the first to systematically study chemical methods for improving the free radical grafting yield onto PP while minimizing degradation [191]. They proposed three routes, all based on increasing the reactivity of the monomer and/or rate of reaction. The comonomer concept was derived, which is fundamentally dependent upon the reactivity ratio of free radical copolymerization. This means that for a monomer to be grafted onto a macromolecular chain, adding comonomer will be beneficial for improving the monomer grafting yield only if this comonomer reacts with a macroradical more rapidly than the grafting monomer and the resulting macroradical is capable of copolymerizing with the grafting monomer.

A consensus from several authors is that grafting yields are higher when styrene comonomer is used, so styrene must preferentially graft onto the polymer macroradical before chain scission occurs [7, 40, 92, 94, 206, 228]. Styrene then forms a stable styryl macroradical which is long lived and invites copolymerization with polar monomers. The intrinsic free radical grafting rate is so much accelerated by the presence of styrene that the overall grafting kinetics becomes controlled primarily by PP melting. Another reason for the high grafting yields may be due to the fact that polyolefins such as HDPE, LLDPE, and PP are soluble in refluxing styrene [138]. A third effect of styrene is that it forms a charge transfer complex with the glycidyl methacrylate, which is more reactive than GMA alone.

2.6 Melt Grafting and *In-situ* Compatibilization

One of the first methods to bond polypropylene and polyethylene was to melt blend them in an extruder in the presence of a peroxide initiator. It was expected that the chain decay of PP and the chain buildup of PE should be balanced in PP-PE blends where coupling of PP and PE macroradicals can lead to graft copolymer chains PE-g-PP. Short PP oligomers were expected to be tied to PE chains so as to prevent crosslinking [70, 229-234]. Contrary to popular belief, the polymers reacted fairly independent of each other. A similar effect was seen for PE-PP copolymers [91, 235, 236].

This interchain coupling is favored only in one phase blends where the compounds are in intimate molecular contact. In two phase blends, the components can react only at the interface between phase domains so grafting is hindered. Although limited bonding exists between the phases, the resulting alloy does have higher toughness and melt strength with low gel content [232, 237]. High melt strength is characteristic of materials with long side branches (LDPE) or high molecular weight (PS) [238].

In order to reduce or prevent the degradation seen in the peroxide/PP/PE blends, a multifunctional monomer was added to the mix. A recent patent focused on using a small percentage of multifunctional coagent in addition to peroxide for the compatibilization of PP and an ethylene copolymer. A very high melt strength is observed and degradation of PP is essentially eliminated without the formation of substantial gel [239]. Yoon et al. reported a tri-functional acrylate monomer (TMPTA) is effective at minimizing PP chain scission by bonding to PP macroradicals before chain scission and stabilizing them via resonance [222]. By crosslinking a blend of PP and LDPE, the interface becomes obscure (indicating some bonding between phases), with a 6X increase in impact strength over pure PP [233]. But it has also been shown that the multifunctional coagent only raises the crosslinking efficiency in PP, not PE [240].

A process called dynamic vulcanization can be used to crosslink rubber in a PP matrix *in-situ* to improve bonding and stress transfer between phases. A thermoplastic vulcanizate (TPV) is thus formed, showing improved impact properties, solvent resistance, and long term elastic recovery over the physical blend, but an insoluble gel is typically formed [136, 241, 242]. Dispersion with these alloys is typically sub-micron and dispersed phases can be as small as 30 nm in size [243].

A nano-structured polypropylene/polyamide 6 (PP/PA6) alloy has been created *in-situ* by anionically polymerizing ϵ -caprolactam in the presence of functionalized PP [244-246]. The resulting material had PP as the continuous matrix and PA6 homopolymer dispersed as very small domains. The reaction is very fast and by proper control of the kinetics of both reactions, it is not difficult to control the particle size of the dispersed domains, leading to enhanced properties.

Flaris and Baker used a unique approach to compatibilize PE and PS in an extruder [247]. A vector fluid approach was utilized, which is simply using a carrier fluid to bring a reactive ingredient to the interface of the immiscible polymers. A vector fluid may be a low molecular weight material which can stay long enough in the blend to carry the reactive material (a peroxide in this case) to the interface and is then fugitive at some later point. For example, it may be drawn off at a vent port close to the end of a twin screw extruder barrel. Using a viscous vector fluid led to little grafting and large dispersed domains in a compatibilized PE-PS blend. This was attributed to low dispersability of the reactive ingredients and a reduction in peroxide activity.

During *in-situ* compatibilization, continuously new interfaces can be generated with proper mixing equipment. An appropriate vector fluid must be used so that the coupling reaction is restricted to the interface of the blend components. It must dissolve the reactive ingredient much more easily than the polymer melt so that little reactive ingredient can diffuse into the polymer phases. If the reactive ingredient contains both a monomer and initiator, both grafting and homopolymerization may occur. But this is likely to happen only at the surface of the minor phase polymer particles, which is surrounded with the vector fluid. In this case, the graft copolymer formed should locate right at the interface and possibly entangle with the other blend components at the polymer-polymer interface [143].

Grafting level and interfacial adhesion are known to be higher for vector fluids of low viscosity. Styrene monomer is used as a reactive vector fluid and grafts onto polyethylene macroradicals. Bridging may occur between PE and PS due to the miscibility imparted by the grafts. The highest graft levels are found with low MW fluids

that are not volatile, partly miscible with the PS phase, but yet remain at the interface of PE and PS. Lagardere and Baker used the vector fluid approach to compatibilize a blend of LDPE and PS in an extruder [248]. A peroxide initiator with styrene monomer was shown to be a very effective system because bonds were created at the interface, thus reducing interfacial tension, altering the morphology, and improving overall mechanical properties. Using this approach, PS domains were approximately 50 nm in diameter which means that the immiscible units of PS and LDPE are interconnected [249]. The *in-situ* polymerization process yielded no crosslinked material and a broader molecular weight distribution than LDPE alone. A similar result was found by Teh and Rudin [250].

Styrene is not the only monomer used to compatibilize two polymers by *in-situ* reactive processing. A patent describes a composition in which an acrylate monomer, initiator, and a diacrylate are adsorbed into one or more polyolefins and reactively processed to create what they call a thermoplastic elastomer [251]. The bonding between polymers and interactions between functional groups enhances properties. *In-situ* graft copolymers can lead to dispersed domain sizes on the order of 50 nm [86]. HDPE and PP have been reactively processed with a dialkyl peroxide and n-butyl methacrylate to suppress unwanted PP side reactions and improve compatibility [148].

Tang's dissertation focused on reactively extruding polyolefins with high molecular weight ethylene- α -olefin copolymers [11]. The alloy was created by adding a peroxide initiator, styrene monomer, and an epoxide-functional methacrylate to PP and ENGAGE® pellets as they entered the extruder so as to graft both polymers *in-situ*. Impact strength jumped by over 8X from the pure polymer, the morphology contained

finer and better dispersed domains of elastomer, and stress strain behavior improved compared to physical blends.

2.7 Conclusions

The process of reactive extrusion is a complex one, to say the least. Once a suitable system is chosen (i.e. free radical polymerization mechanism using high molar mass polymers in a reactive twin screw extruder), many variables have to be defined and optimized in order to get the best possible performance of the alloy. The following chapters will attempt to tie in many aspects of reactive extrusion to the *in-situ* grafting of two polyolefins for the creation of high impact alloys.

CHAPTER 3
PHYSICAL BLENDING OF AN IMPACT MODIFIER WITH POLYPROPYLENE

3.1 Introduction

A fundamental study of the physical blends of a low molecular weight grade of ethylene-1-octene copolymer (EOC) with isotactic polypropylene (PP) is undertaken. Little research has been conducted using low viscosity ethylene-octene copolymers to toughen polypropylene, but this chapter proves that these new copolymers are effective PP modifiers up to a certain concentration. Many concepts and characterization techniques are introduced and explained in detail so as to aid in analysis of results both in this chapter and all following chapters.

3.2 Experimental

3.2.1 Materials

Table 3-1 gives a list of pertinent ethylene-1-octene copolymers produced by Dupont Dow elastomers under the tradename ENGAGE®, but the EOC grade of interest is 8407 [48]. Isotactic polypropylene homopolymer was supplied by Equistar Chemical (grade PP 31S07A) and is contact translucent. All polymers were received in pellet form.

3.2.2 Methods

3.2.2.1 Processing

All polymers were dried in an air circulating oven at 40°C for 24 hours prior to compounding. Before processing, the resins were premixed by hand for about 10 minutes. The blending was carried out in a 34 mm non-intermeshing, co-rotating twin

Table 3-1: ENGAGE® product data table.

ENGAGE® Grade (decreasing comonomer content)	8842	8407	8200	8401	8402
Comonomer Content wt% ¹³ C NMR/FTIR	45	40	38	31	22
Density, g/cm ³ ASTM D-792	0.857	0.870	0.87	0.885	0.902
Melt Index, dg/min ASTM D-1238, 190°C, 2.16kg	1.0	30	5.0	30	30
Mooney Viscosity ASTM D-1646 ML 1 + 4 at 121°C	26	< 5	8	< 5	< 5
Durometer Hardness, Shore A ASTM D-2240	50	72	75	85	94
DSC melting Peak, °C Rate: 10°C/min	33	60	60	78	98
Glass Transition Temp, °C DSC inflection point	-61	-57	-56	-51	-44
Flexural Modulus, MPA ASTM D-790, 2% Secant	3.5	12.1	12.1	25.8	69.9
Ultimate Tensile Strength, MPa ASTM D-638, 508mm/min	2.1	3.3	6.9	6.4	12.9
Ultimate Elongation, % ASTM D-638, 508mm/min	975	>1000	>1000	950	790

screw extruder, APV Chemical Machinery (now B&P Process Systems) with an L/D ratio of 39. The temperature of the extruder was regulated by electrical resistance and water circulation in the barrels. The screw speed, unless otherwise noted was 150 rpm.

The dried, pre-mixed resins were then introduced into the extruder from the hopper of the extruder at 60 g/min through a screw driven dry material feeder from Accu Rate, Inc. Devolatilization was carried out by a vacuum pump, VPS-10A, Brooks Equipment Company. This was placed near the die and created a vacuum of about 15 in Hg. The extruder was always starved to feed. Figure 3-1 is a schematic of the extruder, with a typical temperature profile. After compounding, the resultant strands which exit the die are quenched in a water bath, pelletized, and dried in a vacuum oven at 100°C, 28 in Hg for 24 hours.

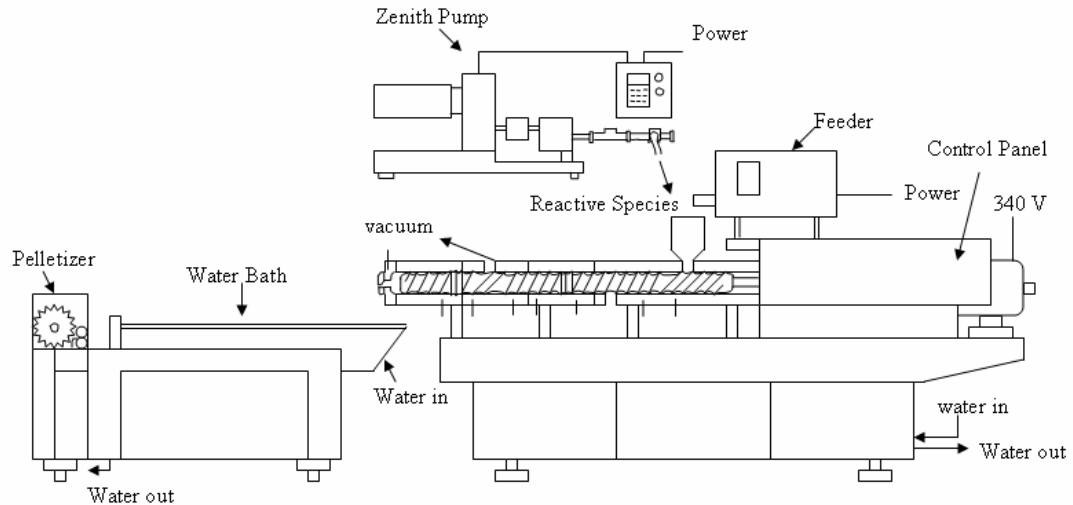


Figure 3-1: Schematic drawing of the reactive twin screw extruder and a common temperature profile.

3.2.2.2 Mechanical properties

In order to measure the strength of the materials at very high testing rates, a notched Izod impact test was performed according to ASTM D256 standards. The pellets were placed in a mold with 6 slots, each measuring $0.5 \times 0.5 \times 2.5 \text{ in}^3$. The mold is put in a Carver press (Fred S. Carver, Inc.) at 200°C and after the material is melted, pressed up to 5000 psi. After waiting for 5-10 minutes, the pressure is slowly increased up to 10,000 psi. After another 5 minutes, the heat is turned off and the sample is let to cool down to room temperature at about $1.5^\circ\text{C}/\text{min}$. The bars were then taken out and notched (0.1 in deep, 0.01 in radius) with a Testing Machines, Inc. (TMI) notching machine. Before testing, they were conditioned at room temperature for 24 hours and a 30 ft-lb hammer was used with test method A on a TMI Izod impact tester. At least 5 bars were broken and impact strength is recorded regardless of full or partial break.

For stress-strain measurements, dried pellets were placed in a mold measuring $15 \text{ cm}^2 \times 1 \text{ mm}$ thick. The mold was put into the Carver press at 200°C and after the

material melts, pressed up to 5000 psi. After a 5-10 minute wait, the sample was slowly pressed to 10,000 psi. Five minutes later, the sample was quenched in a water bath. Specimens were tested according to ASTM D638 standards. Type V specimens were punched out of the compression molded sheet with a die, measuring 1 ± 0.15 mm thickness, 2.95 mm gauge width and 9.5 mm gauge length. Five samples were tested after conditioning at room temperature for 48 hours. The machine used to test the samples was an MTS Model 1120 Instron, using a 1000 lb load cell at a test speed of 12.7 mm/min.

A Seiko DMS220 interfaced with a Seiko Rheostation model SDM/5600H was used to test dynamic mechanical specimens. Testing was conducted from -120°C to 150°C at a heating rate of $5^{\circ}\text{C}/\text{min}$ in dry nitrogen atmosphere maintained at an approximate flow rate of 100 mL min^{-1} . Rectangular samples ($20 \times 10 \times 1 \text{ mm}^3$) were cut from the compression molded sheet and tested in bending mode at a frequency of 1 Hz.

3.2.2.3 Morphology

Scanning Electron Microscopy (SEM) was performed on a JEOL 6335F Field Emission SEM. The microscope was kept under vacuum at 1×10^{-5} Pa, with an accelerating voltage of 5 kV and working distance of 13.4 mm with secondary electron detection at various magnifications. For better phase contrast, etching was done to remove amorphous, elastomeric material. Samples were etched by the following procedure: A notched impact bar was immersed in liquid nitrogen for 10 minutes and immediately fractured using a TMI Izod impact tester. A section of the cryofractured surface (2 cm thick) was then immersed in xylene (purchased from Fisher Scientific) at 60°C for one hour. The sample was removed and dried under vacuum at 40°C for 12 hours. Sample mounting was on an aluminum stub with conductive carbon paint from

Ted Pella, Inc. The sample was then coated with carbon then vacuum dried at room temperature for one hour prior to examination in the microscope.

Image analysis was done using ImagePro software. Three images per sample were recorded and domain size and distribution were quantified. The domains in all images had to be manually outlined for the software to recognize them as discrete phases. For the majority of samples, over 1000 particles were considered for diameter and roundness measurements. The number average (D_n) and weight average (D_w) diameter were determined using the following equations:

$$\bar{D}_n = \frac{\sum N_i D_i}{\sum N_i} \quad (3.1)$$

$$\bar{D}_w = \frac{\sum N_i D_i^2}{\sum N_i D_i} \quad (3.2)$$

where N_i represents the number of particles with diameter D_i .

3.2.2.4 Thermal analysis and rheology

Differential scanning calorimetry (DSC) was used to study the different thermodynamic transitions present in the blends. DSC was performed on a Seiko SII DSC 220C-SSC/5200, Seiko Instruments, equipped with a Seiko Rheostation model SDM/5600H and calibrated with indium and tin standards. Samples (approx. 7 mg in weight) were sealed in crimped aluminum pans, with the reference being 99.99% pure alumina. Purging of the sample was done with dry nitrogen at a flow rate of 100 ml/min. Each sample experienced two heating and cooling cycles (shown in Table 3-2) with the first to erase prior thermal history. The second cycle is reported in all graphs. The % crystallinity is found by first integrating the heat flow curve to a flat baseline then dividing by the heat of fusion of a perfect PP crystal (207 J/g).

Melt Flow Index (MFI) testing was done according to ASTM D1238 (230°C and 2.16 kg weight) on a Tinius Olsen model MP 933 Extrusion Plastometer. For materials

Table 3-2: DSC consecutive heating/cooling cycles

Step	Start Temp (°C)	End Temp (°C)	Heating/Cooling Rate (°C/min)	Hold Time (min)	Sampling (s)
1	-70	200	20	3	3
2	200	-80	20	5	3
3	-80	200	10	5	1
4	200	-80	10	3	1

with a flow rate of 0.5-3.5 g/10 min, the weight of the samples was approx. 3 g, whereas materials with flow rates of 3.5-300 g/10 min, the sample weight was approx. 6 g. All materials were dried under vacuum then conditioned at room temperature before testing.

3.3 Results and Discussion

3.3.1 Mechanical and Rheological Properties

Impact strength (IS) is the ability to resist a high loading rate (approx. 3.6 m/s) and is one of the most important properties for plastics part designers to consider because it sets up the worst possible condition for plastics [252, 253]. It is a critical measure of service life, product safety, and liability. The standard Izod notch ideally functions as an artificial crack because of its sharpness and acts to concentrate the applied stress, minimize plastic deformation, and direct the fracture to the part of the specimen behind the notch. Fracture of the Izod specimen is dominated by bending-moment-induced tensile stress, but extensive plastic deformation is possible.

As can be seen from Figure 3-2, impact strength increases, although not monotonically, with increasing elastomer content and reaches a peak at 20 wt% 8407. This increase is to be expected because the elastomer phase has a much lower glass transition temperature (T_g) than the matrix material and thus promotes various energy

absorbing mechanisms such as cavitation, shear yielding, and crazing. Also, in semicrystalline polymers, elastomers or rubbers act as nucleating agents and thereby reduce spherulite diameter [103, 241, 254-258]. This reduction in spherulite size is known to improve impact strength due to an increase in interfacial thickness, better inter-spherulitic chain mobility, and reduction of spherulitic defects [254, 255, 259, 260].

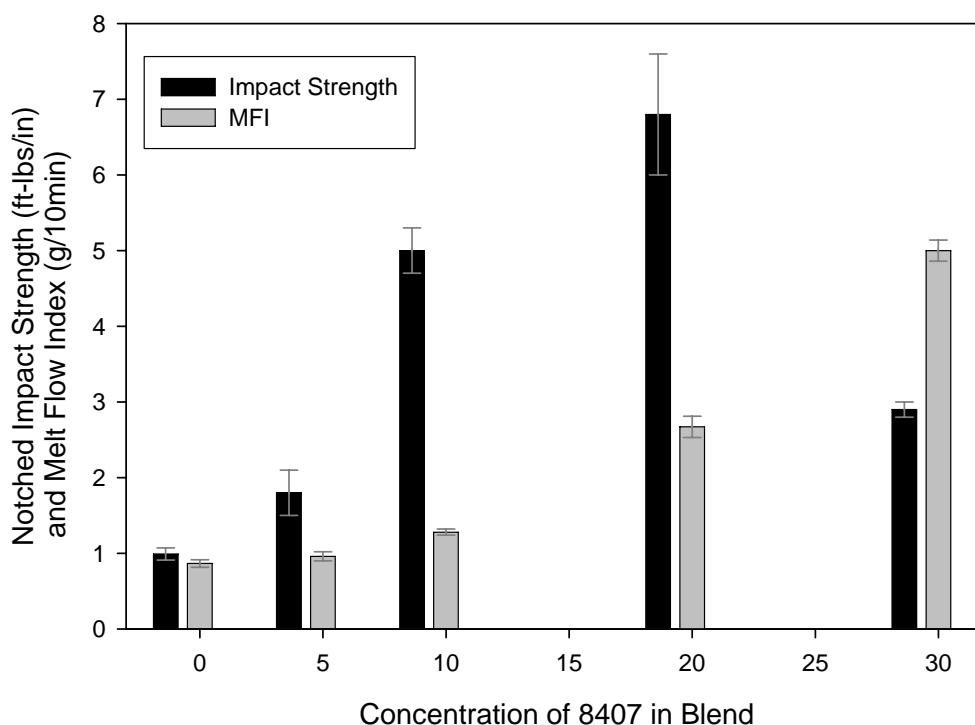


Figure 3-2: Effect elastomer concentration on room temperature notched impact strength and melt flow index.

Above 20 wt% 8407, a drastic decrease in impact strength is observed. At this level of elastomer, the interface between phases becomes of great importance. These two phases are only partially miscible at low elastomer concentrations, so gross phase separation may lead to brittle behavior because of poor stress transfer between phases [254, 261, 262]. At high strain, property deterioration takes place as incompatibility leads to cracks and failure at inter-phase boundaries. Also, at high elastomer loadings, intra-spherulitic regions of PP become very diffuse and do not have the load bearing

capacity of a fully developed spherulite [257, 261, 263, 264]. It should be noted that the impact strengths of samples fractured at liquid nitrogen temperatures (for morphological analysis) were about 0.4 ft-lbs/in, regardless of elastomer concentration.

Melt flow index is a measure of the uniformity of the flow rate of a polymer and is not a fundamental property. It is a relative test which allows one to make inferences on molecular weight and viscosity. MFI is proportional to molecular weight in the region of entanglement and gives a good indication of zero shear viscosity.

From figure 3-2, one can see that the melt flow index increases in a somewhat exponential fashion with increasing elastomer content. The blend with 30 wt% 8407 has the highest MFI, which is expected because the MFI of this elastomer is over 35 times that of PP. As melt flow index increases, impact strength is known to decrease [265]. This is only true for samples containing greater than 20% elastomer.

In stress-strain experiments of semicrystalline polyolefins, deformation first occurs in the amorphous phase followed by activation of crystallographic mechanisms [105, 266-268]. For the initial slope of the force-length curve (2-3% strain is usually reversible and is known as the elastic modulus), the deformation of the disordered interlamellar regions (loose chain folds, tie molecules, cilia, chain entanglements, as well as completely unincorporated molecules) are involved, and the lamellar structure remains intact [269, 270]. The lamellae present in the sample also behave effectively as crosslink junctions and provide resistance to deformation [271], but some authors dispute this mechanism [272]. The initial elastic part is followed quickly by a viscoelastic part, in which the stress gradually increases to reach a maximum at the yield point [273].

Figure 3-3 shows typical stress-strain responses of the physical blends while Figure 3-4 represents tensile property trends as a function of elastomer content. As can be seen from these figures, elastic modulus is a roughly additive function of blend composition and gradually declines with elastomer content [274, 275, 262]. The low crystallinity and relatively low average molar mass of the elastomer means that in the amorphous phase of PP, more chain ends are present (reduction in entanglement density), chain mobility is enhanced, total % crystallinity is reduced, as well as chain stiffness. It should be noted that standard deviations for stress-strain data are given in Appendix B.

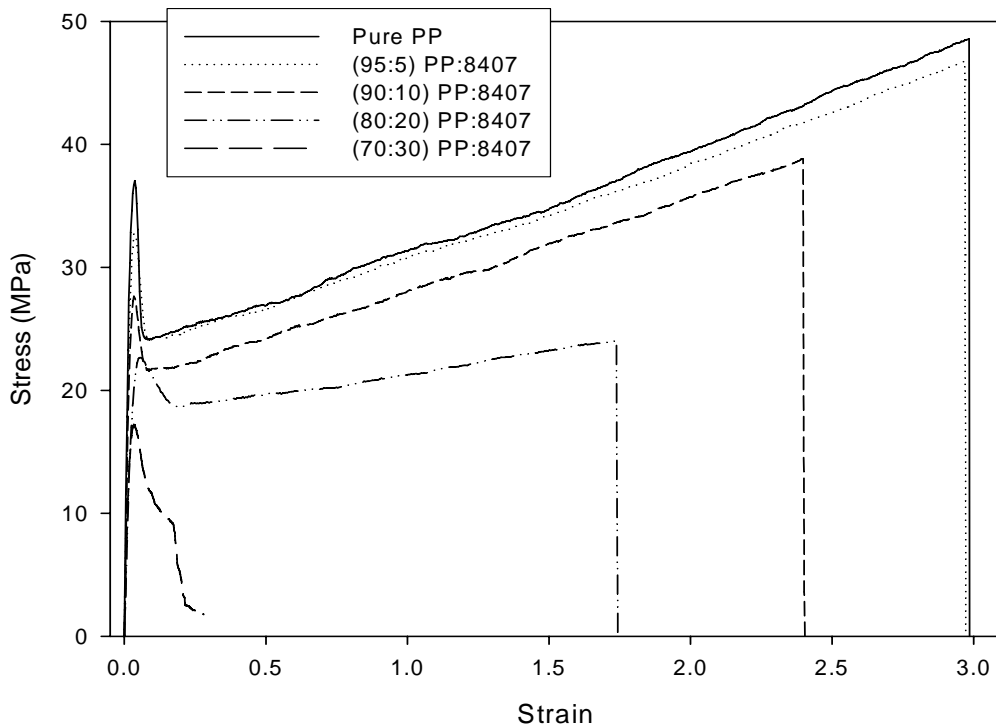


Figure 3-3: Stress-strain behavior of PP:8407 physical blends

When a polymer reaches its yield stress (also termed proportional limit), energy barriers are overcome along with dilation and long range diffusion [269]. At this point, plastic flow localizes in a neck and the stress decreases towards a plateau value (cold drawing) [273]. The dominating mechanisms of yielding is partial or local melting,

stretching of amorphous chains, and subsequent recrystallization, with competing mechanisms controlled by dislocation motion [105, 269, 272, 276]. Yield stress is proportional to lamellar thickness, unlike the elastic modulus.

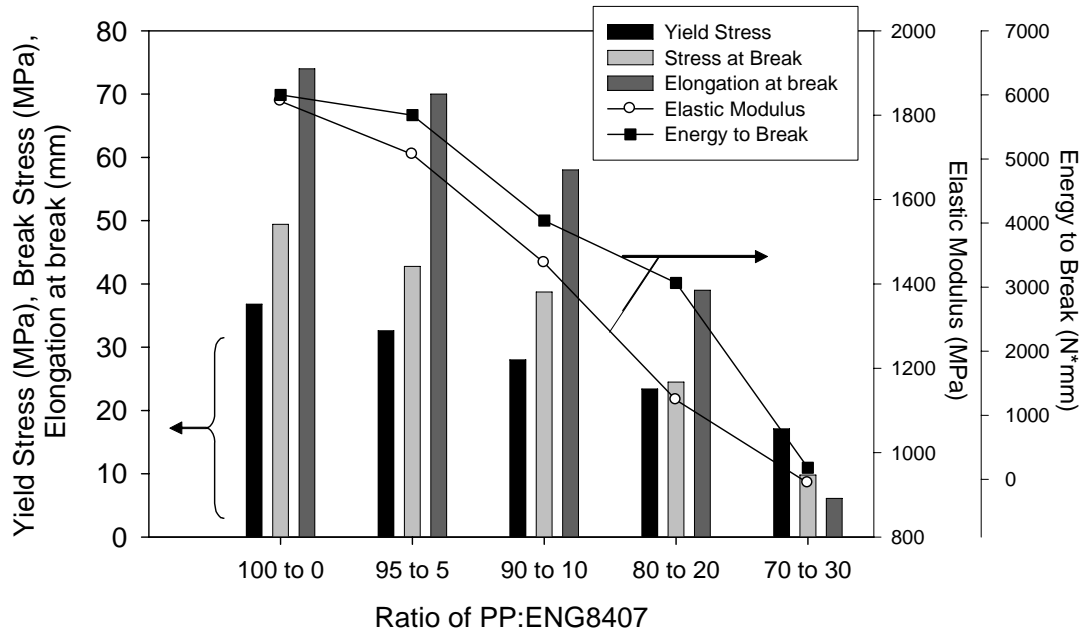


Figure 3-4: Stress-strain properties of PP-8407 blends as a function of elastomer content.

Yield stress, like elastic modulus, appears to be a monotonic function of blend composition and decreases almost linearly with an increase in elastomer concentration. This is directly related to the linear decrease in total % crystallinity of the blend with increasing 8407 content (explained in section 3.3.4). Pure PP shows a characteristically sharp yield point whereas addition of elastomer broadens this peak and increases the strain at yield. The reduction in yield stress with elastomer may be due to the dependence of yield stress on lamellar thickness (the greater elastomer content, the smaller the lamellar thickness). Also the greater mobility of the amorphous region reduces the activation energy needed for crystallographic slip, dislocation motion, and chain disentanglement.

The stress drop after yield (cold drawing) is associated with a decrease in unit cell volume and cross-sectional area which is a direct result of shearing and fragmentation of less perfect crystals [266, 277]. Necking (a form of shear yielding) accompanies this stress drop, where a very extensive reorganization of the polymer is taking place. Spherulites are broken up and the polymer becomes oriented in the direction of the stretch [100, 273]. The number of chain folds decreases, and the number of tie molecules between the new fibrils is increased.

Deviations in post yield behavior can be seen in Figure 3-3 for the various blends. Pure PP exhibits the largest drop in stress but this occurs over a relatively small strain. The high crystallinity of the pure polymer and limited thickness of amorphous layer lends it to a greater degree of rearrangement followed by orientation. The effect of elastomer on cold drawing is obvious at 20% 8407, where the stress drop is relatively small and its slope is much less than pure PP. Diffuse spherulites are likely, with elastomeric material existing in both inter- and intra-spherulitic regions. The presence of elastomer appears to enhance this spherulite breakup process. At 20% 8407 impact strength is highest and this may be related to the high strain reached at the end of cold drawing. The area under the stress-strain curve before strain hardening occurs may be related to energy absorption at high strain rates.

A process known as strain hardening occurs post-yield and is indicated by a positive slope in the stress-strain curve. This is a result of chain unfolding and orientation involving the so-called fibrillar transformation which leads to a continuous increase in crystallinity. Mechanical work reduces the thermodynamic barrier between the metastable and stable crystals and helps chains find their way to more stable potential

energy wells during deformation. The more defective crystals are destroyed during drawing and rebuilt into more perfect crystals with a narrower size distribution [132, 161, 266, 269, 277-279]. The slope therefore decreases with increasing elastomer concentration, indicating PP spherulites have an increasing degree of disorder and decreasing load-bearing capability. Strain hardening doesn't occur at the 30 wt% 8407 level, so the ordering and alignment of crystallizable chains are severely hindered by the large domains of 8407, which are highly mobile, primarily non-crystalline, and immiscible with PP.

Elongation and energy at break for elastomer modified PP are poor at high elastomer concentrations because the high interfacial energy between phases dominates failure [261, 262]. The ability to neck and draw is very defect or morphology sensitive, so at 30% 8407, the amorphous content may act as a defect by promoting spherulite breakup and inhibiting recrystallization.

3.3.2 Morphology

Mechanical performance of the physical blend is highly dependent upon its morphology. For SEM imaging, etching of the elastomer phase was required because the domains could only be seen at 30% concentration. From Figures 3-5(a) thru (e), the etching procedure produces dark pits where elastomeric material once was. Another obvious trend is shown – increasing elastomer concentration results in an increase in domain size and decrease in overall matrix-domain interface. In turn, the ligament thickness or distance between elastomer particles [119] is increased. These ideas will be elaborated upon in the proceeding paragraphs.

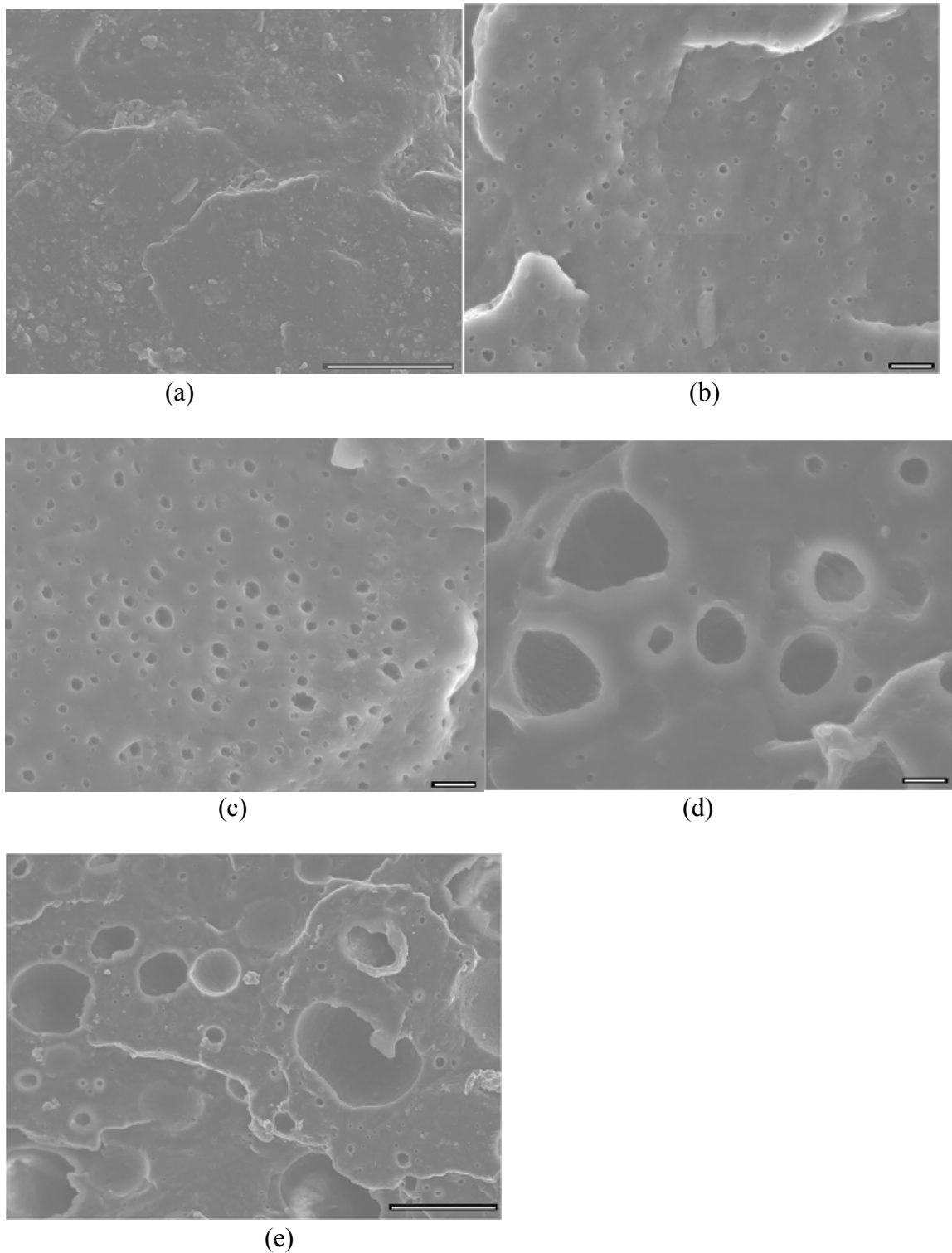


Figure 3-5: SEM images of etched, cryo-fractured surfaces of PP:8407 physical blends as a function of elastomer concentration. (a) Virgin PP at 2,000X, (b) 95:5_0 at 10,000X, (c) 90:10_0 at 10,000X, (d) 80:20_0 at 10,000X, and (e) 70:30_0 at 2,500X. The bar markers for (a) and (e) = 10 μ m, and for (b), (c), and (d) = 1 μ m.

Table 3-3: Image analysis averages taken from etched SEM images of PP:8407 physical blends. At least three images were analyzed from Figures 3(a) thru (e), with data compiled in Appendix D.

Sample ID	D_n (nm)	D_w (nm)	Average Roundness for particles $>1^*$	Ligament Thickness (nm)
95:5_0	77	104	1.08	166
90:10_0	113	167	1.1	194
80:20_0	224	778	1.2	305
70:30_0	269	2630	1.2	321

*Roundness is a measure of how closely the particle's shape matches that of a perfect circle. A value of 1 = a perfect circle.

Table 3-3 (generated from Appendix D) represents image analysis of the SEM pictures and reveals that a relatively narrow particle size distribution exists at low elastomer concentrations. The number average particle diameter (D_n) for the 95:5 blend is approx. 77 nm while at 90:10, D_n increases to 113 nm. The viscosity of the minor phase plays a huge role in determining these values. The matrix viscosity is much higher than the elastomer viscosity, so coalescence is suppressed at low 8407 concentrations.

As the morphology of the blend develops in the extruder and the minor phase is elongated, dispersed, and distributed, the diffusion process of coalescence is kinetically much slower than breakup. So, for the short residence times experienced in the extruder, the domains remain submicron [17, 75]. Also, the particles remain relatively spherical at these low concentrations.

With increasing elastomer concentration, the anisotropy and average domain size of the particles increase. These results are typical of what previous researchers have found regarding PP-elastomer blends [18, 75, 128, 254, 274, 275, 280]. There also seems to be less of a monomodal distribution of elastomer domains at higher concentrations. The smaller interfacial area of the large domains, as well as the large distance between domains, can be directly correlated with mechanical properties. At such high loadings of

8407, the stress field around the elastomer domains is modified and interactions with the matrix are hindered so the blend reacts in a brittle manner to an applied load.

The large size of the dispersed phase at high concentrations is due to coalescence, which is the recombination of particles known to take place during the mixing process arising from forced collisions. Coalescence (collisions) of the minor phase is the rate limiting step during morphology development.

3.3.3 Viscoelasticity

Dynamic mechanical behavior is studied at the molecular level and structural factors affect it, including molecular weight, crosslinking, crystallinity, lamellar thickness, and interfacial interaction between phases [57, 81, 235, 281, 282]. Polymers are examples of viscoelastic materials, which have characteristics of both viscous liquids (only dissipate energy) and elastic solids (only store mechanical energy) [94, 235]. Deformation in solid polymers is dominated by relaxation processes, which are sensitive to morphology and crystallinity [81]. A necessary condition for a highly plastic deformation is the possibility of motions of kinetic elements on a time scale similar to the deformation rate. Dynamic mechanical analysis (DMA) is a valuable tool in the characterization of viscoelastic behavior, which is the mechanical behavior dependence upon time and temperature. It is able to separate the viscous (loss modulus or E'') and elastic response (storage modulus or E') of the material and relates the two by $\tan\delta$ (E''/E').

The first quantity to be studied is the storage modulus (Figure 3-6), which is an indication of the stiffness of the polymer and may be considered inversely proportional to impact strength in physical blends [283]. The stiffness typically increases with increasing density (crystallinity) or entanglement density (from high molar mass) [284].

The behavior in Figure 3-6 is similar to plasticizing a brittle glassy polymer with a low molecular weight compound [285].

There are typically five regions of viscoelastic behavior for semicrystalline polymers [100]. The low temperature (glassy) region in Figure 3-6 occurs at temperatures less than about -45°C . Long range motion is frozen in at these temperatures, so the stiffness of the blend is dependent upon the free volume and

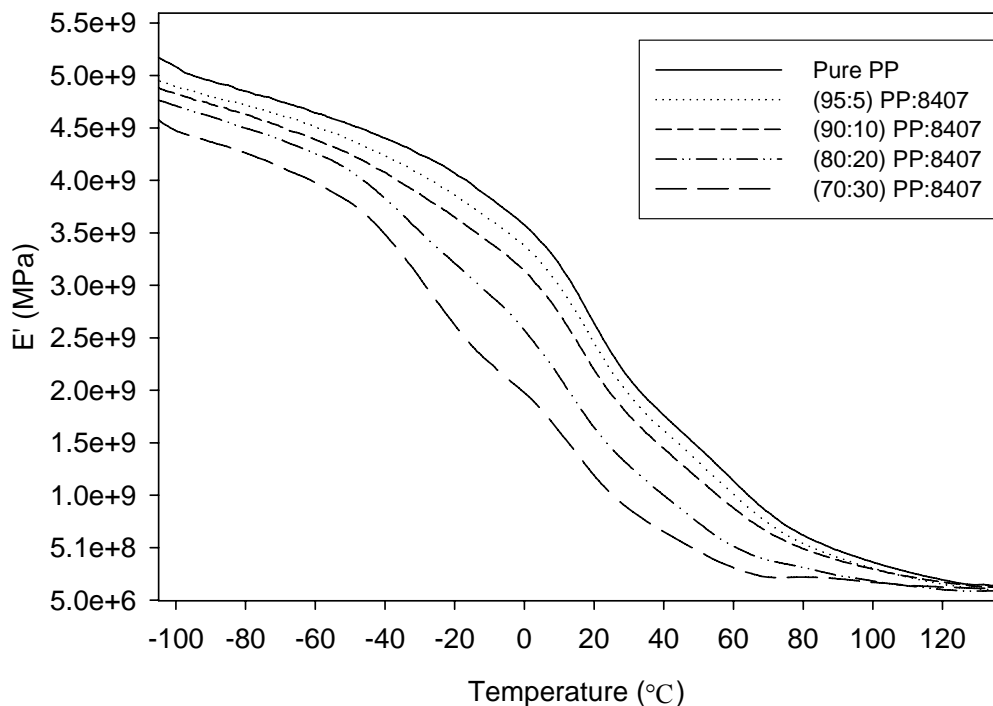


Figure 3-6: Storage modulus vs. temperature for PP:8407 Blends

mobility of side and end groups as well as secondary forces between chains. The long side chains of 8407 renders the blend more pliable due to the increase in free volume.

The glass transition (T_g) region is accompanied by a drop in modulus of about $2 \cdot e^9$ over a range of about 30°C , starting at about -45°C for the elastomeric phase and 10°C for the matrix phase. This is the onset of long range, coordinated molecular motion.

A rubbery plateau region after T_g begins to take shape for the elastomer phase at high concentrations. Long range rubber elasticity is present in this short temperature

range and is likely due to the entanglements associated within the amorphous phase. The rubbery flow region follows at even higher temperatures in the range of about 10-30°C for 8407 and 40-70°C for PP phase. In this region, the polymer is marked by both rubber elasticity (short time scale) and flow properties (long time scale). The response is dependent upon physical entanglements and with the more mobile elastomeric phase present, chains are able to move in a more coordinated motion leading to flow. The liquid flow region occurs at the highest temperatures and represents chain reptation out of entanglements and flow as individual molecules. Segments are free to move from one lattice site to the other, and the hard polymer becomes soft and rubbery. Keep in mind that this behavior is strictly in the amorphous (non-crystalline) phase of the material.

Isotactic polypropylene and ethylene-octene copolymers have three primary viscoelastic relaxations [81, 110, 235, 281, 282, 284, 286-288]: the γ relaxation around -60°C for PP and -120°C for 8407 is attributed to local motion of side groups, end groups, and short main chain -CH₂- links; β relaxation located between 0°C and 30°C for PP and -50°C to -10°C for 8407, represents large scale (non-crystalline amorphous) chain motion due to an increase in amorphous volume and is much broader than in wholly amorphous polymers; α relaxation localized between 40°C and 90°C for PP and 60°C to 80°C for 8407 exists only in the presence of the crystalline phase and originates from diffusion of crystallographic defects, interlamellar slip, and motions of the interfacial regions containing tie molecules, folds, loops, etc.

It is obvious from Figure 3-7 that upon addition of elastomer, two β relaxations are present – the lowest temperature peak representing 8407 and the peak located about 20°C, representing PP. When determining the relative solubility between polymers,

separate $\text{Tan}\delta$ peaks will exist for phase separated blends [8, 9, 81, 289]. The magnitude of each β peak is characteristic of the relative concentrations of the two components, regardless of a dispersed or co-continuous morphology. Broadened peaks and shifts towards an intermediate temperature signify mutual solubility of polymers. Studies have shown that PP is largely immiscible with polyethylene and polyethylene copolymers [290-298] but at low copolymer concentrations, limited partial miscibility is known to

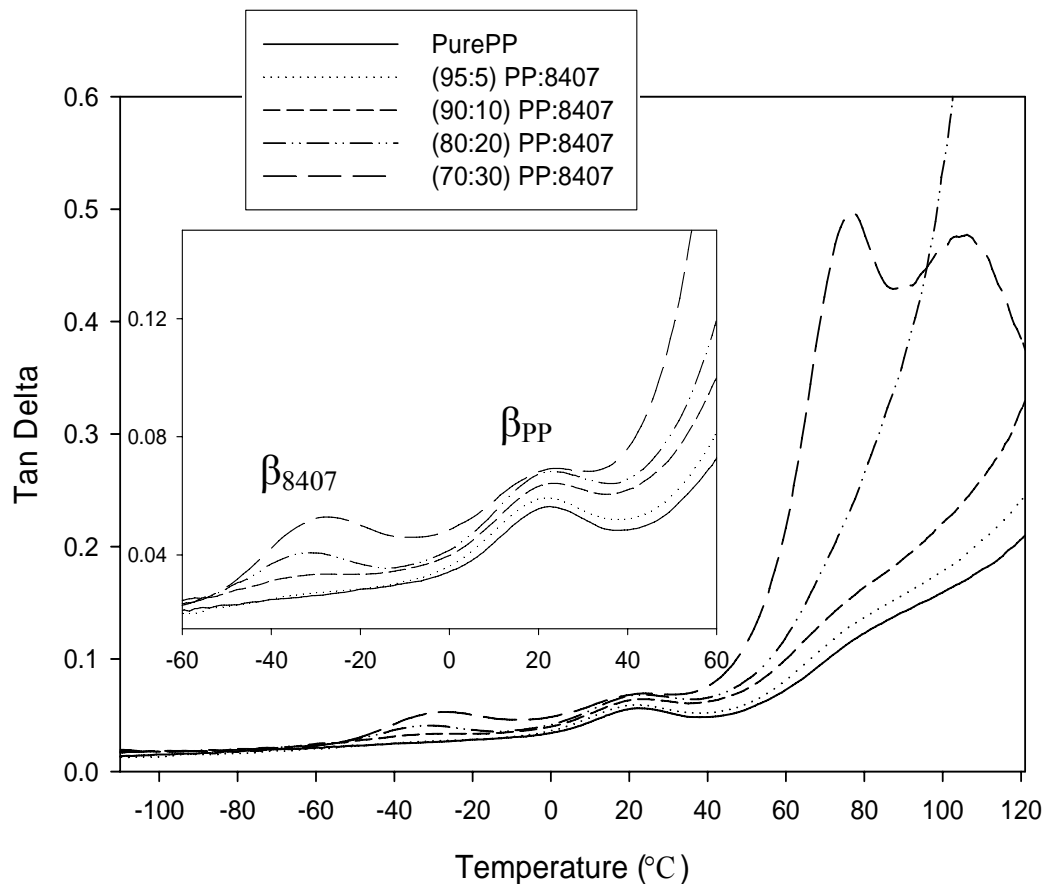


Figure 3-7: $\text{Tan}\delta$ vs. temperature for PP:8407 blends from -120°C to 120°C . Insert represents $\text{Tan}\delta$ vs. temperature from -60°C to 60°C .

exist [18, 299, 300]. The limited miscibility is obvious from the shift of the maximum β_{8407} peak toward higher temperatures with increasing copolymer content. The shift to higher temperatures indicates that the apparent activation energy of the β_{8407} peak slightly increases with concentration in the blends [283, 301]. There may also be a restriction in

8407 mobility due to the trapping of chains in the spherulitic structure of PP. The intensity of both β_{8407} and β_{PP} peaks are known to increase with more elastomer [302] or decrease with increasing degree of crystallinity [81]. PP typically does not show major changes in peak position with crystallinity. The β_{PP} maximum becomes more of a shoulder at decreasing concentrations and overlaps with β_{8407} . The PP peak position is also stationary for all values of elastomer. These findings are similar to that of Xiao et al. [258].

Only at low elastomer concentrations can viscoelasticity of the blend be correlated with impact strength. The time scale involved is comparable to the order of magnitude as the relaxation time of viscoelastic relaxations (milliseconds). In elastomer toughened blends, toughness shows some correlation with the area of the $\text{Tan}\delta$ due to the primary or secondary transition of rubbery component. For an impact test carried out at room temperature, a material will be ductile if it contains one or more prominent subambient relaxation. [109, 281, 283, 303, 304].

Above 40°C, the slope of the $\text{Tan}\delta$ curve increases for all samples but a trend is seen in that the slope upturn is more drastic with increasing elastomer concentration. This should not be surprising because the enhanced mobility afforded by the elastomer enables long range motion and relaxation of chains at lower temperatures. A broad peak/shoulder at about 80°C is seen for Pure PP as well as 95:5 and 90:10 blends. This represents the α relaxation of PP and dramatically increases in intensity with high elastomer concentration. The mobility of defects in the crystalline phase as well as on the surface of the crystallites is enhanced by the presence of highly mobile amorphous elastomeric chains. There is also a slight shift in the α relaxation to lower temperatures

with increasing 8407 concentration, indicating a lower activation energy needed for chain motion. Two distinct high intensity peaks are seen at about 75°C and 100°C for the 70:30 blend and are indicative of the diffuse spherulitic regions of PP, thin lamellae, high defect concentration, and possibly even the onset of crystal melting [283, 305]. Large deformations may be expected to involve the motion or deformation of crystallites or aggregates of segments. So, the high temperature peaks may be associated with the yield stress of the blends at room temperature [306]. The lower activation energies associated with the 70:30 blend can be related to the neck formation during a stress-strain experiment, where unstable deformation and brittle failure occur [105].

The loss modulus (E'') is a measure of the energy absorbed due to relaxation and is useful in clarifying the mechanisms of internal motions. From Figure 3-8, the height of each peak represents the relative mobility of the polymer chains. The peak position (at a given temperature) depends on the chemical structure, flexibility of the molecular chain, steric hindrance, and bulkiness of side groups. The high temperature side of the γ peak of 8407 is seen below -80°C and its intensity characteristically increases with increasing elastomer concentration.

The T_g (β) peak of PP is found at about 20°C and with increasing elastomer concentration it decreases in temperature and intensity. The energy barrier for chain motion therefore decreases with increasing elastomer concentration and this peak becomes more of a shoulder simply due to the fact that the PP concentration in the blend is decreasing. The high temperature peak at about 70°C decreases in intensity due to the lower PP concentration but sharpens possibly due to increased mobility and free volume from the elastomer.

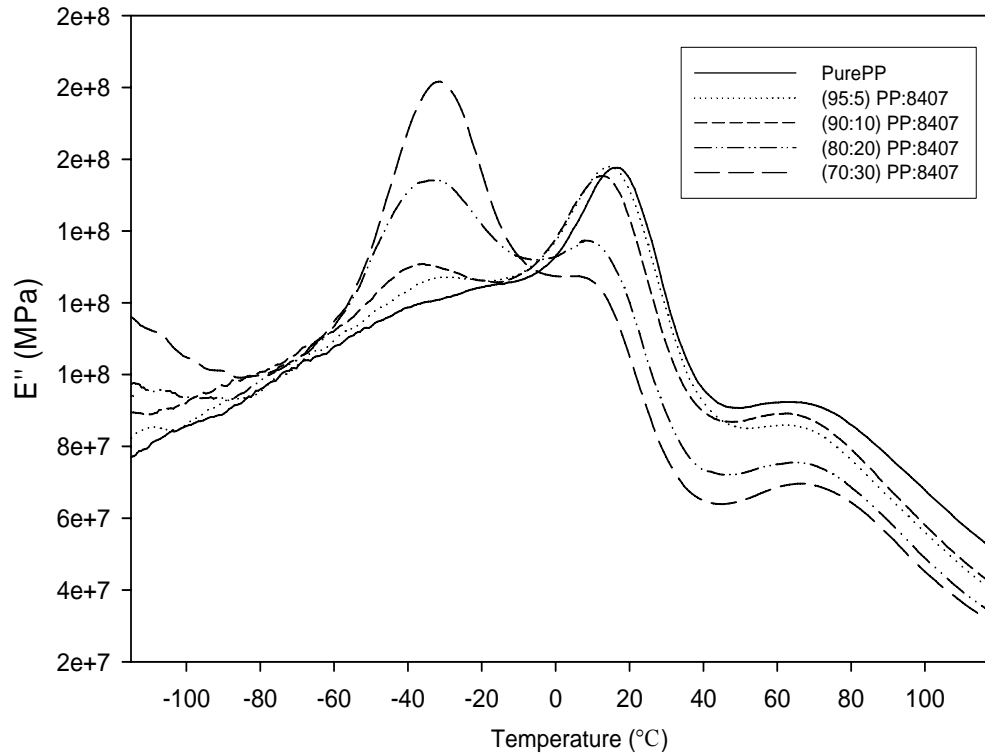


Figure 3-8: Loss modulus vs. temperature for PP:8407 physical blends

It should be noted that the T_g of a polymer is commonly recorded as either the onset or peak temperature on either E'' or $\text{Tan}\delta$ graphs. The values reported in this section are peak temperatures. Differential scanning calorimetry (DSC) is another method to measure T_g and has shown that the T_g of 8407 is about -50°C and PP about -3°C . This is concurrent with the onset temperatures for the β relaxations in both E'' and $\text{Tan}\delta$ graphs.

3.3.4 Crystallinity

The thermal transitions and crystalline character of the blends have been characterized by DSC. This method measures heat flow into (endotherm) and out of (exotherm) the sample in relation to a reference at varying temperatures. For a first order thermodynamic transition like the melting temperature, there is a discontinuity in specific

volume vs. temperature and the DSC thermogram will show an endothermic peak representing the melting of crystalline material in the sample.

From Figure 3-9 and Table 3-4, the α -crystalline phase of isotactic polypropylene (monoclinic bravais lattice) can be identified as a peak at approximately 165°C. The elastomer has a broad melting endotherm from about 30°C to 80°C, signifying that a small degree of fringed micelle material is present [56, 64]. An accurate measure of 8407 % crystallinity is not available due to the broad melting range of the copolymer.

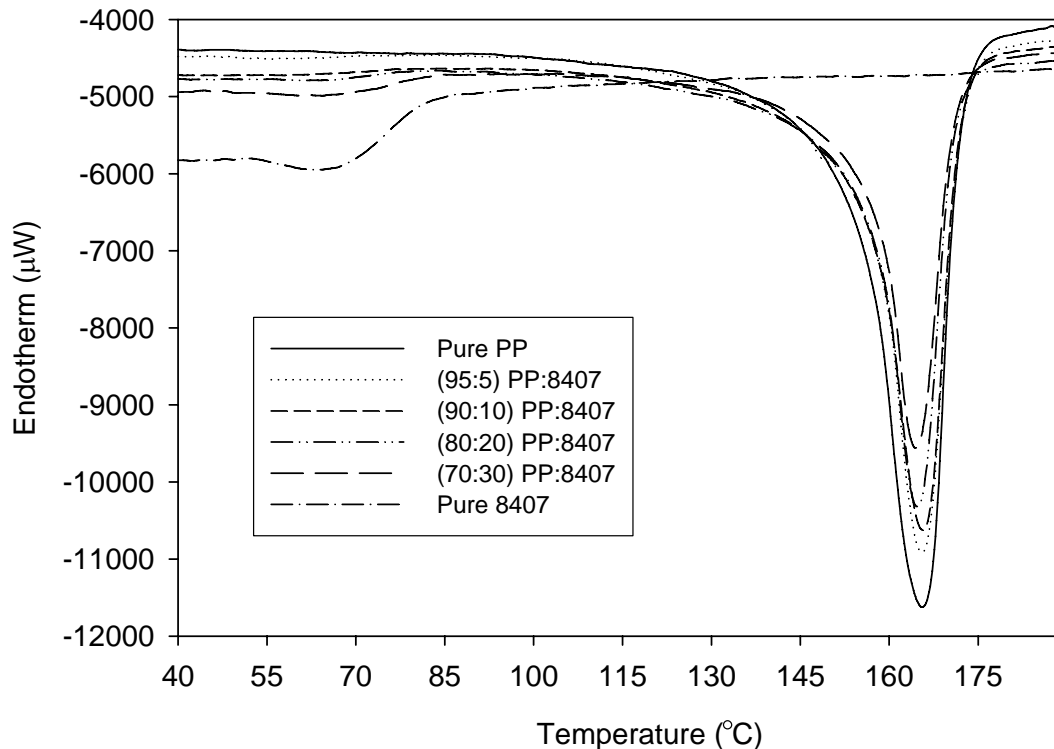


Figure 3-9: DSC melting endotherm of both pure PP and 8407 as well as blends of the two polymers.

The overall % crystallinity of the blends decreases with increasing elastomer content (Figure 3-10) because of the hindrance effect of the melt for the arrangement of the crystallizable chains of PP [128, 190, 264, 307-309]. There is only a slight decrease in the % crystallinity of the PP phase with increasing elastomer concentration, which

indicates that chain alignment and order is not significantly hindered by large pockets of immiscible material. The heat of melting per unit of PP in the blends is independent of elastomer content, signifying that no co-crystallization is taking place [103, 263, 310].

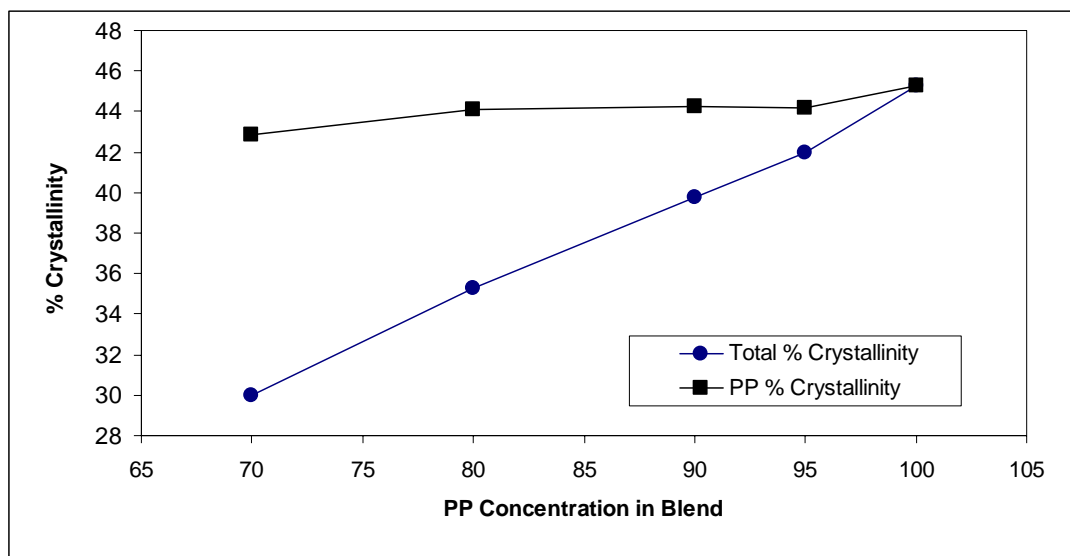


Figure 3-10: Percent crystallinity of the physical blends and pure PP as a function of PP concentration.

Table 3-4: DSC endothermic data comparing pure PP and 8407 to physical blends of PP and 8407. Standard deviation for pure PP is from an average of four samples.

Ratio of PP:8407	α Phase Melting Peak ($^{\circ}\text{C}$)	T_m Onset ($^{\circ}\text{C}$)	Enthalpy of Melting (J/g)	% Crystallinity
100:0	165.9 ± 0.4	154.5 ± 0.5	93.9 ± 0.7	45.4 ± 0.4
95:5	165.5	154.8	87	42
90:10	165.2	152.9	82.3	39.8
80:20	164.7	153.9	72.6	36.6
70:30	164.4	152.5	62.5	30.2
0:100	64.5	-	-	-

Addition of elastomer is also known to decrease the onset of melting and peak melting temperatures which may be due to the localization of elastomer in the intraspherulitic regions and disturbance of spherulite regularity [128, 255, 258, 264, 294, 308, 310]. Also, smaller spherulites have a lower heat capacity, so the melting range of the polymer blend should shift to lower temperatures [255]. When PP crystallizes in the

presence of amorphous, low molar mass, or immiscible material, the second component can either be incorporated into the growing spherulite as occlusions (no effect on growth rate) or rejected into the interspherulitic regions as deformed domains (considerable depression in growth rate) [100, 236, 255, 257, 260, 263, 297, 307, 311-313].

Similar to several other references, elastomer commonly acts as a nucleating agent for the PP and HDPE, therefore increasing crystallization temperature (T_c) and decreasing the average spherulite diameter [17, 23, 24, 103, 241, 255-258, 294]. This is exemplified in Figure 3-11 and Table 3-5. The decrease in spherulite size is an indication of increasing rate of nucleation, likely due to enhanced mobility of PP segments [100, 310]. This reduction also reduces the inhomogeneity of the sample and thus leads to increased impact strength and elongation to break [259]. There may be local defects within the spherulite at high elastomer concentrations which lead to weak spots or holes, thereby reducing impact energy.

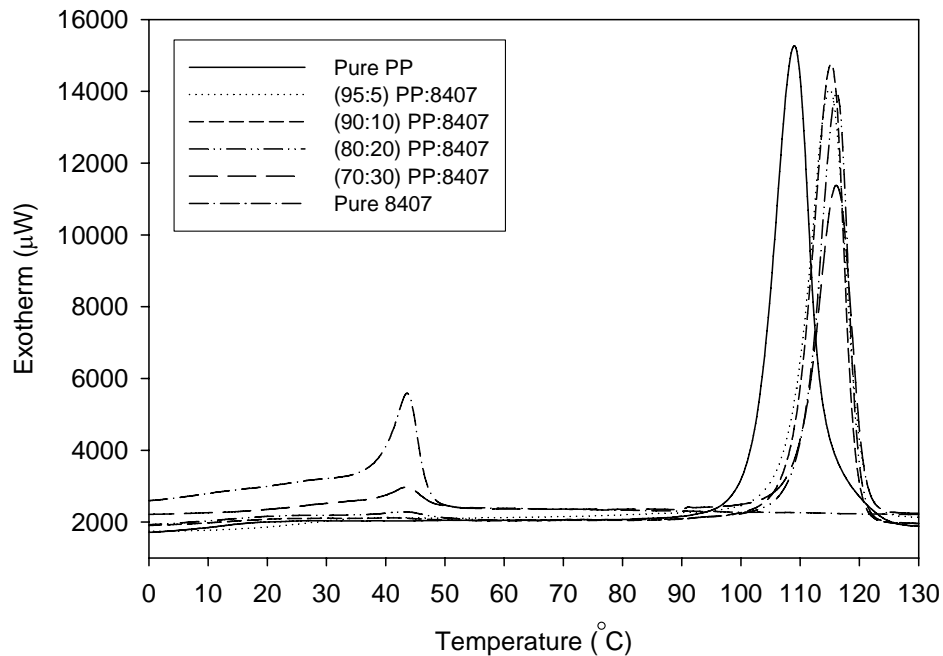


Figure 3-11: DSC cooling exotherm of both pure PP and 8407 as well as blends of the two polymers.

Table 3-5: DSC exothermic data comparing pure PP to 90:10_0, 90:10_A, and 90:10_B. An average of 3 runs were performed on 90:10_B.

Ratio of PP:8407	Peak Temperature of Crystallization (°C)	Enthalpy of Crystallization (J/g)
100:0	109.6 ± 0.9	-90.7 ± 0.6
95:5	114.9	-85.8
90:10	115.2	-82.7
80:20	116.1	-72.1
70:30	116.1	-60.6
0:100	43.6	-34.1

3.4 Conclusions

By simply melt blending a low molar mass grade of ethylene-octene copolymer, a modest jump in impact strength can be seen up to 20 wt% elastomer, above which the material acts in a brittle manner. This is directly related to the morphology of the blends, where elastomer domains increase in size and change in shape from spherical to ellipsoidal. The coalescence of the particles reduces their overall surface area so as to limit interfacial interaction with PP. Melt flow index increases with increasing elastomer content because the elastomer MFI is over 30 times that of the matrix phase. This low molar mass elastomer affects both the crystalline and amorphous phases which in turn deleteriously affect stress-strain performance.

Viscoelastic analysis confirms the thought that PP and 8407 are largely immiscible phases. The low temperature peak of 8407 signifies chain mobility at low temperatures, which is a good indication of impact strength performance. The sheer speed of the impact test renders pure PP brittle but the blends ductile because elastomer chains are able to relax and diffuse in response to the high stress before breaking. The crystallinity of the blend is reduced with addition of 8407, but the % crystallinity of PP remains the same regardless of the amount of elastomer. Also, the crystallization temperature

increases with increasing elastomer content because of the heterogeneous nucleation effect and enhanced molecular mobility.

CHAPTER 4 TOUGHENED POLYPROPYLENE BASED ALLOYS

4.1 Introduction

The focus of this dissertation is based on the results obtained in this chapter, which elaborates on the fundamental differences between PP alloys and physical blends. It will be shown that modification on the nano-scale is necessary to achieve performance enhancements previously unattainable. Many different toughening mechanisms are thought to be involved in improving the impact strength of PP via alloying with an elastomer. This chapter will tie in experimental results to many references and will show that a novel material has indeed been created. When modifying a polymer via reactive blending, the resulting mechanical properties depend on a foundation of controlled morphology, rheology, crystallinity, and chemical structure. A thorough explanation of the alloy's impact strength and stress strain properties will be followed by morphological, chemical, rheological, and crystallographic characterization.

4.2 Experimental

4.2.1 Materials

Table 4-1 gives a list of pertinent ethylene-1-octene copolymers (EOCs) produced by Dupont Dow elastomers under the tradename ENGAGE®, but the grade of interest is 8407 [48]. Isotactic polypropylene homopolymer was supplied by Equistar Chemical (grade PP 31S07A) and is contact translucent. All polymers were received in pellet form. Polyisoprene (NATSYN) was donated by Goodyear. The peroxide and monomers used in this study were reagent grade chemicals (structures are shown in Table 4-2). The

Table 4-1: ENGAGE® product data table.

ENGAGE® Grade (decreasing comonomer content)	8842	8407	8200	8401	8402
Comonomer Content wt% ¹³ C NMR/FTIR	45	40	38	31	22
Density, g/cm ³ ASTM D-792	0.857	0.870	0.87	0.885	0.902
Melt Index, dg/min ASTM D-1238, 190°C, 2.16kg	1.0	30	5.0	30	30
Mooney Viscosity ASTM D-1646 ML 1 + 4 at 121°C	26	< 5	8	< 5	< 5
Durometer Hardness, Shore A ASTM D-2240	50	72	75	85	94
DSC melting Peak, °C Rate: 10°C/min	33	60	60	78	98
Glass Transition Temp, °C DSC inflection point	-61	-57	-56	-51	-44
Flexural Modulus, MPA ASTM D-790, 2% Secant	3.5	12.1	12.1	25.8	69.9
Ultimate Tensile Strength, MPa ASTM D-638, 508mm/min	2.1	3.3	6.9	6.4	12.9
Ultimate Elongation, % ASTM D-638, 508mm/min	975	>1000	>1000	950	790

monomers were purified by passing through an activated alumina column before use.

Styrene monomer, inhibited by 10-15 ppm t-butyl catechol, was purchased from Fisher.

The initiator, 2,5dimethyl-2,5-di-(t-butylperoxy) hexane, was purchased from Atofina

under the tradename Lupersol 101. Diethyleneglycol diacrylate (DEGDA), inhibited by

80 ppm Hq and 120 ppm MEHQ, and trimethylolpropane triacrylate (TMPTA), inhibited

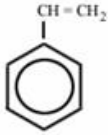
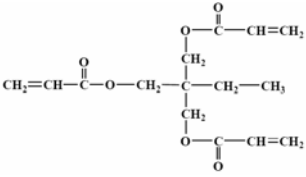
by 125 ppm HQ and 175 ppm MEHQ, were graciously donated by Sartomer, an Atofina

company. Irganox B215 was purchased from Ciba specialty chemicals.

Table 4-2: Structures of reactive materials of interest

Name	Lupersol 101	DEGDA
Structure	$ \begin{array}{c} \text{CH}_3 \quad \quad \text{CH}_3 \\ \quad \quad \\ (\text{CH}_3)_3\text{C}-\text{O}-\text{C}-\text{CH}_2-\text{CH}_2-\text{C}-\text{O}-\text{O}-\text{C}(\text{CH}_3)_3 \\ \quad \quad \\ \text{CH}_3 \quad \quad \text{CH}_3 \end{array} $	$ \text{CH}_2=\underset{\text{H}}{\text{C}}-\overset{\text{O}}{\parallel}{\text{C}}-\text{O}-\text{CH}_2-\text{CH}_2-\text{O}-\text{CH}_2-\text{CH}_2-\text{O}-\overset{\text{O}}{\parallel}{\text{C}}-\underset{\text{H}}{\text{C}}=\text{CH}_2 $

Table 4-2 Continued

Name	Styrene	TMPTA
Structure		

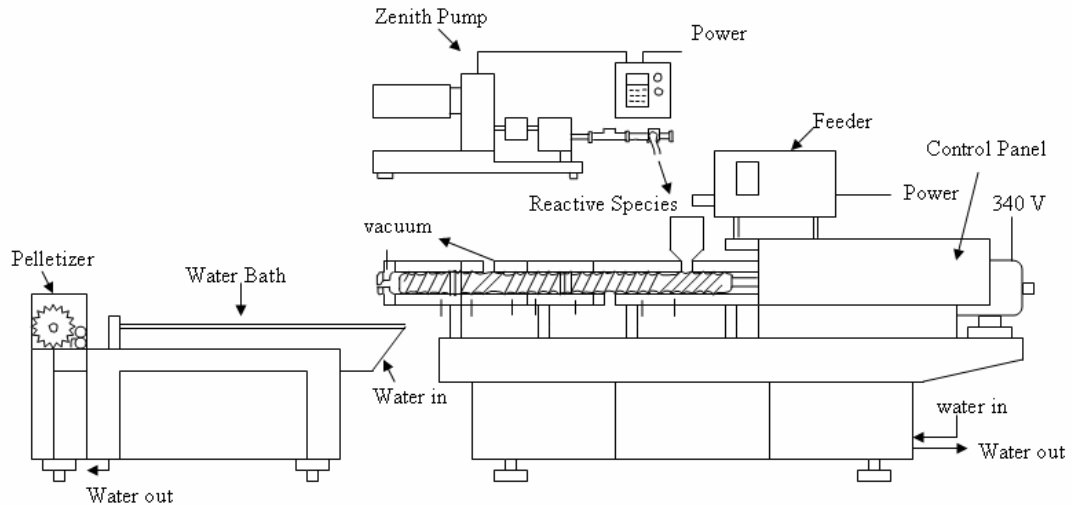
4.2.2 Methods

4.2.2.1 Processing

All polymers were dried in an air circulating oven at 40°C for 24 hours prior to compounding. Before processing, the resins were premixed by hand for about 10 minutes. Monomer/initiator mixtures were magnetically stirred for 10 minutes before processing and a choice amount of the mixture was added to the dry polymer pellets before processing.

The blending was carried out in a 34 mm non-intermeshing, co-rotating twin screw extruder, APV Chemical Machinery (now B&P Process Systems) with an L/D ratio of 39. The temperature of the extruder was regulated by electrical resistance and water circulation in the barrels. The dried, pre-mixed resins were then introduced into the extruder from the hopper of the extruder at 60 g/min through a screw driven dry material feeder (Accu Rate, Inc). A Zenith pump controlled the rate of monomer/initiator solution addition into the extruder. The screw speed, unless otherwise noted was 150 rpm. Devolatilization was carried out by a vacuum pump, VPS-10A, Brooks Equipment Company. This was placed near the die and created a pressure of about 15 in Hg. The extruder was always starved to feed. Figure 4-1 is a schematic of the extruder along with a typical temperature profile. After compounding, the resulting strands which exit the die

are quenched in a water bath, pelletized, and dried in a vacuum oven at 100°C, 28 in Hg for 24 hours.



Die	Zone 1	Zone 2	Zone 3	Zone 4	Zone 5	Zone 6	Zone 7 (Feed)
195°C	205°C	210°C	210°C	200°C	190°C	180°C	165°C

Figure 4-1: Schematic drawing of the reactive twin screw extruder and a common temperature profile.

4.2.2.2 Mechanical properties

In order to measure the strength of the materials at very high testing rates, a notched Izod impact test was performed according to ASTM D256 standards. The pellets were placed in a mold with 6 slots, each measuring 0.5x0.5x2.5in³. The mold is put in a Carver press (Fred S. Carver, Inc.) at 200°C and after the material melts, pressed up to 5000 psi. After waiting for 5-10 minutes, the pressure was slowly increased up to 10,000 psi. Five minutes later, the heat was turned off and the sample was let to cool down to room temperature at about 1.5°C/min. The bars were then taken out and notched with a Testing Machines, Inc. (TMI) notching machine. Before testing, they were conditioned at room temperature for 24 hours and a 30 ft-lb hammer was used with test method A on a TMI Izod impact tester. At least 5 bars were broken and impact strength is recorded regardless of full or partial break.

For stress-strain measurements, dried pellets were placed in a mold measuring 15 cm² x 1 mm thick. The mold was put into the Carver press at 200°C and after the material melts, pressed up to 5000 psi. After a 5-10 minute wait, the sample was slowly pressed to 10,000 psi. Five minutes later, the sample was quenched in a water bath. Specimens were tested according to ASTM D638 standards. Type V specimens were punched out of the compression molded sheet with a die, measuring 1 mm thickness, 2.95 mm gauge width and 9.5 mm gauge length. Five samples were tested after conditioning at room temperature for 48 hours. The machine used to test the samples was an MTS Model 1120 Instron, using a 1000 lb load cell at a test speed of 12.7 mm/min

A Seiko DMS220 interfaced with a Seiko Rheostation model SDM/5600H was used to test dynamic mechanical specimens. Testing was conducted from -120°C to 150°C at a heating rate of 5°C/min in a dry nitrogen atmosphere maintained at an approximate flow rate of 100 mL min⁻¹. Rectangular samples (20x10x1 mm³) were cut from the compression molded sheet and tested in bending mode at a frequency of 1Hz.

4.2.2.3 Morphological characterization

Scanning electron microscopy (SEM) was performed on a JEOL 6335F Field Emission SEM. The microscope was kept under vacuum at 1x10⁻⁵ Pa, with an accelerating voltage of 5 kV and secondary electron detection at various magnifications. Two different etching procedures were performed for better phase contrast – one using fractured impact bars and the other using compression molded films. The etching was done to remove amorphous (or elastomeric) material. Impact bar samples were etched by the following procedure: A notched impact bar was immersed in liquid nitrogen for 10 minutes and immediately fractured using a TMI impact tester. A section of the cryofractured surface (2 cm thick) was immersed in xylene (purchased from Fisher

Scientific) at 60°C for one hour. The sample was removed and dried under vacuum at 40°C for 12 hours.

Compression molded thin films were etched so as to view the lamellar morphology of the polymers. They were produced by heating the Carver press up to 200°C, pressing samples to desired thickness (about 10 μm), and cooling at a rate of about 30°C/min. The films were then etched according to the procedure originally reported by Olley et al. [314] and duplicated by various other authors [315-318]. The following materials and their concentrations were purchased from Sigma Aldrich and used as received: Potassium permanganate (1.3 wt%), phosphoric acid (32.9 wt%), and sulfuric acid (65.8 wt%). Potassium permanganate crystals were slowly added to a phosphoric/sulfuric acid solution in a conical flask and stirred until they all dissolved, producing a dark green color. Dissolving the crystals took over an hour. The samples were then immersed in the permanganic acid solution for five hours. The next consecutive steps include: washing with a mixture of 2:7 sulfuric acid:distilled water which has been cooled to near its freezing point, decanting the solution, washing with hydrogen peroxide (35% solution in water, purchased from Acros Organics) for two minutes, washing with distilled water several times over two minutes, and washing with acetone (Fisher Scientific) for two minutes.

Sample mountings for SEM were on aluminum stubs with conductive carbon paint from Ted Pella, Inc. The sample was then coated with carbon (for impact bar specimens) or a thin layer of gold-palladium (for thin films) then vacuum dried at room temperature for one hour prior to examination in the microscope.

Image analysis was done using ImagePro software. Domain size and distribution were quantified, but the domains had to be manually outlined for the software to recognize them as discrete phases. For the majority of images, over 1000 particles were considered for diameter and roundness measurements. The number average (D_n) and weight average (D_w) diameter were determined using the following equations:

$$\bar{D}_n = \frac{\sum N_i D_i}{\sum N_i} \quad (4.1)$$

$$\bar{D}_w = \frac{\sum N_i D_i^2}{\sum N_i D_i} \quad (4.2)$$

where N_i represents the number of particles with diameter D_i .

For transmission electron microscopy (TEM), Samples were embedded in a room temperature cure epoxy, using a flat silicon mold, and let cure overnight. These were trimmed with a razor blade to expose as small an area as possible and then cryo-ultramicrotomed on a Reichert UltraCut at -110°C using a 35° diamond knife. Sections were approximately 70-100 nm thick. Ethanol was used in the knife boat to float the sections and the sections were picked up using 600 mesh copper grids. These grids were stained with a 0.5% aqueous solution of ruthenium tetroxide, purchased from Electron Microscopy Sciences, for 30 minutes. After letting the grids outgas for about 24 hours, the sections were imaged with a Philips 420T TEM at 100 kV.

In order to assess the crystalline structure of the polymer samples, wide angle x-ray diffraction (WAXD) was used. This was done on a Phillips MRD X'pert high resolution XRD using $\text{Cu } k_\alpha$ radiation at a wavelength of 1.54056nm. The scan rate was $6^\circ/\text{min}$ over a 2θ range from 5° to 50° .

A polarized light microscope (PLM), Olympus model BX60 with CCD camera and quarter wave plate attachments, was used to study the crystalline morphology of the materials as they cooled from the melt. A hot stage (Linkam TMS 91) allowed for crystallization studies on ~5 μm thick compression molded samples. Images were captured using Scion software. Table 4-3 gives the heating and cooling cycles for each specimen. The first cycle was performed to erase previous cooling history and the second cycle is reported in the results and discussion section.

Table 4-3: PLM consecutive heating/cooling cycles

Step	Start Temp (°C)	End Temp (°C)	Heating/Cooling Rate (°C/min)	Hold Time (min)
1	30	200	10	5
2	200	30	10	5
3	30	200	10	5
4	200	30	10	-

For stress whitening qualification of impact bars, digital images were taken post-fracture using a Kodak EasyShare CX7300.

4.2.2.4 Chemical composition and molecular structure

Fourier Transform Infrared Spectroscopy (FTIR) was performed on a Nicolet 20SXB Spectrometer. 256 Scans were taken from 3500 to 500 cm^{-1} wavenumbers with a resolution of 4. Measurements were done in transmission mode on thin films (~2-3 μm). Films were produced by melting the polymer in a Carver press at 180°C and 10,000 psi for 2 minutes then quenching in a water bath at room temperature. For quantification of the grafted styrene, a calibration curve had to be established as explained in Appendix A. Areas under the 700 cm^{-1} and 1376 cm^{-1} peaks were compared and related to absolute styrene amounts to get the grafting efficiency (GE). This is defined by the following equation:

$$GE = \frac{\text{Amount of Monomer Grafted to Polymer Backbone}}{\text{Original Amount of Monomer Pumped into Extruder}} \times 100\% \quad (4.3)$$

For FTIR, all reactively extruded materials must be purified before quantification of grafting yield. This first involved dissolving the pellets of crude graft copolymer in hot xylene at a concentration of ca 4% (wt/vol). The hot solution was precipitated into ten volumes of acetone (a known non-solvent for the LLDPE, HDPE and PP, and a solvent for styrene monomer and homopolymer based on solubility parameters [162]). The unreacted monomers, styrene, and DEGDA or TMPTA homopolymers and copolymers remained soluble in acetone and were separated out from the grafted polyolefins. The precipitated graft modified alloy was filtered, washed, and then vacuum dried at 70°C for 24 hours. FTIR showed that the GE level remained unaltered upon further rounds of purification. Therefore, one purification step was sufficient for removal of all the residual impurities.

Gel permeation chromatography (GPC) was performed on a Waters GPCV 2000 calibrated using crosslinked polystyrene standards for relative molar mass determination. The set temperature was 40°C with THF as the solvent at a flow rate of 1.0mL/min. Samples (about 9 mg) were dissolved in 9.5 ml (8.44 g) of HPLC grade THF purchased from Acros Organics and passed through 0.45 µm filters before analysis.

4.2.2.5 Thermal analysis and rheology

Differential scanning calorimetry (DSC) was used to study the different thermodynamic transitions present in the blends. DSC was performed on a Seiko SII DSC 220C-SSC/5200, Seiko Instruments, equipped with a Seiko Rheostation model SDM/5600H and calibrated with indium and tin standards. Samples (approx. 7 mg in weight) were sealed in crimped aluminum pans, with the reference being 99.99% pure

alumina. Purging of the sample was done with dry nitrogen at a flow rate of 100 mL/min. Each sample experienced two heating and cooling cycles (shown in Table 3-2) with the first to erase prior thermal history. The second cycle is reported in all graphs. The % crystallinity is found by first integrating the heat flow curve to a flat baseline then dividing by the heat of fusion of a perfect PP crystal (207 J/g).

Table 4-4: DSC consecutive heating/cooling cycles

Step	Start Temp (°C)	End Temp (°C)	Heating/Cooling Rate (°C/min)	Hold Time (min)	Sampling (s)
1	-70	200	20	3	3
2	200	-80	20	5	3
3	-80	200	10	5	1
4	200	-80	10	3	1

Thermal Gravimetric Analysis (TGA) was performed on a select few samples using a SEIKO TG/DTA 320. This measures weight loss as a function of temperature with a typical heating run from 25°C to 1000°C at 10°C/min.

To determine the gel content of the alloys, ASTM D2765 test method A was followed and repeated three times for the materials of interest. Samples weighing 0.300 ± 0.015 g were placed in a 120-mesh stainless steel cloth pouch and immersed into a round bottom flask through a reflux condenser. The 500 ml flask was filled with 350 g of xylene and 1% antioxidant (Irganox B215 from Ciba Specialty Chemicals) was added to it. Xylene was boiled at 140°C and refluxing was done for 12 hours. After extraction, the samples were immediately placed in a vacuum oven preheated to 150°C and dried at 28 in Hg for 24 hours. The difference in weight between the sample + cage before and after extraction is reported.

Melt Flow Index (MFI) testing was done according to ASTM D1238 (230°C and 2.16 kg weight) on a Tinius Olsen model MP 933 Extrusion Plastometer. For materials

with an flow rate of 0.5-3.5 g/10 min, the weight of the samples was approx. 3 g, whereas materials with flow rates of 3.5-300 g/10 min, the sample weight was approx. 6 g. All materials were dried under vacuum then conditioned at room temperature before testing.

The extensional flow properties of the melt were investigated using a Göttfert Rheotens tester operated at a constant acceleration of the rollers (120 mm/s). A polymer melt strand is extruded vertically downwards from a capillary die and drawn by rotating rollers, with the stretched polymer melt undergoing uniaxial extension. The force at which the polymer melt breaks is designated the “melt strength.”

4.3 Results and Discussion

ENGAGE® polyolefin elastomers have an advantage over polyisoprene (PI), polybutadiene (PB), or elastomers containing unsaturated bonds because ENGAGE® possesses no main chain unsaturation, therefore oxidation and discoloring are limited. An argument may be made that PI may be better suited for this reactive extrusion process than ethylene- α -olefin copolymers because the peroxide initiated grafting is expected to be facilitated by the presence of double bonds in the polymer backbone. A typical formulation of 0.3 wt% initiator, 6 wt% styrene, and 0.8% DEGDA, with a PP:PI ratio of 80:20 was reactively extruded and analyzed by FTIR to detect whether all PI double bonds had reacted. Figure 4-2 shows both a full scan from 500 cm^{-1} to 3300 cm^{-1} and an insert of the peaks of interest. The presence of styrene, 8407, and polypropylene caused overlapping of some peaks, but some characteristic peaks have been identified. The carbonyl stretch from DEGDA represents the peak at 1740 cm^{-1} and the 1600 cm^{-1} peak is due to the C=C aromatic stretch from the phenyl pendant group of styrene. The peak at 1660 cm^{-1} is most significant because it represents an alkenyl C=C stretch, characteristic of the polyisoprene main chain unsaturation [319, 320]. This signifies that the free

radical grafting process does not consume every double bond in the backbone of PI and therefore unsaturated rubbers are not suitable alternatives to fully saturated elastomers.

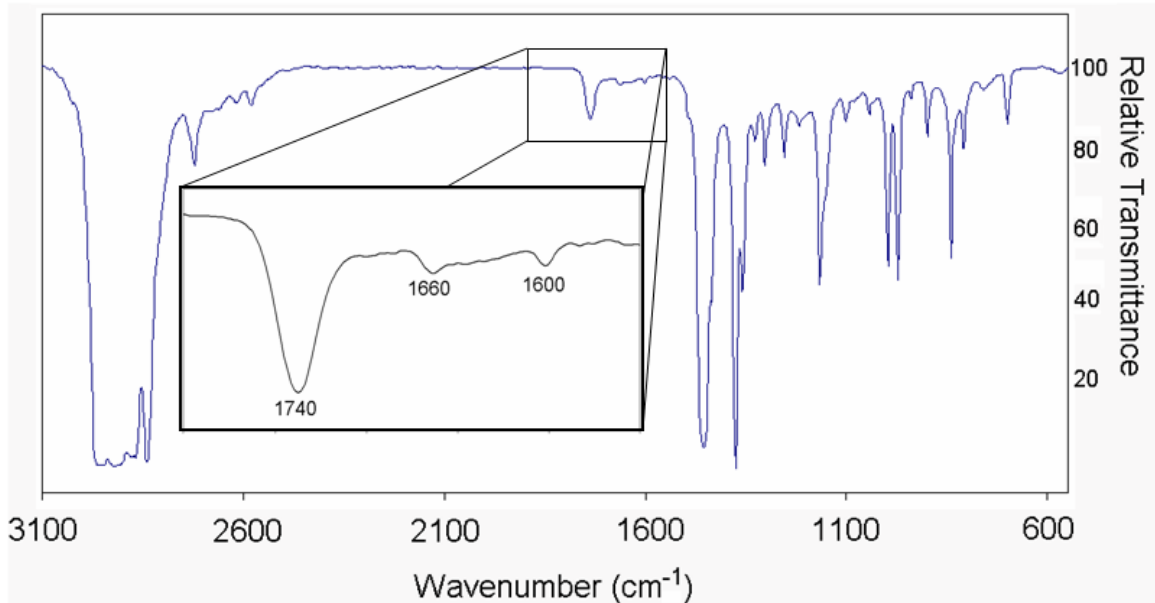


Figure 4-2: FTIR image of PP:polyisoprene reactive blend.

The elastomer of interest is 8407, having a combination of low viscosity and crystallinity compared to many commercially available ethylene-octene copolymers. A systematic study has been undertaken which encompasses the effect of reactive materials (initiator, styrene, and multifunctional monomer) in alloys with varying amounts of 8407. To simplify referencing samples, a code has been established for each formulation (Figure 4-3 and Table 4-5).

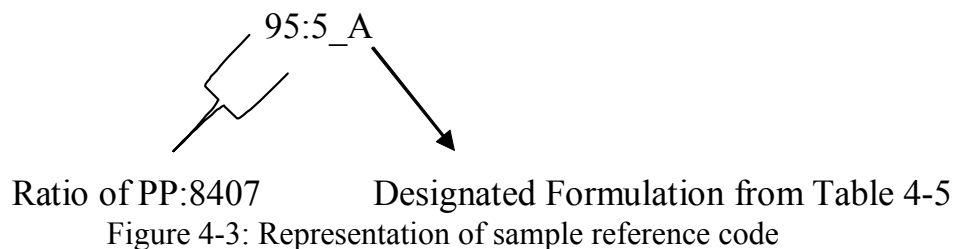


Figure 4-3: Representation of sample reference code

The weight % is defined as the percentage of material added in relation to the total weight of all ingredients. For example, a PP:8407 ratio of 95:5, 0.3 wt% Initiator and 6

wt% styrene means that out of a total of 100 grams, Initiator = 0.3 g, Styrene = 6 g, PP = 89 g, 8407 = 4.7 g.

Table 4-5: Identification of formulations

Alloy ID	wt% Initiator	wt% Styrene	Multifunctional Monomer (0.8 wt%)
0 (Physical Blend)	0	0	-
A	0.3	6	-
B	0.3	6	DEGDA
C	0.3	6	TMPTA

4.3.1 Notched Izod Impact Analysis

A quick comparative measure of the toughness of thermoplastics at high deformation rates is the Izod impact test. Figure 4-4 shows that by physical blending 8407 with PP, impact strength is marginally improved. The same holds true when a peroxide initiator and styrene monomer are added to the mix. It should be noted that impact bars of pure PP and 95:5_A completely broke, but all others were only partial breaks. Addition of 0.8 wt% multifunctional monomer (either di- or tri-functional) improves the room temperature notched Izod impact strength dramatically. The greatest jump in impact strength is seen at a PP:8407 ratio of 80:20, having over a 13X improvement over pure PP. This result is indicative of a modified material with enhanced energy absorption and dissipative mechanisms. The high functionality of DEGDA and TMPTA has several effects on the alloys. They incorporate a greater degree of entanglements and intercrystalline tie molecules, better efficient trapping of radicals on the polymer backbones, homogeneity on the micron scale, and they limit the degree of PP degradation.

The high deformation rate leads to adiabatic heating in the sample (upwards of 70-80°C at the surface of a rubber toughened polypropylene [116]) which means an increase

in free volume in the amorphous phase and an increase in T_g [129, 242, 321]. More free volume means greater chain mobility, a high degree of grafting, and higher impact strength. Another possibility is the idea of crystalline phase transformation toughening, where melting (energy absorption) and recrystallization (dissipation of energy) take place as a result of the high temperatures [129, 132, 134]. The phase transformation may be associated with the retractive (elastic) behavior of the impact bars. Defective or small crystals are destroyed and recrystallized into an oriented thermodynamically stable α

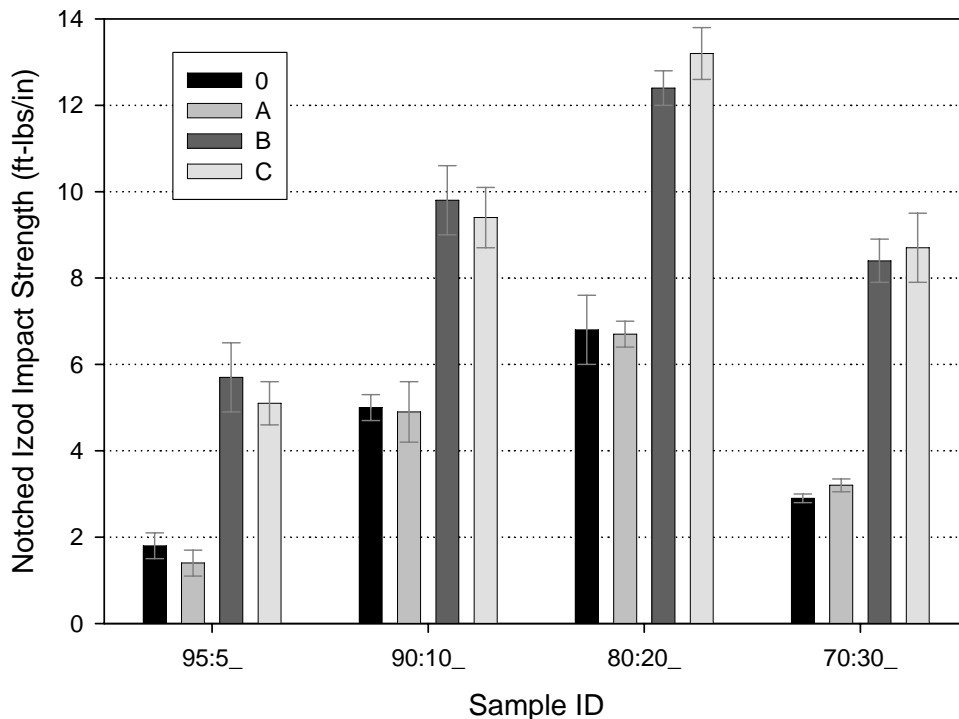


Figure 4-4: Room temperature notched Izod impact strength of PP blends and alloys. Reference material is virgin PP at 0.99 ft-lbs/in.

phase [287, 322-327]. In other words, a type of strain hardening is experienced. Another phenomenon could be that the elastomer phase experiences a large extension of its chains along with a rise in temperature. By applying rubber elasticity theory, a decrease in entropy is opposed by a more energetically favorable random coil conformation [100,

161]. So during notched impact tests, impact energy is absorbed primarily during the bending of the specimens (i.e. under tensile deformation) [252, 253].

The tri-functional acrylate gives the highest impact strength at high concentrations of elastomer. TMPTA has a higher grafting efficiency than DEGDA (from its greater functionality), which will be shown in the next section. A more network-like structure may be formed with TMPTA present, therefore improving bonding between phases (improved stress transfer) and increasing the retractive force of the alloy. At low elastomer concentrations, grafting, crosslinking, and entanglements may be so high with TMPTA that the impact strength is not as significantly affected.

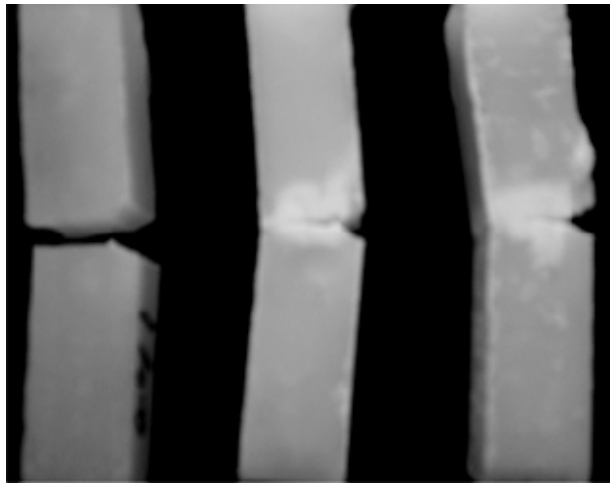


Figure 4-5: Izod Impact test specimens post-fracture. Left– Pure PP, Middle – 90:10_0, Right – 90:10_B.

Figure 4-5 shows that stress whitening occurs when 10% elastomer is added to PP, regardless of whether it is an alloy or physical blend. This is commonly seen in rubber toughened polymer and is attributed to the dilation and cavitation of rubber domains as well as shear yielding and crazing [103, 328]. Pure PP was one of a few materials that broke completely in this test. For the partially broken samples, the crack traveled further for the physical blend than reactive blend, which may be due to the increased elastic restorative force caused by the multifunctional monomer.

A corollary to Figure 4-5 would be to use SEM to probe the actual crack tips of the physical and reactive blends. From Figures 4-6 and 4-7, there is a clear difference between the cracks tips for the partially broken samples. An important feature is the shape of the crack tip itself and morphology of immediately surrounding material. For the physical blend (Fig. 4-6), the crack tip is blunted and curved. There is little

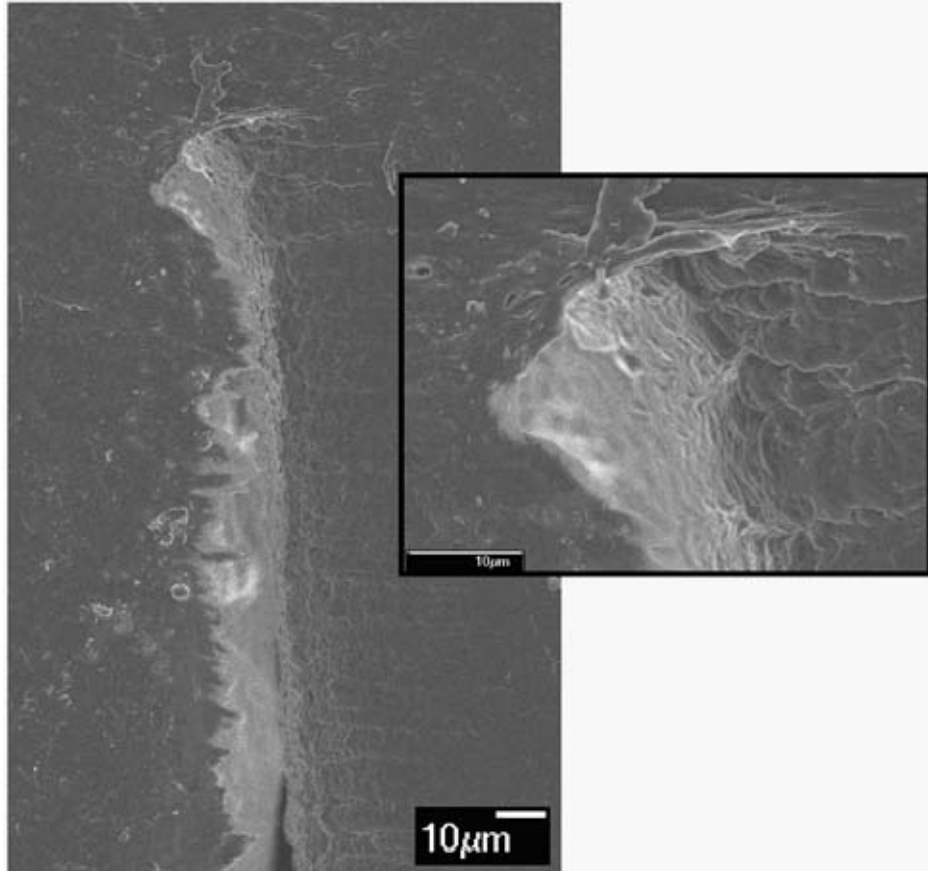


Figure 4-6: SEM image showing the tip of an arrested crack from a room temperature notched Izod impact test of 90:10_0. Insert is a magnified image of crack tip.

stretching and drawing of material into the crack front, which spans over 10 μm.

Elongated voids are present at the crack surface and are oriented approximately parallel to the fracture surface, a feature also found by Wei and Sue [329]. For the alloyed polypropylene (Fig. 4-7), the crack retains its ellipsoidal shape (approx. 2 μm in diameter) and there appears to be a high degree of yielding and melting of material

completely surrounding the crack tip. The uniform shape of the tip may be related to the homogeneous distribution of sub-micron elastomer particles and thin lamellar crystals. As a crack propagates through the sample, it encounters a large number of extremely small energy absorbing particles which do not blunt the tip as typical large rubber particles would.

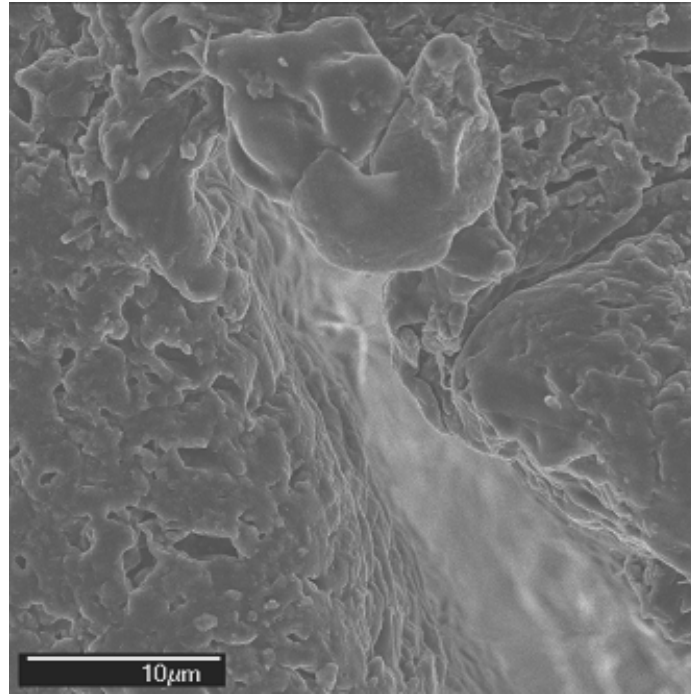


Figure 4-7: SEM image showing the tip of an arrested crack from a room temperature notched Izod impact test of 90:10_B.

The morphology of room temperature fractured surfaces of pure PP and an alloy are also remarkably different. Figure 4-8 is a comparison between fracture surfaces of brittle PP (a) and tough 80:20_C (b), imaged at the center of the impact bars. The most striking feature is the coarse morphology in the toughened material compared to the relatively flat surface of the brittle material. A flat surface is indicative of a fast, brittle fracture, whereas an extremely rough surface indicates energy dissipation and absorption leading to a tough response to the impact test. As previously noted, adiabatic heating takes place at the surface of the sample [21, 130, 131, 133]. The rise in temperature

results in a void-free relaxation layer, which is due to a high degree of plastic deformation. The existence of this relaxation layer indicates an increase in impact strength and slows the propagation of a crack.

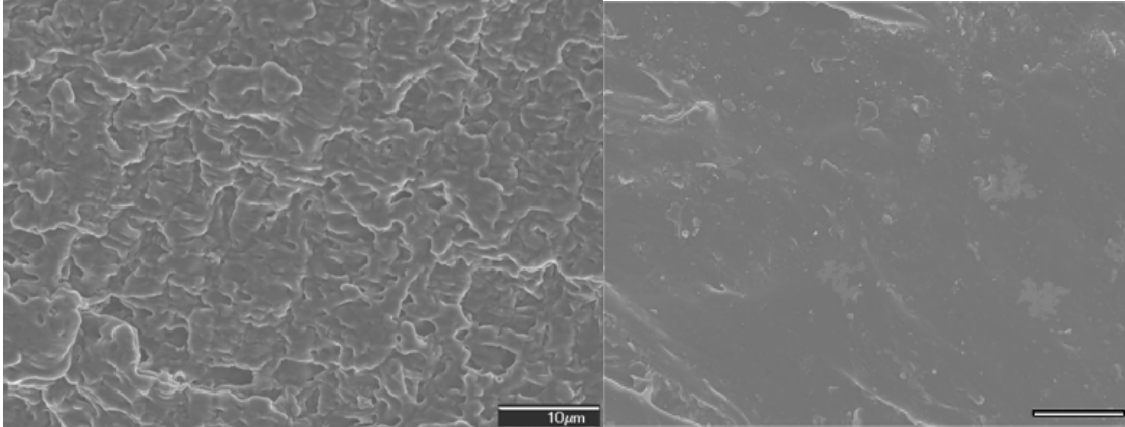


Figure 4-8: SEM image of 80:20_C (left) and Pure PP (right) fractured at room temperature without etching. Each image is located at the center of the impact bar, with magnification = 2,000X and marker bar = 10µm.

It should be noted that the impact strengths of samples fractured at liquid nitrogen temperatures (for morphological analysis) were around to 0.4 ft-lbs/in, regardless of elastomer concentration.

4.3.2 Stress-Strain Behavior

Stress-strain measurements have been conducted on all of the previous impact strength samples. These low deformation rate tests give a different perspective as to how the material responds to a tensile load. Figures 4-9 thru 4-12 represent the stress-strain behavior of these materials, with Appendix B showing both statistical data and representative plots of each sample.

The low strain portion of the stress strain curve is dominated by the amorphous phase response to the applied load. When comparing each of these graphs, the elastic modulus is highest for the samples containing multifunctional monomer at all concentrations of elastomer. This is intuitive because of the greater degree of

entanglements and intercrystalline tie molecules afforded by the multifunctional monomer. At a constant percent crystallinity, the smaller the crystallite size (which generally implies more tie molecules), the higher the modulus [330]. Section 4.3.7 will show that unusually small lamellar crystals exist for the alloys. The amorphous component of semicrystalline polymers, although macroscopically isotropic, can consist of micro- or submicron domains with considerable degree of order [105]. There is an amorphous layer (fold surface) which increases in thickness because defects locate in this area [331]. Grafted material cannot crystallize and thus may reside at the surface of lamellar crystals rather than be incorporated into them. Typically, elastic modulus and yield strength increase upon grafting of monomer [184, 222, 230, 250].

Yield stress remains approximately the same between the physical blends and alloys containing only styrene and initiator, but is slightly higher for samples containing

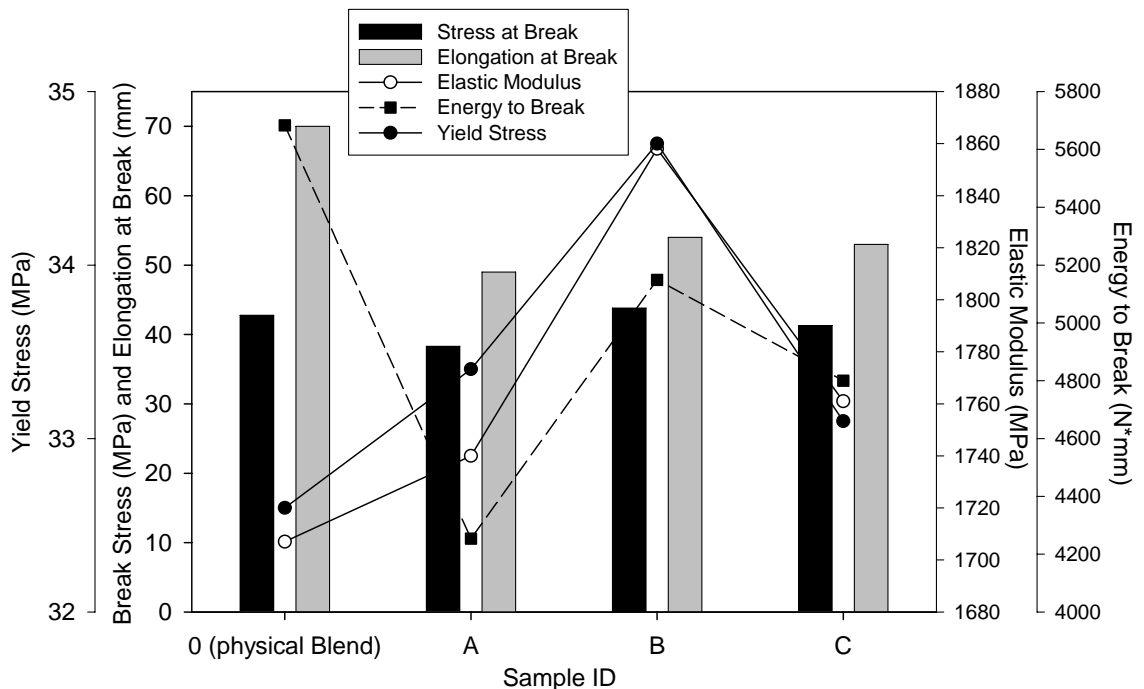


Figure 4-9: Stress-strain properties of 95:5 alloys compared to the 95:5 physical blend.

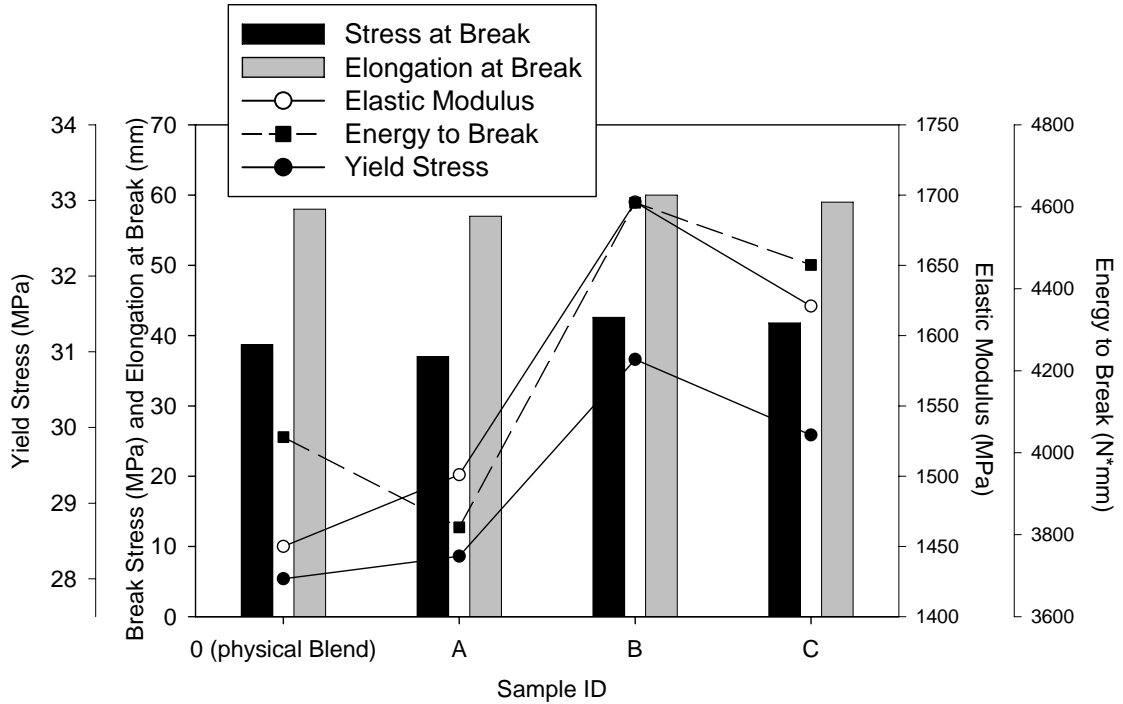


Figure 4-10: Stress-strain properties of 90:10 alloys as compared to the 90:10 physical blend.

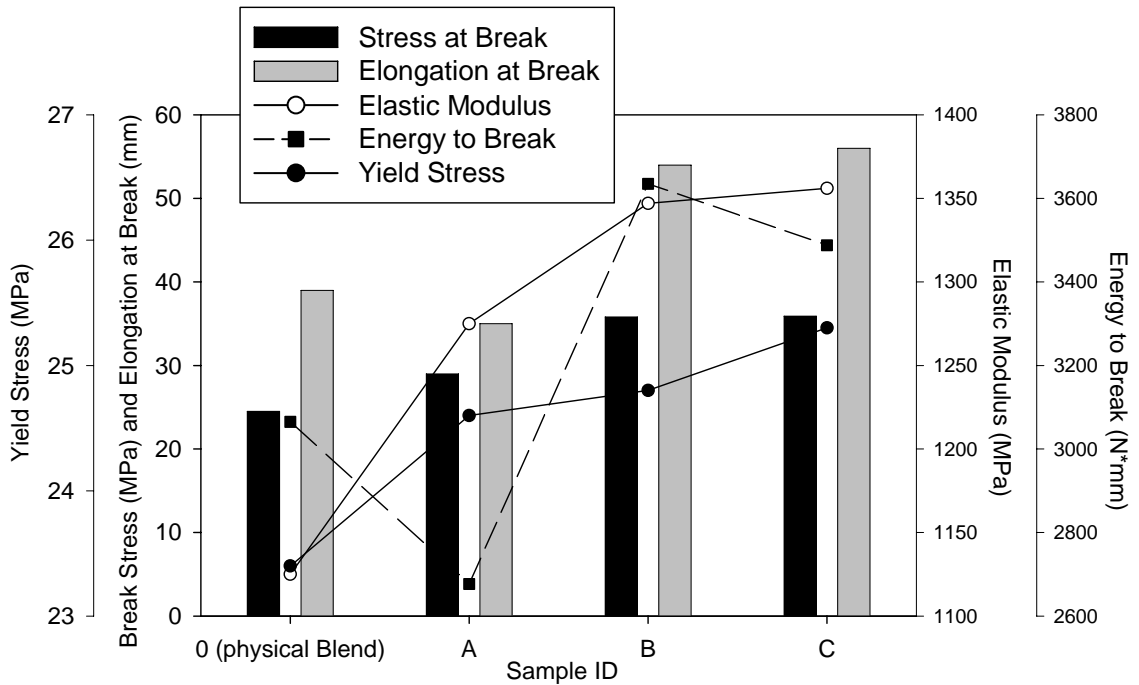


Figure 4-11: Stress-strain properties of 80:20 alloys as compared to the 80:20 physical blend.

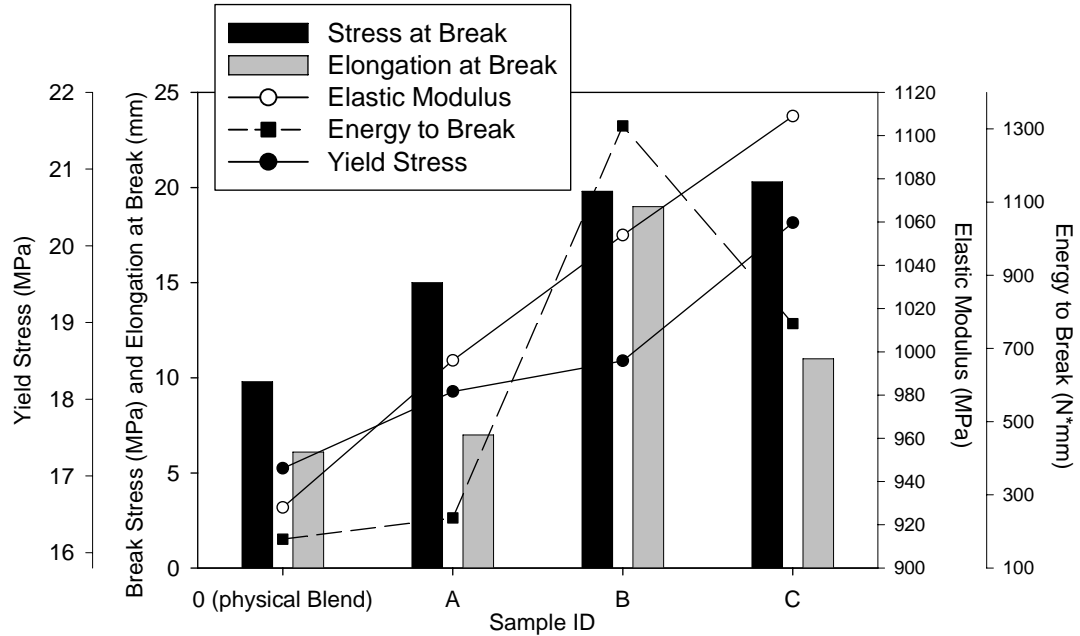


Figure 4-12: Stress-strain properties of 70:30 alloys as compared to the 70:30 physical blend.

multifunctional monomer. The higher yield stress may signify a greater energy barrier to molecular motion, lamellar unfolding, and orientation. This may also be connected to the unique cross-hatch structure of the alloys. The density of tie molecules affects the deformation mode of lamellar blocks (slippage, breakup, defolding) and thus the macromolecular rearrangements in the crack tip [134].

From Figure 4-9, energy to break, elongation at break, and stress at break are all greater for the physical blend than of the high impact strength alloys, a trend not seen at higher concentrations of elastomer. This may be due to the fact that multifunctional monomer cannot completely prevent degradation of PP, so small non-crystalline PP chains will fail beyond a certain extension. Also, slight crosslinking may exist in the elastomer phase, creating a phase separated gel which is known to decrease these tensile properties. Elastic modulus and yield stress are highest for the DEGDA-containing samples. This is somewhat surprising given the higher functionality of TMPTA. This

result may be due to the greater overall number of DEGDA molecules (about 1.4:1 molar ratio) and therefore greater number of branch points homogeneously distributed throughout the material. Also, the lower viscosity of DEGDA allows better diffusion in the highly viscous PP melt.

At the 90:10 level, the DEGDA containing sample shows the best overall stress-strain performance (Figure 4-10). In the physical blend, the higher elastomer content leads to a greater degree of phase separation, larger elastomeric domains, altered spherulitic morphology, and greater amorphous interfacial thickness. At higher levels of 8407, the elastic modulus increases in magnitude to a greater extent with multifunctional monomer present. This may be an indication that the PE phase is imposing a greater influence on the free radical grafting process and a high degree of branches or entanglements may be formed due to excess free radicals.

The increase in elastomer concentration has a much more drastic effect on elastic modulus for 70:30_C than 70:30_B. As can be seen in Figure 4-12, the elastic modulus of 70:30_C actually surpasses that of 70:30_B. One may visualize that the 8407 phase melts first, acting as a cage by trapping liquid reactants. Once the initiator decomposes, the 8407 phase is affected to a greater degree than PP, and because of the high functionality of the TMPTA molecule, crosslink density will be higher. At low 8407 concentrations the grafting reaction happens so fast that the less viscous, less sterically hindered molecule (DEGDA) compensates for the speed. For high elastomer concentrations, radicals are longer lived in the 8407 phase, therefore increasing the probability of being trapped by TMPTA vinyl groups.

The strain hardening for 70:30_0 and 70:30_A are poor (similar to impact strength results), which indicates the ease in which crystalline lamellae are destroyed and recrystallized. The temperature rise experienced from adiabatic heating, low interfacial energy, and large elastomer domains may all contribute to the poor performance. 70:30_B has a low strain at break and energy to break likely due to the greater entanglement or crosslink density of the sample. The sample containing DEGDA must limit both the degradation of PP and crosslinking of PE while facilitating a highly branched, diffuse macromolecular structure with crystallizable PP chains in close proximity to one another. A higher tie chain density indicates an increasing ability to strain harden [132, 332-334]. And a semblance of order before strain hardening may facilitate a stress-induced phase transformation of crystalline phase stabilization [132, 134]. A material with a less dense crystal structure and thicker amorphous layer of connecting chains typical of β phase of PP, has a higher inherent ductility and overall macroscopic toughness than the α phase [278, 287, 332, 333, 335-340]. Smaller blocks of crystallites translate easier than larger ones and therefore orient preferentially in the direction of deformation leading to greater toughness [260]. Also, elongation at break and hence energy to break has already been proven to increase with increasing degree of grafting [7, 250].

For all stress-strain plots, reactive blends not containing multifunctional monomer show poor properties in relation to all other materials, including the physical blends. PP is known to undergo β -chain scission during melt free radical grafting, so isotactic high molecular weight chains that may otherwise be able to crystallize are chopped up and rendered defective or amorphous material. Thus, their contribution to stress strain

performance is a negative one. These materials have lower percent crystallinity and higher MFI, as will be shown in the following sections, so the energy barriers for molecular motion are reduced. The degradation and lower molecular weight are analogous to adding an excess amount of peroxide to the system, which reduces the overall crystallinity [148, 220, 233, 341] as well as melting temperature [222, 233].

4.3.3 Grafting onto Polyolefins

FTIR is a very versatile technique which determines the presence of certain types of bonds and functional groups in an organic molecule [319, 320]. Molecules are excited to a higher energy state when they absorb infrared (IR) radiation, corresponding to stretching and bending frequencies of covalent bonds and unique to every compound. A brief explanation of the peaks present for a typical toughened PP alloy is needed to understand what groups are present and how they respond to IR radiation. Figure 4-13 is a typical FTIR image containing PP, 8407, initiator, styrene, and multifunctional monomer. The relevant peaks are characterized according to the strength and type of deformation of the bond and location with regards to frequency.

The purpose of using FTIR is to both quantify the amount of styrene grafted onto the polyolefin backbone and verify the existence of grafted multifunctional monomer. Grafting efficiency, as described in the experimental section and Appendix A, is shown in Figure 4-14. This figure is direct evidence that PP is more likely to be grafted over 8407 because GE decreases almost linearly with increasing 8407 content. Chapter 2 explained this decrease as a result of the higher bond dissociation energy of primary and secondary hydrogen atoms in 8407 compared to the abundant tertiary hydrogens in PP. The long side groups of the copolymer may also hinder approach of primary free radicals to its backbone.

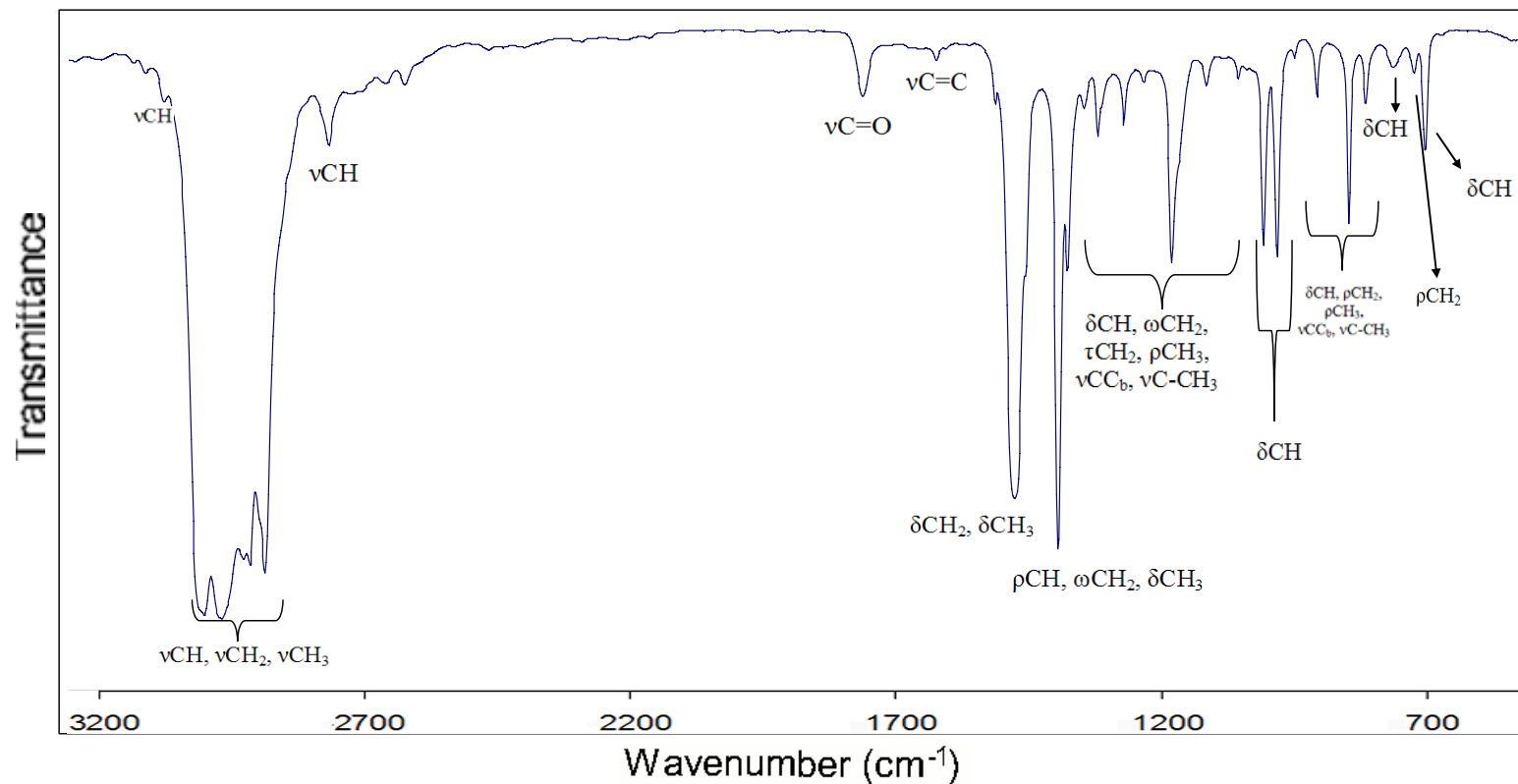


Figure 4-13: FTIR image of a typical PP:8407 alloy containing styrene and multifunctional acrylate. At 3085cm^{-1} , aromatic ring C-H stretch; from $2970\text{-}2721\text{cm}^{-1}$ there are C-H stretching vibrations from methyl (CH_3), methylene (CH_2) and methyne (CH) groups; At 1738cm^{-1} , C=O stretch from acrylate containing monomers; 1660cm^{-1} peak is a C=C stretch from styrene; 1460cm^{-1} is from CH_2 scissoring, and both CH_2 and CH_3 bending; 1376cm^{-1} gives CH_2 wagging, CH_3 bending, and C-H deformation of CH_3 ; from $1340\text{-}1050\text{cm}^{-1}$, C-H bending, CH_2 twisting and wagging, C-C skeletal stretching vibrations, C- CH_3 stretching take place; peaks at 997cm^{-1} and 974cm^{-1} are from C-H out of plane bending; peaks in the region of $953\text{--}790\text{cm}^{-1}$ are from C-H bending, CH_2 rocking, CH_3 rocking, C-C stretching, C- CH_3 Stretching; 766cm^{-1} peak from an aromatic C-H out of plane bend; the 720cm^{-1} peak from CH_2 methylene rocking; and 700cm^{-1} peak from an aromatic C-H out of plane bend.

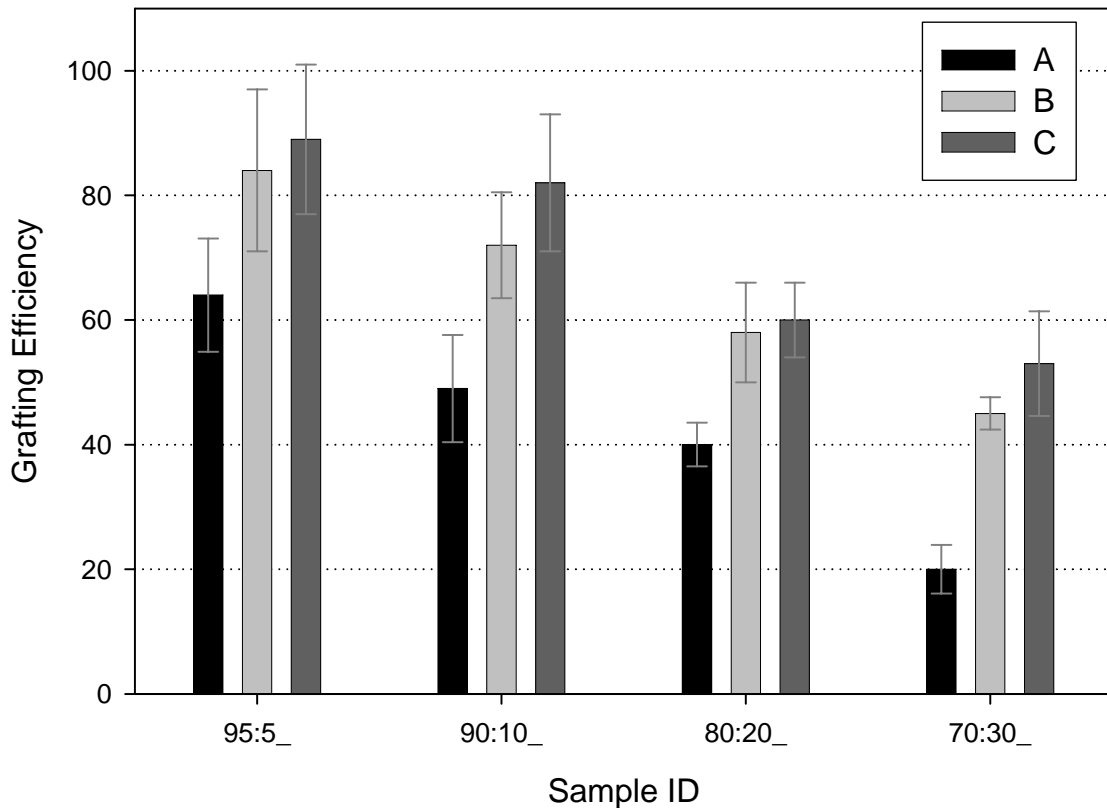


Figure 4-14: Styrene grafting efficiency at various 8407 concentrations both with and without multifunctional monomer.

The amount of styrene grafted onto the polyolefins is noticeably increased with multifunctional monomer present. The chemistry behind this phenomenon implies that the reaction kinetics are much faster with styrene plus comonomer as opposed to styrene alone. This reduces the extent of PP chain scission and traps radicals before they can cause unwanted side reactions. Also, the fact that the multifunctional monomers have more than one site to start a growing chain or bond to another one creates more opportunity to increase the total amount of graft copolymer. The grafting of styrene onto 8407 or PP rather than acrylate monomers is energetically favored, but it is still unclear whether grafting occurs before or after β -chain scission and whether multifunctional monomer links degraded PP chains back together. Besides its inherent stability to radical

attack, styrene monomer improves the dissolution of multifunctional monomer, initiator, and the polymers, which is known to improve grafting efficiency [7, 40, 92, 94, 138, 206, 228]. Studies have shown that grafting does take place in the copolymer phase likely because of its lower T_m and lower viscosity than PP [240]. The tri-functional acrylate has a higher GE than the di-functional acrylate at all concentrations because of the extra free radical-trapping pendant group. Grafting and branching may originate from a single monomer unit or include intermolecular bonding of homopolymer or copolymer networks.

It should be noted that the ratio of isotactic polypropylene segments can be quantified using FTIR by comparing the area under two peaks: 998 cm^{-1} (isotactic helical conformation) and 975 cm^{-1} (internal standard) [342, 343]. The grafted materials do not show any appreciable change in isotacticity.

Gel permeation chromatography (GPC) is a universal technique for determining polymer molar mass averages and distribution of chains within the given sample. Figure 4-15 reveals that grafting does occur on 8407 when reactively extruded absent PP. TMPTA is shown to have a much greater influence on the higher molecular weight chains than DEGDA, which is due to the higher functionality of TMPTA. This is evidence that the stress-strain behavior and grafting efficiency is more favorable with TMPTA present at high 8407 concentrations. Teh and Rudin have shown that when grafting polyethylene, molecular weight increases with increasing monomer concentration [250]. There is also a more pronounced increase in molecular weight of the longer polymer chains (i.e. M_z and M_{z+1}). Grafting is shown to occur on this copolymer, but Chapter 6,

section 6.3.1.2 will give conclusive evidence that the monomers do graft onto 8407 in the presence of PP.

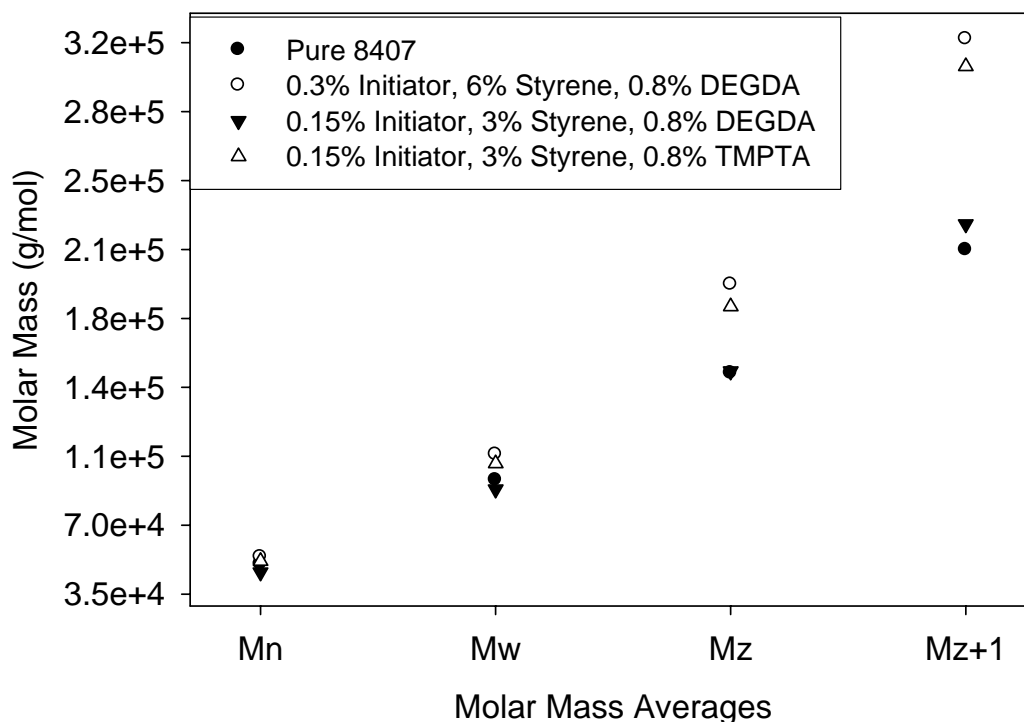


Figure 4-15: Molecular weight averages for pure 8407 and three grafted 8407 materials.

A broadening of the copolymer's molecular weight distribution is due to the random, uncontrolled nature of the free radical grafting process. The polydispersity index (or molecular weight distribution) increases from 1.85 for pure 8407 to 1.97 for the grafted 8407 at 0.3% initiator, 6% styrene, and 0.8% DEGDA. The PDI of 8407 at lower initiator and styrene concentrations containing DEGDA and TMPTA are 1.91 and 1.96, respectively.

4.3.4 Morphology

Scanning electron microscopy has been utilized to study the elastomer domain size, shape and distribution in both the physical blends and alloys. Figures 4-16 shows SEM pictures of alloys with varying elastomer concentration. In a similar fashion to the

physical blends, the more elastomer in the alloy, the larger the etched domains. The number of domains present for the alloys is much less than the corresponding physical blends, which is an indication of covalent bonding of the elastomer to the matrix.

The diameter of particles in the alloys are significantly smaller and more elongated than the physical blend counterparts, with averages in Table 4-6 and particle size distributions in Appendix D. The reason for both of these effects is likely due to the stabilizing influence of the reactive materials [32, 87-89]. The number average particle diameter is smaller for all alloys when compared to the physical blends. This trend is even more obvious for weight average diameter, where larger particles are much more influential.

Table 4-6: Image analysis of etched SEM surfaces of several blends and alloys. This information is gathered from Appendix D, Figure 4-16, and Figure 3-5. Ligament thickness is calculated using the number average diameter.

Sample ID	D _n (nm)	D _w (nm)	Average Roundness for particles >1*	Ligament Thickness (nm)	Impact Strength (ft-lbs/in)
95:5_0	77	104	1.08	166	1.8 ± 0.3
95:5_B	55	76	1.27	119	5.7 ± 0.8
90:10_0	113	167	1.11	194	5.0 ± 0.3
90:10_B	93	164	1.37	159	9.8 ± 0.8
80:20_0	224	778	1.15	305	6.8 ± 0.8
80:20_B	127	337	1.34	173	12.4 ± 0.4
70:30_0	269	2630	1.16	321	2.9 ± 0.1
70:30_B	162	860	1.35	193	8.4 ± 0.5
*Roundness is a measure of how closely the particle's shape matches that of a perfect circle. A value of 1 = a perfect circle.					

The images in Figure 4-16 are composed of non-circular particles, which is unique when compared to the physical blends in the previous chapter. As explained in section 2.4.4, Sundararaj, Macosko, and Scott developed their own theory of morphology development when melt blending polymers [32, 83]. At an intermediate step of droplet breakup, a fragile lace structure forms which is composed of spheres of the matrix phase

surrounded by a thin sheet of minor phase. The sheet then begins to break apart into irregularly shaped pieces of a wide distribution in size. With addition of initiator, styrene, and multifunctional monomer, these pieces are very small (<100 nm in diameter) and are stabilized as non-spherical shapes. Without stabilization, as shown in Chapter 3, the irregular pieces continue to break down until all of the particles become nearly spherical which is accompanied by coalescence.

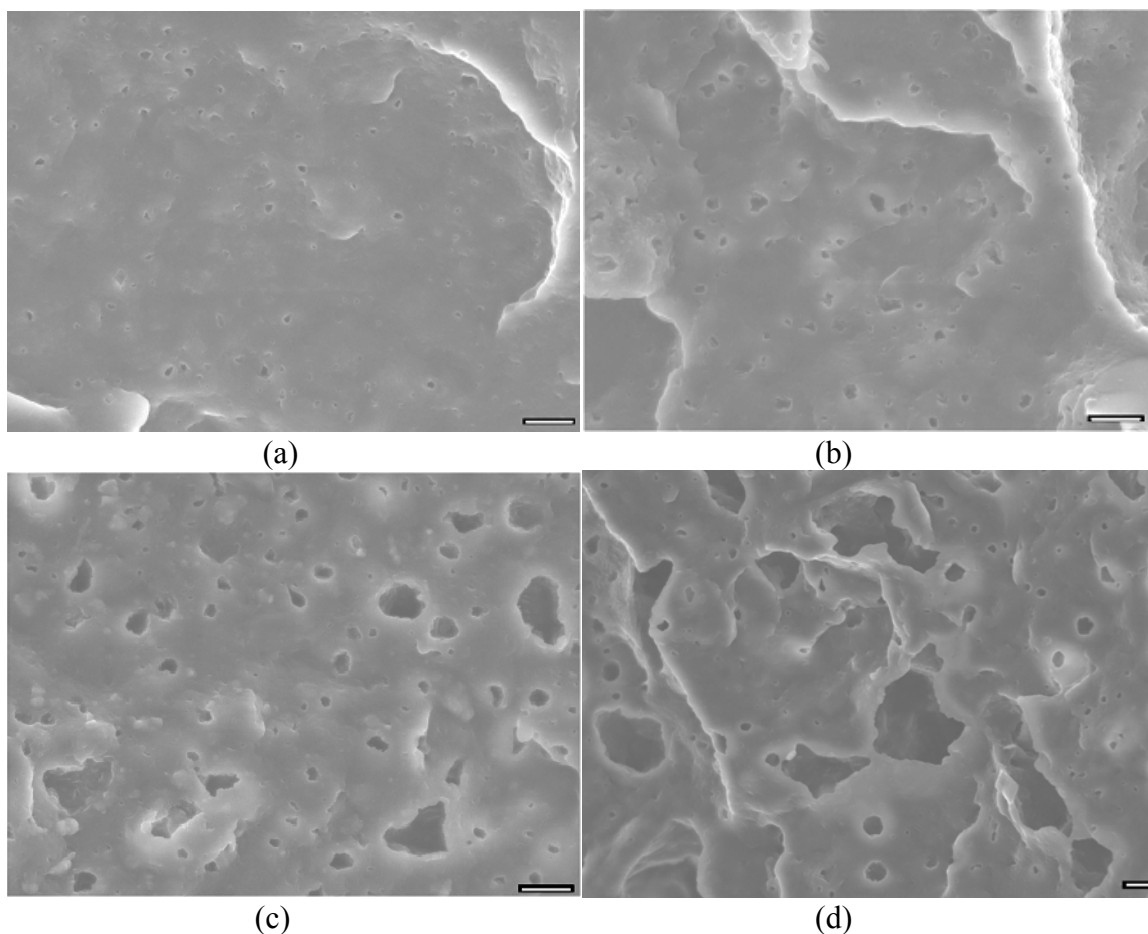


Figure 4-16: SEM images of (a) 95:5_B at 10,000X, (b) 90:10_B at 10,000X, (c) 80:20_B at 10,000X, and (d) 70:30_B at 5,000X. Each bar marker = $1\mu\text{m}$.

Ligament thickness (surface-to-surface distance between domains) was introduced in Chapter 2 as a key component to toughening brittle semicrystalline polymers. This is

based on volume percent of rubber concentration, which is found by using the following equation:

$$\text{Volume fraction of rubber phase } (\phi_{8407}) = w_{8407} / [(w_{PP} * (\rho_{8407} / \rho_{PP})) + w_{8407}] \quad (4.4)$$

where w_{8407} = weight fraction of 8407 phase, w_{PP} = weight fraction of PP phase, ρ_{8407} = density of 8407 (0.87 g/cm³), and ρ_{PP} = density of PP (assumed to be 0.91 g/cm³). The matrix ligament thickness (T) is found from Wu [120]:

$$T = d[(\pi/6\phi)^{1/3} - 1] \quad (4.5)$$

where d = rubber particle diameter and ϕ is the rubber volume fraction.

The matrix ligament theory was founded on research that limited the dispersed particle size to about 300 nm. From SEM and TEM (explained in future paragraphs), the domain size of these blends and alloys are much smaller, so this theory may not be directly applicable. Many authors have shown that ligament thickness should decrease with increasing rubber concentrations. They were able to control the degree of dispersion and coalescence by using high viscosity rubbers (i.e., viscosity ratio is close to one) [119-121, 125, 274]. From Table 4-6 and Figure 4-17, the opposite trend is witnessed. The viscosity of 8407 is much less than polypropylene, so breakup, diffusion, and coalescence of 8407 domains throughout the melt is easier than higher viscosity elastomers.

As the percentage of 8407 increases, the size of the dispersed phase increases. From data in Chapter 3, this is due to diffusion and coalescence, but grafting is able to prevent coalescence by stabilizing the dispersed phase. One aspect of the matrix ligament theory is the fact that below a critical interparticle distance, the material behaves in a tough manner (high impact strength) and above which it behaves in a brittle manner. Figure 4-17 shows that the ligament thickness of the alloys is lower than the physical

blends at all concentrations of elastomer. This translates into higher impact strength, as exemplified in Figure 4-18.

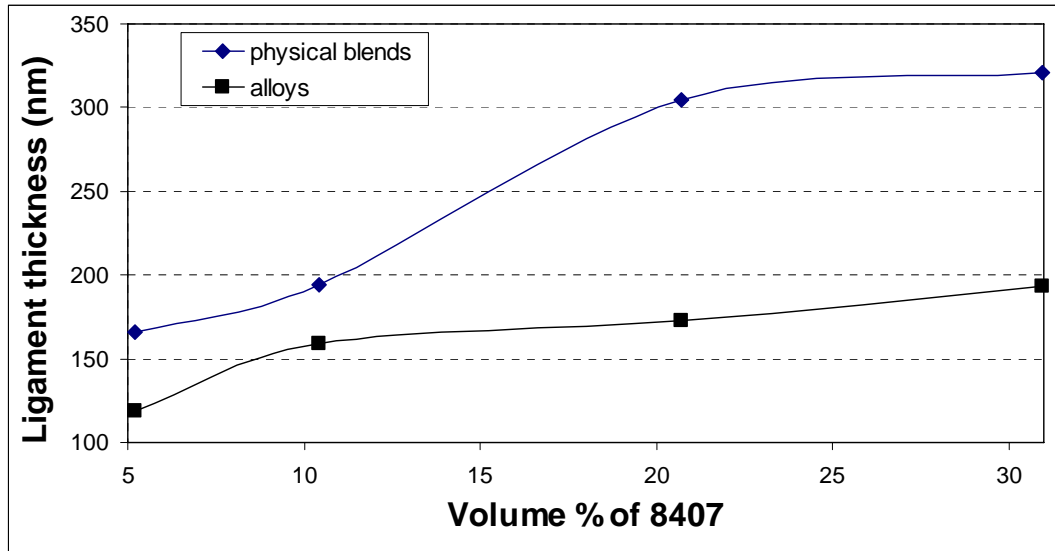


Figure 4-17: Matrix ligament thickness of PP blends and alloys as a function of volume % of 8407.

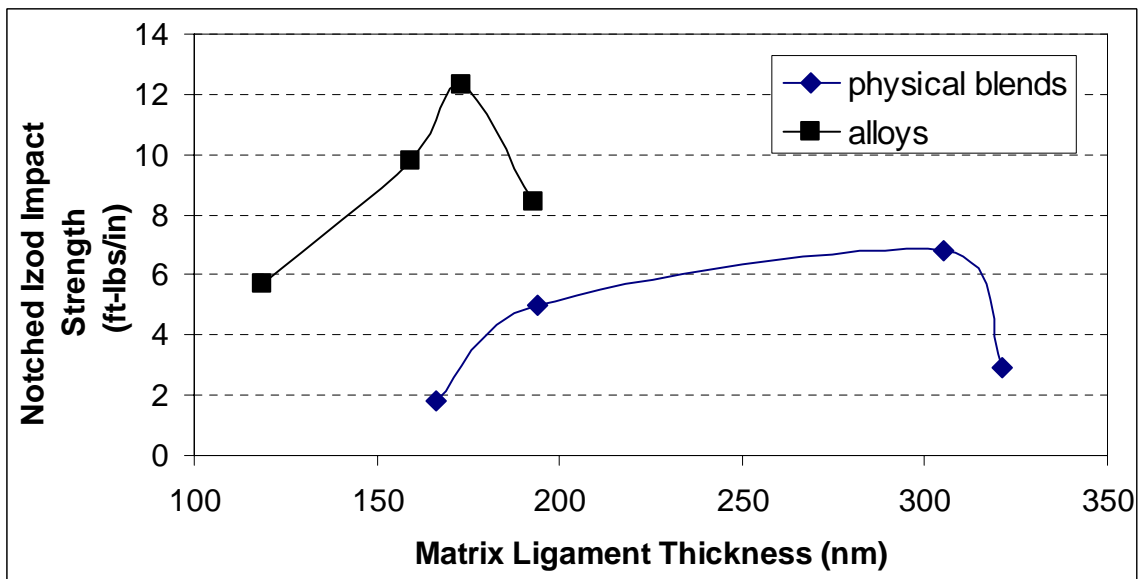


Figure 4-18: Room temperature notched Izod impact strength as a function of matrix ligament thickness for blends and alloys at various volume % 8407.

The alloys and blends have about the same matrix ligament thickness at 175 – 200 nm, but the impact strength of the alloy is much higher. This is a testament to the need for high interfacial bonding between the matrix and dispersed phase. For physical

blends, there appears to be a minimum and maximum ligament thickness. At high concentrations of elastomer, coalescence is common which leads to smaller surface area and weaker interfacial interactions. At low elastomer concentrations, the matrix ligament is smallest but a decrease in impact strength is observed, contrary to what the theory predicts. At such a small number average particle diameter, the particles may not be able to effectively promote energy absorption mechanisms like dilation, cavitation, crazing, and shear yielding. Typically, the rubber phase should be approximately the size of the crack it is trying to stop [100].

Transmission electron microscopy (TEM) is utilized because it gives more detailed structural information than SEM. Contrast in bright field TEM depends on the relative electron transparency of the phases present in the material. Ruthenium tetroxide (RuO_4) has been used as a stain to impart contrast enhancement in polymers because of its high electron density [344-349]. It locates in amorphous, low density regions of the polymer, thus scattering electrons more efficiently and creating a dark area in the TEM image. This is a valuable staining technique for rubber toughened plastics or polymers containing aromatic unsaturation because the rubber/unsaturated materials are preferentially stained.

As can be seen in Figure 4-19(a), pure PP shows a blurry picture, which may be because of the limited diffusion of the staining agent in a highly crystalline matrix whose T_g is close to room temperature. For a blend containing 10 wt% 8407, the staining agent preferentially locates in the elastomer phase, which is distributed in a range from about 10 nm to 150 nm diameter domains (Figure 4-19(b)). The particles are dispersed at such

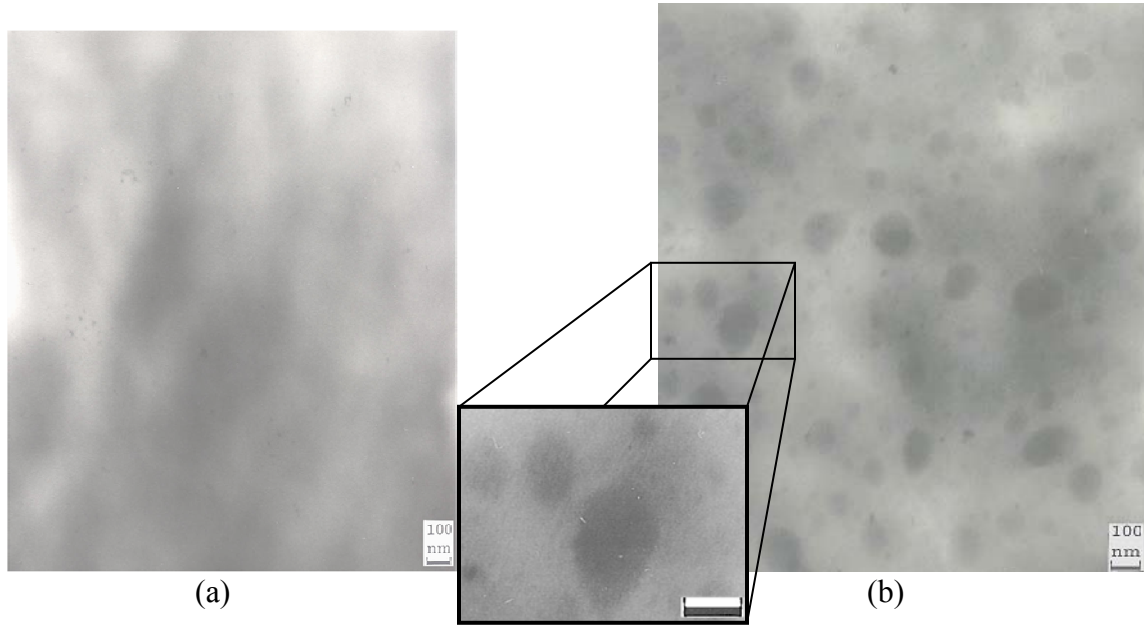


Figure 4-19: TEM bright field images of (a) virgin PP and (b) 90:10_0 stained with RuO₄ at a magnification of 63,500X. Bar marker on insert = 100nm.

a small scale presumably because the viscosity of the PP is much larger than 8407. At low elastomer concentrations, the higher viscosity matrix does not allow diffusion and coalescence of the elastomer domains so a fine morphology is observed. Also, the presence of these domains solidifies the fact that 8407 and PP are immiscible polymers, but at a relatively small scale.

Addition of styrene and initiator to the physical blend results in a unique multi-phase morphology, as can be seen in Figure 4-20. There are various levels of darkness in the image – the darkest domains being attributed to styrene and the lighter, gray domains are 8407. Small dark domains (10 nm or less) are distributed throughout the image but some are locally clustered in the elastomer phase. There are also a few 100 nm solid dark domains present in the image. These larger domains may be styrene material that has phase separated (possibly as homopolymerized material). For the elastomeric domains that contain several sub-10 nm styrene-based domains, one might conclude that the

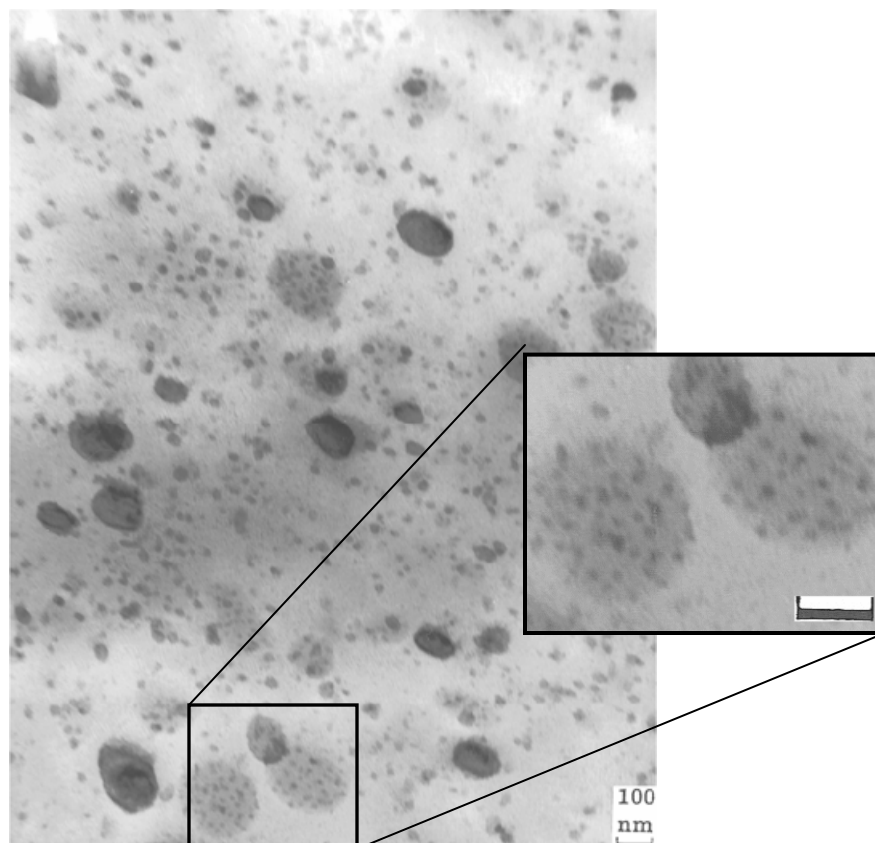


Figure 4-20: TEM image of 90:10_A at 63,500X. All marker bars = 100nm.

styrene has grafted to the elastomer phase. But it is quite possible from the phase inversion mechanism [78, 79] that some PP phase may be trapped inside the elastomer phase along with grafted styrene. Grafts may locate at interlamellar or lateral intercrystalline regions, forming microdomains which differ structurally from larger domains of PS homopolymer [350].

By adding 0.8 wt% of multifunctional monomer to the styrene/initiator system, the morphology is altered (Figure 4-21). The overall area of stained material increases compared to Figure 4-20, a qualification of the difference in grafting efficiency of the two systems. Similar to Figure 4-20, relatively large elastomer domains containing a cluster of small dark domains about 10 nm in diameter are present (insert 1, Fig. 4-21).

However, this domain is connected to a larger, more highly stained domain with a cluster of particles approx. 50 nm in diameter. Because grafting (and dark staining of styrene) is

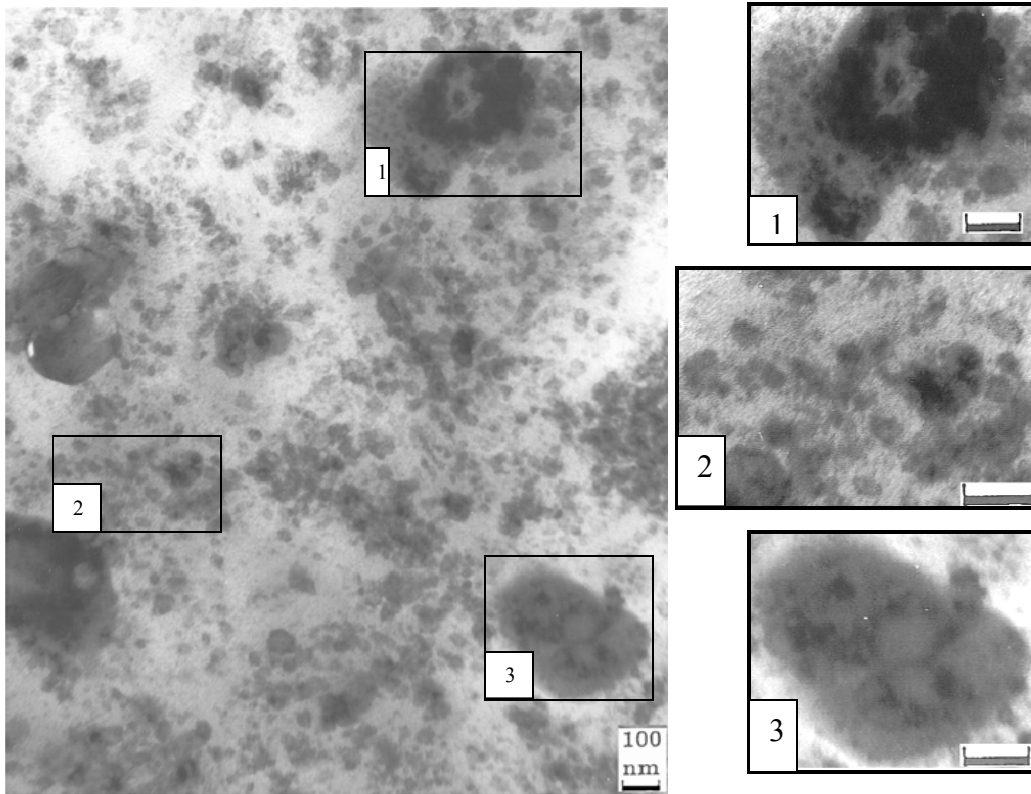


Figure 4-21: TEM image of 90:10_B at 63,500X. All marker bars = 100nm.

thought to occur primarily in the PP phase, these highly stained domains may contain polypropylene chains. With the high degree of bonding/grafting that is taking place between the phases, the phase inversion mechanism of trapping PP inside 8407 domains is highly likely [78, 79, 89]. Insert 2 in Figure 4-21 shows many dispersed stained domains ranging from 10 -100 nm in size, but unlike Figure 4-20, these domains are within close proximity to each other. The distribution of extremely small domains (presumably elastomeric) has a very noticeable effect on macro-scale properties like impact strength. The morphology for insert 3 is very interesting because the stained material is a web-like structure encapsulated in an elastomeric domain. Keep in mind

that these TEM images are of non-purified material, so the morphology may look much different when only grafted chains are present.

A change in morphology is observed when there is an increase in elastomer concentration (Figure 4-22). As expected, more elastomer results in larger gray domains, with one domain elongated to approximately 1 μm in length. There is also an increase in the size of dark stained domains for 80:20_A, which may be an indication of agglomeration or because of the “cage effect” leading to longer grafted chains. For 90:10_A, the stained material located in the elastomer phase (<10 nm in diameter) were dispersed relatively uniformly on the interior, but at the 80:20 level, these domains are

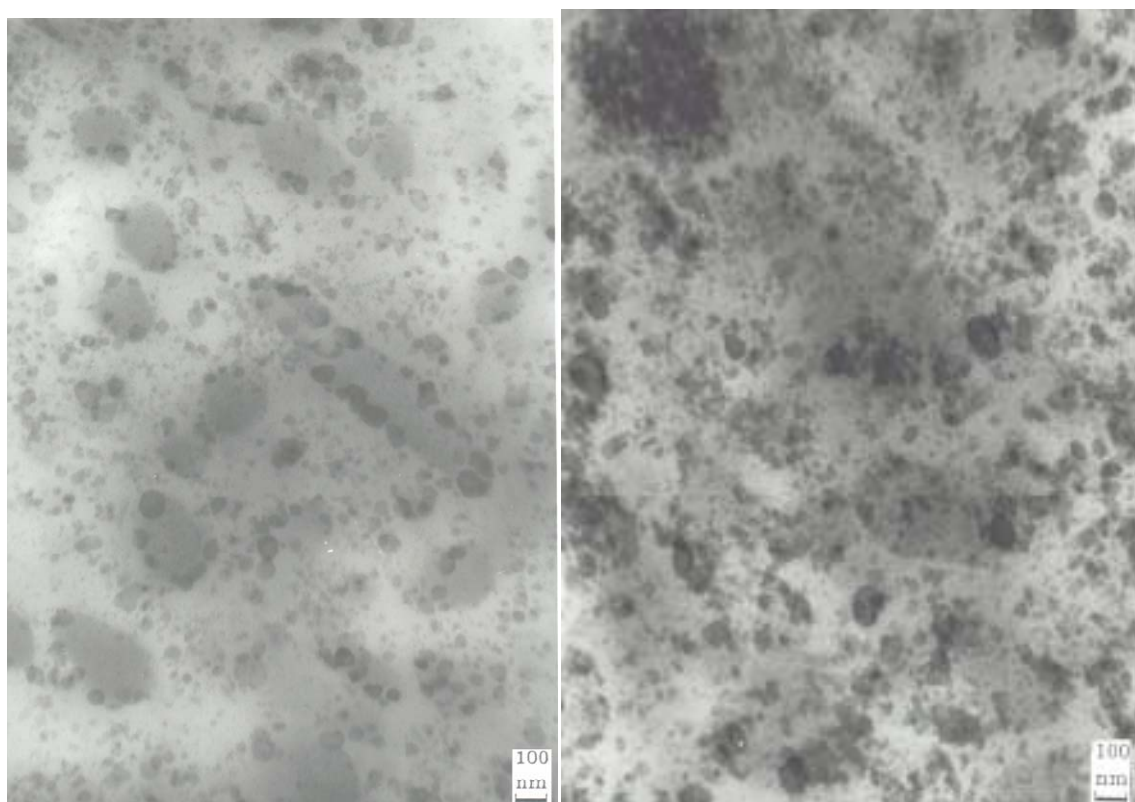


Figure 4-22: TEM images of 80:20_A (left) and 80:20_B (right) at 63,500X.

primarily found at the outer edges of the elastomer and are larger in size. With higher elastomer concentration, the monomers are likely partitioned in that phase, but because of

the low grafting efficiency and slow kinetics, are phase separating from the low viscosity melt as the blend proceeds down the barrel of the extruder.

80:20_B shows a more highly stained image than 80:20_A, which is directly related to its superior styrene grafting efficiency. The staining agent will partition in the amorphous regions of the polymer and since polystyrene is non-crystalline, a darker image is to be expected. The number of light gray domains (purely elastomer phase) in the high impact sample is much less than in the samples without multifunctional monomer. This could mean that the elastomer phase is distributed throughout the sample as styrene-grafted material. Like 90:10_B, clusters of highly stained domains exist in the sub-100 nm range.

4.3.5 Possible Crosslinking of the System

In order to verify whether the alloy contains an insoluble gel, which will hinder processability and compromise mechanical properties, both soxhlet extraction according to ASTM D2765 and thermogravimetric analysis (TGA) were performed. Dynamic mechanical analysis, in section 4.3.9, will also indicate any crosslinking in the alloy. The extraction technique was run on 3 different samples: 95:5_B, 90:10_B, and 80:20_C but did not reveal any insoluble gel. Gel is known to absent when grafting polyolefins, even for materials susceptible to crosslinking such as HDPE and LLDPE [7, 40, 94, 138, 196].

TGA is a popular method to quantify material degradation as a function of temperature [351]. Figure 4-23 shows an unexpected response of the alloy – it begins to degrade at a lower temperature than the physical blend. The opposite trend would be expected for a crosslinked system because the mobility of the chains is restricted and there are a greater number of bonds to break. The alloy degrades in this manner possibly due to residual initiator, monomer, or reaction byproducts not vented out of the extruder

vacuum port. Another reason for the lower degradation temperature may be due to an increase in the number of tie molecules, which have a lot of stored energy therefore making them more susceptible to scission [352].

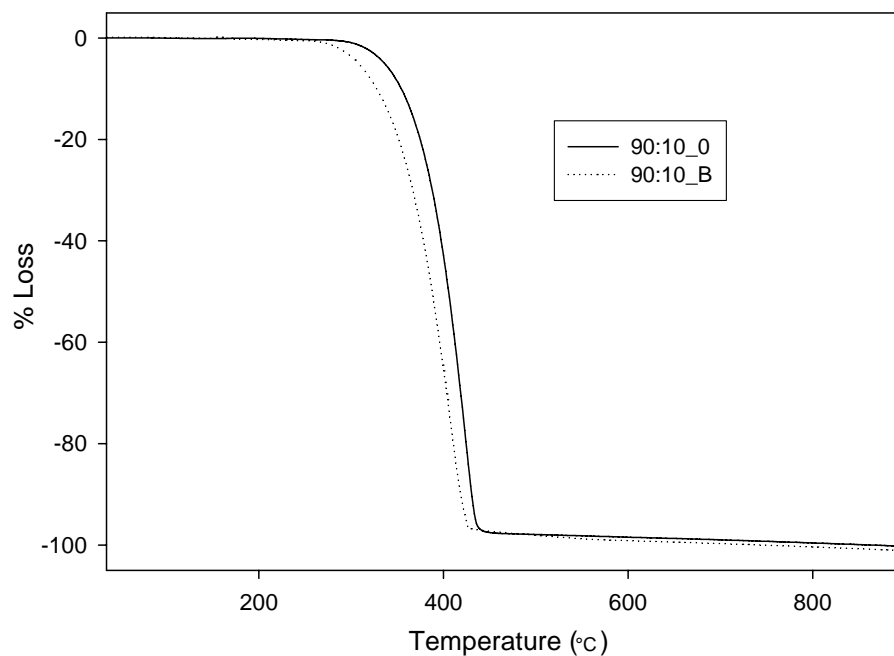


Figure 4-23: TGA graphical comparison of a physical blend (90:10_0) and alloy (90:10_B).

4.3.6 Rheological Properties

Melt strength (MS) and melt flow index (MFI) arguably are two of the most important material parameters when the thermoplastic processing technique involves stretching flow (i.e. blow molding, film extrusion, and thermoforming). The relevance of MFI has been described in the previous chapter, but MS needs further explanation. The MS of a polymer is a measure of its resistance to extensional deformation. This is a comparative measurement like MFI and is useful in providing information on the drawability of different polymers [353-355].

Isotactic polypropylene has a characteristically sharp melting point and poor melt strength [356], therefore limiting its use in these processes. Poor melt strength is

indicative of parison collapse in blow molding, cell-rupture in foaming, married fibers in melt spinning, excessive sag in thermoforming, melt drool in profile extrusion, and low extrusion coating speeds [357, 358]. Several ways to improve melt strength include increase molecular weight, broaden molecular weight distribution, incorporate comonomer to reduce crystallinity, add nucleating agents, additives to form high viscosity interpenetrating networks, incorporation of short or long chain branches (most effective), grafting, or crosslinking. High melt strength polypropylene resins have been created, commonly via solid phase grafting, which drastically improve its rheological properties [179, 353]. Solid phase grafting has the lowest incidence of PP chain scission of free radical grafting methods.

The melt strength (Table 4-7) and MFI (Figure 4-24) data indicate long chain branched molecules present in the PP alloy, not necessarily a crosslinked gel. Solidification temperature of 95:5_B is higher than 95:5_0, which is to be expected because DSC results indicate an increase in crystallization temperature. The upper service temperatures are not very different probably because the T_m of the PP phase does not change significantly. The melt strength of all alloys is much greater than the physical blends, with MFI decreasing in a parallel fashion [353, 354]. Long chain molecules are present in the system, thereby increasing the degree of entanglement and therefore having a higher resistance to extensional deformation. A linear relationship exists between melt strength and zero-shear viscosity which is dependent upon the average molecular weight of the polymer. The alloy has the ability to deform longer distances and at faster rates than the physical blend, as revealed by its melt extensibility and melt toughness.

From previous section, grafting efficiency is the lowest for alloys not containing multifunctional monomer. And because MFI is the highest for these same alloys (Figure 4-24), degradation (β -chain scission) of PP is most likely taking precedence. Without multifunctional monomer, branching is not detectable by MFI measurements.

Molecular weight increases with increasing monomer concentration along with a broadening of MWD and increase in the high MW tail [250]. Some authors have found that at high monomer concentrations, MS and MFI decrease while viscosity and graft yield increase [40, 92, 215, 228]. The decrease in MS may be related to homopolymerized material.

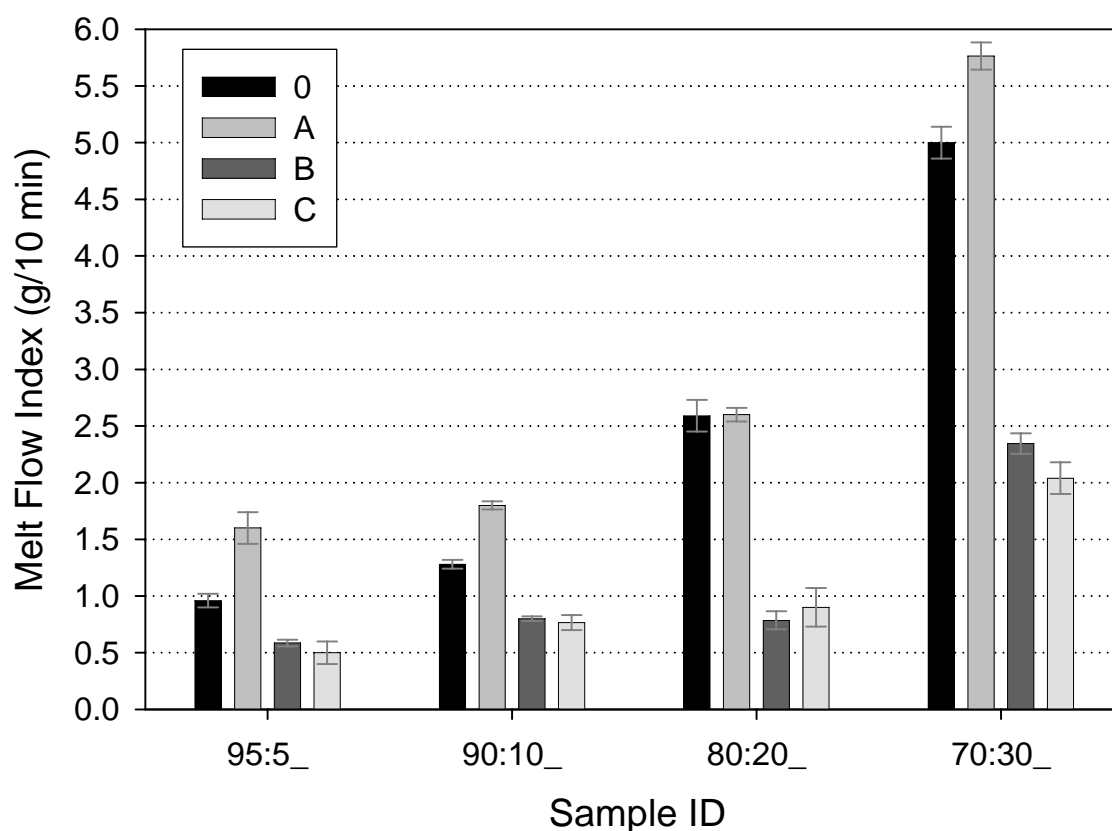


Figure 4-24: Melt flow index of physical blends and alloys as a function of 8407 content.

Table 4-7: Melt Behavior of PP, PP-8407 physical Blends, and PP-8407 alloys.

Sample ID	Solidification Temperature, ST (°C)	Upper Service Temperature, UST (°C)	Melt Strength, MS (cN)	Melt Extensibility, ME (mm/s)	Melt Toughness, MS * ME (cN*mm/s)
95:5_0	113	155	17.8	60.7	1080
95:5_B	129	156	56.1	86.5	4853
90:10_0	-	157	23.9	42.6	1018
90:10_B	-	155	43.1	93.5	4030
80:20_0	-	157.5	16.8	40.4	679
80:20_B	-	157.1	50.8	83.0	4216
Pure PP	107	163	-	-	-

The free radicals formed on the backbone of PP are effectively trapped by the styrene-multifunctional monomer branched system, therefore eliminating degradation. materials with a low MFI value tend to have longer molecular chains and higher average molecular weights which lead to molecular entanglements in the polymer melt [359]. The MFI of polypropylene is mainly dependent upon the average MW of the polymer. At a given MFI, a polymer with a higher melt strength has a broader MWD [360], with the long chain polymers (M_z) more important to MFI [73]. For a long chain molecule, only short segments of the molecular chain can move at time, taking to Eyring's theory into consideration [110]. As melt flow index increases, impact strength has been shown to decrease [265]. When comparing a di- to tri-functional monomer, the higher functionality monomer results in a lower MFI at the 70:30 level. The higher functionality means higher density of crosslink junctions and expectedly lower MFI.

4.3.7 Crystallinity and Crystallization

Isotactic polypropylene's mechanical properties are highly dependent on its crystalline state, which is a function of processing conditions, molecular weight, molecular weight distribution, and chain configuration and conformation. PP is a unique semicrystalline polymer because of its four possible crystalline phases [100, 267, 287, 327, 361, 333, 361-364]. Commercial grades of PP essentially crystallize into the α (monoclinic) modification with sporadic occurrence of the β (trigonal or pseudo-hexagonal) phase at higher temperatures [279, 287, 333, 365, 366]. The γ (triclinic) phase is only observed in low MW or stereoblock fractions crystallized at high pressures above 200 MPa. The so-called smectic phase is created by quenching PP and is composed of a mixture of monoclinic and pseudo-hexagonal structures [334, 367].

Wide angle x-ray diffraction is a precise technique used to determine the crystal structures present in polymers as well as the relative size and orientation of the crystalline lamellae. Both long range and short range order must exist for the peaks to be present in Figure 4-25, so an amorphous halo exists underneath them because of the presence of non-crystalline material. The peak positions in the figure represent specific planes which diffract the x-rays and the peak heights at these positions indicate the relative number of crystalline planes diffracting. The alpha phase has a monoclinic structure with unit cell dimensions: $a=6.65 \text{ \AA}$, $b=20.96 \text{ \AA}$, $c=6.5 \text{ \AA}$, and $\theta = 99^\circ$ [364]. This crystal structure contains four chains/unit cell, unit cell volume of 905 \AA^3 , and density of 0.936 g/cm^3 [162, 338, 339, 364, 368]. Of all the possible crystalline phases of PP, the α phase is the most thermodynamically stable [267] with a melting enthalpy of 207 J/g [162] and melting temperature of about 165°C . For faster quenching, this phase is created due to its higher growth rate.

The Bragg reflections at 14.1° , 16.8° , 18.5° , 21.1° , 22° , 25.5° , 28.5° , and 42.5° correspond to the following indexed planes of the monoclinic crystal: (110), (040), (130), (111), (131) and (041), (060), (220), and (-113), respectively [162, 267, 287, 369]. A strong (110) reflection represents lamellae growth in a radial direction (perpendicular to the chain axis) along with (130) at a 45° azimuth [339, 369-371]. The (010) planes, with the lowest density of methyl groups, are most likely to be involved in epitaxial interactions of tangential lamellae growth [369, 372-374]. Fold surfaces are parallel to (101) [375] and the (-113) plane is the best measure of the packing and orientation of chain axes [369]. The most intense (110) diffraction of polyethylene overlaps with the (111) reflections of α PP [314].

The alpha phase peaks are labeled in Figure 4-25 and the difference in peak heights could be due to variation in the mean lamellar crystal size or their distribution, deformation at the spherulite boundaries, or any long range order induced in the structure. At low angles (large d-spacing) 90:10_B has the largest number of diffracting planes which may signify a large number of smaller lamellar crystals. The $\alpha(110)$ peak intensity is high for pure PP, which is to be expected because with long chains and larger, more

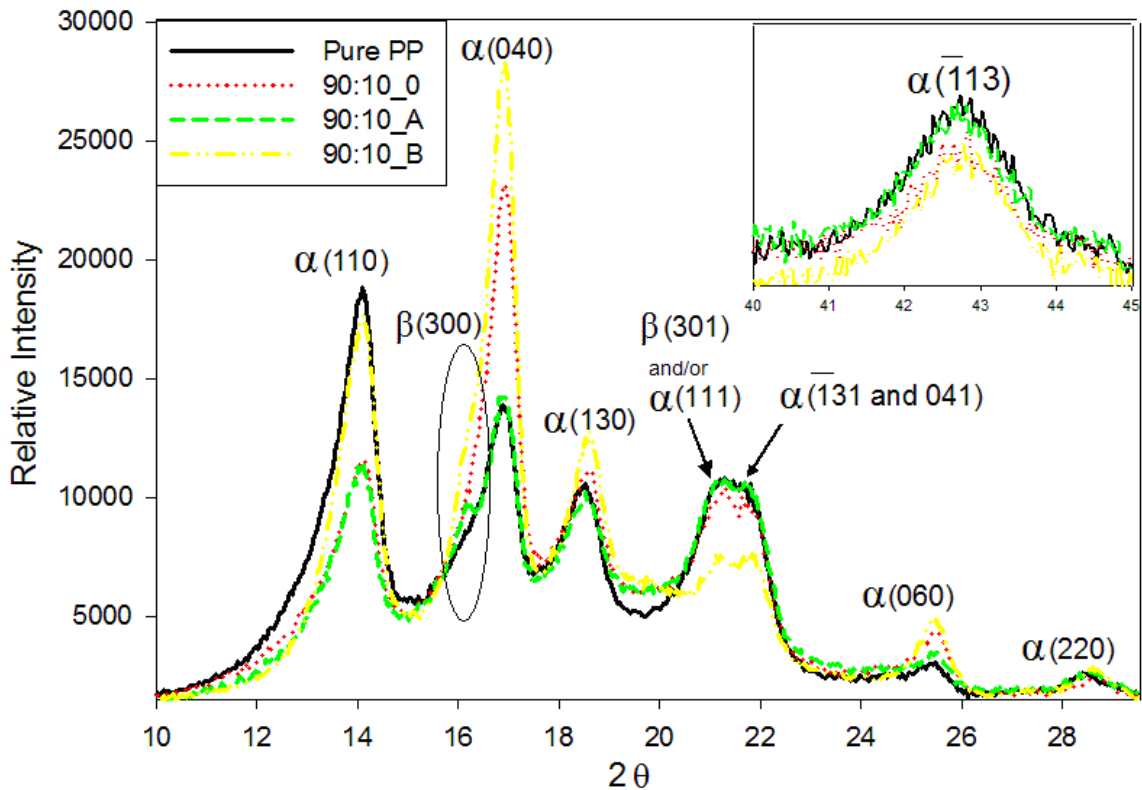


Figure 4-25: XRD pattern of pure PP, 90:10_0, 90:10_A, and 90:10_B.

uniform spherulites comes a greater degree of radial growth out from the spherulite center. This peak is low for 90:10_0 and 90:10_A because impurities or diluents may prevent or inhibit growth in the radial direction [128, 255, 258, 264, 203, 307, 310]. The fact that 90:10_B has a peak intensity similar to pure PP reveals that the total number of planes diffracting in the radial direction are high even though this sample has just as

many if not more impurities as 90:10_0 and 90:10_A. The relatively high peak intensity of the (040) plane in 90:10_B may help clarify things.

Structurally in PP, the tangential lamellae epitaxially grow on the lateral (010) crystallographic plane of the radial lamellae by a satisfactory interdigitation of the methyl groups of facing planes at a substantial angle (80° or 100°) [373, 374, 376]. Only open textures may lead to well developed tangential lamellae, which may be prevented by the high degree of branching in 90:10_B. But epitaxial crystallization of helical polymers like PP is dictated primarily by interchain and inter-helical distances [373]. So if chains are in close proximity to each other, crystallization may be facilitated. The high intensity of the (110) and (040) peaks, therefore, represent a high density of both radial and tangential lamellae. The multifunctional monomer is promoting a large number of very small, highly cross-hatched lamellar structures.

Differential scanning calorimetry will show that 90:10_A has a low % crystallinity which may be due to an alteration of the isotacticity of the chains. With decreasing isotacticity, the capability to retain such a regular (010) plane is reduced due to the configurational defects caused by random appearance of methyl groups along the chain direction. As a consequence, the epitaxial nucleation process is increasingly hampered and the cross-hatching density is thus reduced.

The packing and chain orientation peak intensity (at 42.5°) is smaller for alloys (90:10_B and 90:10_A) than 90:10_0 or pure PP, which is consistent with poor crystallographic packing in the chain direction and defective crystal surfaces. Organization of such crystals resembles the smectic packing of conformationally distorted chains [364]. Grafting is known to increase d-spacing and create more

imperfections of the crystallite surface [331, 350]. A crystalline lattice can accommodate various kinds of imperfections in the form of short branches [331, 362]. When comparing pure PP to 90:10_B, the d-spacing of the alloy is 0.01 nm lower for the (110) planes and 0.012 nm greater for the (040) plane.

The width of the (040) and (130) peaks increase upon modification with initiator, styrene, and DEGDA. This indicates a wider distribution of crystal size, a size reduction of these crystals, and/or a lower degree of order in the crystalline phase [267, 279]. At 14°, there is a shift in peak position to higher values for 90:10_A and B, indicating tighter packing in unit cell direction perpendicular to the chain direction [369]. Tighter packing of chains in the crystal unit cell of PP can be caused by higher isotacticity and/or higher crystallization temperature. This idea is elaborated upon later on in this section within the discussion about crystallization.

The only sample that shows a distinct peak at 16° is 90:10_A, which represents the β crystalline phase of PP. All other samples show more of a broad shoulder than a distinct peak. There are two primary peaks assigned to this phase, namely (300) at 16.1° and (301) at 21.1° [162, 279, 287]. Like the (110) plane for the alpha phase, (300) correspond to the crystal growing planes and to the largest lateral dimensions (perpendicular to chain axis) of lamellar crystallites [339].

The β crystalline unit cell is composed of 9 chains, with parallel-stacked lamellae tending to pack into bundles [162, 337, 340, 364, 377]. Figure 4-26 compares the relative size and orientation of beta crystals compared to alpha crystals. The dimensions of the beta crystallites are approximately three times larger than the corresponding dimension of the alpha crystallites, having a unit cell volume of 3150 Å³, dimensions of a=10.98 Å,

$b=10.98 \text{ \AA}$, $c=6.47 \text{ \AA}$, and $\theta =90^\circ$, and density of 0.921g/cm^3 [162, 267, 338, 339, 363, 368]. The metastable higher energy trigonal phase has a melting enthalpy of 166 J/g [162, 363, 378] and melting temperature of about 152°C . It grows up to 70% faster than the α phase in a temperature window extending from 105°C up to 141°C but is nucleated less profusely than α [255, 287, 322, 325, 333, 338, 364, 370, 379-382].

The β phase of PP can be created by specific nucleating agents (most common), temperature gradients, orientation by shear, orientation by phase separation, copolymerization, or from addition of elastomer [267, 325, 333, 339, 363, 383-385]. But authors have found that use of multifunctional monomers during the crosslinking of PP results in the formation of this unique phase [114, 128, 350]. They attribute it to the presence of multiple molecular structures/architectures composed of branched and/or intermolecularly crosslinked macromolecules. The β phase is not created simply by grafting polystyrene onto PP [386].

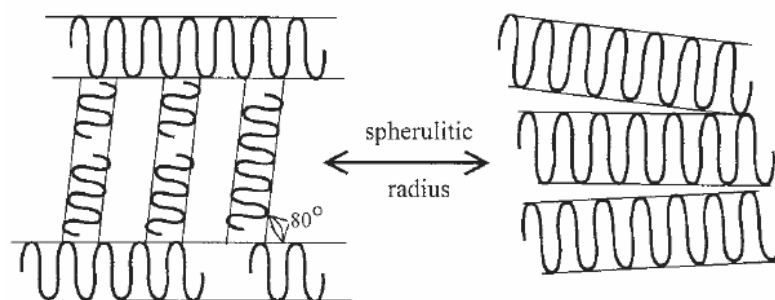


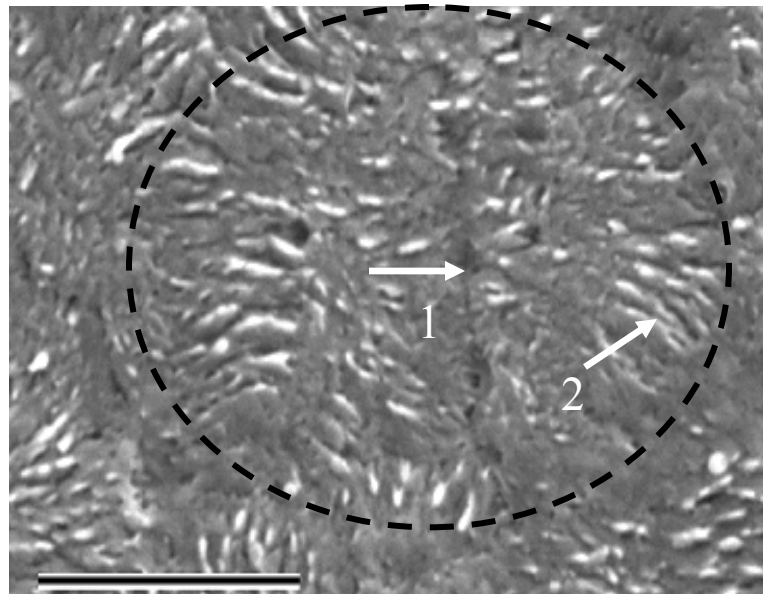
Figure 4-26: Alignment of lamellae within spherulites of α -PP (left) and β -PP (right) from reference 278.

The smectic phase may be present in this material, which is stable at temperatures below 70°C , shows order in the chain axis direction, but the lateral packing of the PP helices are not as well formed as in the alpha monoclinic crystalline phase [334, 367]. The quenched material is composed of a mixture of monoclinic and pseudo-hexagonal

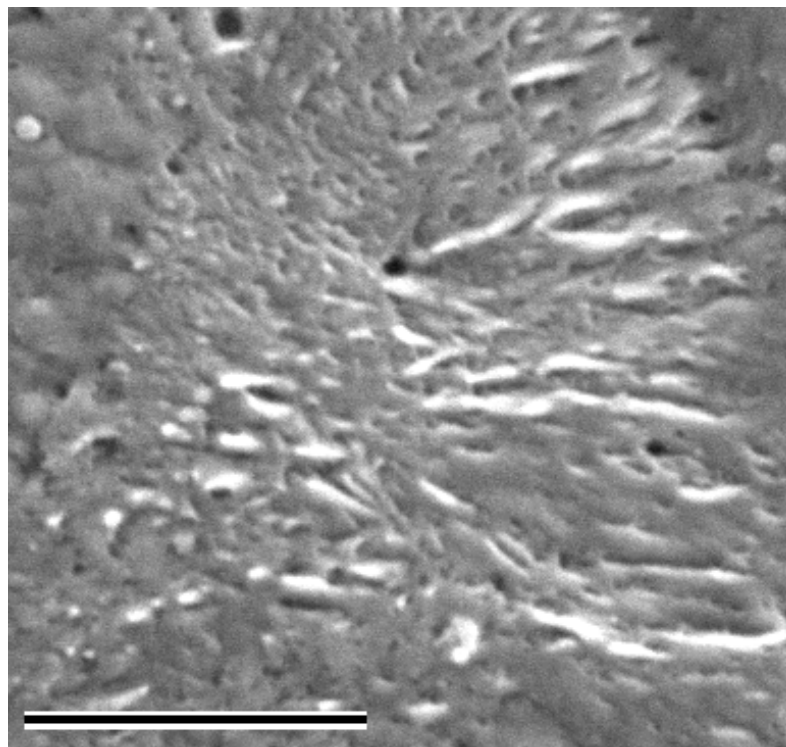
structures and has reflections at 14.8° representing inter-chain packing and 21.2° for inter-chain registration.

X-ray diffraction introduces many interesting possibilities of how the lamellar morphology is structured in these materials. A permanganic acid etching technique pioneered by Olley et al. [387] has shown to be able to reveal lamellar crystals in both isotactic polypropylene and polyethylene [314-318]. Figure 4-27 is an etched SEM image of pure polypropylene crystallized nonisothermally from the melt. In Figure 4-27(a), arrow #1 points to the center of a spherulite which is about $4\ \mu\text{m}$ in diameter, while arrow #2 locates many radial lamellae at the fringe of the spherulite. Figure 4-27(b) shows the periphery of a spherulite where many radial lamellae are visible. These lamellae are less than $100\ \text{nm}$ thick and can extend out over $2\ \mu\text{m}$ from the center. The acid etch procedure for these samples is not optimized and the experiment was nonisothermal, so large, well-defined spherulites were not visible. But throughout this image, holes may be mistaken for amorphous, non-cross-hatched material. The cross hatches of pure polypropylene are relatively thick lamellae and will not be etched by the acid treatment.

The next image (Figure 4-28) is an etched film of 90:10_0, the physical blend of PP and 8407. Large dark pits about $0.5\text{-}2\ \mu\text{m}$ in diameter are dispersed in this sample, which are most likely remnants of elastomeric particles. In this image, both radial (arrow #1) and tangential (arrow #2) lamellae can be seen within a non-circular spherulite in the center of the image.



(a)



(b)

Figure 4-27: Etched lamellar morphology of isotactic polypropylene of a well defined spherulite at 15kX magnification (a), bar marker = $2\mu\text{m}$ and periphery of a spherulite at 20kX magnification (b), bar marker = $2\mu\text{m}$.

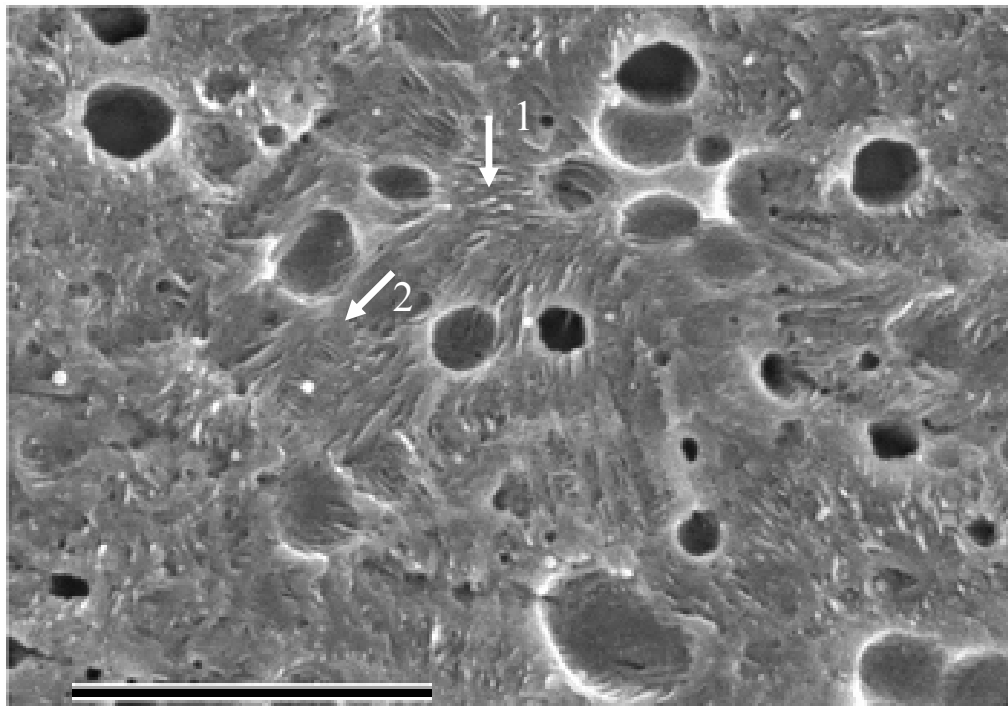


Figure 4-28: Etched lamellar morphology of 90:10_0 at 10.5kX magnification, with the bar marker = 5 μ m.

X-ray diffraction has introduced the possibility of 90:10_B having a dense cross-hatched structure, and SEM reveals its morphology in Figure 4-29. A highly dense network of crystalline lamellae is in fact present throughout the image. It should be noted that this type of structure was commonly seen throughout the sample (about 5 cm²). The network (or cross-hatched) structure is a combination of radial and tangential lamellae. A defined spherulitic structure was not seen, but arrow #1 is believed to be radial lamellae and arrow #2 tangential lamellae. The most interesting aspect of this material is pointed out by arrow #3, which is a unique combination of interwoven tangential and radial lamellae. Some lamellae measure to be below 100 nm in length and about 10-20 nm in width. This aspect ratio is much smaller than what is observed in the previous two images. The presence of etched pits, like 90:10_0, represent elastomeric domains of

8407. Notice that these are much smaller in diameter than in the physical blend (a trend observed in section 4.3.4).

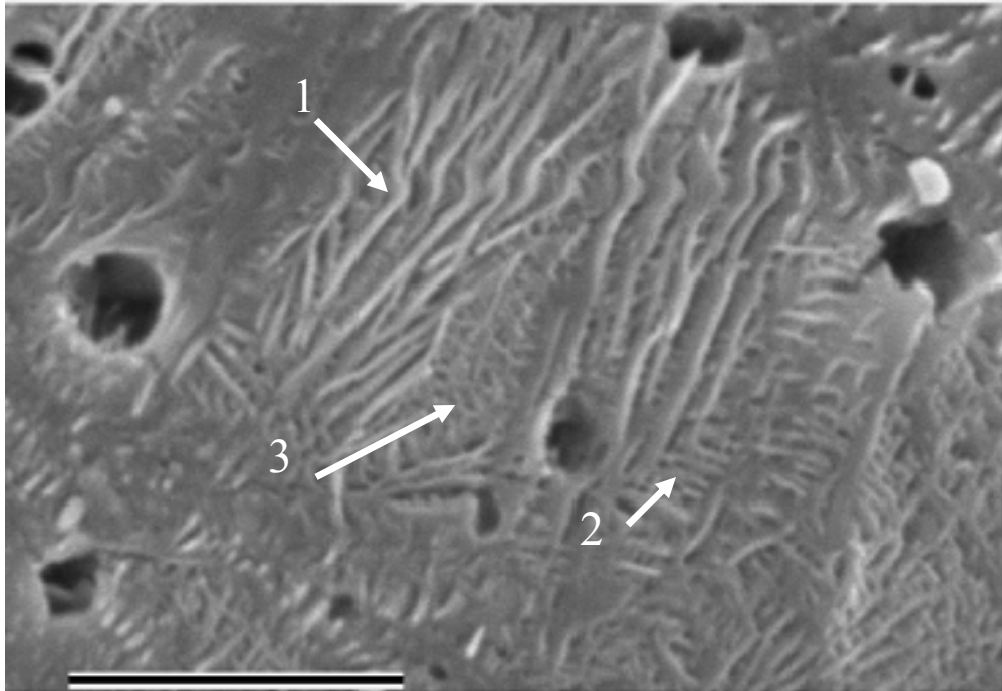


Figure 4-29: Etched lamellar morphology of 90:10_0 at 20kX magnification, with the bar marker = 2 μ m.

Differential scanning calorimetry is a versatile tool which allows precise measurement of the melting and subsequent recrystallization of semicrystalline polymers. The heating run described in the experimental section should eliminate all traces of melt orientation [388]. Nonisothermal experiments were performed instead of isothermal measurements in order to simulate the nonisothermal conditions of processing. From Figure 4-30 and Table 4-10, T_m of the PP phase at about 165°C does not decrease with addition of elastomer, but it does decrease upon addition of liquid reactants, similar to the findings of Borsig et al. [343]. When grafting polyolefins, their melting temperature and % crystallinity are known to decrease compared to the pure polymer [7, 148, 184, 215]. The decrease in T_m along with decrease in crystallinity is seen for 90:10_A. The point in

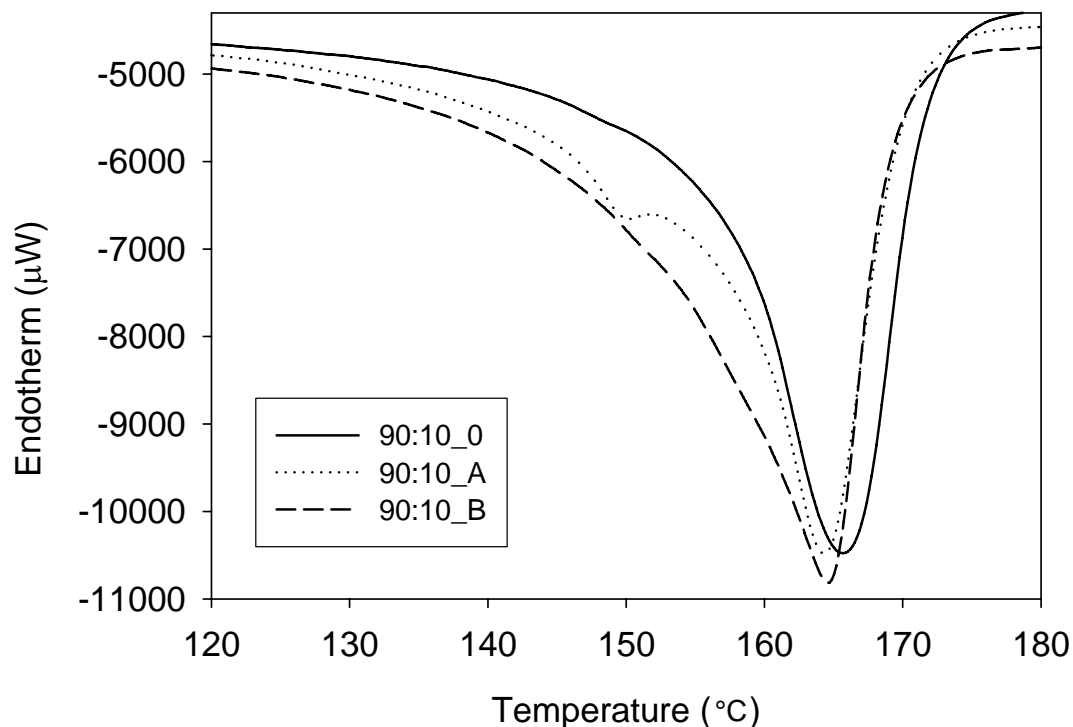


Figure 4-30: DSC heating traces of a physical blend (90:10_0) and alloys (90:10_A and 90:10_B).

which melting comes to completion occurs than 90:10_0 (173°C vs. 175°C, respectively).

This means that larger, more perfect crystals composed of longer crystallizable PP chains exist in the physical blend. The disappearance of the last traces of crystallinity in 90:10_B means that the crystals are either relatively more imperfect or there is an increase in entropy of fusion [389].

The % crystallinity is estimated by taking the area of the melting endotherm and dividing by the melting enthalpy of a perfect crystal [390]. A value of 207 J/g was taken to be the standard melting enthalpy, with the alloy containing multifunctional monomer having a higher % crystallinity than both 90:10_0 and 90:10_A. The physical blend has a low crystallinity because the amorphous elastomer acts as a diluent. 90:10_A, on the other hand, likely contains degraded PP chains which could once crystallize but are now chopped into smaller non-crystallizable segments. The high crystallinity of 90:10_B will

be explained later in this section. Remember that initiator derived free radicals attack the high molecular weight chains first, and these are the same chains that contribute most to the high level of crystallinity in pure PP. Grafted chains will not crystallize because they are strictly amorphous materials.

Table 4-8: DSC endothermic data comparing pure PP to 90:10_0, 90:10_A, and 90:10_B. An average of three runs were performed on 90:10_B.

Sample ID	α Phase Melting Peak ($^{\circ}\text{C}$)	T_m Onset ($^{\circ}\text{C}$)	Enthalpy of Melting (J/g)	% Crystallinity
Pure PP	165.9 ± 0.4	154.5 ± 0.5	93.9 ± 0.7	45.4 ± 0.4
90:10_0	165.2 ± 0.5	152.9 ± 0.9	82.3 ± 1	39.8 ± 0.4
90:10_A	164.3 ± 0.2	149.5 ± 1.1	81.7 ± 0.8	39.5 ± 0.5
90:10_B	164.8 ± 0.4	143.9 ± 1.1	86 ± 1.8	41.5 ± 0.9

The onset of melting temperature (T_m onset) is derived from the intercept of the tangent to the steepest gradient of the leading edge of the fusion curve with the baseline of the thermal curve. By taking a close look at 90:10_B, melting begins at a much lower temperature than the physical blend. The melting point of lamellar crystals reflects the energy stored in the fold surfaces and hence their stability [362, 369]. Regions of intermediate order should melt at lower temperatures than highly ordered internal regions. The melting transition broadens for PP due to degradation [148] or creation of larger molecules [215]. The onset of melting in a LLDPE/PP/peroxide system decreased by 9°C with 0.25% peroxide and the endotherm was consistently bimodal, attributed to the existence of two different crystal forms [222]. The melting point should also be depressed also if the crystallite is very small (i.e. smaller crystallizable polymer chain segments), owing to higher surface free energy and lower heat capacity [255, 279, 327, 362, 369, 389, 391-397]. Diluents, copolymerized units, grafts/branches/crosslinks, and end groups should have an equivalent effect on depressing the melting point at low

concentrations [161, 185, 260, 331, 389, 393-395, 398]. Small amounts of crosslinks or branches could limit the maximum lamellar thickness because of a reduction in long range mobility, the presence of pre-existing tie molecules, and/or the production of stress along the crystallizing chain so as to oppose the incorporation of additional members of the same chain [389, 393-395]. One may argue that there may be a reduction in melting entropy of the crystals in the presence of crosslinks, resulting in T_m elevation [393], but this trend is not seen.

Another set of experiments focused on the melting of these materials is shown in Figure 4-31. The PP:8407 ratio is 80:20 and these samples show many similarities to the 90:10 blend and alloys. 80:20_A shows the characteristic melting peak of the β phase of PP at 149.4°C, but without styrene present in the system, this peak is not seen. The sample labeled 80:20_C without styrene contains 0.8wt% TMPTA and 0.3% initiator, but not styrene monomer. This material has the lowest % crystallinity and lowest peak melting temperature, which is indicative of a highly degraded PP phase. This is reinforced by the fact that the melt flow index of this material is extremely high (Chapter 5, Figure 5-7).

The physical blend (80:20_0) shows an intermediate % crystallinity with a well defined melting endotherm, high T_m onset, and high peak melting temperature. This is to be expected because the high molecular weight chains of PP are not altered by the grafting process. The high impact strength alloy (80:20_B) shows the typical broad melting endotherm (a high number of small, defective lamellar crystals), high % crystallinity, but unlike 90:10_B, a high peak T_m . Briefly, this difference is the result of

enhanced crystal motion at the 90:10 level and reduced motion at the 80:20 level. The viscoelasticity of the alloys (section 4.3.8) will help explain this phenomenon.

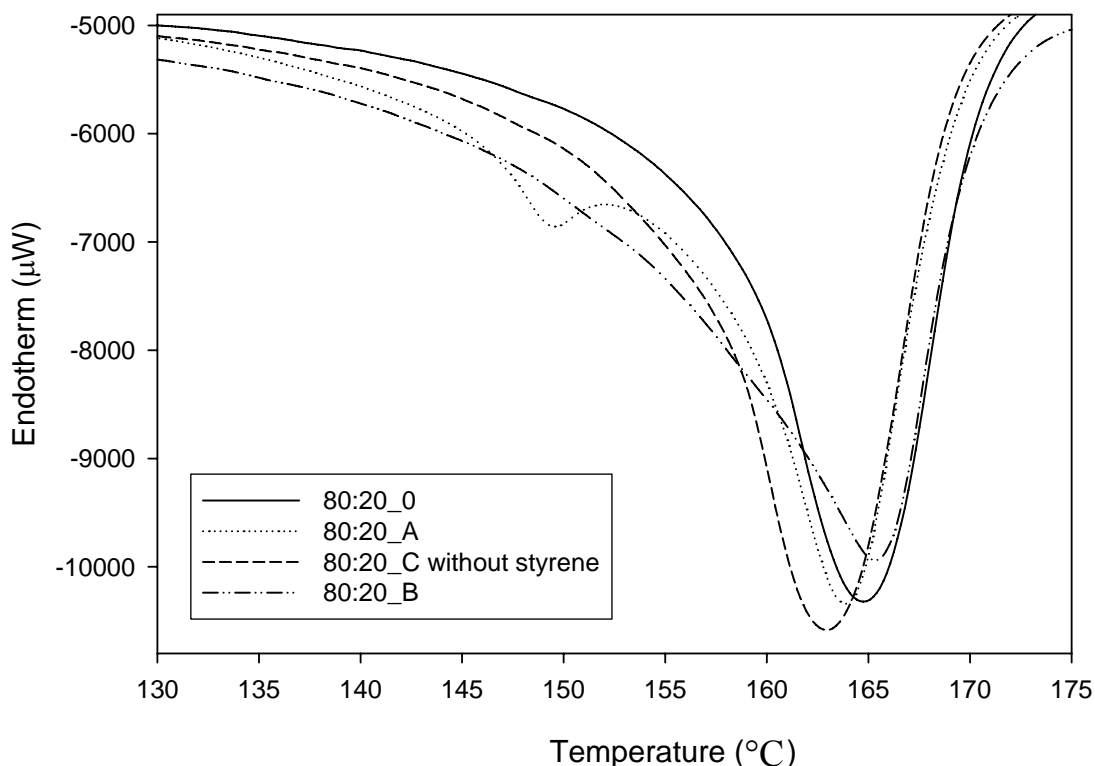


Figure 4-31: DSC heating traces of a physical blend (80:20_0) and alloys (80:20_A, 80:20_B, and 80:20_C without styrene).

Crystallization of long macromolecular chains involves the transfer of consecutive sequential chain units from the amorphous to the crystalline phase [100, 161, 313, 362, 392, 393, 399]. It is complicated by the requirement that many consecutive units of each participating chain must enter systematically in the same crystallite via chain sliding and diffusion. Crystallization will be restricted to very long crystallites slightly below T_m but the critical chain length for crystallization decreases with temperature. The minimum sequence length for crystallization of PP has been reported to range from 8 to 11 monomer units [400, 401].

From Figure 4-32 and Table 4-9, the crystallization peak temperature is highest for 90:10_B, followed by 90:10_A, and finally 90:10_0. Nucleation and growth rate are known to increase with addition of peroxide [220]. Also, T_c increases for grafted polymers because of the nucleating affect [7, 148, 179, 221, 245]. Branching in polyolefins has a nucleating effect by increasing crystallization temperature and crystallization rate [238, 357, 402]. Grafting monomers onto PP increases its crystallization temperature, so they in effect act as nucleating agents. Nucleating agents increase the crystallization rate and temperature, give a more uniform morphology, improve mechanical properties and optical properties (from reduction of spherulite dimensions), and shorten process cycle time [338, 361]. They also retard the relaxation of chains from the polymer melt, producing more tie molecules which improve molecular entanglement between crystal grains and increase boundary strength between spherulites [260].

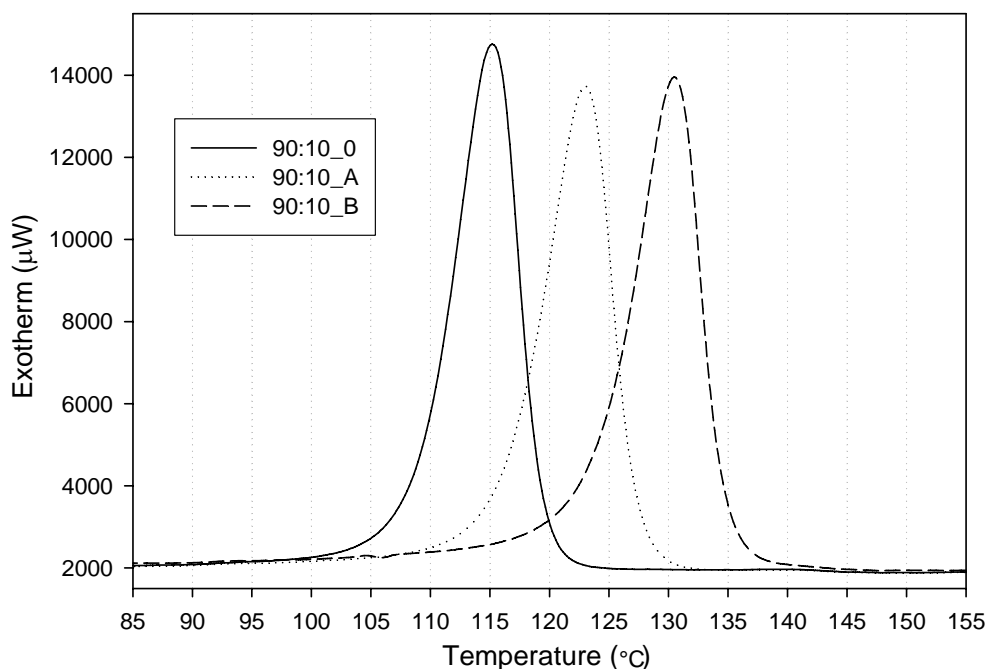


Figure 4-32: DSC cooling traces of a physical blend (90:10_0) and alloys (90:10_A and 90:10_B).

A higher crystallization temperature implies a faster crystallization rate, which infers an increase in the stereoregularity of the chain [378, 401]. Although PP may have the same overall isotacticity (from FTIR), the non-isotactic units may be distributed differently and hence lead to a variation in crystallizability. This may be the reason that the percent crystallinity in 90:10_B and 80:20_B are higher than the physical blends at these levels of elastomer. The most important thermal parameter for crystallization is the supercooling (ΔT defined as $T_m - T_c$), which shows how far the polymer crystallizes from its melt-crystal equilibrium state [378]. With increasing T_c (smaller supercooling), the fraction of the stable α phase increases [375, 398]. The thickness of the lamellar crystallites in the α form is inversely proportional to the supercooling below 191°C. The onset of nucleation follows the same trend as T_c for the set of samples, which means that there may be a lower number of non-isotactic defects associated with the small crystals in 90:10_B [401].

The introduction of a small number of crosslinks is known to considerably increase the nucleation density of the polymer [402]. There may also be a unique interface of the graft copolymer [128]. Beta nucleated samples crystallize with a much lower supercooling than the alpha phase, which might also explain its higher crystallinity [378].

Table 4-9: DSC exothermic data comparing pure PP to 90:10_0, 90:10_A, and 90:10_B.

Sample ID	Peak Temperature of Crystallization (°C)	Enthalpy of Crystallization (J/g)
Pure PP	109.6 ± 0.9	-90.7 ± 0.6
90:10_0	115.3 ± 0.4	-83.1 ± 2.1
90:10_A	124 ± 1.4	-80.7 ± 0.7
90:10_B	130.8 ± 0.65	-84.4 ± 1.4

Perturbations in the mobility of chains during crystallization hinder the formation of the most compact alpha phase [327]. It should be noted that the crystallization and melting behavior of blends and alloys at the 95:5 and 70:30 levels follow the same trends as those at the 90:10 and 80:20 levels.

Polarized light microscopy was utilized to elaborate upon the unique and unexpected crystalline features of these materials. This tool, when used with a heating stage and first order wave plate, gives detailed *in-situ* morphological information on the crystalline phases of the materials. Figures 4-33 thru 4-36 are collections of still photographs describing the non-isothermal crystallization of pure polypropylene, 90:10_0, and two reactive blends (90:10_A and 90:10_B). Because this is the end of a second heating/cooling cycle, many of the β phase spherulites originally present in pure PP has re-crystallized into the thermodynamically more favorable α phase. The relatively slow cooling rate (10°C/min) allows this transformation to take place [287, 322-327].

Contrast in polarized light microscopy is dependent upon a change in refractive index and is positive when the refractive index of light polarized parallel to the long axis of the object is larger than that of light polarized perpendicular to the long axis [370]. The birefringence of a spherulite is positive when the refractive index for light polarized parallel to the radius of the spherulite is larger than for tangentially polarized light (alpha phase of PP) and negative when oriented tangentially (beta phase of PP). The α phase spherulite is characterized by a central region composed of an interwoven array of short lamellae, stacked edge-on, and the spherulite periphery of long, radially-oriented lamellae with short lateral branches oriented approximately perpendicular to the radial lamellae, therefore building a rigid 3-D “crosshatched” network with weakly positive birefringence

[337, 370, 371, 374, 375, 388, 403]. The β phase spherulites show a radial lamellar morphology (banded structure) which is not as rigid as the monoclinic cross-hatched morphology and shows a highly negative birefringence [287, 314, 325, 333, 359, 366, 370, 403].

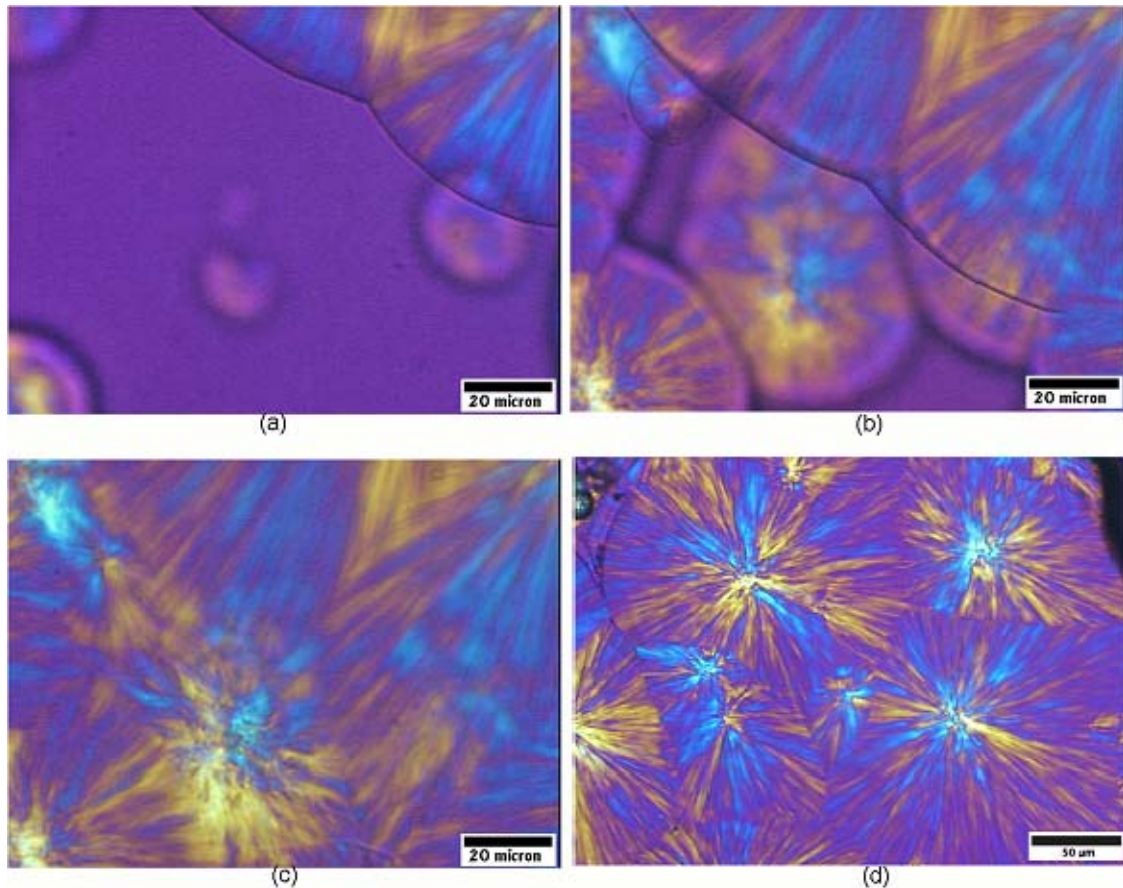


Figure 4-33: Polarized optical images of virgin PP cooled from the melt. (a) = 115.5°C at 50X, (b) = 113.5°C at 50X, (c) = 110°C at 50X, and (d) = 25°C at 20X magnification.

The alpha phase typically shows the characteristic maltese cross extinction pattern but may appear blurry as fibrils radiate from the center of the spherulite [396]. This is a mixed spherulite and consists of crosshatched lamellae in which subsidiary lamellae grow tangentially to the primary radiating lamellae. In Figure 4-33, nucleation of spherulites commences at random times, therefore creating a distribution of spherulites that range in

size from about 10 μm to about 100 μm . Notice that the spherulites, which are composed of twisting lamellae radiating out from a nucleating center, have a mottled maltese cross pattern of positively birefringent material. If the color using a first order wave plate is uniformly blue or yellow, lamellae are arranged in parallel in one direction and run through domain from end to end [398]. A blue color indicates positive birefringence in the direction of the chain axis [370, 396].

Moving on to the physical blend (Figure 4-34), crystallization appears to mimic that of pure PP, except for the dark circular domains dispersed throughout the spherulite. These domains are probably the phase separated elastomer particles, incorporated into the

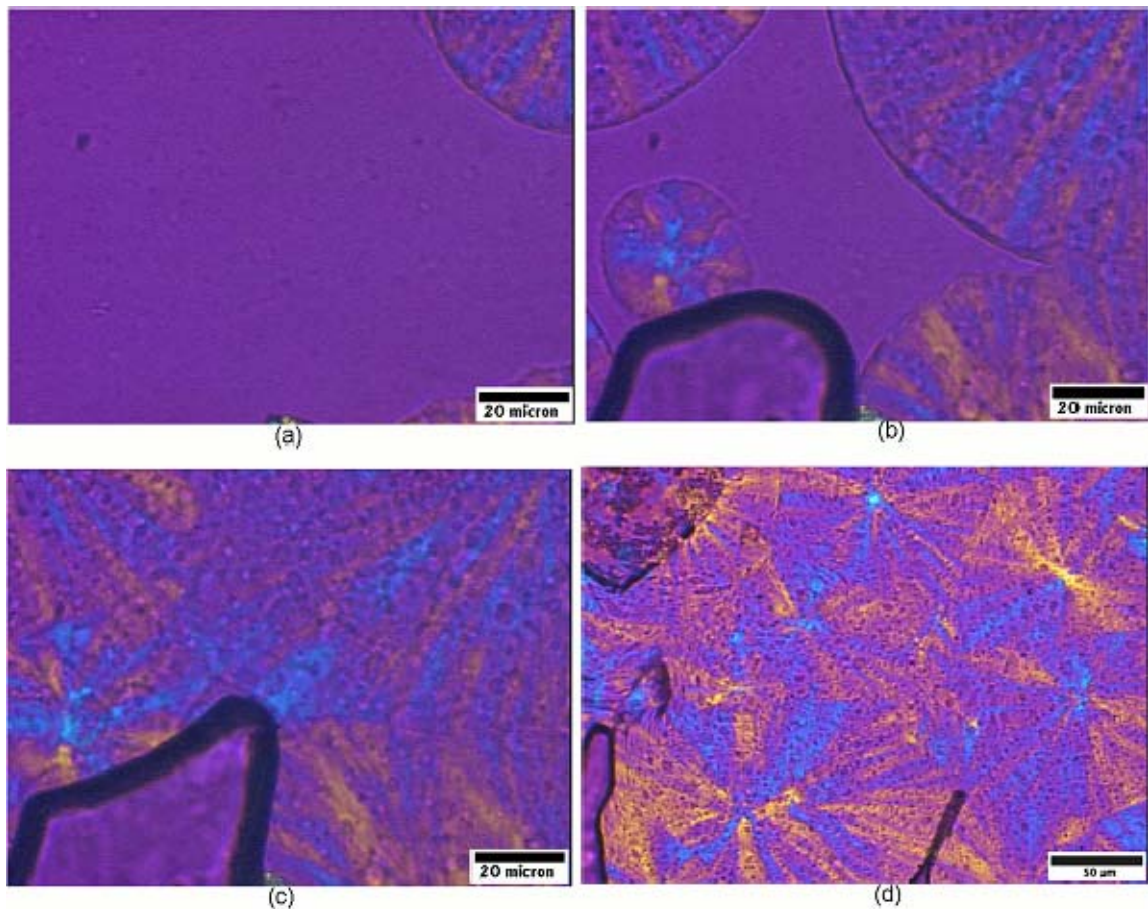


Figure 4-34: Polarized optical images of 90:10_0 cooled from the melt. (a) = 118°C at 50X, (b) = 114.5°C at 50X, (c) = 105°C at 50X, and (d) = 25°C at 20X magnification. A bubble (artifact) appears in the lower left hand of (b) and (c) and along the edges of (d).

growing spherulite as occlusions (no effect on growth rate) [100, 236, 255, 257, 260, 263, 297, 307, 311-313]. The spherulites remain roughly spherical until they impinge on each other and range in size from about 10 μm to about 100 μm .

The crystallization behavior of grafted PP has already been proven to be much different than the pure polymer. And from Figure 4-35, there appears to be no semblance of the typical spherulite seen in the previous two examples. A distribution of oval and round spherulites nucleate at the beginning stages of crystallization, with some showing completely positive birefringence and some completely negative. This means that the orientation of the crystallite is either completely in-phase with the polarized light or

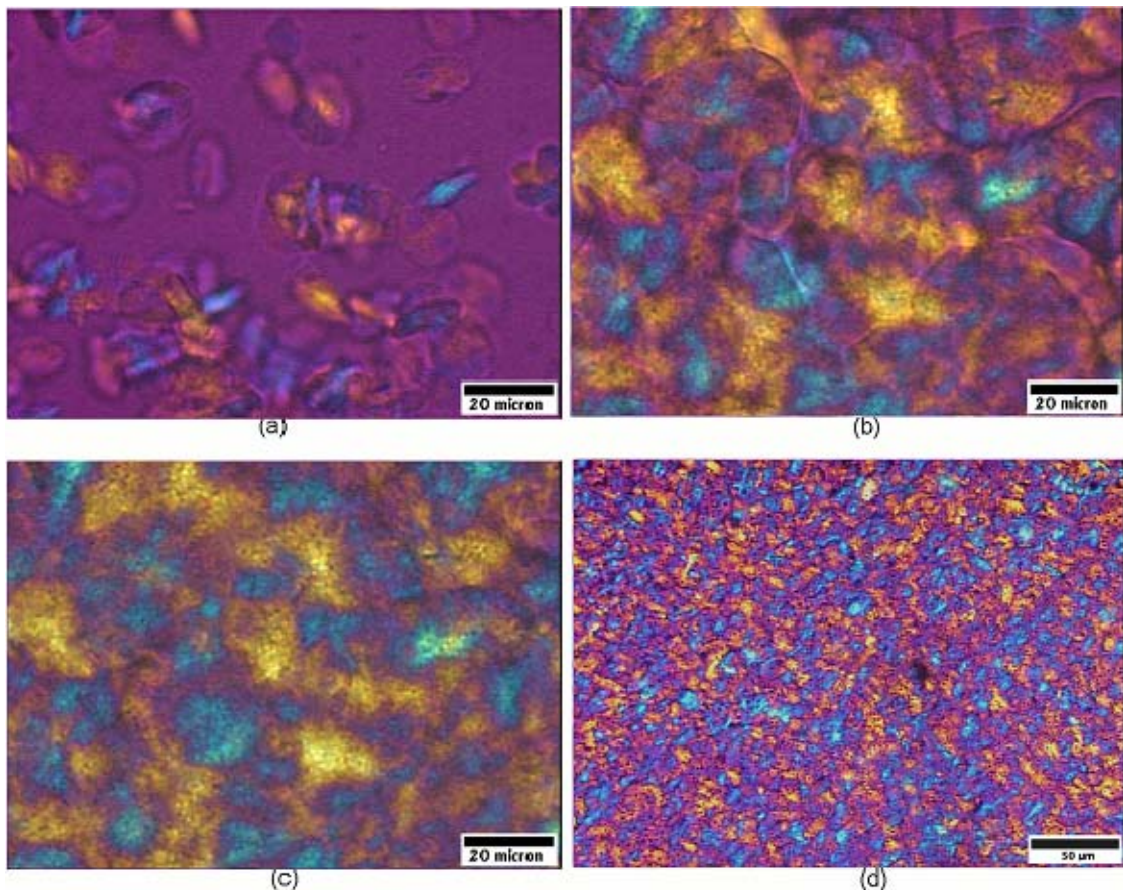


Figure 4-35: Polarized optical images of 90:10 A cooled from the melt. (a) = 128°C at 50X, (b) = 124°C at 50X, (c) = 122°C at 50X, and (d) = 25°C at 20X magnification.

completely out-of-phase. Also, elliptical crystals with uniform optical anisotropy are characteristic of liquid crystalline polymers having rigid molecular chains with local ordering. These morphologies rarely occur in the crystallization of flexible polymers like PP [396]. A network-like color scheme of blue or yellow regions is found for 4-35(c), which could mean a disruption of crystalline order in the sample. The last image in the Figure (4-35(d)) shows a much finer distribution of birefringent material as compared to Figures 4-33(d) and 4-34(d). When monomers are grafted onto polymers, the polymer is known to crystallize at higher temperatures and result in smaller spherulite dimensions [230, 238, 357, 402]. The DSC and XRD results for 90:10_A show the presence of β phase polypropylene, which is characteristically more highly birefringent than α phase. This difference cannot be discerned from the images in Figure 4-35.

The sample with the highest T_c and presumably highest crystallization rate, 90:10_B, reveals the most interesting morphology of all the samples (Figure 4-36). The nuclei are very small and distributed uniformly throughout the sample and appear at approximately the same time. The ellipsoidal and spherical shapes common in the previous three figures are not present in Figure 4-36. A network-like appearance of birefringent material is present, likely associated with the branching afforded by multifunctional monomer. The final image in the group shows a macroscopically uniform distribution of extremely small, presumably crystalline structures below 1 μm in diameter.

The extensive branching present in this alloy appears to have a significant effect on the entire crystallization process and is explained as follows: Classical nucleation and growth is known to be preceded by an induction period, where parallel orientation and

segregation of polymer segments induces a spinodal decomposition type microphase separation [110, 327, 389, 397, 398, 400, 404, 405]. Density fluctuations of about

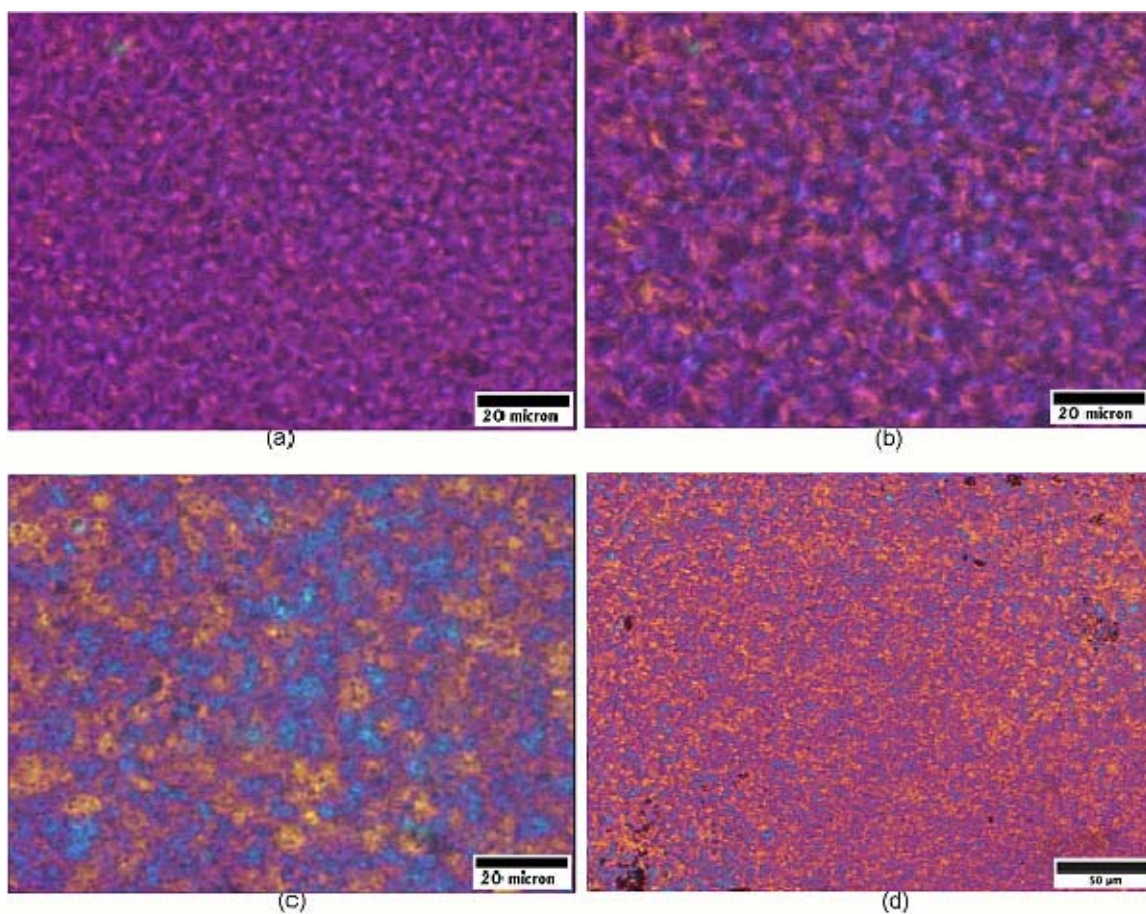


Figure 4-36: Polarized optical images of 90:10 B cooled from the melt. (a) = 135°C at 50X, (b) = 133°C at 50X, (c) = 130°C at 50X, and (d) = 25°C at 20X magnification.

20 nm periods in the amorphous phase are associated with the induction period, but long range ordering and local orientation with domain sizes about 300-1000 nm takes place before the formation of crystal nuclei [404-406]. The early stages of crystallization of polymers can be ascribed to a physical gelation-type process [392, 406, 407]. After the crystal network is set up, the amorphous defects can continue locally to crystallize with very little or no long distance diffusion in a secondary crystallization process [61-63]. A small number of crosslinks is known to form a sample-spanning network and produce a

considerable increase in nucleation density [390, 393-395, 407]. Also, crystallinity is easier with a stretched conformation over some distance [408].

4.3.8 Viscoelasticity

Dynamic mechanical testing can reveal a lot about a polymer's response to temperature, time, and load. The transitions allow one to determine the relative compatibility of the existing components as well as degree of crosslinking and crystalline phase characteristics.

Storage modulus is an indication of the stiffness of the polymer and may be considered inversely proportional to impact strength in physical blends [283]. The stiffness typically increases with increasing density (crystallinity) or entanglement density (from high molar mass) [284]. Figure 4-37 plots E' and $\text{Tan}\delta$ vs. temperature of 95:5_0 and 95:5_B. The alloy's response to the oscillating load deviates from the physical blend in several instances. The storage modulus of 95:5_B is equal to or lower than the physical blend at all temperatures. This may be a result of a greater free volume from grafted and ungrafted styrene/DEGDA molecules, the presence of smaller PP chains, and a nanometer length scale distribution of elastomer which changes the intrinsic relaxation time distribution of the polymers. Also, the entire range of molecular chains in the amorphous phase of the physical blend may frozen in to form a fully glassy state at low temperatures [302, 409].

Between about 0°C and 40°C (onset of long range molecular motion of PP) there is a smaller slope for the E' for 95:5_B than 95:5_0 which is an indication of crosslinking or decrease in crystallinity [410]. A gel is not present and % crystallinity actually increases, so this is likely due to the branched architecture or an increase in molar mass from the

reaction [81]. For $\text{Tan}\delta$ graph comparisons, the alloy's intensity is lower than the physical blend up until 40°C . This may be due to the simple fact that the overall

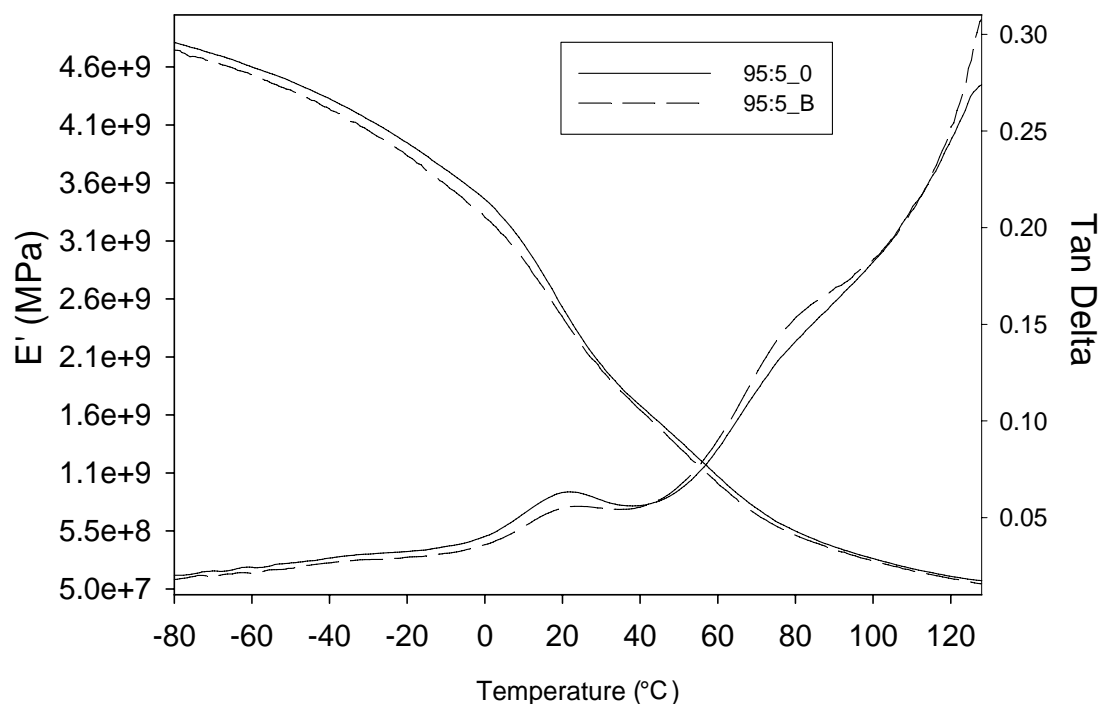


Figure 4-37: Storage modulus (E') and $\text{Tan}\delta$ comparison of 95:5_0 and 95:5_B as a function of temperature

concentrations of PP and 8407 are reduced because of the presence of the reactive materials. Another explanation is because molecular motion is hindered by a highly entangled network of chains or a greater nucleation density of crystals [301]. The higher intensity of 95:5_0 at T_g ($\sim 20^\circ\text{C}$) indicates greater amorphous content of the material. DSC measurements have shown that the % crystallinity of the alloy is actually higher than the physical blend so the intensity of T_g would be lower. Also, a decrease in intensity reveals an increase in molar mass [81].

Above 40°C , the molecular motion in the amorphous phase is more pronounced for the alloy. The smaller lamellar crystals in the alloy may allow for easier crystal glide and amorphous phase rearrangement. Authors have attributed this increase in shoulder/peak

height at about 80°C to the existence of the β crystalline phase of PP, which is known to have a wider, diffuse amorphous and crystalline region than the α phase [260, 287, 301, 337, 340]. The decrease in intensity after this shoulder may be due to lamellar reorganization (annealing) into a more thermodynamically stable phase [132]. There was no evidence of polystyrene's T_g in this or any $\text{Tan}\delta$ graph possibly because the concentration was too low and became masked by other relaxations. At the highest temperature of the test, the intensity of the alloy is higher than the physical blend, also lending to the notion that crystallographic defect motion is probable, surface defects are more mobile, and long range amorphous motion and crystal glide are present.

At the 90:10 level of PP:8407 (Figures 4-38 and 4-39), three different samples are compared: 90:10_0, 90:10_A, and 90:10_B. For the storage modulus graphs, the high impact sample is again lower than the physical blend at all temperatures and shows a

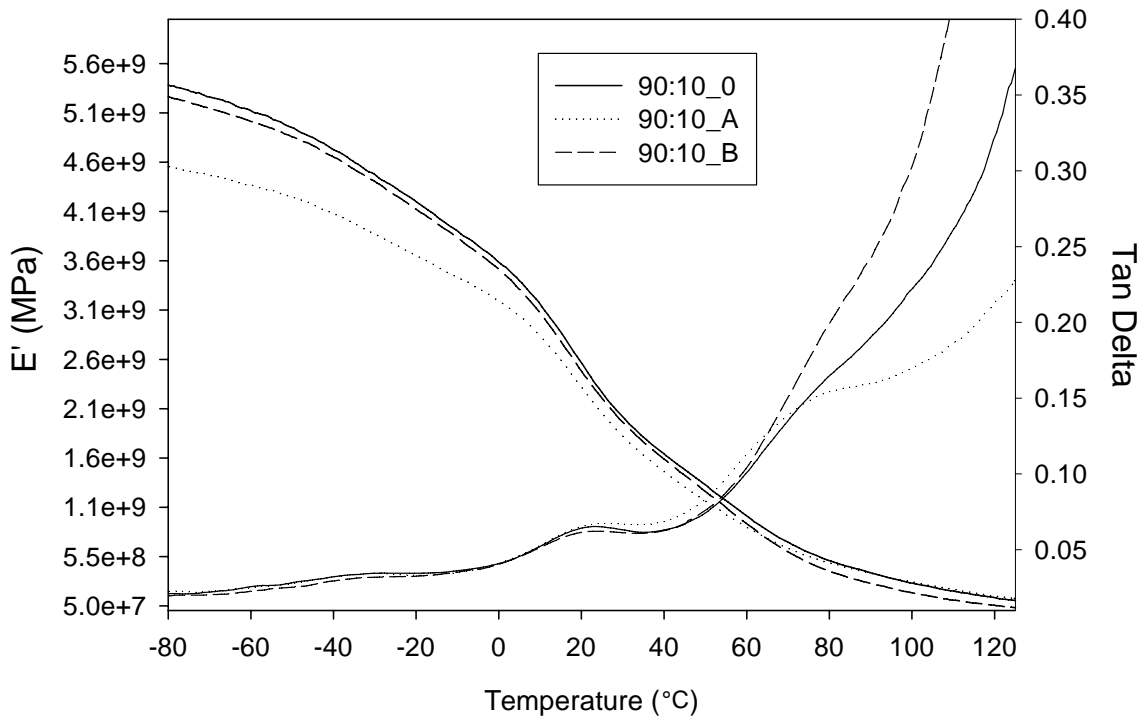


Figure 4-38: Storage modulus (E') and $\text{Tan}\delta$ comparison of 90:10_0, 90:10_A, and 90:10_B as a function of temperature.

similar decrease in slope at about 20°C. But one subtle difference between 90:10_B and 90:10_0 is at the high temperature region of the graph, where E' shows a greater negative deviation from the physical blend. This may be due to softening of the material and may be a consequence of a change in the relaxation behavior brought about by nano-elastomer domains or the enhanced mobility of smaller lamellar crystals. T_g of both the PP and 8407 phases are lower than the physical blend, a trend explained in the 95:5 comparison. The alloy not containing the multifunctional monomer (90:10_A) has a much lower storage modulus at low temperatures than either 90:10_0 or 90:10_B. This may be the result of an excess homopolymerized (not grafted) material which may exist as oligomers and have little chain mobility restrictions. But at high temperatures, 90:10_A mimics the physical blend which may signify that while the amorphous phase is severely affected by this modification, the lamellar crystals and its corresponding defects are not.

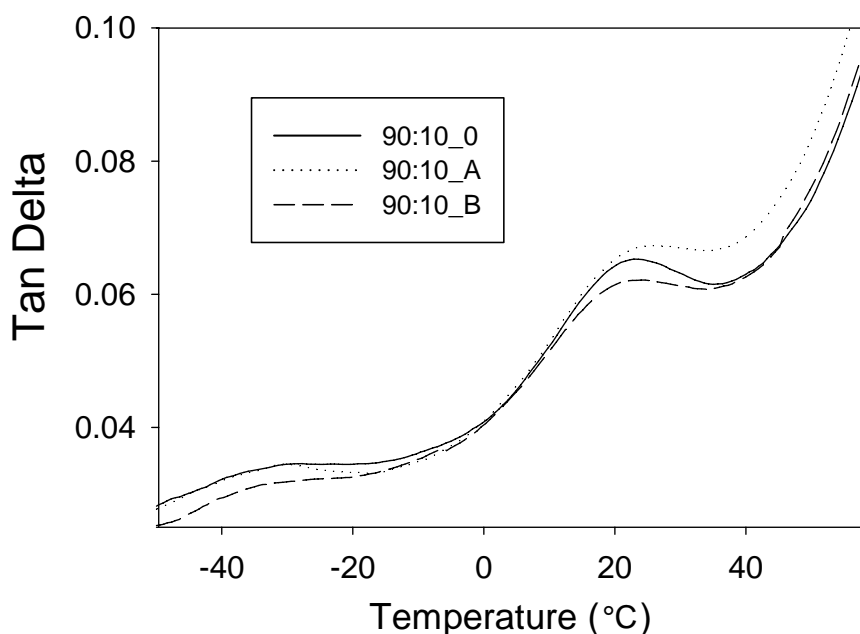


Figure 4-39: $\text{Tan}\delta$ comparison of 90:10_0, 90:10_A, and 90:10_B between -50°C and 60°C to show a magnified graph of β_{8407} and β_{PP} .

When studying the $\text{Tan}\delta$ peaks of the materials in Figures 4-38 and 4-39, the elastomer phase appears to be affected to a greater extent in 90:10_B than 90:10_A. This means that in 90:10_B, the reactive materials are able to localize and react in a more efficient fashion than 90:10_A, leading to a branched architecture and reduction in molecular mobility. At the T_g of polypropylene, 90:10_A has a higher molecular mobility than the other two samples. This is to be expected from melt flow index results, where it was shown that by reactively extruding without multifunctional monomer, the high molecular weight tail of PP is attacked and degradation ensues [233]. An interesting comparison at about 80°C can be seen – there is a more prominent peak/shoulder for 90:10_A but above this temperature the intensity is less than both 90:10_B and 90:10_0. X-ray diffraction and DSC studies have already shown that the β crystalline phase of PP is more pronounced in 90:10_A. DSC also confirmed that the overall % crystallinity is lower for this sample. So, one may conclude that this peak/shoulder does represent the unique β crystal phase of PP but the material crystallizes predominantly in the alpha phase. The alpha phase may not be distributed as small lamellar crystals, as in 90:10_B. 90:10_B does have a shoulder at about 80°C, similar to the shoulder found in XRD for the β or smectic phase. At high temperatures, the $\text{Tan}\delta$ graph drastically increases for 90:10_B compared to 90:10_0. This behavior is indicative of inter- and intra-crystalline mobility, and is a direct result of the large distribution of small lamellar crystals with high surface energy [132]. DSC results have shown that the peak melting temperature of 90:10_B is lower than 90:10_0, reinforcing the idea of greater crystal mobility in the alloy.

For higher concentrations of elastomer (Figures 4-40 and 4-41), the storage modulus results are similar. In both cases, the high impact alloys are not as stiff as their physical blend counterparts at low temperatures (until the T_g of PP is surpassed). The distribution of nano-elastomer domains throughout the alloy may be affecting its overall relaxation behavior. In other words, there are likely many soft domains with highly mobile polymer chains composing them, but they may be anchored at a few points so as to stabilize them. The slope of the storage modulus for each alloy is smaller than the physical blends, and MFI and melt strength data reinforce the idea that a high molar mass branched structure is the cause. When processing at these high elastomer levels, the reactive materials may have a tendency to crosslink and branch while trapped in the elastomer phase. Above the rubbery flow region (40-70°C), E' is higher for the alloys

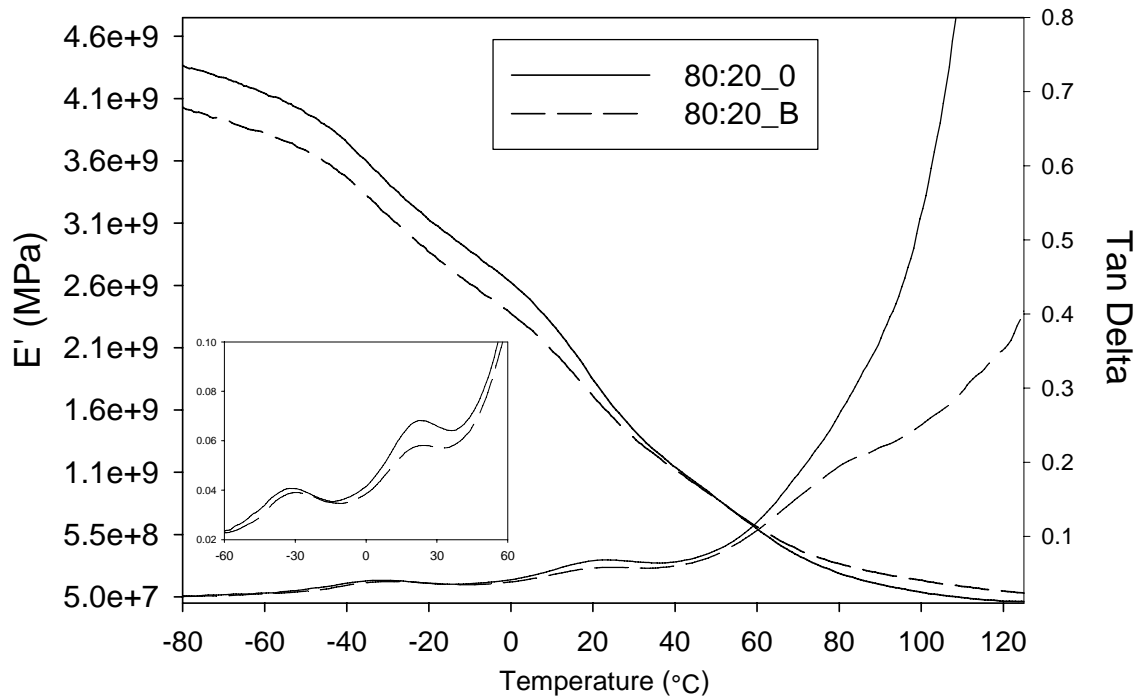


Figure 4-40: Storage modulus (E') and $\text{Tan}\delta$ comparison of 80:20_0 and 80:20_B as a function of temperature

because of chemical and physical links in the amorphous phase and at the surface of the crystalline phase.

Internal friction ($\text{Tan}\delta$) measurements of these samples show that the T_g of 8407 decreases in intensity but also shifts to a slightly higher temperature. A higher energy barrier for molecular motion is present (possibly due to branching or crosslinking) and the phases are more compatible due to grafting agents [8, 9, 258, 289, 321]. The T_g of PP decreases in intensity upon modification, a trend seen in all samples and attributed to a decrease in chain mobility or concentration of PP. At high temperatures, Figures 4-40 and 4-41 show different behavior. 80:20_0 experiences a drastic increase in intensity above 60°C which indicates that the spherulite morphology may be disrupted and the amorphous regions surrounding the lamellar crystals greatly influence inter- and intra-crystalline mobility. For 80:20_B, a single peak exists at 80°C , which may represent the

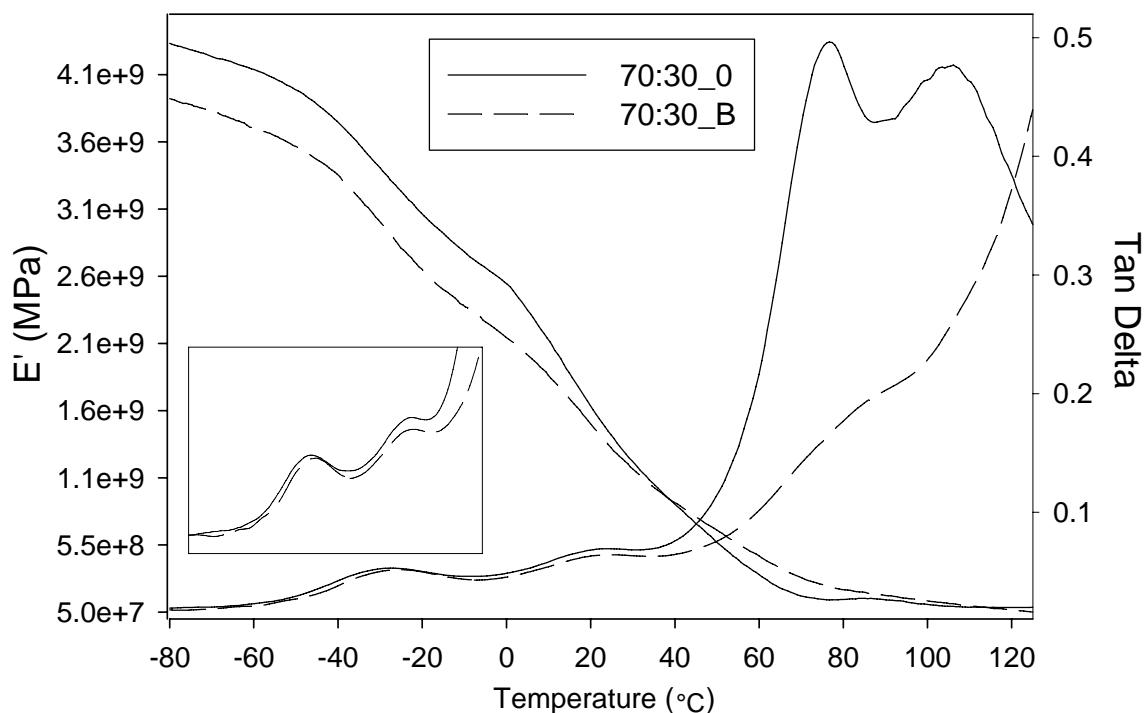


Figure 4-41: Storage modulus (E') and $\text{Tan}\delta$ comparison of 70:30_0 and 70:30_B as a function of temperature.

β phase of PP. Like the 70:30 alloy, the slope of the curve increases continuously due to the slippage and diffusion of amorphous regions around stable lamellar crystals. A close look at 70:30_0 reveals two peaks at about 60°C and 100°C.

The peak at 60°C may represent the melting of any 8407 crystalline lamellae. At 100°C, there may be pre-melting of the PP crystals and very high rate of slippage and mobility of the crystals. Very diffuse and unstable spherulites are known to exist in PP-elastomer blends at high elastomer concentrations [257, 261, 263, 264]. For 70:30_B, these two peaks disappear and a single peak forms at 80°C, not unlike 80:20_B. The creation of this one peak shows that the reactive constituents lead to compatibilization between phases. The decrease in intensity of the alloys compared to the physical blends at high temperature reveals a restriction in PP chain mobility and a high entanglement density. DSC comparisons of 80:20_0 and 80:20_B have shown that T_m of 80:20_B is higher than 80:20_0.

4.4 Conclusions

Many types of reactions are present in this complex reactive extrusion process. Understanding free radical polymerization mechanisms is extremely important and key to controlling the microstructure of the alloys and the resulting macro-scale properties. Initiator decomposition is the rate determining step, but once the given energy barrier is overcome, several reactions happen at once. These include monomer polymerization, hydrogen abstraction from polymers, grafting of monomers onto polymers, and degradation reactions. The end result, which is reinforced by all of the data presented in this chapter, is an interconnected, branched collection of macromolecules with unique

morphology, excellent mechanical properties and melt extensibility, and characteristic crystalline morphology.

Impact strength has been shown to be dependent upon a high degree of grafting between the phases present, distribution of extremely small elastomer domains, a highly entangled amorphous phase, small crystalline structures, and a low glass transition impact modifier. Literature has primarily concentrated on the modification of either the amorphous phase or crystalline phase, but this work was able to tie in both concepts for the creation of a novel super high impact semicrystalline polymer.

The crystalline state of the alloys appears to be unique, with a finely dispersed, highly cross-hatched spherulitic structure. DSC has shown that relatively smaller crystals are indeed present which have the ability to slide and diffuse more efficiently than pure PP lamellar crystals. A combination of the aforementioned characteristics give the alloys the unique ability to both absorb energy by typical mechanisms but also to resist deformation by phase transformation toughening and elastic retractive forces.

CHAPTER 5
THE EFFECT OF PROCESSING CONDITIONS ON ALLOY PROPERTIES

5.1 Introduction

This chapter delves deeper into how mechanical properties and grafting efficiency change with varying processing parameters and reactive ingredient concentrations. The effect of screw speed, temperature, initiator concentration, multifunctional monomer concentration, and styrene concentration are studied. Properties such as notched Izod impact strength, elastic modulus, yield strength, melt flow index, and grafting efficiency can be tailored and optimized by varying these parameters.

5.2 Experimental

5.2.1 Materials

Table 5-1 gives a list of pertinent ethylene-1-octene copolymers produced by Dupont Dow elastomers under the trade name ENGAGE®, but the EOC grade of interest is 8407 [48]. Isotactic polypropylene homopolymer was supplied by Equistar Chemical (grade PP 31S07A) and is contact translucent. All polymers were received in pellet form. The peroxide and monomers used in this study were reagent grade chemicals (structures are shown in Table 5-2). The monomers were purified by passing through an activated alumina column before use. Styrene monomer, inhibited by 10-15 ppm t-butyl catechol, was purchased from Fisher. The initiator, 2,5dimethyl-2,5-di-(t-butylperoxy) hexane, was purchased from Atofina under the trade name Lupersol 101. Diethyleneglycol diacrylate (DEGDA), inhibited by 80 ppm Hq and 120 ppm MEHQ, and trimethylolpropane triacrylate (TMPTA), inhibited by 125 ppm HQ and 175 ppm MEHQ,

were graciously donated by Sartomer, an Atofina company. Table 5-1 lists structures of the reactive materials.

Table 5-1: ENGAGE® product data table.

ENGAGE® Grade (decreasing comonomer content)	8842	8407	8200	8401	8402
Comonomer Content wt% ¹³ C NMR/FTIR	45	40	38	31	22
Density, g/cm ³ ASTM D-792	0.857	0.870	0.87	0.885	0.902
Melt Index, dg/min ASTM D-1238, 190°C, 2.16kg	1.0	30	5.0	30	30
Mooney Viscosity ASTM D-1646 ML 1 + 4 at 121°C	26	< 5	8	< 5	< 5
Durometer Hardness, Shore A ASTM D-2240	50	72	75	85	94
DSC melting Peak, °C Rate: 10°C/min	33	60	60	78	98
Glass Transition Temp, °C DSC inflection point	-61	-57	-56	-51	-44
Flexural Modulus, MPA ASTM D-790, 2% Secant	3.5	12.1	12.1	25.8	69.9
Ultimate Tensile Strength, MPa ASTM D-638, 508mm/min	2.1	3.3	6.9	6.4	12.9
Ultimate Elongation, % ASTM D-638, 508mm/min	975	>1000	>1000	950	790

Table 5-2: Structures of reactive materials of interest

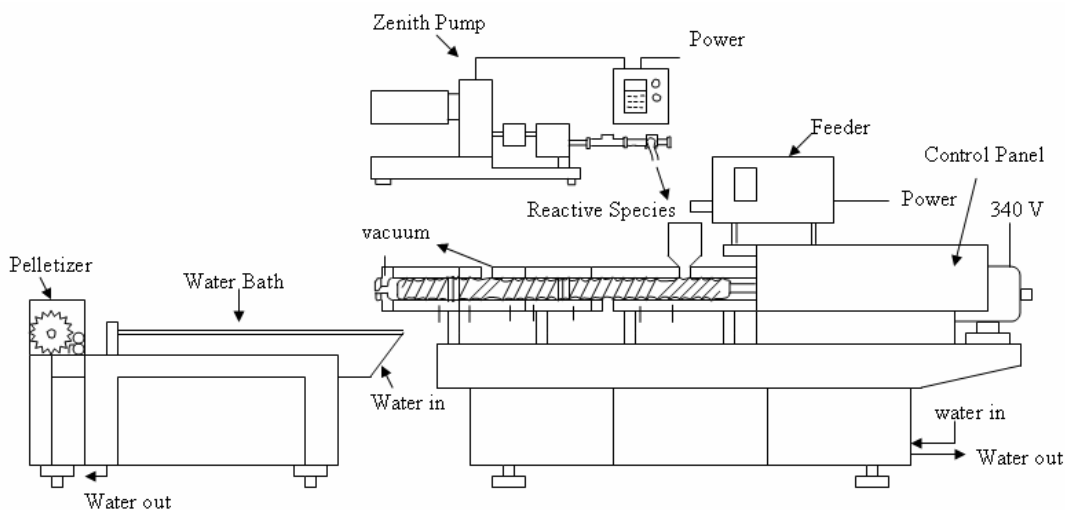
Name	Lupersol 101	DEGDA
Structure	$ \begin{array}{c} \text{CH}_3 \qquad \text{CH}_3 \\ \diagdown \quad \diagup \\ (\text{CH}_3)_3\text{C}-\text{O}-\text{O}-\text{C}-\text{CH}_2-\text{CH}_2-\text{C}-\text{O}-\text{O}-\text{C}(\text{CH}_3)_3 \\ \diagup \quad \diagdown \\ \text{CH}_3 \qquad \text{CH}_3 \end{array} $	$ \text{CH}_2=\text{C}(\text{H})-\overset{\text{O}}{\parallel}{\text{C}}-\text{O}-\text{CH}_2-\text{CH}_2-\text{O}-\text{CH}_2-\text{CH}_2-\text{O}-\overset{\text{O}}{\parallel}{\text{C}}-\text{C}(\text{H})=\text{CH}_2 $
Name	Styrene	TMPTA
Structure		$ \begin{array}{c} \text{O} \\ \parallel \\ \text{O}-\text{C}-\text{CH}=\text{CH}_2 \\ \\ \text{CH}_2 \\ \\ \text{CH}_2-\text{CH}-\text{CH}_2-\text{CH}_3 \\ \\ \text{CH}_2 \\ \\ \text{O}-\text{C}-\text{CH}=\text{CH}_2 \\ \parallel \\ \text{O} \end{array} $

5.2.2 Methods

5.2.2.1 Processing

All polymers were dried in an air circulating oven at 40°C for 24 hours prior to compounding. Before processing, the resins were premixed by hand for about 10 minutes. Monomer/initiator mixtures were magnetically stirred for 10 minutes before processing and a choice amount of the mixture was added to the dry polymer pellets before processing.

The blending was carried out in a 34 mm non-intermeshing, co-rotating twin screw extruder, APV Chemical Machinery (now B&P Process Systems) with an L/D ratio of 39. Figure 5-1 is a schematic of the extruder along with a typical temperature profile.



Die	Zone 1	Zone 2	Zone 3	Zone 4	Zone 5	Zone 6	Zone 7 (Feed)
195°C	205°C	210°C	210°C	200°C	190°C	180°C	165°C

Figure 5-1: Schematic drawing of the reactive twin screw extruder and a common temperature profile.

The temperature of the extruder was regulated by electrical resistance and water circulation in the barrels. The dried, pre-mixed resins were then introduced into the extruder at 60 g/min through a screw dry material feeder, Accu Rate, Inc. A Zenith pump controlled the rate of monomer/initiator solution addition into the extruder. The screw

speed, unless otherwise noted was 150 rpm. Devolatilization was carried out by a vacuum pump, VPS-10A, Brooks Equipment Company. This was placed near the die and created a pressure of about 15 in Hg. The extruder was always starved to feed. After compounding, the resulting strands which exit the die are quenched in a water bath, pelletized, and dried in a vacuum oven at 100°C, 28 in Hg for 24 hours.

5.2.2.2 Mechanical properties

In order to measure the strength of the material at very high testing rates, a notched Izod impact test was performed according to ASTM D256 standards. The pellets were placed in a mold with 6 slots, each measuring 0.5x0.5x2.5in³. The mold was put in a Carver press (Fred S. Carver, Inc.) at 200°C and after the material melts, the pressure was raised to 5000 psi. After waiting for 5-10 minutes, the pressure was slowly increased up to 10,000 psi. After another 5 minutes, the heat was turned off and the sample was let to cool down to room temperature at about 1.5°C/min. The bars were then taken out and notched with a Testing Machines, Inc. (TMI) notching machine. Before testing, they were conditioned at room temperature for at least 24 hours. A 30 ft-lb hammer was used with test method A on a TMI Izod impact tester. At least 5 bars were broken and impact strength is recorded as an average regardless of full or partial break.

For stress-strain measurements, dried pellets were placed in a mold measuring 15x15 cm² x 1 mm thick. The mold was put into the Carver press at 200°C and after the material melts, pressed up to 5000 psi. After a 5-10 minute wait, the sample was slowly pressed to 10,000 psi. Five minutes later, the sample was quenched in a water bath. Specimens were tested according to ASTM D638 standards. Type V specimens were punched out of the compression molded sheet with a die, measuring 1 mm thick, 2.95 mm gauge width and 9.5 mm gauge length. Five samples were tested after conditioning

at room temperature for 48 hours. The machine used to test the samples was an MTS Model 1120 Instron, using a 1000 lb load cell at a test speed of 12.7 mm/min

5.2.2.3 Chemical composition

Fourier Transform Infrared Spectroscopy (FTIR) was performed on a Nicolet 20SXB Spectrometer. 256 Scans were taken from 3500 to 500 cm^{-1} wavenumbers with a resolution of 4. Measurements were done in transmission mode on thin films (~2-3 microns). Films were produced by melting the polymer in a Carver press at 180°C and 10,000 psi for 2 minutes then quenching in a water bath at room temperature. For quantification of the grafted styrene, a calibration curve had to be established as explained in Appendix A. Areas under the 700 cm^{-1} and 1376 cm^{-1} peaks are compared and related to absolute styrene amounts to get the grafting efficiency (GE). This is defined by the following equation:

$$\text{GE} = \frac{\text{Amount of Monomer Grafted to Polymer Backbone}}{\text{Original Amount of Monomer Pumped into Extruder}} \times 100\% \quad (5.1)$$

All reactively extruded materials must be purified before quantifying the GE. This first involved dissolving the pellets of crude graft copolymer in hot xylene at a concentration of ca 4% (wt/vol). The hot solution was precipitated into ten volumes of acetone (a known non-solvent for the LLDPE, HDPE and PP, and a solvent for styrene monomer and homopolymer based on solubility parameters [162]). The unreacted monomers, styrene and DEGDA or TMPTA homopolymers and copolymers remained soluble in acetone and were separated out from the grafted polyolefins. The precipitated graft modified alloy was filtered, washed, and then vacuum dried at 70°C for 24 hours. FTIR showed that the GE level remained unaltered upon further rounds of purification. Therefore, one purification step was sufficient for removal of all the residual impurities.

5.2.2.4 Rheology

Melt Flow Index (MFI) testing was done according to ASTM D1238 (230°C and 2.16 kg weight) on a Tinius Olsen model MP 933 Extrusion Plastometer. For materials with an flow rate of 0.5-3.5 g/10 min, the weight of the samples was approx. 3 g, whereas materials with flow rates of 3.5-300 g/10 min, the sample weight was approx. 6 g. All materials were dried under vacuum then conditioned at room temperature before testing, with an average of two runs reported.

5.3 Results and Discussion

5.3.1 Effect of Processing Temperature

Controlling the extruder barrel temperature allows one to control or influence several parameters, specifically the point in which reactions will start and reach completion, rate of plastification/melting of polymers, rate of initiator decomposition and hence rate of reaction, length of polystyrene grafts and homopolymer, and degradation/crosslinking of polymers. These all have implications on the final mechanical properties of the alloy. Table 5-3 gives the three different temperature profiles of interest, with the highest temperature experienced in Zone

Table 5-3: Three different temperature profiles for the extrusion of 80:20 C.

	Zone 8 (Die)	Zone 7	Zone 6	Zone 5	Zone 4	Zone 3	Zone 2	Zone 1 (Feed)
Sample 1	180°C	185	190	190	185	180	175	165
Sample 2	195°C	205	210	210	200	190	180	165
Sample 3	215°C	225	230	230	220	210	190	165

At low temperatures, the initiator dissociation will occur at a later point along the extruder because of a longer half life. Therefore, attack onto molten PP by primary radicals is more likely because the concentration of initiator derived radicals will be higher at a later point along the barrel. Initiator and monomer may be “caged” in the

highly viscous melt as concentrated pockets which likely preferentially attack the major phase polypropylene. So, the benefits of polymers co-melting and maximum monomer conversion may not be realized.

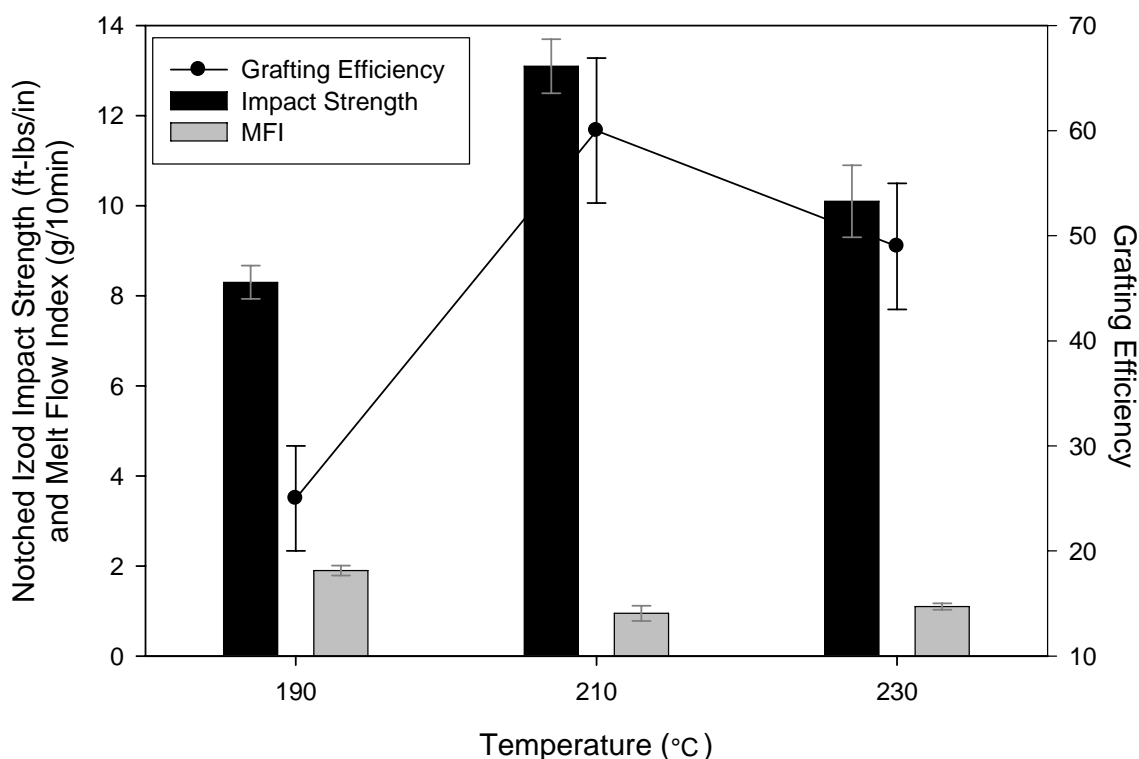


Figure 5-2: Effect of extruder barrel temperature on room temperature impact strength, melt flow index, and grafting efficiency of 80:20_C.

The sensitivity of alloy performance on barrel temperature is seen in Figure 5-2. Grafting efficiency is lowest for the low temperature sample, peaks at an intermediate temperature, and decreases at the highest temperature. It typically increases with temperature because the activation energy for graft initiation is less than homopolymerization [7, 249] but another author found that at 220°C, efficiency drops off because of premature reaction of monomer and initiator before proper mixing in the polymer melt [166]. At the highest temperature, initiator radicals become less selective as far as hydrogen abstraction is concerned. There will be a large concentration of

radicals, but initiator decomposition occurs at such a fast rate that the grafting reaction cannot keep up with all other competing reactions. It should also be noted that no grafting will occur after all initiator decomposes [152].

The low impact strength for the low temperature sample is due to the degradation of PP and reduction of entanglements. But the reason for the low impact strength at the high temperature could be due to the fact that homopolymerization dominates over polyolefin grafting. Excess homopolymerized material can deleteriously affect impact strength [68]. Also, increasing temperature leads to a lower viscosity of both polymer melts, which promotes coalescence of the dispersed phase [411]. Chapters 3 and 4 prove that coalescence of the dispersed phase is not conducive to high impact strengths.

Melt flow index is also graphed in Figure 5-2, which is highest for the low temperature samples. This is due to a high concentration of primary free radicals generated in the polypropylene melt, leading to β chain scission. MFI is low for the high temperature sample because consumption of radicals by monomers is fast. There may be a highly entangled network of homopolymerized material and slightly crosslinked ethylene copolymer, with a relatively lower degree of PP degradation.

Stress-Strain behavior (Table 5-4) parallels the response of impact strength at various barrel temperatures. Elastic modulus is a measure of the stiffness of the amorphous phase of the alloy and is highly dependent upon the chain entanglement density as well as distribution of crystallites which act as pseudo-crosslink junctions. At

Table 5-4: Stress-strain behavior of 80:20 C as a function of temperature.

Max Extruder Temp (°C)	Modulus (MPa)	σ_{Yield} (MPa)	Elongation at Break (mm)	σ_{Break} (MPa)	Energy to Break (N*mm)
190	1220 ± 39	24.1 ± 0.8	50 ± 10	32.9 ± 3.2	3112 ± 844
210	1356 ± 110	25.3 ± 2	56 ± 10	35.9 ± 4.6	3488 ± 1208
230	1203 ± 62	23.8 ± 1.8	44.5 ± 4	32.4 ± 2	2970 ± 745

low extrusion temperatures, degradation is high and chain entanglement density is lowest from MFI data. For the highest temperature, there may be a high degree of homopolymerized materials, which may be entangled, but does not have the load bearing capacity of the PP phase which has both a highly entangled amorphous phase and crystal blocks reinforcing it. Yield stress is highly dependent upon the crystalline state and if mobility at and around the surface of lamellar crystals is easier, yield stress will decrease. Yield stress is low for both 190°C and 230°C samples which coincidentally have low grafting efficiencies resulting in phase separated homopolymer. Elongation at break, stress at break, and energy to break are all dependent upon the breakup of crystals and subsequent recrystallization. Defects and high interfacial tension decrease the magnitude of each of these properties [261, 262]. So, a high GE at 210°C reduces chain degradation (defects) and improves interfacial adhesion between phases.

5.3.2 Effect of Screw Speed

The size of the dispersed phase is known to decrease with increasing shear rate but at very high shear rates, the particles actually increase in size [41]. Polymer melts are shear-thinning materials, so with increasing shear rate, the matrix viscosity can decrease sharply. At higher shear rates, the droplets have higher approach velocities and thus the coalescence probability can increase [41, 341].

Besides its effect on domain size, screw speed also dictates the residence time (length of time polymer exists in the extruder), degree of mixing, and point at which the polymers become fully molten. The overall grafting yield is dictated by the local residence time in the plastification zone and not by the overall time in the entire extruder [90]. Table 5-5 lists the actual residence times at varying screw speeds for the reactive twin screw extruder. Two heat sources are responsible for plastification of polymers:

barrel heating by conduction and viscous dissipation by the rotation of the screws (interparticle friction). The higher the screw speed, the greater amount of heat from viscous dissipation, but the lower amount of heat transferred to the polymers by conduction due to reduced residence time. Plastification is a physical process, while grafting is a chemical one. Figure 5-3 indicates that at varying screw speeds, MFI, impact strength, and grafting efficiency are interrelated for each alloy.

Table 5-5 Screw speed relationship to residence time

Screw Speed (rpm)	75	100	150	200	250
Residence Time (min:sec)	2:38	2:12	1:46	1:35	1:28

An increase in rotation rate results in a decrease of monomer conversion because of a decrease in mean residence time as well as a decrease in the number of fully filled chambers and overall volume of extruder barrel [7, 77, 90]. Also, the reaction will start at a later point in the extruder. Figure 5-6 shows that there is a reduction in grafting efficiency of PP as screw speed increases. Grafting will start at a later point along the extruder so homopolymerization may dominate because monomer is not able to diffuse within the PP phase. Also, the liquids may prematurely react within the copolymer phase, which is known to decrease the grafting efficiency of PP. Immiscible mixtures always have multiple melt phases regardless of the intensity of mixing [10].

Melt flow index decreases with increasing screw rpm or residence time, which is confirmed by another author [72]. This may also be related to the grafting or crosslinking of the PE phase, while also reducing the degradation of PP. MFI continually decreases with increasing screw speed because of better dispersion of elastomer and therefore greater surface area to bond the phases at the interface. There is an increasing rate of plastification and a low residence time, so PP degradation is limited.

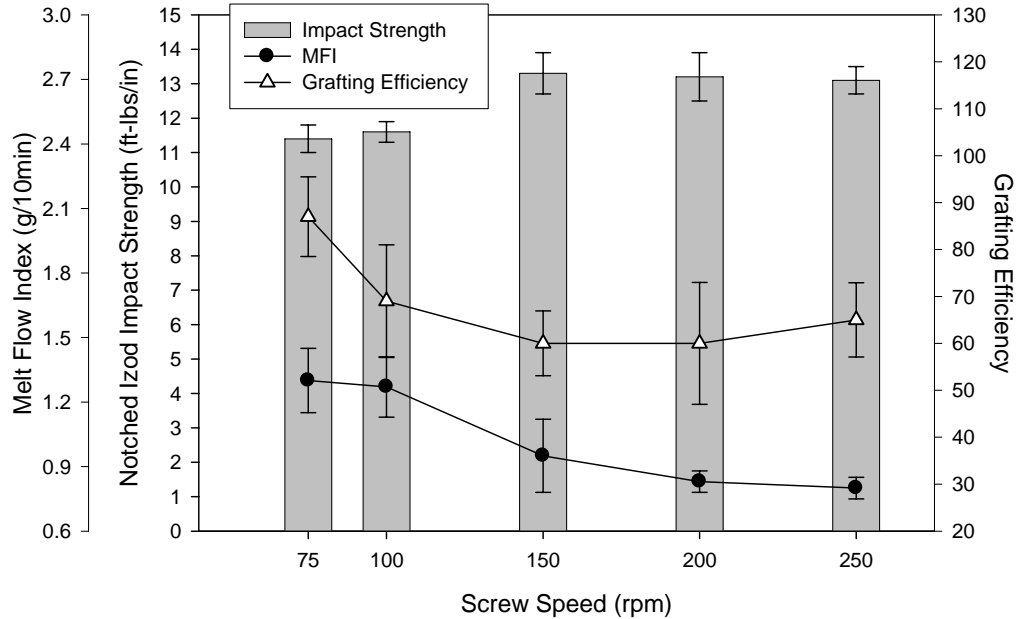


Figure 5-3: Impact strength, MFI, and grafting efficiency of 80:20_C as a function of screw speed.

Longer residence times lead to larger dimensions of the dispersed phase [411], which may have a negative effect of impact strength, as shown in Figure 5-3. Increasing shear rate enhances reaction rate but levels off after a certain screw speed [71], and 150 rpm appears to be the critical point where both impact strength and grafting efficiency level off. At higher screw speeds, particles collide less [74, 148, 245], leading to a higher impact strength. But the slight decrease in impact strength and increase in grafting efficiency at 250 rpm may be due to the fact that polymer melts are shear thinning. So with increasing shear rate, the matrix viscosity can decrease sharply leading to increasing particle size [32]. Impact strength increases with screw speed but plateaus at high screw speeds along with elongation at break and elastic modulus [148].

From stress strain data in Table 5-6, the optimal screw speed appears to be at 150 rpm. At low screw speeds, degradation of PP is present which means the high molecular weight, crystallizable chains are affected. So, the breakup of lamellar crystals is easier

but the recrystallization and alignment of chains is severely restricted. Cha and White also found that elongation at break increases with increasing screw speed [147]. Elastic modulus increases with increases with screw speed but tails off similar to the behavior of impact strength at the highest speed. This may be due to coalescence of the low viscosity elastomer phase.

Table 5-6: Stress-strain behavior of 80:20 C as a function of screw speed.

Screw Speed (rpm)	Modulus (MPa)	σ_{Yield} (MPa)	Elongation at Break (mm)	σ_{Break} (MPa)	Energy to Break (N*mm)
75	1309 ± 52	22.3 ± 0.7	30.5 ± 13	26.2 ± 3	1708 ± 822
100	1320 ± 60	24.3 ± 1.7	35 ± 14	28.5 ± 2.1	1981 ± 999
150	1356 ± 110	25.3 ± 2	56 ± 10	35.9 ± 4.6	3488 ± 1208
200	1310 ± 80	24.2 ± 1.1	50 ± 10	33.9 ± 1.8	3292 ± 1123
250	1234 ± 58	24.5 ± 0.3	46 ± 4	33.2 ± 1.9	3089 ± 658

5.3.3 Effect of Initiator Concentration

A basic concept of free radical grafting is that a peroxide initiator must be present so as to abstract hydrogen atoms from the polyolefin to start the grafting process. But side reactions like β -chain scission (PP) and crosslinking (PE and PE copolymers) take effect with excess peroxide. Figure 5-4 shows that grafting efficiency increases continuously as initiator concentration increased. By adding more peroxide, the number of primary free radicals increases, thus improving the probability for hydrogen abstraction from the PP or 8407 backbone. Grafting degree has been shown to increase with initiator level for a variety of polyolefins, including LLDPE [95, 196], HDPE [7, 249], EPR [412], and PP [40, 94, 138, 205]. Monomer conversion also increases [7, 92]. Although the grafting efficiency does increase, the monomers grafted may actually bond to chains that have already undergone chain scission.

Melt flow index continually increases with increasing peroxide concentration. This indicates that the PP phase is preferentially degraded (as opposed to 8407 crosslinking).

This same result has also been found by a variety of authors [7, 40, 73, 228]. Initiator concentration and its efficiency were the most important variable affecting MW, MWD,

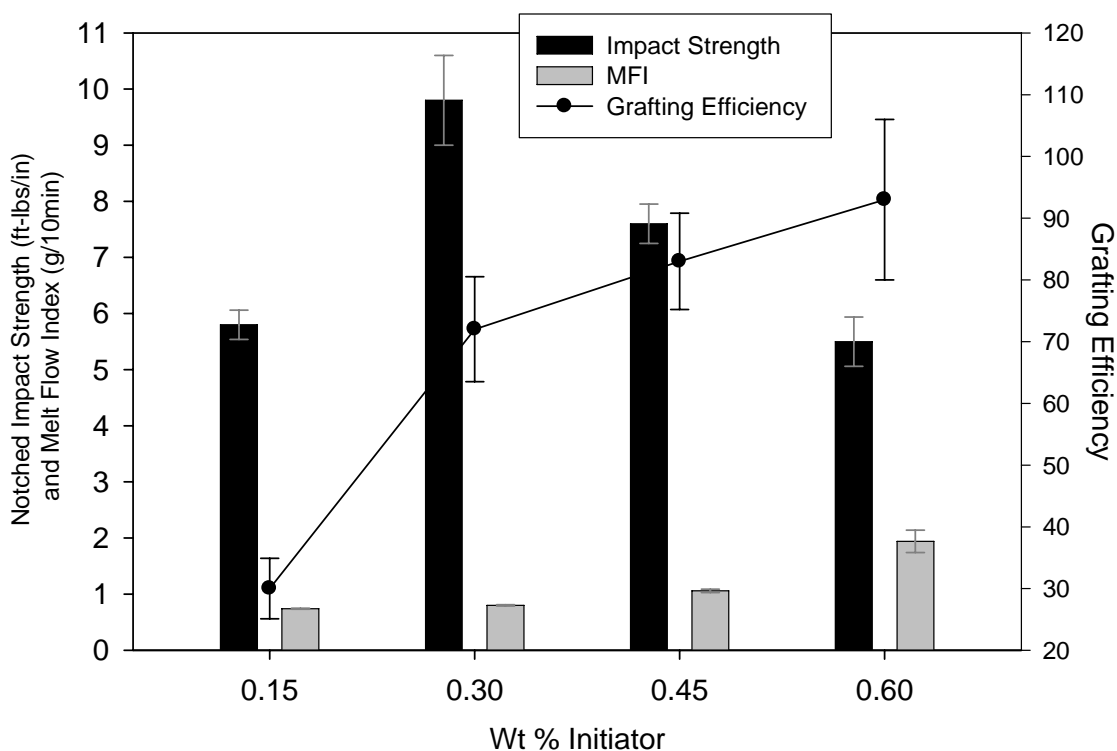


Figure 5-4: Impact strength, MFI, and grafting efficiency of 90:10_B as a function of initiator concentration.

and the rheological properties of the product [4]. An increase in peroxide efficiency decreases all MW averages, with M_z most sensitive [70, 73, 148].

Izod impact strength increases from 0.15% to 0.3% initiator, but decreases in a linear fashion at increasing concentrations. This could be a direct result of the degradation of the PP chains [7, 73, 148, 233]. Also, the PE phase may be crosslinking to a greater extent, so its mobility and energy absorption capabilities are diminished. There is a drastic increase in grafting efficiency at 0.3% initiator and a peak in impact strength, which are likely interrelated. This must be the point in which grafting and

homopolymerization are balanced to give the highest grafting efficiency with the lowest amount of degradation.

Tensile properties, such as yield stress, elastic modulus, elongation at break, stress at break, and energy to break, are given in Table 5-7. Similar to impact strength, elastic modulus and break stress reach a peak at 0.3% peroxide and decrease at higher concentrations. Yield stress remains about the same for all samples, although the lowest initiator concentration has the lowest yield stress [341]. Elongation, degree of strain hardening, and energy to break decrease continuously with increasing peroxide, concurrent with other results [148, 184, 186, 220, 233, 413]. In one case, elongation at break and hence energy to break was not found to be reproducible [222].

Table 5-7: Stress-strain behavior of PP:8407 alloys at a ratio of 90:10 as a function of initiator concentration.

wt% Initiator	Modulus (MPa)	σ_{Yield} (MPa)	Elongation at Break (mm)	σ_{Break} (MPa)	Energy to Break (N*mm)
0.15	1502 ± 74	30.5 ± 1.7	60 ± 8	40.6 ± 3.3	5164 ± 1091
0.3	1695 ± 110	30.9 ± 1.5	60 ± 4	42.6 ± 1.5	4294 ± 155
0.45	1657 ± 44	30.9 ± 0.6	54 ± 8	39.3 ± 3	4002 ± 898
0.6	1617 ± 103	31 ± 1.8	35 ± 11	29 ± 3.4	1944 ± 892

The reason for the low stress-strain properties at high initiator concentrations could be due to the fact that the % crystallinity is known to decrease [148, 220, 233, 341] as well as melting temperature [222, 233]. Also, the onset of melting of a PP/LLDPE/peroxide alloy decreases by 9°C with 0.25% peroxide [222]. So, the size and distribution of the lamellar crystals are affected.

5.3.4 Effect of Multifunctional Monomer Concentration

The multifunctional monomer serves several purposes in this reactive extrusion process and is an integral part in improving mechanical properties. Figure 5-5 reveals that melt flow index, as expected, decreases with increasing DEGDA content. This

multifunctional monomer has four effective branching sites, which act to reduce degradation by linking up degraded PP chains, enhance crosslinking of the 8407 phase, and consume free radicals. Previous grafting studies show that MFI decreases and viscosity increases with increasing monomer concentration, attributed to reduced chain

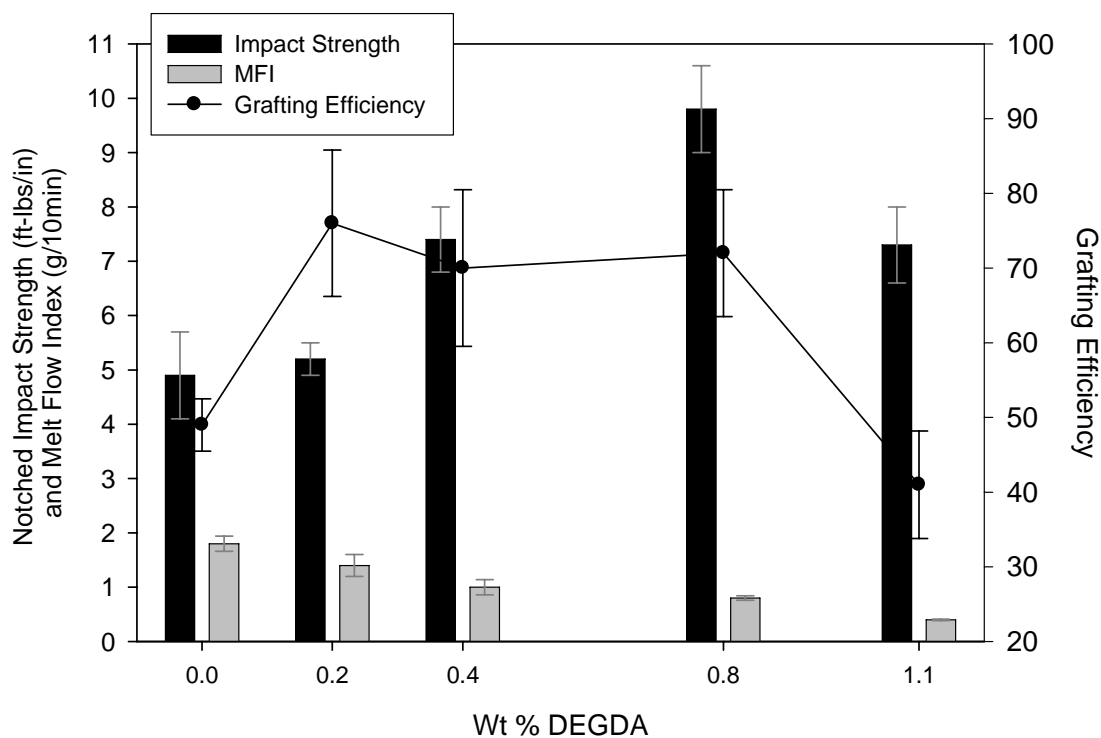


Figure 5-5: Notched impact strength, melt flow index, and grafting efficiency of PP:8407 alloys at a ratio of 90:10 as a function of multifunctional monomer concentration.

degradation [40, 92, 228]. Molecular weight increases with increasing monomer concentration as well as broadening of molecular weight distribution and increase in the high MW tail [250]. High monomer concentrations reduce the melt strength of the alloy [215] and could have implications on elongation at break.

Impact strength increases concurrently up to a point (0.8 wt%) then dramatically decreases at the highest concentration, where homopolymerization begins to dominate over grafting. Both homopolymer and grafted monomer positively affect impact strength

[148]. A monomer coagent is known to improve impact strength for PP-LLDPE alloys [230, 250]. At the highest DEGDA concentration, a more densely branched material is present along with the possibility of phase separated homopolymer. Impact strength is reduced because the ability to absorb and dissipate stress is low and there may be weak interfaces with reduce stress transfer capability. A high degree of crosslinks respond in a brittle manner to high deformation rate tests. At high concentration, homopolymer or copolymer can phase separate [68], which deleteriously affects all mechanical properties.

Grafting efficiency also drops at the same point as impact strength. Increasing monomer concentration increases amount of material grafted but grafting efficiency levels off and in some cases decreases at high monomer concentrations [7, 40, 92, 94, 95, 180, 187, 190, 205, 228]. This indicates that DEGDA is trapping radicals and creating a high degree of branched homopolymer material. Although styrene is still grafting onto the polymer phases, DEGDA is causing styrene to preferentially copolymerize over grafting. Addition of only 0.2 wt% DEGDA shows the greatest styrene grafting efficiency, which means that at higher concentrations, the materials being grafted may not necessarily be as single monomer units or chains but as branched macromolecules. At 0% DEGDA, grafting is low because the rate of reaction is slower and chain scission more likely [153, 161]. Also, styrene would prefer to add more monomer than chain transfer to PP or PS [162a].

Table 5-8 shows that the stress-strain properties increase up to 0.8 wt% DEGDA, then decrease just as impact strength and grafting efficiency decrease. Typically, elastic modulus and yield strength increase with increasing monomer concentration [184, 222, 230, 250]. Elongation at break does slightly increase with increasing monomer

concentration, a trend also shown in literature [7, 259]. The crosslinked sample gave the lowest energy to break and elongation at break, but a lower modulus than the 0.8 wt% DEGDA sample. The low strain portion of a stress strain curve is dependent upon the amorphous nature of the material, tie molecules, short range defects, etc. With the possibility of a gel present in the vicinity of crystalline phase and

Table 5-8: Stress-strain behavior of PP:8407 alloys at a ratio of 90:10 as a function of multifunctional monomer concentration.

wt% DEGDA	Modulus (MPa)	σ_{Yield} (MPa)	Elongation at Break (mm)	σ_{Break} (MPa)	Energy to Break (N*mm)
0	1501 ± 74	28.3 ± 0.9	57 ± 4	37 ± 1.1	4205 ± 736
0.2	1458 ± 59	29.6 ± 1.7	56 ± 6	38.3 ± 3.9	4192 ± 649
0.4	1526 ± 14	29.3 ± 0.9	55 ± 11	38.5 ± 3	3961 ± 1300
0.8	1695 ± 110	30.9 ± 1.5	60 ± 4	42.6 ± 1.5	4294 ± 155
1.2	1572 ± 52	29.6 ± 1	39 ± 8	34.1 ± 3.7	3064 ± 1200

glassy tie molecules, there may be phase separated, long-chained branched or crosslinked material that prevents tie molecules from becoming taut upon application of stress. Also, there may be a reduction in % crystallinity at such high monomer concentrations [7, 148, 184, 215]. The melting transition is seen to broaden for PP due to degradation [148] or creation of larger molecules [215].

5.3.5 Effect of Styrene Concentration with DEGDA as Multifunctional Monomer

Styrene monomer has proven to be an integral part in the toughness improvement of these alloys. Figure 5-6 shows the effect of styrene on the room temperature impact strength, grafting efficiency, and MFI of alloys with a PP:8407 ratio of 90:10. For impact strength at various styrene concentrations, a peak is found at 6% styrene, an intermediate concentration. As in the previous section, a combination of homopolymer and graft copolymer will improve impact strength [148, 230, 250]. But with more monomer, longer grafts may be possible and the formation of large glassy polystyrene domains may phase separate and decrease impact strength.

MFI decreases with increasing monomer concentration, presumably because the probability that a PP macroradical will react with styrene monomer is enhanced. One author believes that crosslinking of PP during free radical grafting of styrene occurs by termination through combination of two PP-styrene radicals [95]. With more monomer, a greater concentration of highly entangled chains is more likely.

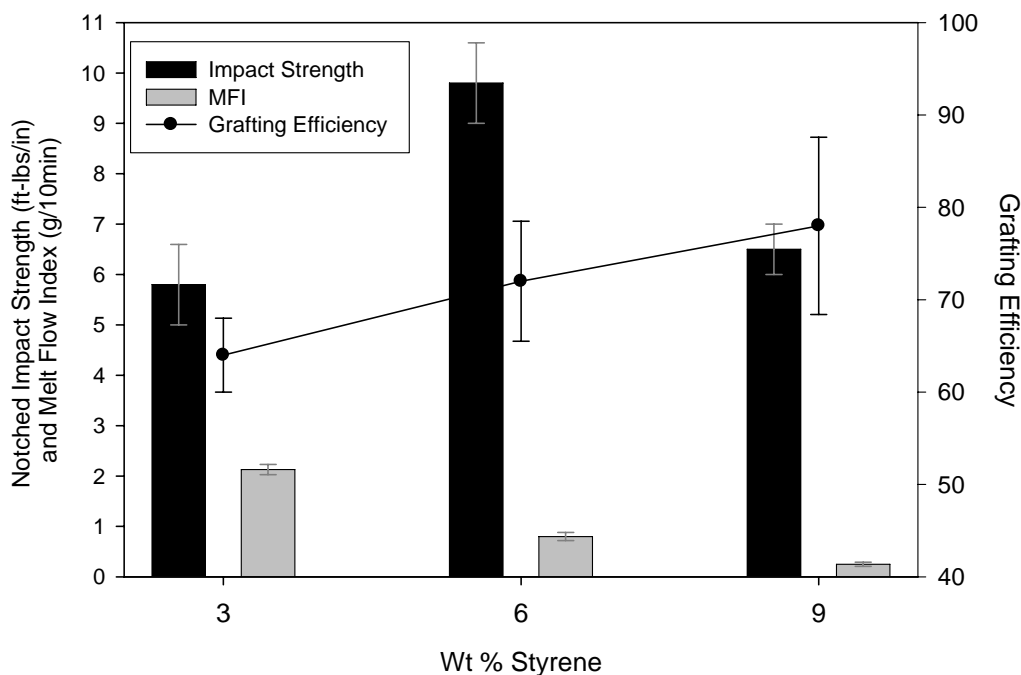


Figure 5-6: Notched impact strength, melt flow index, and grafting efficiency of PP:8407 alloys at a ratio of 90:10 as a function of styrene monomer concentration

The grafting efficiency increases with increasing styrene content, which is to be expected because as hydrogen atoms are being abstracted from the polymer backbones, the larger amount of styrene available leads to greater probability of styrene grafting onto the polymer rather than chain scission or crosslinking. Also, longer grafts may also be present at this high styrene concentration.

The stress-strain performance of the materials as a function of styrene concentration is given in Table 5-9. At low styrene content, break stress and energy to break are significantly less than high concentration samples. This may be due to the

degradation of PP and disruption of crystalline phases. For a high strain rate test like Izod impact, the material acts in a brittle manner, but for low strain rates, the polymer chains are given time to disentangle and stretch. For this reason, the stress-strain properties are better for the highest monomer concentration over the lowest.

Table 5-9: Stress-strain performance of PP:8407 alloys at a ratio of 90:10 as a function of styrene concentration.

wt% Styrene	Modulus (MPa)	σ_{Yield} (MPa)	Elongation at Break (mm)	σ_{Break} (MPa)	Energy to Break (N*mm)
3	1612 ± 83	29.8 ± 1.1	50 ± 13	37 ± 4.7	3339 ± 1103
6	1695 ± 110	30.9 ± 1.5	60 ± 4	42.6 ± 1.5	4294 ± 155
9	1613 ± 37	29.6 ± 1.4	57 ± 10	41.8 ± 4.6	4955 ± 1071

5.3.6 Effect of Styrene Concentration with TMPTA as Multifunctional Monomer

In another study at higher ENGAGE content (80:20 ratio of PP:8407 vs. 90:10 in the previous section) and using TMPTA rather than DEGDA as the multifunctional monomer, similar trends are observed at increasing styrene concentration. The data in Figure 5-7 shows that Impact strength and grafting efficiency follow similar paths. At low styrene contents, degradation of the polymer chains dominate because the ratio of initiator-derived free radicals to monomer is great. Addition of only 2 wt% styrene to the system results in a 10-fold decrease in MFI and a 4-fold increase in impact strength. This is due to the ability of styrene to both act as a vector fluid and locate the peroxide at the interface but also to polymerize and graft onto the polyolefin backbones.

At the highest concentration of styrene (10 wt%), grafting efficiency falls off most likely due to homopolymerization. For higher 8407 concentrations, there is less PP for styrene to graft onto, which may be the reason why GE drops off in Figure 5-7 and not in Figure 5-6. Hu et al. gives a very good explanation as to why there would be a difference in grafting yield [205]. In PP, each polypropylene moiety contains one tertiary hydrogen

atom, two secondary hydrogen atoms, and three primary hydrogen atoms, with concentrations of 0.238, 0.475, and 0.713 mpr (moles per hundred grams of resin),

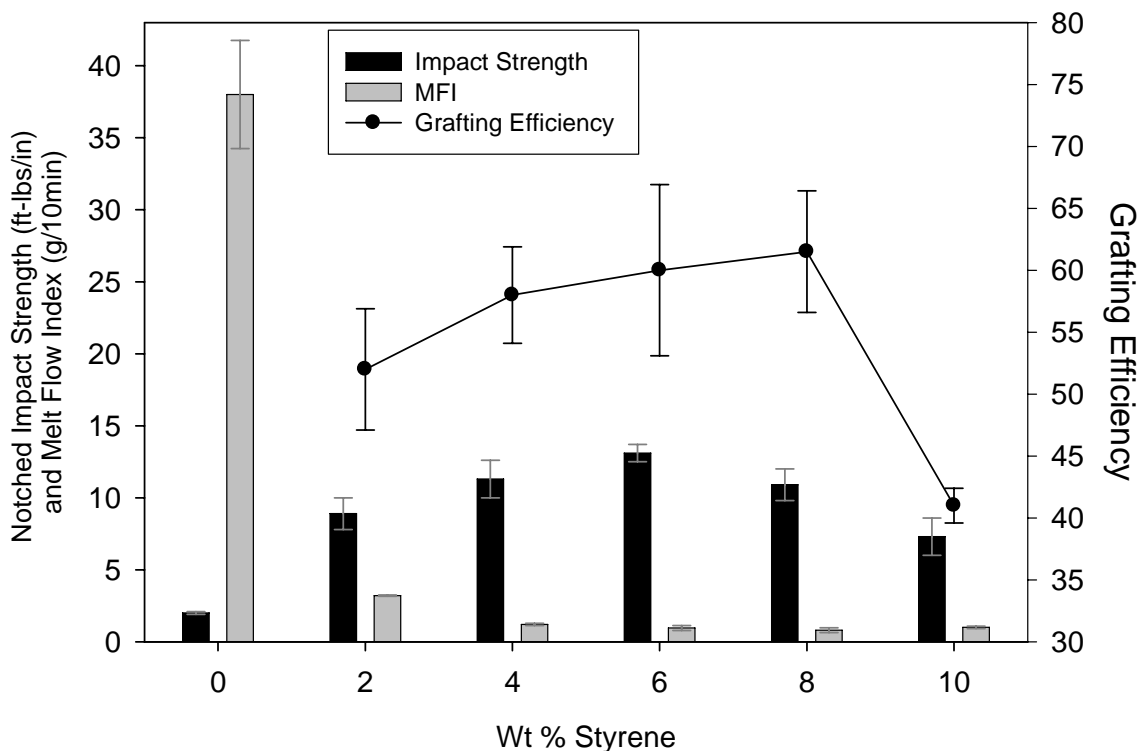


Figure 5-7: Notched impact strength, melt flow index, and grafting efficiency of PP:8407 alloys at a ratio of 80:20 as a function of styrene concentration.

respectively. This means that if a monomer (molar mass = 196 g/mol) has a grafting yield of 10 phr (0.0497 mpr) it represents only one-fifth of the molar number of the tertiary hydrogen atoms. Because the number of consumed tertiary hydrogen atoms is small, every additional amount of the grafting solution leads to a proportional increase in the monomer's grafting yield as seen in Figure 5-6. Addition of 8407 (or a reduction in polypropylene tertiary hydrogen atoms) will limit the available sites for grafting and thus promote homopolymerization while reducing grafting efficiency.

5.4 Conclusions

This chapter elaborates on the idea that when creating and developing materials with complex architectures and many components, processing can play an important role in defining its macroscopic properties. A high screw speed has been shown to give the best mechanical properties, which is related to better mixing and grafting within the alloys. If the barrel temperature of the extruder is too low, polypropylene will degrade preferentially, but if too high, homopolymerization rather than grafting of monomers will dominate. There is an optimum styrene, initiator, and multifunctional monomer concentration for these alloys, but these results reveal that a high grafting efficiency does not necessarily translate into great mechanical properties. Reactive extrusion of PP and 8407 involves degradation and crosslinking reactions, which if not restricted, diminish the mechanical integrity of the alloy. So, a high grafting efficiency may come at the price of a largely degraded PP phase.

CHAPTER 6
CONTROLLING ALLOY PERFORMANCE BY VARYING ELASTOMER
PROPERTIES

6.1 Introduction

Very few studies have been conducted on elastomer toughened polypropylene blends with varying elastomer crystallinity or molecular weight. Regarding reactive blends of PP-elastomer blends, there have been no systematic studies that focus on alloy performance as a function of elastomer molecular weight or crystallinity. A comparative study of several alloys with varying grades of ENGAGE® polyolefin elastomers was done in order to assess the robustness and further explain the fundamentals of the reactive extrusion process introduced in Chapter 4. The elastomers were categorized according to their density (% crystallinity) and melt flow index (viscosity or molecular weight). At approximately the same density, low crystallinity elastomers with varying molecular weight are focused on. A high molecular weight translates into more entanglements, higher viscosity, and difficulty dispersing, which all should have some effect on the properties of the alloys. The low molecular weight (high MFI) elastomers were chosen because they are easily dispersed in the highly viscous PP matrix and should not compromise processability.

6.2 Experimental

6.2.1 Materials

Table 6-1 gives a list of pertinent ethylene-1-octene copolymers produced by Dupont Dow elastomers under the trade name ENGAGE®, but the EOC grade of interest

is 8407 [48]. Isotactic polypropylene homopolymer was supplied by Equistar Chemical (grade PP 31S07A) and is contact translucent. All polymers were received in pellet form.

Table 6-1: ENGAGE® product data table.

Engage® Grade (decreasing comonomer content)	8842	8407	8200	8401	8402
Comonomer Content wt% ¹³ C NMR/FTIR	45	40	38	31	22
Density, g/cm ³ ASTM D-792	0.857	0.870	0.87	0.885	0.902
Melt Index, dg/min ASTM D-1238 190°C, 2.16 kg	1.0	30	5.0	30	30
Mooney Viscosity ASTM D-1646 ML 1 + 4 at 121°C	26	< 5	8	< 5	< 5
Durometer Hardness, Shore A ASTM D-2240	50	72	75	85	94
DSC melting Peak, °C Rate: 10°C/min	33	60	60	78	98
Glass Transition Temp, °C DSC inflection point	-61	-57	-56	-51	-44
Flexural Modulus, MPA ASTM D-790, 2% Secant	3.5	12.1	12.1	25.8	69.9
Ultimate Tensile Strength, MPa ASTM D-638, 508 mm/min	2.1	3.3	6.9	6.4	12.9
Ultimate Elongation, % ASTM D-638, 508 mm/min	975	>1000	>1000	950	790

The peroxide and monomers used in this study were reagent grade chemicals (structures are shown in Table 6-2). The monomers were purified by passing through an activated alumina column before use. Styrene monomer, inhibited by 10-15 ppm t-butyl catechol, was purchased from Fisher. The initiator, 2,5dimethyl-2,5-di-(t-butylperoxy) hexane, was purchased from Atofina under the trade name Lupersol 101. Diethyleneglycol diacrylate (DEGDA), inhibited by 80 ppm Hq and 120 ppm MEHQ was graciously donated by Sartomer, an Atofina company. Table 4-3 lists structures of the reactive materials.

Table 6-2: Structures of reactive materials of interest

Name	Lupersol 101	TMPTA
Structure	$ \begin{array}{c} \text{CH}_3 \qquad \text{CH}_3 \\ \qquad \quad \\ (\text{CH}_3)_3\text{C}-\text{O}-\text{O}-\text{C}-\text{CH}_2-\text{CH}_2-\text{C}-\text{O}-\text{O}-\text{C}(\text{CH}_3)_3 \\ \qquad \quad \\ \text{CH}_3 \qquad \text{CH}_3 \end{array} $	$ \begin{array}{c} \text{O} \\ \\ \text{O}-\text{C}-\text{CH}=\text{CH}_2 \\ \\ \text{CH}_2 \\ \\ \text{CH}_2-\text{CH}_2-\text{CH}_3 \\ \\ \text{O}-\text{C}-\text{CH}=\text{CH}_2 \\ \\ \text{O} \end{array} $
Name	Styrene	DEGDA
Structure		$ \begin{array}{c} \text{O} \qquad \qquad \qquad \text{O} \\ \qquad \qquad \qquad \\ \text{CH}_2=\text{C}-\text{C}-\text{O}-\text{CH}_2-\text{CH}_2-\text{O}-\text{CH}_2-\text{CH}_2-\text{O}-\text{C}-\text{C}=\text{CH}_2 \\ \qquad \qquad \qquad \\ \text{H} \qquad \qquad \qquad \text{H} \end{array} $

6.2.2 Methods

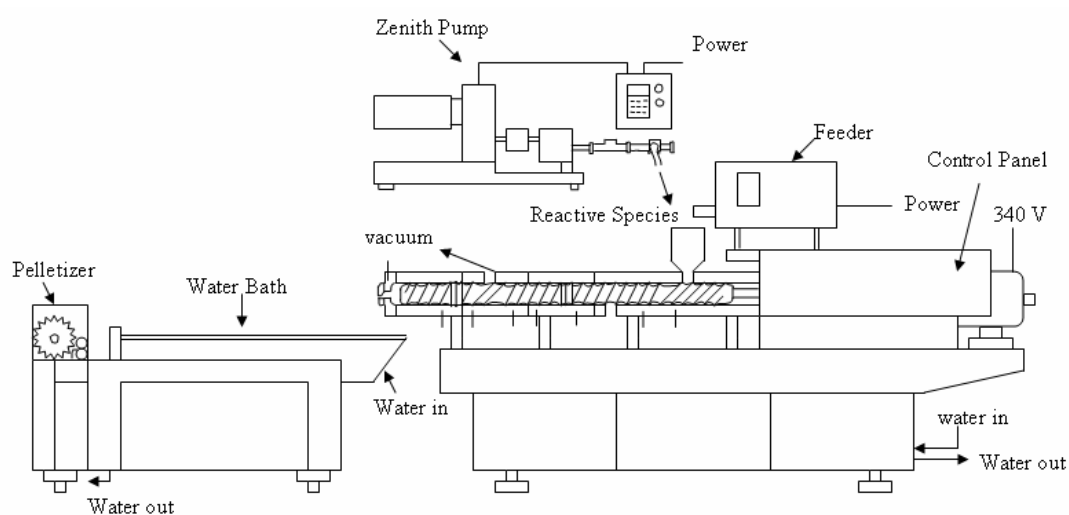
6.2.2.1 Processing

All polymers were dried in an air circulating oven at 40°C for 24 hours prior to compounding. Before processing, the resins were premixed by hand for about 10 minutes. Monomer/initiator mixtures were magnetically stirred for 10 minutes before processing and a choice amount of the mixture was added to the dry polymer pellets before processing.

The blending was carried out in a 34 mm non-intermeshing, co-rotating twin screw extruder, APV Chemical Machinery (now B&P Process Systems) with an L/D ratio of 39. The temperature of the extruder was regulated by electrical resistance and water circulation in the barrels. The dried, pre-mixed resins were then introduced into the extruder at 60 g/min through a screw dry material feeder, Accu Rate, Inc. A Zenith pump controlled the rate of monomer/initiator solution addition into the extruder. The screw speed, unless otherwise noted was 150 rpm. Devolatilization was carried out by a vacuum pump, VPS-10A, Brooks Equipment Company. This was placed near the die and created a pressure of about 15 in Hg. The extruder was always starved to feed.

Figure 6-1 is a schematic of the extruder, with a typical temperature profile. After compounding, the resulting strands which exit the die are quenched in a water bath, pelletized, and dried in a vacuum oven at 100°C and 28 in Hg for 24 hours.

Supercritical CO₂-assisted processing was carried out in the twin screw extruder with an Isco 260D syringe pump connected at zone 5. Industrial grade carbon dioxide was supplied by Praxair.



Die	Zone 1	Zone 2	Zone 3	Zone 4	Zone 5	Zone 6	Zone 7 (Feed)
195°C	205°C	210°C	210°C	200°C	190°C	180°C	165°C

Figure 6-1: Schematic drawing of the reactive twin screw extruder and a common temperature profile.

6.2.2.2 Mechanical properties

In order to measure the strength of the material at very high testing rates, a notched Izod impact test was performed according to ASTM D256 standards. The pellets were placed in a mold with 6 slots, each measuring 0.5x0.5x2.5in³. The mold was put in a Carver press (Fred S. Carver, Inc.) at 200°C and after the material melts, pressed up to 5000 psi. After the material melts, the pressure was slowly increased up to 10,000 psi. After another 5 minutes, the heat is turned off and the sample is let to cool down to room temperature at about 1.5°C/min. The bars were then taken out and notched with a

Testing Machines, Inc. (TMI) notching machine. Before testing, they were conditioned at room temperature for 24 hours and a 30 ft-lb hammer was used with test method A on a TMI Izod impact tester. At least 5 bars were broken and impact strength is recorded as an average regardless of full or partial break.

A Kodak EasyShare CX7300 was used to take digital images of fractured impact bars.

For stress-strain measurements, dried pellets were placed in a mold measuring 15x15 cm²x1 mm thick. The mold is put into the Carver press at 200°C and pressed up to 5000 psi after the material melts. After a 5-10 minute wait, the sample was slowly pressed to 10,000 psi. Five minutes later, the sample was quenched in a water bath. Specimens were tested according to ASTM D638 standards. Type V specimens were punched out of the compression molded sheet with a die, measuring 1 mm thickness, 2.95 mm gauge width and 9.5 mm gauge length. Five samples were tested after conditioning at room temperature for 48 hours. The machine used to test the samples was an MTS Model 1120 Instron, using a 1000 lb load cell at a test speed of 12.7 mm/min

A Seiko DMS220 interfaced with a Seiko Rheostation model SDM/5600H was used to test dynamic mechanical specimens. Testing was conducted from -120 to 150°C at a heating rate of 5°C/min in dry nitrogen atmosphere maintained at an approximate flow rate of 100 mL min⁻¹. Rectangular samples (20x10x1mm³) were cut from the compression molded sheet and tested in bending mode at a frequency of 1Hz.

6.2.2.3 Chemical composition and molecular structure

Fourier Transform Infrared Spectroscopy (FTIR) was performed on a Nicolet 20SXB Spectrometer. 256 Scans were taken from 3500 to 500 cm⁻¹ wavenumbers with a resolution of 4. Measurements were done in transmission mode on thin films (~2-3

microns). Films were produced by melting the polymer in a Carver press at 180°C and 10,000 psi for 2 minutes then quenching in a water bath at room temperature. For quantification of the grafted styrene, a calibration curve had to be established as explained in Appendix A. Area under the 700cm⁻¹ and 1376cm⁻¹ peaks are compared and related to absolute styrene amounts to get the grafting efficiency (GE). This is defined by the following equation:

$$GE = \frac{\text{Amount of Monomer Grafted to Polymer Backbone}}{\text{Original Amount of Monomer Pumped into Extruder}} \times 100\% \quad (6.1)$$

All reactively extruded materials must be purified first before quantification using FTIR. This first involved dissolving the pellets of crude graft copolymer in hot xylene at a concentration of ca 4% (wt/vol). The hot solution was precipitated into ten volumes of acetone (a known non-solvent for the LLDPE, HDPE and PP, and a solvent for styrene monomer and homopolymer based on solubility parameters [162]). The unreacted monomers, styrene and DEGDA or TMPTA homopolymers and copolymers remained soluble in acetone and were separated out from the grafted polyolefins. The precipitated graft modified alloy was filtered, washed, and then vacuum dried at 70°C for 24 hours. FTIR showed that the GE level remained unaltered upon further rounds of purification. Therefore, one purification step was sufficient for removal of all the residual impurities.

Gel permeation chromatography (GPC) was performed on a Waters GPCV 2000 calibrated using crosslinked polystyrene standards for relative molecular weight determination. The set temperature was 40°C for THF as the solvent at a flowrate of 1.0 mL/min. Samples (about 9 mg) were dissolved in 9.5 ml (8.44 g) of HPLC grade THF purchased from Acros Organics and passed through 0.45 µm filters.

6.2.2.4 Thermal analysis and rheology

Differential scanning calorimetry (DSC) was used to study the different thermodynamic transitions present in the blends. DSC was performed on a Seiko SII DSC 220C-SSC/5200, Seiko Instruments, equipped with a Seiko Rheostation model SDM/5600H and calibrated with indium and tin standards. Samples (approx. 7 mg in weight) were sealed in crimped aluminum pans, with the reference being 99.99% pure alumina. Purging of the sample was done with dry nitrogen at a flow rate of 100 ml/min. Each sample experienced two heating and cooling cycles (shown in Table 6-3) with the first to erase prior thermal history. The second cycle is reported in all graphs.

Table 6-3: DSC consecutive heating/cooling cycles

Step	Start Temp (°C)	End Temp (°C)	Heating/Cooling Rate (°C/min)	Hold Time (min)	Sampling (s)
1	-70	200	20	3	3
2	200	-80	20	5	3
3	-80	200	10	5	1
4	200	-80	10	3	1

Melt Flow Index (MFI) testing was done according to ASTM D1238 (230°C and 2.16 kg weight) on a Tinius Olsen model MP 933 Extrusion Plastometer. For materials with an flow rate of 0.5-3.5 g/10 min, the weight of the sample was approx. 3 g, whereas materials with flow rates of 3.5-300 g/10 min, the sample weight was approx. 6 g. All materials were dried under vacuum then conditioned at room temperature before testing.

6.3 Results and Discussion

6.3.1 Effect of Elastomer Density on Alloy Performance

Three different ethylene-octene copolymers (8407, 8401, and 8402) are ranked according to their % crystallinity. All other material properties and processing parameters are held constant unless otherwise noted. Also, the ratio of PP to EOC was kept constant at 90:10. Table 6-4 and Figure 6-2 give a key code and designated

formulations to ease in the identification of each sample. The first number given is the grade of EOC, the second number/letter signifies a formulation which can be referenced in Table 6-4.

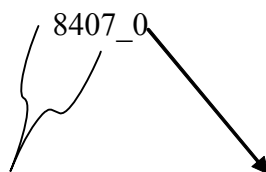


Figure 6-2: Representation of sample reference code

The weight % is defined as the percentage of material added in relation to the total weight of all ingredients. For example, a PP:8407 ratio of 90:10, 0.3 wt% Initiator and 6 wt% styrene means that out of a total of 100 grams, Initiator = 0.3 g, Styrene = 6 g, PP = 84.3 g, 8407 = 9.4 g.

Table 6-4: Identification of Formulations in relation to Figure 6-2

Alloy ID	wt% Initiator	wt% Styrene	wt% DEGDA
0 (Physical Blend)	0	0	0
A	0.3	6	0
B	0.3	6	0.8
C	0.15	3	0.8

6.3.1.1 Physical blends

From Figure 6-3, blend impact strength scales linearly with both copolymer density and copolymer melting temperature, both of which are interrelated. Melting temperature of the copolymers is known to be inversely proportional to comonomer content [51]. The highly crystalline elastomer behaves in a brittle manner at high impact because the crystalline domains are not able to absorb and dissipate energy efficiently. Low temperature transitions cease to exist for these blends because chain mobility is hindered and the number of copolymer side groups is diminished. Low temperature transitions/relaxations contribute to energy dissipation at high impact [100, 105, 107], so

it is no surprise that impact strength decreases with decreasing number of octene units in the copolymer backbone. A direct indication that a polymer absorbs energy upon impact is through stress whitening. The whiter the impact bar, the greater amount of cavitation and dilation, and hence the greater impact strength [103, 328]. From Figure 6-6, the blend with the highly crystalline elastomer, 8402_0, completely breaks and shows only a slight amount of stress whitening at the surface of the broken bars. As the amorphous

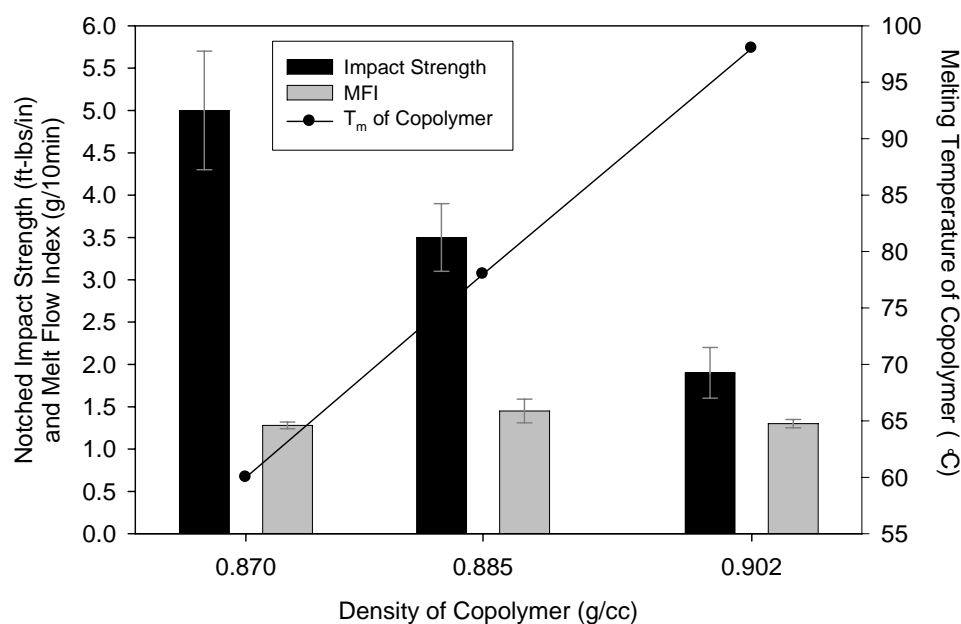


Figure 6-3: Impact strength, melt flow index, and melting temperature of physical blends as a function of the density of the copolymer.

content of the elastomer increases, the impact strength and degree of stress whitening follow suit. This is a visual confirmation that elastomer density can have a profound effect on blend performance and morphology, even at 10 wt% elastomer. The melt flow index remains approximately the same for all blends and this is to be expected because the elastomers each have the same melt flow index as reported by the manufacturer.

Stress-strain behavior of ethylene-octene copolymers links crystallinity to stress response [51, 52, 57, 59, 414]. The uniform elastomeric response of these copolymers is

accounted for by a physical network built on fringed micellar crystal junctions and perhaps entanglements. Because the small fringed micellar crystals are within their broad melting range at ambient temperature, they melt and reform during deformation.

By physically blending the polymers, there should be an additive relationship between the mechanical performance and density of the elastomer [262, 274, 275]. Stress strain behavior is shown in Figure 6-4 and tabulated in Table 6-5. Elastic modulus and



Figure 6-4: Digital images of room temperature fractured Izod impact bars as a function of elastomer density in the physical blends. From left to right: 8407_0, 8401_0, 8402_0.

yield stress are highest for the high density blend (8402_0), whereas elongation at break is lowest for the low crystalline elastomer blend (8407_0). This is to be expected because the elastomer phase, which resides primarily in the interspherulitic regions of PP, will experience the applied load before the crystalline phase will. A higher elastomer

Table 6-5: Stress-strain data of 8407_0, 8401_0, and 8402_0.

Effect of Copolymer Density					
Blend ID	Modulus (MPa)	σ_{Yield} (MPa)	Elongation at Break (mm)	σ_{Break} (MPa)	Energy to Break (N*mm)
8407_0	1450 ± 59	28 ± 1.6	58 ± 12	38.7 ± 4.8	4038 ± 825
8401_0	1459 ± 40	29.6 ± 1.1	68 ± 10	42 ± 4.4	5983 ± 1059
8402_0	1596 ± 89	29.8 ± 1.4	64 ± 5	39.2 ± 3	4978 ± 474

crystallinity leads to a quicker, stiffer response to the applied load, with crystals acting like filler particles. Yield stress is lowest for 8407_0 likely due to its diffuse, fringed micelle crystalline structure which has limited load bearing capability [52, 59]. The intermediate density copolymer blend, 8401_0, exhibits the highest elongation at break, energy to break, and stress at break, which may be due to greater interfacial interaction with PP or optimal combination of chain mobility and lamellar crystal distribution.

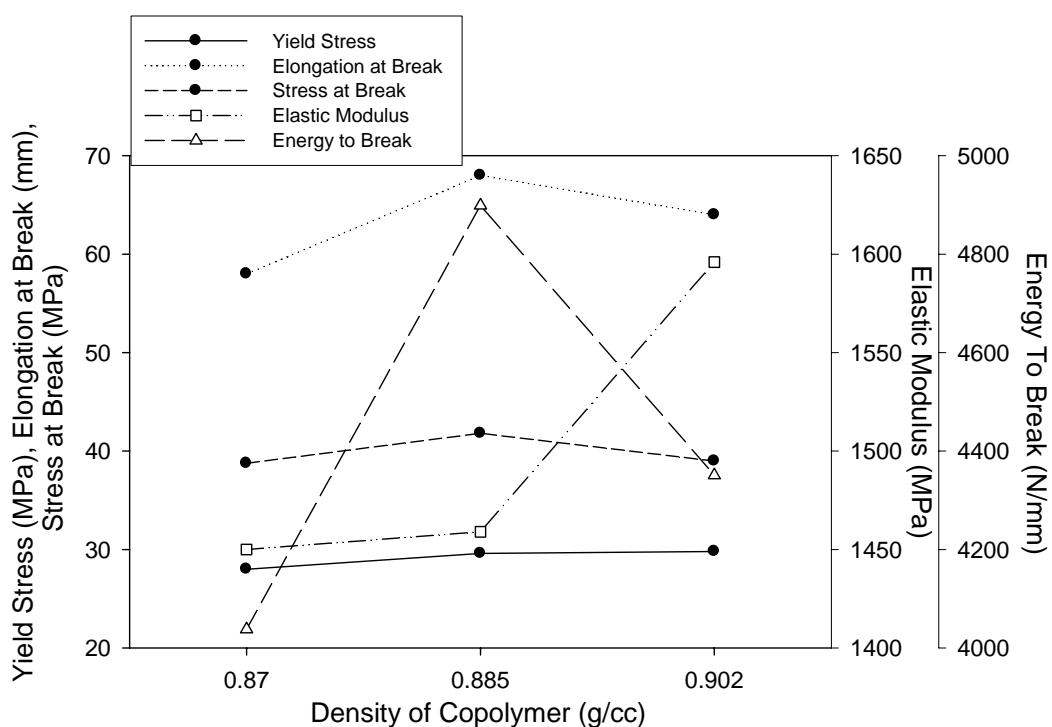


Figure 6-5: Stress-strain performance of PP/elastomer physical blends as a function of elastomer density.

Because so many physical properties of the blend are dependent upon the crystallinity of the PP, DSC experiments were performed. From Figure 6-6, the general shape of each PP melting peak does not change with elastomer density (i.e. onset temperatures are approximately the same from Table 6-6). There are two distinct differences between the samples, though. Firstly, the peak at approximately 95°C in 8402_0 can be attributed to the melting of PE crystals [48, 49, 51, 58]. This peak

decreases in temperature and area as the density (% crystallinity) of the elastomer decreases. Secondly, a small dip at about 150°C is seen for each sample but decreases in intensity with decreasing elastomer crystallinity. This melting peak is likely associated with the β phase of PP. This crystal phase is known to be nucleated by many routes, including addition of elastomers [267, 325, 333, 339, 363, 383-385]. One reason for its creation is the disturbance of crystallization of PP into the α form. So, 8402 appears to have the greatest effect on the crystallization process of PP, but this will be confirmed in Figure 6-7 and Table 6-7.

Table 6-6: DSC endothermic data of 8407_0, 8401_0, and 8402_0

Sample ID	PP α phase melting peak temperature (°C)	T _m Onset (°C)	Melting Enthalpy (J/g)	% Crystallinity
8407_0	165.2	152.9	82.3	39.8
8401_0	164.7	153.0	78.9	38.1
8402_0	164.9	152.6	75.1	36.3

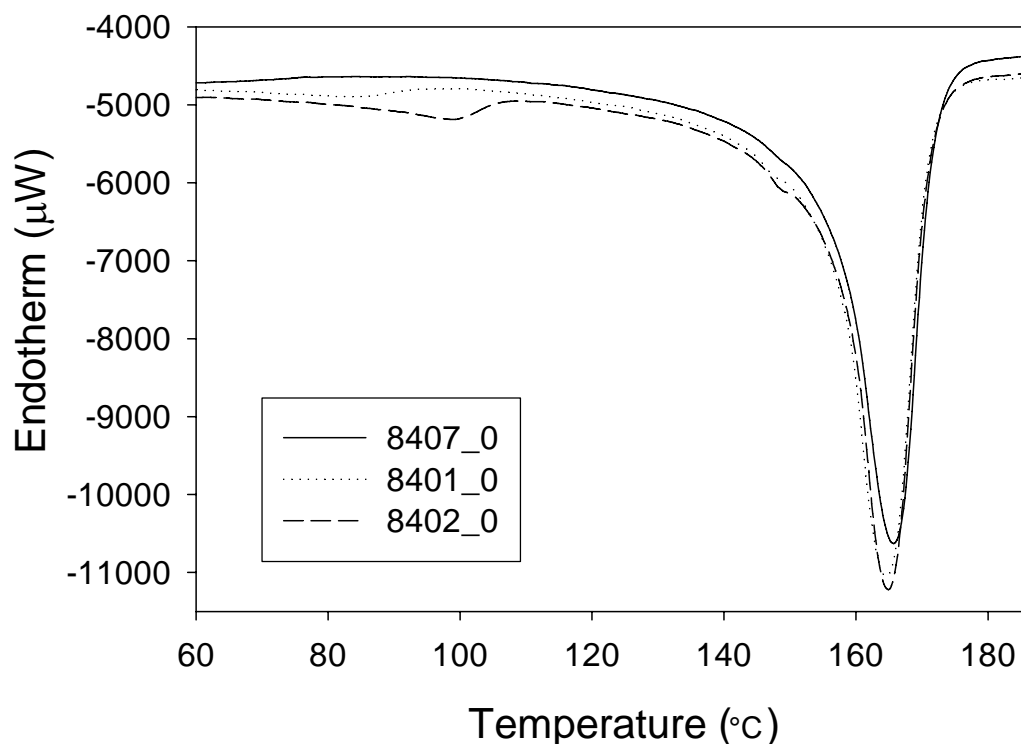


Figure 6-6: DSC melting endotherm of 8407_0, 8401_0, and 8402_0.

The % crystallinity noticeably decreases with increasing elastomer density. This may be attributed to the idea that lamellar crystals in 8401 and 8402 inhibit the secondary crystallization of PP. Secondary crystallization is defined as further crystallization behind the crystallization front (i.e. within the spherulite) [362]. The peak temperature of these alloys is highest for 8407_0, which may be due to the secondary crystallization process of PP being less restricted by the highly amorphous 8407.

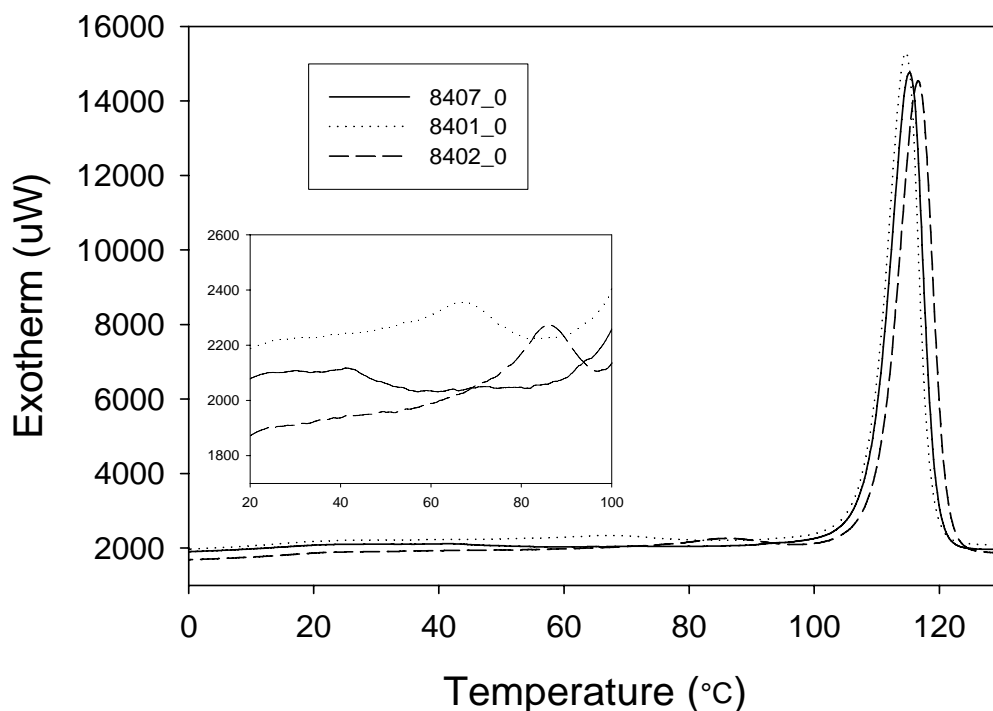


Figure 6-7: DSC cooling exotherm of PP/elastomer physical blends as a function of elastomer density. Insert is for the temperature range of 20 to 100°C.

The physical blends can also be characterized by their crystallization behavior from the melt. Figure 6-7 and Table 6-7 show that the peak crystallization temperature (of PP) is highest for 8402_0, which also has the lowest crystallization enthalpy. From this result, the crystal phase of 8402 may disrupt the primary or secondary crystallization processes of PP. Towards the end of primary crystallization, chain reptation and diffusion are the limiting factors. 8402 may be in its induction period before re-

crystallization and towards the end of PP primary crystallization. The insert in Figure 6-6 is a magnified image of crystallization from 100°C down to 20°C. A distinct observation is the crystallization of polyethylene in 8402_0. Long linear chains are able to organize and align in a parallel fashion for crystallization into lamellar structures. The PE phase of 8402_0 has a higher T_c , greater peak intensity, and a well defined peak, all attributed to the lower branch content and hence greater percent crystallinity.

Table 6-7: DSC exothermic data of 8407_0, 8401_0, and 8402_0

Sample ID	Peak temperature of crystallization (°C)	Enthalpy of crystallization (J/g)
8407_0	115.3	-83.1
8401_0	114.5	-80
8402_0	116.1	-74.5

The viscoelastic behavior of these physical blends has been characterized and typical results are seen in Figure 6-8. Dynamic mechanical testing has shown that the α -relaxation of polyethylene, which is related to the crystalline phase, does not exist for the low density copolymers [51, 415]. This is due to increased translational mobility of chain stems from crystal thickness and the low degree of surface order. The β -relaxation, which is attributed to glass transition temperature (T_g) of constrained, non-crystalline segments, increases in intensity with increasing comonomer content (more branching), leading to lower density. In the temperature range of -60°C to 0°C, an increase in molar volume of PE due to branching leads to the creation of the β relaxation. Higher comonomer content in the copolymer increases $Tan\delta$ peak intensity and shifts it to lower temperatures [415, 416]. This is related to the increased chain mobility and the decrease in activation energy for bond rotation and chain movement. The next peak at about 20°C represents the glass transition temperature of PP. Both 8401_0 and 8407_0 are at lower peak intensities than 8402_0. A decrease is an indication of an increase in % crystallinity of the blend. DSC

experiments (Figure 6-5, Table 6-5) come to the same conclusion that crystalline content in 8402_0 is lower than the other two blends. At temperatures above 40°C, 8407 shows the highest slope and intensity up to 125°C, followed by 8401_0 and finally 8402_0 (with

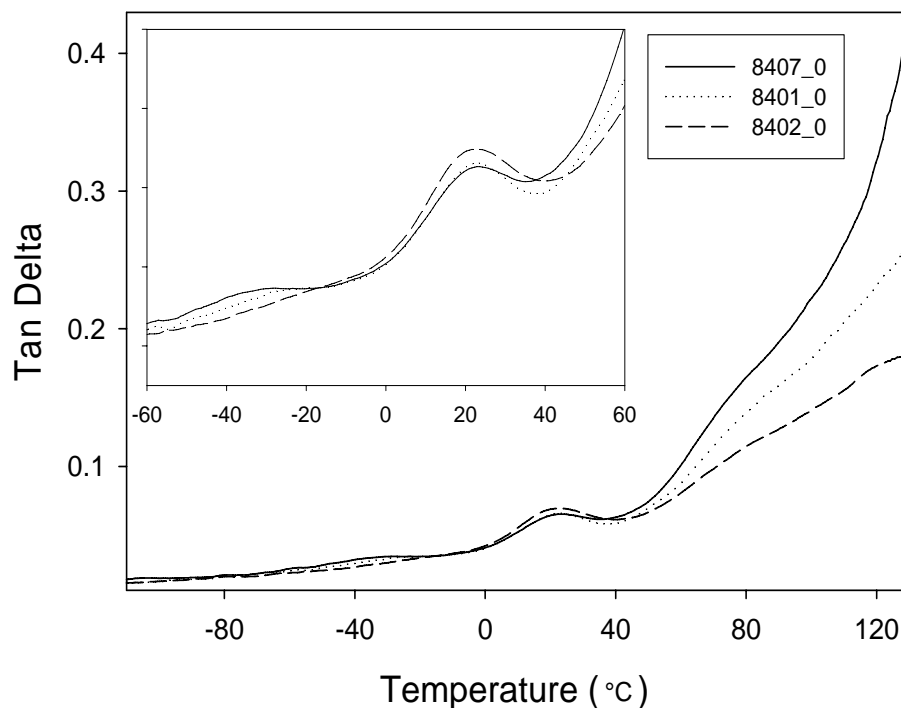


Figure 6-8: Dynamic mechanical analysis of 8407_0, 8401_0, and 8407_0. Insert is a magnified graph from -60°C to 60°C of the β relaxation of PE.

the smallest slope and lowest intensity). The α peak (or shoulder) of PP represents lamellar crystal slippage and defect motion in and around them [45, 55, 197]. This is known to occur at about 80°C which is 20°C higher than the T_m of 8407, 2°C higher than the T_m of 8401, and 18°C below the T_m of 8402. The diffuse lamellar crystals in 8407 melt early, thereby increasing the intercrystalline mobility of PP. It should also be noted that at the same molecular weight, 8407 will have a smaller radius of gyration than either 8401 or 8402 because of a higher branch content and hence a lower number of entanglements in the amorphous phase. The greater branch content leads to enhanced mobility due to greater free volume.

6.3.1.2 Alloys

Upon modification of the physical blends with initiator, styrene, and multifunctional monomer, mechanical property enhancement is drastic. But this section aims to make relative comparisons between the alloys based on the density of the elastomeric component. Figure 6-9 is an example of how a slight increase in branch

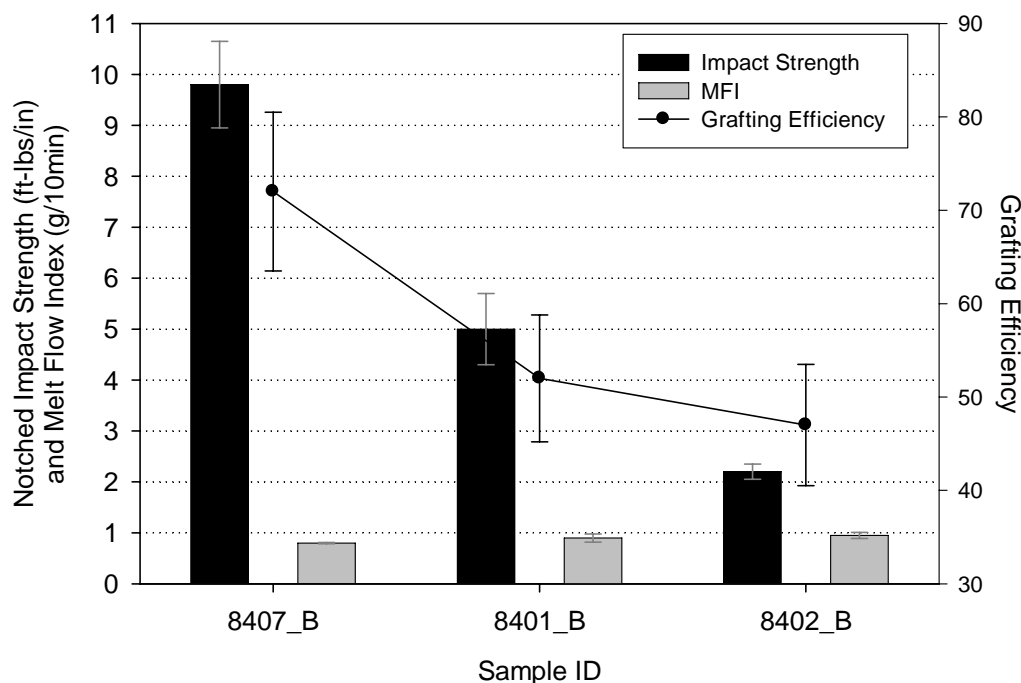


Figure 6-9: Room temperature impact strength, melt flow index, and grafting efficiency of 8407_B, 8401_B, and 8402_B.

content can affect mechanical properties and grafting efficiency of the alloys. From the data gathered in the previous section on physical blends, impact strength is highest for 8407_0, followed by 8401_0 and 8402_0. The same trend follows for alloyed systems, with impact strength decreasing in the following order: 8407_B > 8401_B > 8402_B.

The most striking aspect of this graph is a comparison of grafting efficiency. 8401_B has a GE that is 28% lower than 8407_B, while 8402_B is 35% lower than 8407_B. This result has several important implications. It is direct evidence that styrene monomer grafts onto the elastomer phase. It also proves that the monomer/initiator mixture

partitions in the elastomer phase as well as at the interface of the EOC and PP. The partitioning is likely due to the lower melting temperature of the EOC compared to PP [240]). Free radical grafting reactions happen fast ($> 70\%$ completion after the melting zone [90-93]), so the majority of the monomers may react before all 8402 pellets are molten. Researchers have shown that monomers will reside in the amorphous regions of a solid and not the crystalline portions [212]. With a more crystalline polymer, monomer may polymerize in the extruder before it is able to diffuse into the polymer and graft onto it. The higher the T_m of copolymer, the lower the plastification rate [90] and the longer the length of the solids conveying zone and melting zones needed for grafting.

Another aspect of this graph is the melt flow index. MFI appears to increase with increasing density of elastomer, so more chain degradation is associated with using a higher T_m elastomer phase. The minor phase will soften first and coat PP particles, which then delay the melting of PP [13]. 8402 will soften at a later point along the extruder when compared to 8407, so PP will melt quicker and thus degrade in the presence of a higher concentration of primary radicals. This is proof that in order to get a higher grafting efficiency and higher impact strength, the elastomer must have some degree of solubility in the monomer mixture. This may promote long chain branching, prevent homopolymerization due to contact with the extruder barrel wall, and reduce chain scission of PP.

At lower concentrations of styrene and initiator, the differences in grafting efficiency, impact strength, and melt flow index are not as contrasting as in Figure 6-9. From Figure 6-10, the impact strength does increase in a linear fashion with decreasing elastomer density, which is to be expected. Melt flow index is only slightly higher for

8402_C than 8401_C or 8407_C. This is similar to the trend in Figure 6-9. The grafting efficiency and impact strength of these samples are much lower than in Figure 6-9 because of the lower styrene and initiator concentrations in these samples. The standard deviation of grafting efficiency in Fig. 6-10 is too large to pinpoint a trend; therefore GE

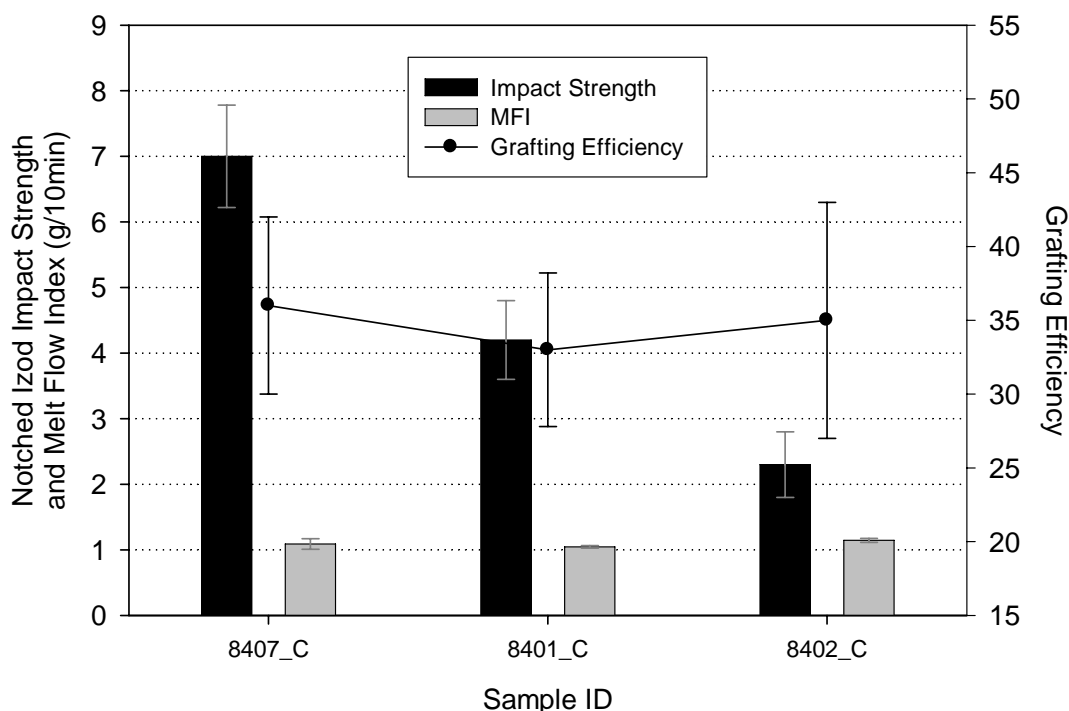


Figure 6-10: Room temperature impact strength, melt flow index, and grafting efficiency of 8407_C, 8401_C, and 8402_C

does not appear to change much with elastomer density. At these low levels of styrene and initiator concentration, homopolymerization may be favored over grafting.

Stress-strain performance is exemplified in Table 6-8 with typical graphs in Appendix B. For the alloys that contain only styrene and initiator as the reactive ingredients, tensile properties follow the same trend as the physical blends – the higher the density of elastomer, the better the properties. The PP chains degrade to a certain extent with initiator and styrene regardless of which elastomer is present, which results in relatively poor mechanical properties.

Upon addition of multifunctional monomer to the alloys, all properties improve except for elongation at break. The reason for the lower elongation at break may be because of a high degree of grafting in the PP phase. This property is very sensitive to defects (i.e. grafted chains) which may disturb the linearity of the polymer chains. 8407_B and 8407_C have higher elastic modulus than 8401_B and 8401_C, respectively. This may be due to the fact that the grafting efficiency is much higher for 8407 alloys, so a more highly branched structure exists in amorphous intercrystalline regions.

Table 6-8: Stress-strain data of PP:ENGAGE alloys as a function of elastomer density.

Effect of Copolymer Density					
Blend ID	Modulus (MPa)	σ_{Yield} (MPa)	Elongation at Break (mm)	σ_{Break} (MPa)	Energy to Break (N*mm)
8407_A	1501 ± 74	28.3 ± 0.9	57 ± 4	37 ± 1.1	4205 ± 736
8401_A	1557 ± 67	30.1 ± 1.3	62 ± 9	40 ± 1.4	4812 ± 1092
8402_A	1606 ± 34	31.4 ± 1.2	53 ± 7	37.6 ± 2.5	4025 ± 771
8407_B	1695 ± 110	30.9 ± 1.5	60 ± 4	42.6 ± 1.5	4294 ± 155
8401_B	1680 ± 51	31.1 ± 0.7	50 ± 11	41.6 ± 1.7	5457 ± 689
8402_B	1744 ± 43	34.5 ± 0.9	33 ± 12	33.7 ± 2.6	3491 ± 693
8407_C	1589 ± 58	31.4 ± 1.3	55 ± 9	40 ± 4	4167 ± 986
8401_C	1509 ± 98	29 ± 1	61 ± 8	39.8 ± 3	4833 ± 946
8402_C	1639 ± 57	32.7 ± 1.5	42 ± 10	32.3 ± 3.3	3282 ± 839

The yield stress is highly dependent upon the material's lamellar thickness, so σ_{Yield} increases with increasing elastomer density for the A and B series. One interesting note is that alloys containing 8402 have consistently lower elongation at break, stress at break, and energy to break. These properties are all dependent upon crystal breakup and the ability to strain harden, or recrystallize into a more ordered structure. Regarding the PP phase, % crystallinity of alloys containing 8402 are lower than 8407 alloys from Table 6-7, so the ability of PP to recrystallize may be hindered by the mere presence of PE crystals.

The melting behavior of four different alloys is shown in Figure 6-11. Alloys with high and low density both with and without DEGDA are shown and actual data is given

in Table 6-9. Those containing 8402 show a characteristic melting peak of PE crystals at about 95°C. The position and area of this peak does not significantly change with addition of multifunctional monomer, but compared to 8402_0, the peak is shifted to lower by about 15°C. So, the linear, crystallizable chains in 8402 are slightly affected by

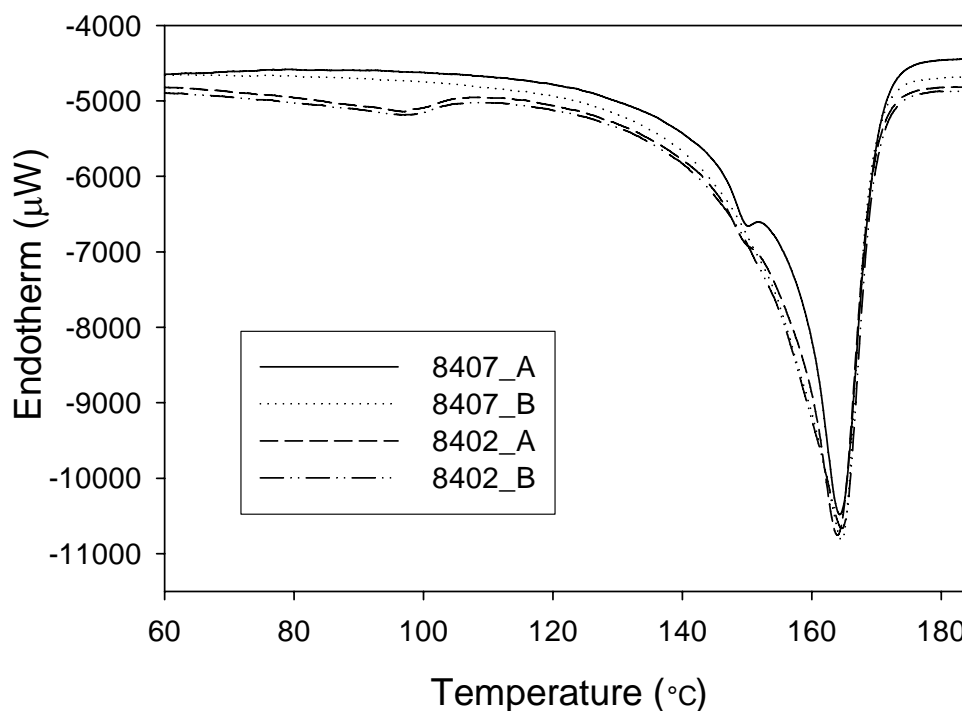


Figure 6-11: DSC melting endotherms of 8407_A, 8407_B, 8402_A, and 8402_B ranging from 60°C to 180°C. Insert is a magnified graph of the α melting peak of PP.

the reactive extrusion process, resulting in less ordered, thinner lamellae [389, 393-395, 398]. The melting peak of PP is slightly higher for 8402_B than 8402_A, possibly due to reduced degradation of the longer PP chains. Like in 8402_0, 8402_A has a second melting peak at about 150°C attributed to the β phase of PP [162, 363, 378]. The crystalline nature of 8402 may inhibit the formation of the alpha phase and so the less stable β phase forms. Comparing 8407_A and 8402_A, the β phase is more prominent for 8407_A. This may be due to the higher grafting efficiency of 8407, leading to more PS-DEGDA chains to disrupt the crystallization of the α phase.

Table 6-9: DSC endothermic data of 8407_A, 8407_B, 8402_A, and 8402_B.

Sample ID	PP α phase melting peak temperature ($^{\circ}\text{C}$)	T _m Onset ($^{\circ}\text{C}$)	Melting Enthalpy (J/g)	% Crystallinity
8407_A	164.3	149.5	81.7	39.5
8407_B	164.8	143.9	86.0	41.5
8402_A	164.0	148.7	77.2	37.3
8402_B	164.7	145.7	81.6	39.4

The onset of melting is higher for 8407_A than 8402_A, so the PP phase is degraded more so with 8402 present. 8407 softens early and may encapsulate the monomer/initiator mixture, which promotes grafting onto the copolymer phase, reduces homopolymerization, and controls hydrogen abstraction from PP by primary radicals. There are likely a high number of small lamellar crystals in 8407_A, whereas for 8402_A the crystallization of PP is inhibited by the crystal nature of the elastomer. Neither 8407_B nor 8402_B show the β phase peak of PP, likely due to the reduced degradation of PP and improved crystallization temperature (Figure 6-12). Both 8407_B and 8402_B show an increase in the % crystallinity compared to 8407_A and 8402_A, respectively.

Upon studying the crystallization behavior of these alloys (Figure 6-12 and Table 6-10), addition of DEGDA increases the crystallization temperature and enthalpy of crystallization of the alloys regardless of ENGAGE® crystallinity. This phenomenon was explained in Chapter 4 and is attributed to an increase in the nucleation density from branching [238, 357, 402]. The peak representing the crystallization of PE does not

Table 6-10: DSC exothermic data of 8407_A, 8407_B, 8402_A, and 8402_B.

Sample ID	Peak temperature of crystallization ($^{\circ}\text{C}$)	Enthalpy of crystallization (J/g)
8407_A	124	-80.7
8407_B	130.8	-84.4
8402_A	124.5	-75.7
8402_B	131.4	-80.3

change upon addition of multifunctional monomer. This may be an indication that there is no crosslinking in the elastomer, which would naturally reduce the % crystallinity and shift the peak to higher temperatures.

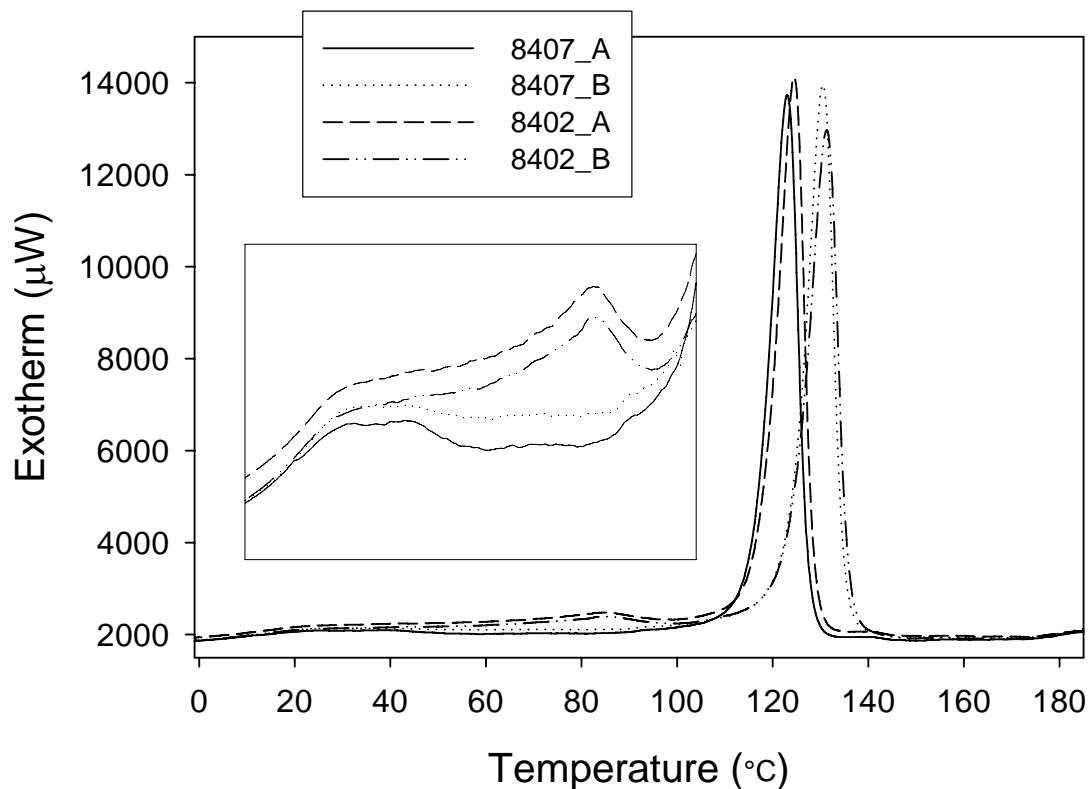


Figure 6-12: DSC cooling exotherms of PP/elastomer physical blends as a function of elastomer density. Insert is for the temperature range of 20 to 100°C.

The viscoelastic behavior of both alloys containing multifunctional monomer and physical blends are compared in Figure 6-13. In each graph, the sample containing DEGDA results in a lower peak intensity for the T_g of polypropylene at about 20°C. This means that the % crystallinity is higher, a result verified by DSC measurements. Also, a peak becomes more prominent around 80°C with addition of DEGDA. The formation of this relaxation is symbolic of the triclinic β phase in PP, which has greater toughness and impact strength than the α phase [260, 287, 301, 337, 340]. Another interesting note is that at high temperatures ($> 100^\circ\text{C}$), the intensity of the $\text{Tan}\delta$ graph is affected to greater

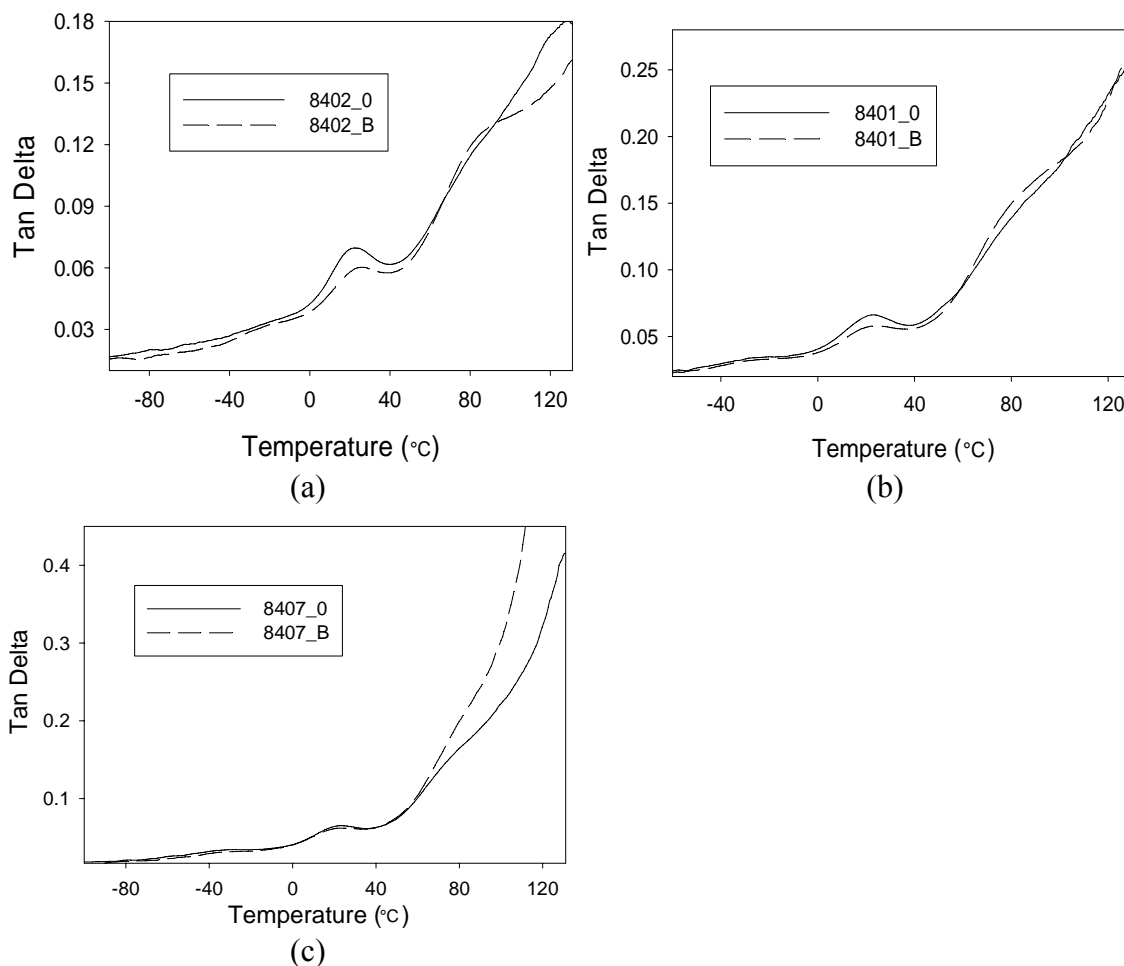


Figure 6-13: Dynamic Mechanical Analysis comparison of (a) 8402_0 and 8402_B, (b) 8401_0 and 8401_B, and (c) 8407_0 and 8407_B.

extent with decreasing density of elastomer. This may be related to the grafting efficiency of each alloy. At higher elastomer densities, the overall grafting efficiency is lower resulting in less molecular mobility at high temperatures. So, 8407 may be dispersed and distributed at a much smaller scale and to a much greater extent than its high density counterparts and so facilitates inter-crystalline motion.

6.3.2 Effect of Elastomer Molecular Weight on Alloy Performance

Four different ethylene-octene copolymers (002, 8407, 8200, and 8842) are ranked according to their melt flow index and molecular weight. All other material properties and processing parameters are held constant unless otherwise noted. Also, the ratio of PP

to EOC was kept constant at 90:10. Table 6-4 and Figure 6-2 give a key code and designated formulations to ease in the identification of each sample. The first number is the grade of copolymer, the second number/letter signifies a formulation which can be referenced in Table 6-4.

Figure 6-14 shows the molecular weight averages for each of the elastomer grades according to their melt flow index. Polymers are mixtures of molecules of various molecular weights and molecular sizes, so molecular weight averages are used to characterize them. With polystyrene standards, these molecular weights are relative in relation to the hydrodynamic volume of the standards. Decreasing melt flow index means increasing average molecular weight and polydispersity (M_w/M_n).

The number average molecular weight (M_n) is simply the total weight of all the polymer molecules in a sample, divided by the total number of polymer molecules in a sample. This is very sensitive to changes in the weight-fractions of low molecular weight species, which is why its magnitude is less than all other averages. Large molecules have a relatively low effect on this average, so it decreases only slightly with increasing MFI. Higher moments of molecular weight, (M_w or weight average, M_z , and M_{z+1}) rely more heavily on the number of high molecular weight chains. A large M_w often means high tensile strength, M_z and M_{z+1} relates to the stiffness and long fatigue life of polymers, and M_n is often associated with improving flow properties for processing and low temperature flexibility. At an MFI of 1 or 5, the molecular weight of M_{z+1} is much higher than at 30 or 500 g/10min. An interesting note is that at an MFI of 5, M_{z+1} is relatively much higher

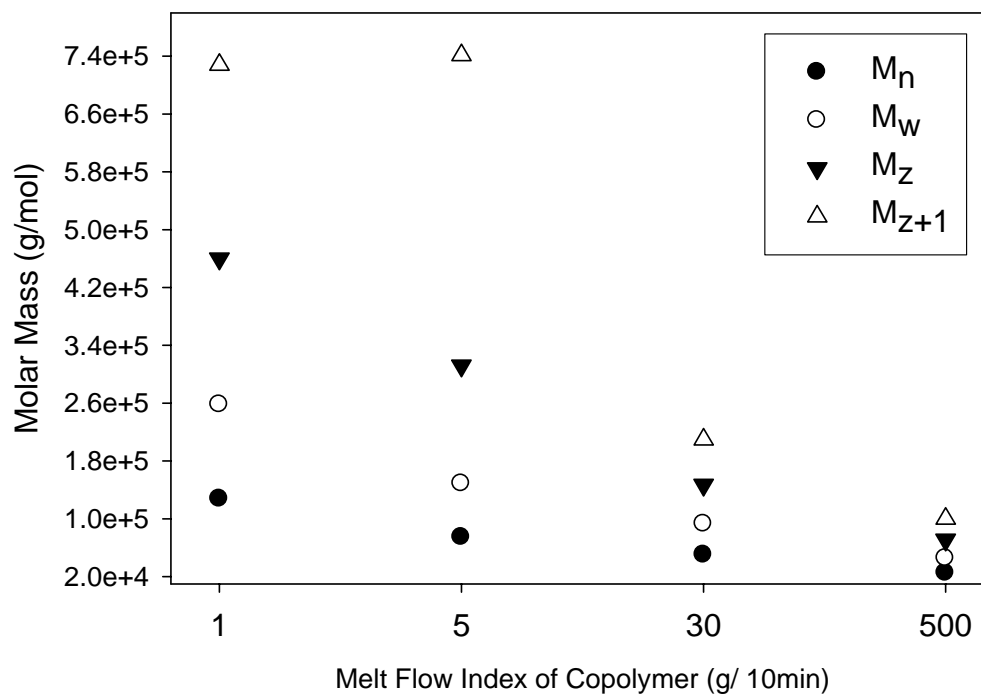


Figure 6-14: Molecular weight averages of the polyolefin elastomers of interest, ranked according to their melt flow index.

than M_z , which may favor phase separation of chains from entropy considerations. This has implications on mechanical properties which will be discussed later in the chapter. The critical entanglement molecular weight (M_c) for polyethylene is 4000 g/mol [185, 417], which is directly related to viscoelasticity and chain mobility and dictates the polymer's viscosity and ultimate mechanical properties. Each grade of copolymer has a M_n above this value, which means that enough physical entanglements are present to give some resistance to deformation.

The closer the polydispersity approaches a value of one, the narrower is the molecular weight distribution. The low MFI polymers (Figure 6-15) have a relatively high PDI, which means that the distribution is skewed towards larger chains.

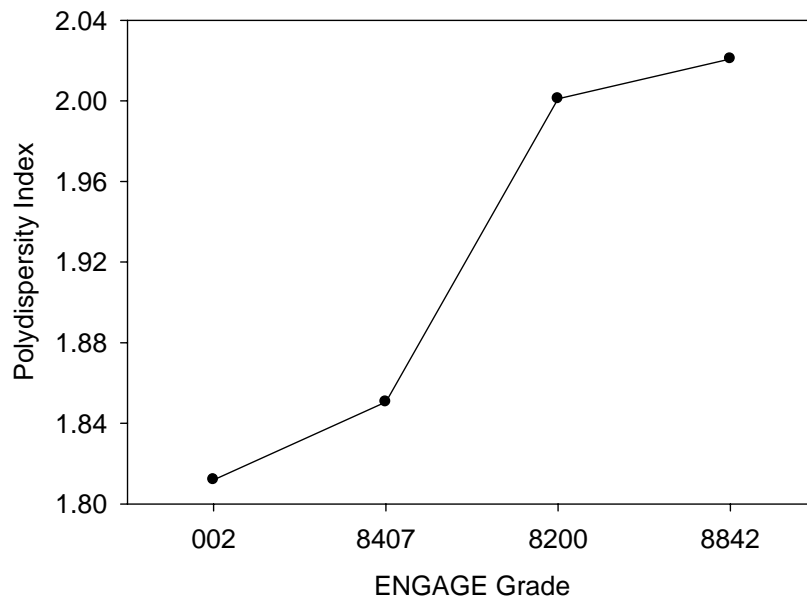


Figure 6-15: Polydispersity (molecular weight distribution) of the polyolefin elastomers of interest.

6.3.2.1 Physical blends

The notched Izod impact strength and stress-strain behavior are highly dependent upon intercrystalline thickness and molecular weight of the constituents [270, 409, 410]. From Figure 6-16, impact strength is highest for the high molecular weight 8842_0 sample, followed by 8407_0, 8200_0, and 002_0, respectively. The highest impact strength corresponds to the lowest elastomer MFI, so there is a highly entangled network of mobile chains within the amorphous regions in PP which are able to relax, diffuse, and respond at the speed of the impact test. 8200_0 has a lower impact strength than 8407_0, which can be traced back to the molecular weight and density of 8200. 8200 has a slightly lower comonomer content than 8407, and a disproportionate amount of high molecular weight chains (M_{z+1}). This means that 8200 is more dense than 8407, the high molecular weight chains in 8200 give stiffness to the blend, and there may also be a greater degree of phase separation within the blend. The lowest impact strength is seen for the blend containing the lowest molecular weight elastomer. This is likely due to the

fact that 002 has a high number of chain ends along with a relatively low bulk cohesive strength and so cannot transfer stress effectively. There may also be coalescence of 002 because of its extremely low viscosity, which results in a low degree of interfacial surface area and adhesion [12, 69]. Another plausible theory is that at high deformation rates, rubber elasticity theory can be applied to the elastomer phase [15, 161]. So, by stretching out the chains, a greater retractive force is needed for further deformation and the temperature rise experienced in an impact test promotes a conformational change from extended to random coil.

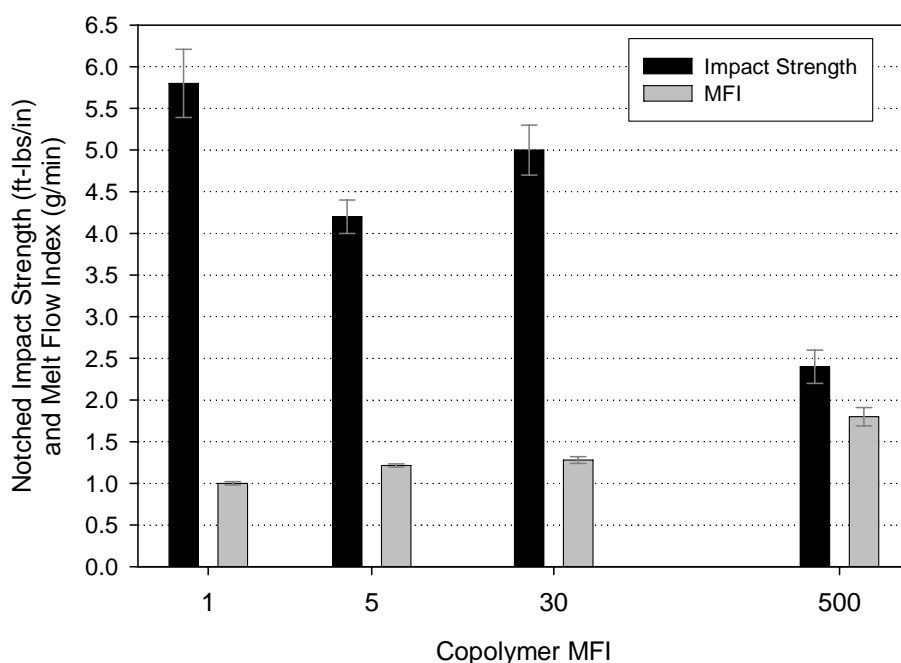


Figure 6-16: MFI and room temperature notched Izod impact strength of 8842_0 (highest molecular weight), 8200_0, 8407_0, and 002_0 (lowest molecular weight).

As expected, the melt flow index of the blends rise as the MFI of the elastomer phase increases. Notice that a proportionately large jump is seen from 8407_0 to 002_0, indicative of the 17X jump in elastomer MFI. This can be related to the high number of low molecular weight chains in 002_0. 8407 is essentially made up of chains that are

double in length than that of 002₀, which gives it the cohesive strength and elongational viscosity needed to prevent coalescence and resist deformation.

The stress-strain deformation of the elastomers at low strains is related to the slip-link theory of rubber elasticity, which states that entanglements are visualized as slipping links that can slide along the chain contour between crosslinks [58]. At intermediate and high strains, crosslinks are considered to be entangled knots that tighten as strain increases. By decreasing molecular weight, there is an increase in the number of chain ends, which reduces the number of effective network chains.

At high MW, deformation is homogeneous and is governed primarily by the strain-hardening process for stress-strain behavior. A ductile deformation requires that there be an adequate number of sequences of disordered chain units connecting crystallites. Furthermore, the number of units involved must be large so that each connector is deformable and can sustain large deformations. So in order to avoid embrittlement, the interlamellar region must possess chains that display rubber-like behavior. They cannot be straight chains in planar zigzag conformation. The effective number of deformable sequences will be tempered by chain entanglements and interlinking. These factors are sensitive to MW, % crystallinity, and interlamellar thickness. For low MW materials, there are not enough disordered sequences connecting the crystallite to transmit the tensile force. And with a high crystallinity level, the thickness of the interlamellar region is small. Hence, the disordered connecting units would not be able to sustain large deformations [269].

A few trends are obvious from Figure 6-17 regarding tensile deformation of the physical blends. All stress-strain properties (yield strength, elongation at break, stress at

break, elastic modulus, and energy to break) decrease in a somewhat linear fashion with decreasing molecular weight to a point. If elastomer particles are trapped within a growing PP spherulite, it will change its growth and final morphology, which in-turn will affect these properties. A low elastomer MW will result in a reduction in the number and degree of entanglements in the amorphous phase (tie molecule population), thereby decreasing boundary strength. So the elastic response to an applied load is reduced (decrease in elastic modulus) and the mobility given to lamellar slippage, rotation, and

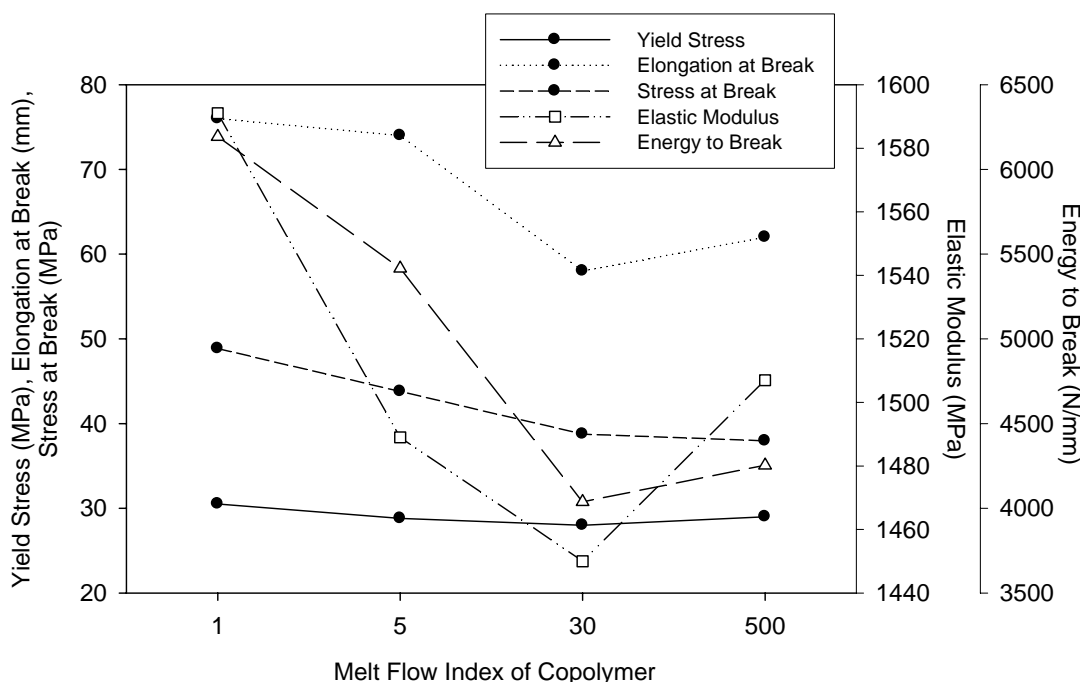


Figure 6-17: Stress-strain performance of physical blends as a function of MFI of the copolymer.

orientation is increased due to the greater free volume afforded by more chain ends (decrease in yield stress). The short chain nature of 8407 reduces the extent of strain hardening, so stress at break, elongation at break, and energy to break all decrease. With increasing MW, the plateau region beyond yield decreases, and the slope of strain hardening becomes steeper [269]. However, these trends are reversed when 002_0 and 8407_0 are compared. In fact, the elastic modulus of 002_0 is comparable to that of

8200_0. This brings up an interesting point – at what molecular weight or melt flow index will the elastomer phase be completely rejected from a growing PP spherulite? The spherulitic morphology of these blends need to be studied in detail to further understand the distribution and perfection of the PP spherulites. Also the extent of physical aging (densification of non-crystalline material below T_g) may give an indication of why this occurs. It should be noted that standard deviations and typical stress strain graphs are given in Appendix B.

The melting behavior of the physical blends is shown in Figure 6-18 and Table 6-11. The results indicate that as the molecular weight of the elastomer increases, the onset of melting temperature and enthalpy of fusion also increase. The reason that 8842_0 has a higher % crystallinity than 002_0 may be traced to the blend's crystallization behavior and will be explained over the next few paragraphs. The peak at approximately 150°C is related to the melting of the β phase of PP and is known to be nucleated by elastomers.

Table 6-11: DSC endothermic data of 002_0, 8407_0, 8200_0, and 8842_0

Sample ID	PP α phase melting peak temperature (°C)	Tm Onset (°C)	Melting Enthalpy (J/g)	% Crystallinity (from Refs. 170, 391)
002_0	165	152.5	82.3	39.8
8407_0	165.2	152.9	82.3	39.8
8200_0	165	152.6	85.2	41.2
8842_0	164.5	153	88.9	43

The early stage of crystallization may be based on Flory's theory of crystallization of copolymers [161, 392]. He visualizes crystals linked rather quickly by amorphous defects and set up a metastable, global network of interlinked crystals. This type of gelation is reached at 5% of crystallization. After the crystal network is set up, the amorphous defects can continue locally to crystallize with very little or no long distance diffusion in a secondary crystallization process [61-63]. Crystallization occurs by a

straightening out of short coil sequences without a long range diffusion process [100]. A larger average molecular weight of elastomer leads to a higher crystallization temperature and enthalpy of crystallization. Long sequences of a given polymer repeat unit are known to crystallize at a higher temperatures than shorter sequences [271]. But a recent study found that a higher MFI elastomer reduces the spherulite growth rate, showing that the diffusion process dominates over crystallization rate [290].

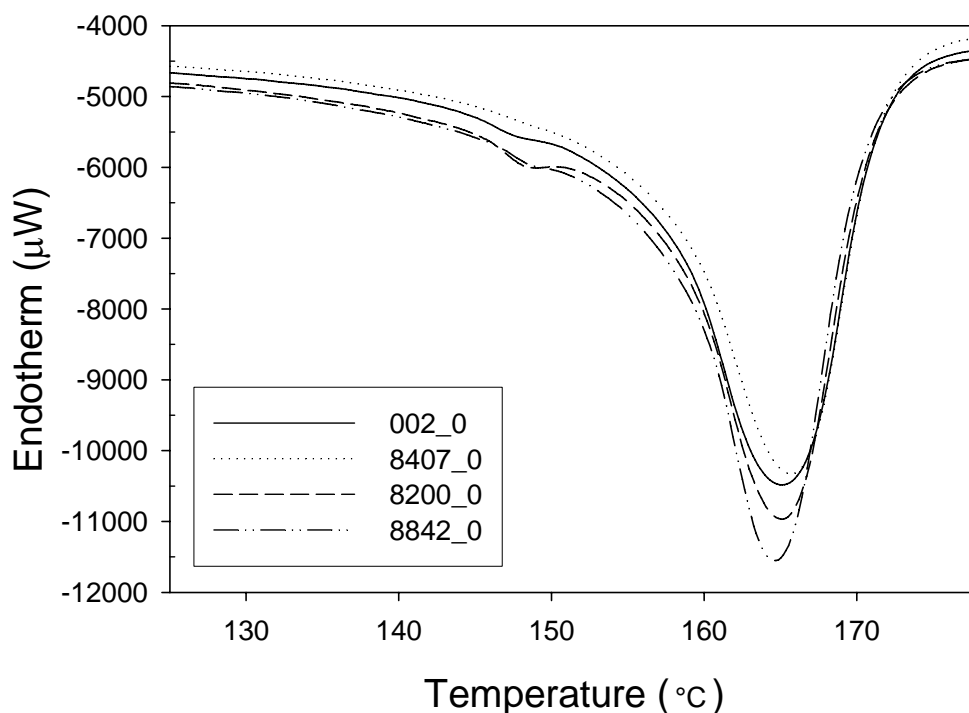


Figure 6-18: DSC melting endotherms of 002_0, 8407_0, 8200_0 and 8842_0.

Figure 6-19 and Table 6-12 show the crystallization behavior of these blends. The long copolymer chains and high degree of entanglements in 8842 prevent long range diffusion of polypropylene chains (melt memory effects) and therefore facilitate crystallization [100, 399]. When polypropylene segments are in close proximity to each other, they are more likely to nucleate. A higher crystallization temperature signifies a higher packing density, faster crystallization kinetics, and thus greater % crystallinity for 8842_0 than the lower molecular weight copolymers. Also, the lower molecular weight

Table 6-12: DSC exothermic data of 002_0, 8407_0, 8200_0, and 8842_0

Sample ID	Peak temperature of crystallization (°C)	Enthalpy of crystallization (J/g)
002_0	114	-78.9
8407_0	115.3	-83.1
8200_0	116.8	-83.5
8842_0	117.7	-84.3

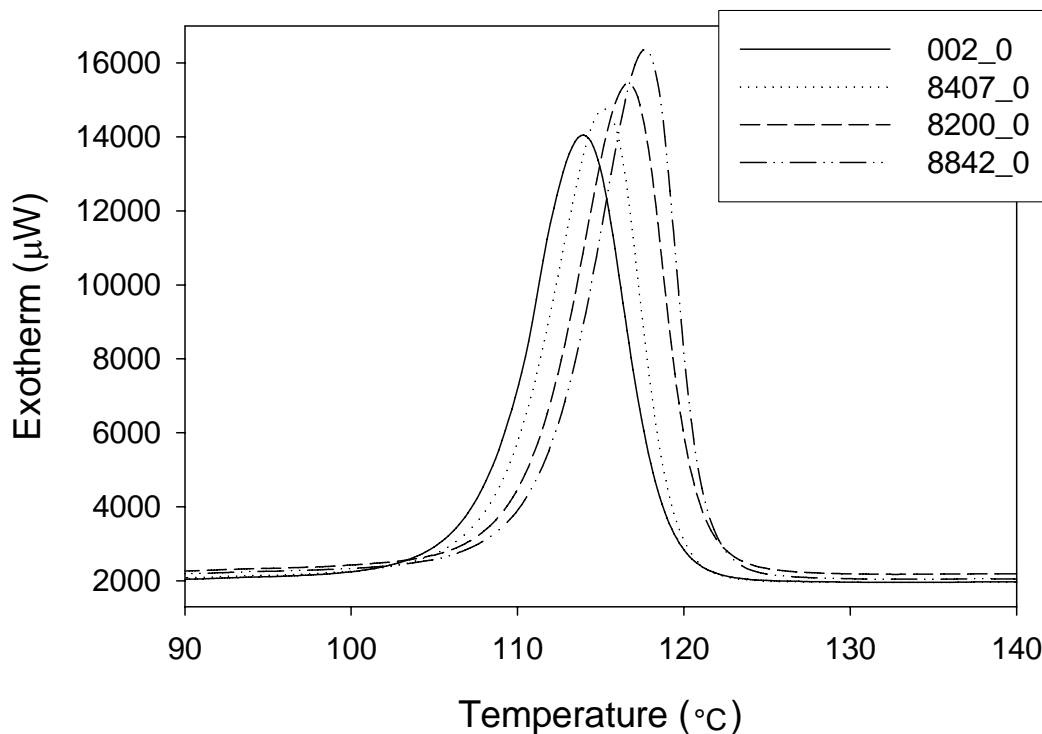


Figure 6-19: DSC crystallization exotherms of 002_0, 8407_0, 8200_0, and 8842_0.

material is likely rejected into the interspherulitic regions of PP as deformed domains, resulting in a considerable depression in growth rate [100, 236, 255, 257, 260, 263, 297, 307, 311-313]. The density of 8842 is less than all the other copolymers, so this may not inhibit the crystallization processes of PP. All of these factors point to the fact that a high molecular weight elastomer result in thicker, more perfect PP crystalline lamellae with high melting temperature. This, along with a high degree of entanglements is what gives 8842_0 a balance of both impact strength and stress-strain properties.

6.3.2.2 Alloys

Reactively extruding the physical blends while changing elastomer MW allows one to analyze several aspects of the process, namely:

- Whether the liquid reactants become trapped in the elastomer phase (higher viscosity = higher MW = lower MFI) and thus limited in dispersion within the PP phase,
- Whether an increase in the entanglement density means a greater degree of grafting,
- Whether the impact strength can be optimized,
- And whether chain scission of PP can be reduced.

From Figure 6-20, addition of styrene and initiator to the blends results in a slight decrease in impact strength for all samples but 8200_A, when compared to their physical blends. The decrease in impact strength is likely due to the degradation of the PP phase and the increase may be due to a change in the percent crystallinity of 8200 (grafting has been shown to decrease the % crystallinity of polyolefins [7, 148, 184, 215]). Degrading PP chains is evidenced by higher MFI values. It appears that 002_A has the highest MFI and is affected the most by the modification with styrene and initiator. 002_0 may not be trapping liquid reactants as the higher molecular weight elastomers, so PP is experiencing a higher concentration of primary free radicals. During morphology development, 002 may not coat PP pellets or be stretched out like a higher MW copolymer because of its low number of entanglements and relatively low softening temperature [13]. The sheet formation during morphology development is crucial to proper dispersion [32, 83] and after phase inversion takes place, the low viscosity of 002 likely does not trap any of the PP phase via grafting or crosslinking.

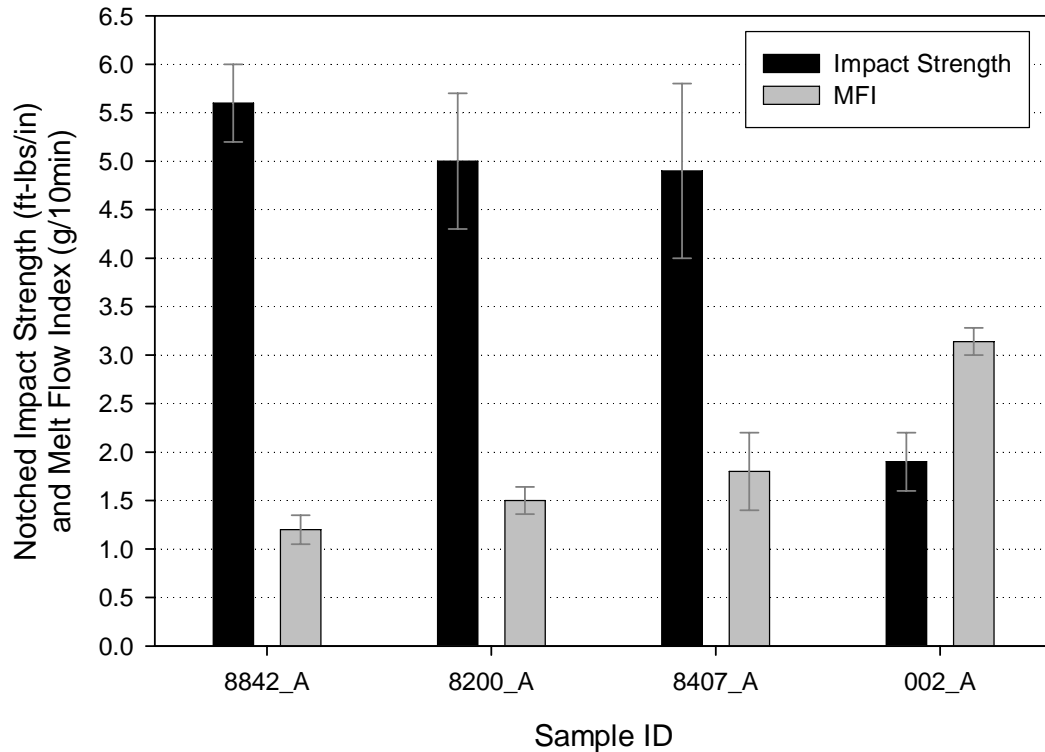


Figure 6-20: Impact Strength and melt flow index of 8842_A, 8200_A, 8407_A, and 002_A.

Addition of DEGDA and reduction in styrene and initiator concentrations results in a significant increase in impact strength for all alloys but 002_C from Figure 6-21. Once again, 002 likely does not participate in the grafting process because of its low number of physical entanglements, low viscosity, high number of secondary and tertiary hydrogen atoms, and tendency to coalesce from such a drastic difference in viscosity between 002 and PP [420]. The melt flow index of 002_C is 66% lower than 002_A which is significantly greater than all other alloy combinations. The PP phase is preferentially degraded in 002_0, so addition of a radical trapping agent and reduction in the overall

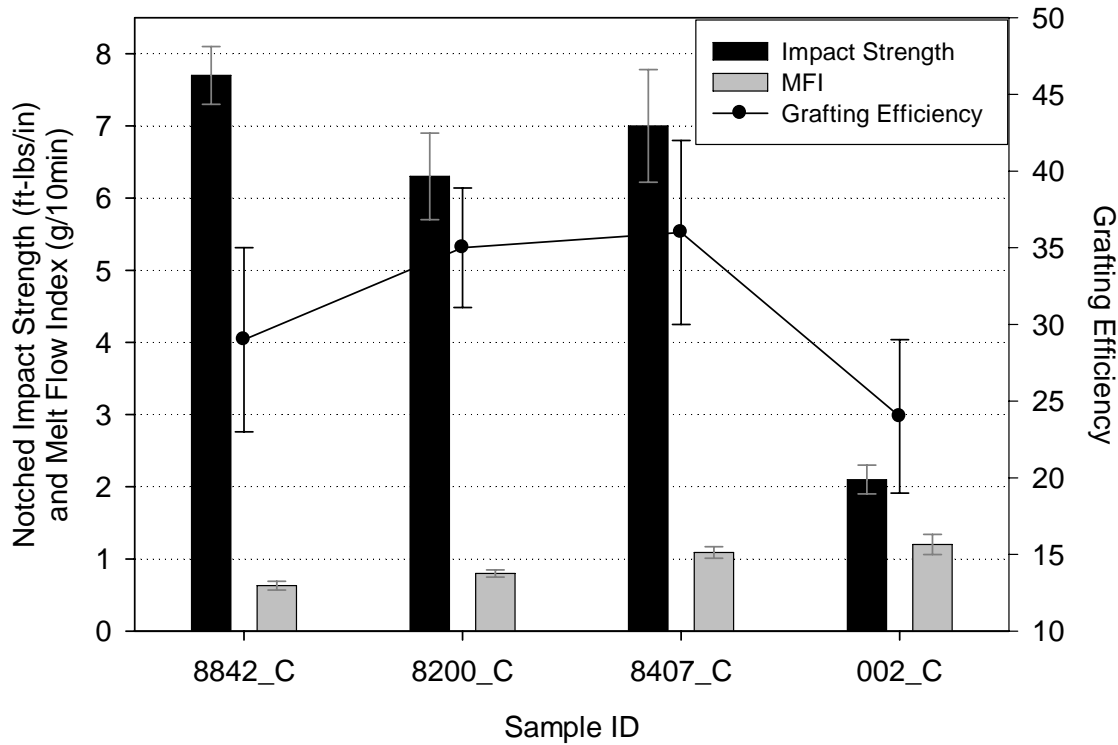


Figure 6-21: Izod impact strength and melt flow index of 8842_C, 8200_C, 8407_C, and 002_C.

concentration of free radicals should give this result. An interesting trend is the steady increase in grafting efficiency with reduction in elastomer molecular weight from 8842_C to 8407_C. Since styrene grafting primarily occurs on PP rather than the elastomer phase, 8407 is most efficient at dispersing the liquid reactants throughout the system. This grade of ENGAGE® appears to have the optimal combination of molecular weight, viscosity, and melting or softening temperature at this styrene concentration. 8842_C has a lower grafting efficiency possibly due to the cage effect that long, entangled chains may have on the free radical polymerization process. At the lowest elastomer molecular weight, grafting efficiency drops to a very low value. This may be because monomer is lost to homopolymerization by touching extruder barrel wall (no encapsulation of liquids) and gross phase separation from PP.

Alloys having the highest impact strengths are seen in Figure 6-22. These materials have the highest concentration of initiator, styrene, and multifunctional monomer which reinforces that fact that the right combination of initiator and monomers will lead to outstanding alloy performance. A few features in this graph must be noted and elaborated upon. The grafting efficiency remains roughly constant when elastomer MFI stays between 1 and 30 g/10min. The initiator concentration is likely so high that there are enough free radicals facilitate high grafting yields and the high styrene concentration, acting as a vector fluid, encompasses all phases and particles as the morphology evolves in the melting portion of the extruder. The overall degree of

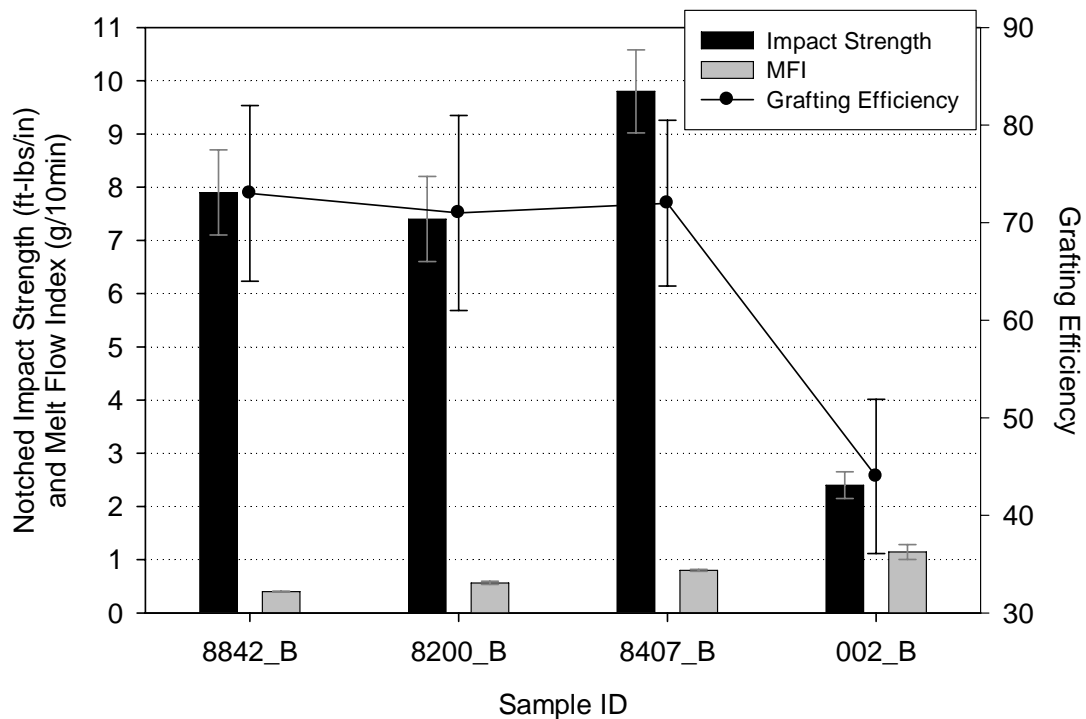


Figure 6-22: Izod impact strength and melt flow index of 8842_B, 8200_B, 8407_B, and 002_B.

entanglements is sufficient even at the 8407 level to improve dispersion of the liquid reactants. The fact that 8407 and 8842 have similar grafting efficiencies but a different

molecular weight leads one to believe that at such high monomer and initiator concentrations, the higher moments of molecular weight may not play a significant role.

In the presence of initiator, the highest molecular weight fractions of polyethylene will be consumed first and a higher amount of crosslinking agent shifts the distribution towards lower molecular weights [149, 185]. The low MW fraction is believed to act as grafted pendant chains in the presence of longer polymer chains. The network formed within the low MW fraction consists mainly of chemical crosslinks, whereas high MW material comprises both physical entanglements and chemical crosslinks. Trapped entanglements generate the major part of the styrene grafting points at low peroxide concentrations. At high number average molecular weight values, dense networks are easily created with only a small amount of chemical crosslinks and branches, as the probability of entanglement formation is very high.

Impact strength is highest for 8407_B, which may be due to the high dispersability of the 8407 phase compared to its high molecular weight counterparts. The smaller elastomeric domains allow for more efficient energy absorption mechanisms. Melt flow index, to no surprise, steadily increases with increasing elastomer MFI. MFI is roughly additive for the alloys, similar to physical blend results.

An interesting trend is shown in Table 6-13 regarding the elastic modulus and yield stress of the high impact specimens. The lower the molecular weight of the elastomer, the higher the modulus of the alloy. The modulus is directly dependent upon the amorphous phase of the alloy, which is likely highly branched from addition of multifunctional monomer. At both high and low deformation rates, 002_B responds in a brittle manner. The PP phase is affected more drastically with the low molecular weight

elastomer present, having a highly branched amorphous phase and many reinforced cross-hatched lamellar crystals. For grafting of high molecular weight polyethylenes (like 8842), grafting reactions are known to result in little, if any, crosslinked material. So, for higher viscosity elastomers, dispersion and distribution may be improved so as to

Table 6-13: Stress-strain behavior of 002_B, 8407_B, 8200_B, and 8842_B.

Effect of Copolymer Molecular weight					
Blend ID	Modulus (MPa)	σ_{Yield} (MPa)	Elongation at Break (mm)	σ_{Break} (MPa)	Energy to Break (N*mm)
002_B	1782 ± 109	31.8 ± 1.8	46 ± 10	37.6 ± 4	4048 ± 881
8407_B	1695 ± 110	30.9 ± 1.5	60 ± 4	42.6 ± 1.5	4294 ± 155
8200_B	1598 ± 54	30.2 ± 0.6	62 ± 7	43.2 ± 1.5	5699 ± 485
8842_B	1545 ± 40	29.3 ± 1.1	56 ± 6	42.7 ± 2.5	4945 ± 710

increase chain mobility in the PP phase. Elongation at break, stress at break, and energy to break are all lowest for 002_B, a relatively brittle alloy.

Dynamic mechanical behavior has already been shown to be a vital technique in establishing relaxation behavior of polymer chains in both blends and alloys. It gives a wealth of knowledge regarding miscibility, crystallinity and/or crosslinking, degradation, branching, and intercrystalline mobility. Figure 6-23(a) thru (d) compares physical blends and alloys for all grades of elastomer. The storage modulus is seen to be higher for 002_B than 002_0 but this trend is opposite for all other samples. From stress-strain data, the elastic modulus and yield stress are also extraordinarily high for 002_B. In this alloy, PP may retain its spherulite structure and with a slight degree of crosslinks, the cross-hatched structure may be reinforced. At temperatures above 20°C, the rubbery plateau regions of 8407_B and 8200_B decrease in a steeper manner when compared to their physical blends, but for 8842_B the graph plateaus to a slightly greater extent. The length of the rubbery plateau region is known to increase with molecular weight [81], so

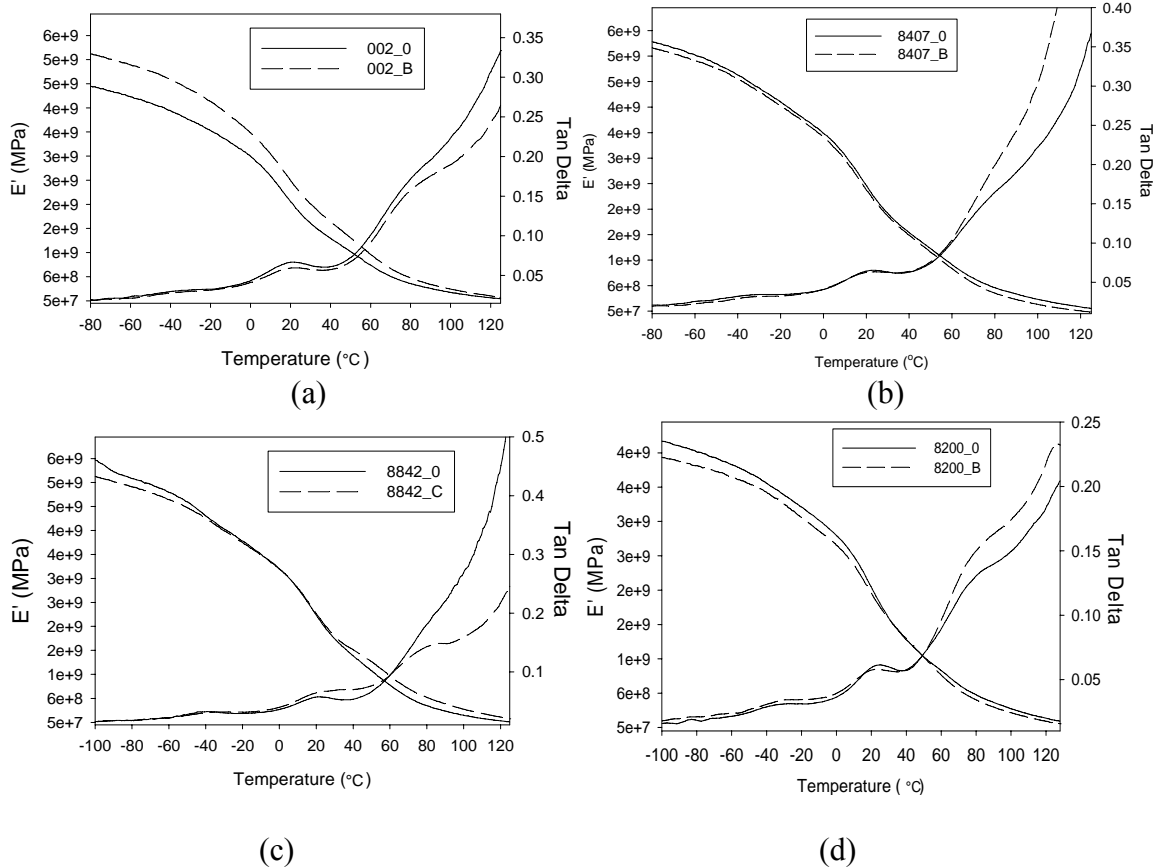


Figure 6-23: Dynamic mechanical behavior (E' and $\text{Tan}\delta$) of various alloys and blends. (a) 002_0 vs. 002_B, (b) 8407_0 vs. 8407_B, (c) 8200_0 vs. 8200_B, and (d) 8842_0 vs. 8842_B.

the high degree of physical entanglements in 8842 likely promotes rubber-like behavior of the alloy.

For $\text{Tan}\delta$ comparisons, the T_g of the elastomer phase is slightly lower for all alloys than blends except in the case of 8200_0. This material has a slightly higher % crystallinity than all other elastomers, so the crystalline phase may be disturbed by the grafting of monomer. The intensity of polypropylene's T_g increases with increasing elastomer MW. This is surprising because one may expect that elastomers with more chain ends and more mobility would have the greatest effect on the intensity of PP's T_g . But these low molecular weight species may be rejected more easily from the inter- and intra-spherulitic regions in PP. The T_g of 8842_B is highest probably because the long

polymer chains of 8842 are grafted onto PP over a larger volumetric space. In 8407_B there may be smaller domains but a greater number of domains. At higher temperatures (approaching and eclipsing the α relaxation), 8200_B and 8407_B have greater intensities than 8842_B and 002_B when compared to their physical blends. This poses an interesting question about the morphology of these alloys – it appears that at extreme values of elastomer molecular weight, domain size may be too large. So, the lamellar crystals of PP do not slide past one another readily because they are not surrounded by elastomer particles. Also notice the drastic decrease in intensity from 8842_0 to 8842_B at high temperatures. A proportionately high number of entanglements and crosslinks are present which reduce intercrystalline mobility so the elastic nature of the material increases.

The relaxation behavior, mechanical properties, and rheological properties are known, but the crystalline state of these alloys has to be defined. Figure 6-24 and Table 6-14 show that the onset of melting is lower and % crystallinity of PP higher for alloys containing DEGDA than those without. This is true regardless of the molecular weight of elastomer and it is significant because it reinforces the idea that the method of radical attack, polymerization, branching, grafting, and PP chain scission are the same as long as the elastomer viscosity remains within a certain range. As stated in the previous sections and chapters, the lamellar crystals in 8407_B and 8842_B are smaller and greater in number than 8407_0 and 8842_0, respectively. A lower onset of melting temperature is linked to the greater surface energy of the smaller crystals and the higher % crystallinity is associated with a branched structure containing short crystallizable PP sequences which are in close proximity to each other [255, 279, 327, 362, 369, 389, 391-397].

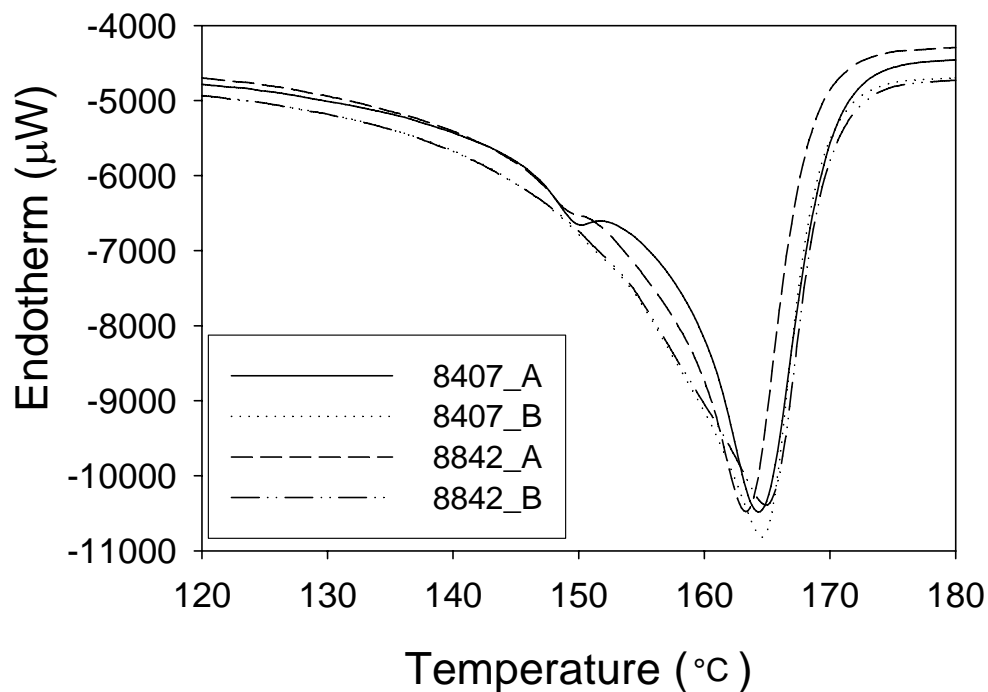


Figure 6-24: DSC melting endotherm of 8407_A, 8407_B, 8842_A, and 8842_B.

The β phase of PP at 150°C is more pronounced for 8407_A than 8842_A, which may be due to the lower degree of PP chain scission experienced by 8842_A. The presence of this phase has been attributed to degraded PP chain segments and a high degree of homopolymerized monomer that hinder the formation of the traditional α phase. The increase in % crystallinity from 8407_A to 8407_B is more drastic than 8842_A to 8842_B. This may be due to the high MFI of 8407_A (more degraded chains) which are then linked up by multifunctional monomer (8407_B). 8842 may trap some of the initiator and slightly crosslink or extensively branch.

Table 6-14: DSC endothermic data of 8407_A, 8407_B, 8842_A, and 8842_B.

Sample ID	PP α phase melting peak temperature (°C)	T _m Onset (°C)	Melting Enthalpy (J/g)	% Crystallinity
8407_A	164.3	149.5	81.7	39.5
8407_B	164.8	143.9	86	41.5
8842_A	163.5	149.7	80.8	39
8842_B	164.9	144.6	85.4	41.3

The crystallization behavior of the alloys is shown in Figure 6-25 and Table 6-15, both including 8407_A, 8407_B, 8842_A, and 8842_B. With addition of multifunctional monomer, T_c and enthalpy of crystallization both increase, regardless of elastomer MFI. So, dispersion of liquid reactants is adequate, grafting is widespread, and a network-like morphology is likely present. The increase in T_c from 8407_A to 8407_B is slightly higher than from 8842_A to 8842_B. This may be due to the greater dispersability of 8407 and therefore better distribution of grafts and branch points.

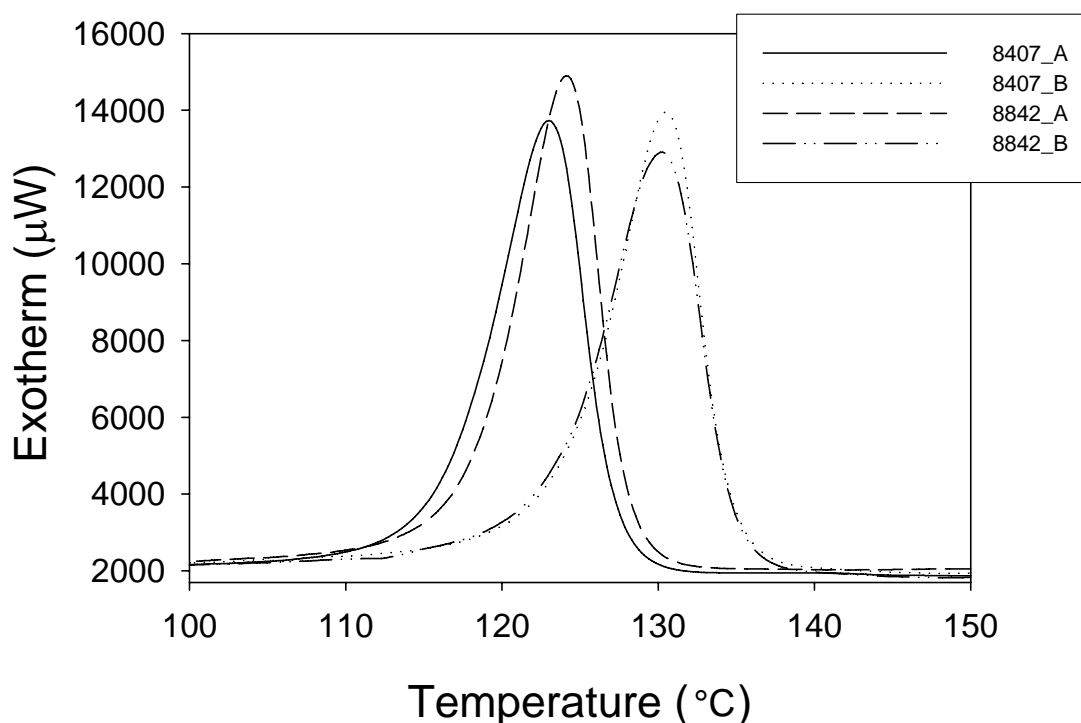


Figure 6-25: DSC crystallization exotherm of 8407_A, 8407_B, 8842_A, and 8842_B.

Table 6-15: DSC exothermic data of 8407_A, 8407_B, and 8842_A, and 8842_B

Sample ID	Peak temperature of crystallization (°C)	Enthalpy of crystallization (J/g)
8407_A	124	-80.7
8407_B	130.8	-84.4
8842_A	124.1	-78.6
8842_B	130.3	-83.6

6.3.3 Supercritical CO₂ as a Possible Route to Improve Grafting Efficiency

A new route to improve the processability of thermoplastics and their blends is to utilize supercritical carbon dioxide (scCO₂) to plasticize the system and reduce interfacial tension between phases [421-426]. Many authors have also found scCO₂ useful in free radical polymerization of monomers as well as grafting of polyolefins [425-433]. This high pressure additive has many other uses, including extraction and infusion of low molecular weight materials, foaming agent, plasticizer, etc. [425, 426, 434-436].

Carbon dioxide, above its critical point of 1037 psi and 31.7°C, has the diffusivity of a gas and viscosity similar to a liquid [425, 426]. These properties, along with its safe storage and handling and low cost make CO₂ an interesting candidate to improve the processing of polymers. scCO₂ has been shown to enhance free radical reactions in the polymerization of vinyl monomers but also to improve the mixing of immiscible polymers. Some authors have found that solid state and melt free radical grafting of monomers onto polypropylene is facilitated by the increased diffusivity and high pressures from scCO₂. The purpose of the following experiment was to identify whether this additive can improve the grafting efficiency of reactive extrusion, which correlates positively with mechanical properties.

Figure 6-26 reveals that when scCO₂ is injected into zone 5 of the extruder, grafting efficiency decreases in a linear fashion. This result is not necessarily surprising because scCO₂ is a solvent for low molecular weight organic liquids, such as styrene. Also, the temperature of the injected fluid is much lower than the normal reaction conditions, which could adversely affect efficiency because the peroxide decomposition rate and polymerization rate is slowed. Many of the previous studies used batch mixers and experiments that lasted hours to study the grafting efficiency, but the residence time is so

short in the extruder that this may prevent scCO₂ from promoting grafting. Several suggestions for improving the grafting yield using scCO₂ are given in Chapter 8 under future recommendations.

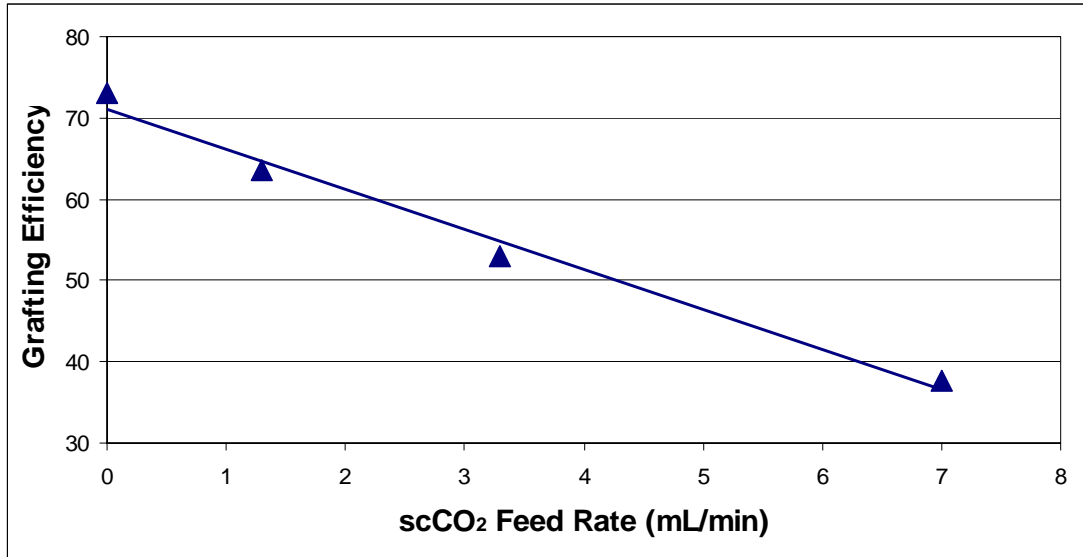


Figure 6-26: Effect of supercritical carbon dioxide at 1500 psi on the grafting efficiency of 8842_B. Injection was in zone 3.

6.4 Conclusions

This chapter exemplifies the idea that material selection of the elastomer is crucial to balancing blend and alloy mechanical properties while maintaining processability. The crystalline content and chain length of the elastomer plays a large role in dictating alloy and blend mechanical properties. Some obvious trends are seen in blends and alloys: as elastomer density increases, impact strength decreases but elastic modulus and yield strength increase. The grafting efficiency is drastically lower for 8402_B than 8407_B, which can be traced back to fact that 8402 has a higher % crystallinity and T_m so it melts at a later point along the extruder barrel. This leaves more time for homopolymerization to take place. If one were to maximize both impact strength and elastic modulus of PP, a combination of 8402 and 8407 may give the desired result.

Elastomer MFI (molecular weight) also has a profound effect on mechanical properties. A high MFI is preferential for an optimal balance of properties because below a molecular weight limit, the blend/alloy behaves in a brittle manner. This can be directly related to the higher degree of physical entanglements, higher viscosity, and lower number of chain ends in the low MFI elastomer. The processability of 8842_B may be compromised as evidenced by its low melt flow index value of 0.4 g/10min, which is why a lower molecular weight elastomer may be preferred (i.e. 8407).

CHAPTER 7 REACTIVE EXTRUSION OF HIGH DENSITY POLYETHYLENE

7.1 Introduction

Impact modification of polypropylene was very successful, so the reactive extrusion process was applied to another commodity plastic – high density polyethylene (HDPE). Polyethylene is one of the largest volume polymers produced in the last decade [437]. It is expected to have an average annual growth rate of 5.2% in terms of demand-production during the decade spanning 2000-2010. The objective of this chapter is to design a set of experiments so as to identify the most crucial aspects of modifying HDPE and to improve its impact strength while balancing stress-strain properties. HDPE normally crosslinks in the presence of peroxide, but the reactive extrusion process described in previous chapters has shown that an insoluble gel does not form for PP alloys.

7.2 Experimental

7.2.1 Materials

Table 7-1 gives a list of ethylene-1-octene copolymers and manufacturer's data. The impact modifier of interest was ENGAGE® 8842 [48]. HDPE was supplied by ExxonMobil as the grade Paxon AM 55-003. All polymers were received and used in pellet form. Table 7-2 lists structures of the reactive materials. The peroxide and monomers used in this study were reagent grade chemicals. The monomers were purified by passing through an activated alumina column before use. Styrene monomer, inhibited by 10-15 ppm t-butyl catechol, was purchased from Fisher.

Table 7-1: ENGAGE® product data table.

Engage® Grade (decreasing comonomer content)	8842	8407	8200	8401	8402
Comonomer Content wt% ¹³ C NMR/FTIR	45	40	38	31	22
Density, g/cm ³ ASTM D-792	0.857	0.870	0.87	0.885	0.902
Melt Index, dg/min ASTM D-1238 190°C, 2.16 kg	1.0	30	5.0	30	30
Mooney Viscosity ASTM D-1646 ML 1 + 4 at 121°C	26	< 5	8	< 5	< 5
Durometer Hardness, Shore A ASTM D-2240	50	72	75	85	94
DSC melting Peak, °C Rate: 10°C/min	33	60	60	78	98
Glass Transition Temp, °C DSC inflection point	-61	-57	-56	-51	-44
Flexural Modulus, MPA ASTM D-790, 2% Secant	3.5	12.1	12.1	25.8	69.9
Ultimate Tensile Strength, MPa ASTM D-638, 508 mm/min	2.1	3.3	6.9	6.4	12.9
Ultimate Elongation, % ASTM D-638, 508 mm/min	975	>1000	>1000	950	790

Table 7-2: Structures of reactive materials of interest

Name	Lupersol 101	DEGDA
Structure		
Name	Styrene	
Structure		

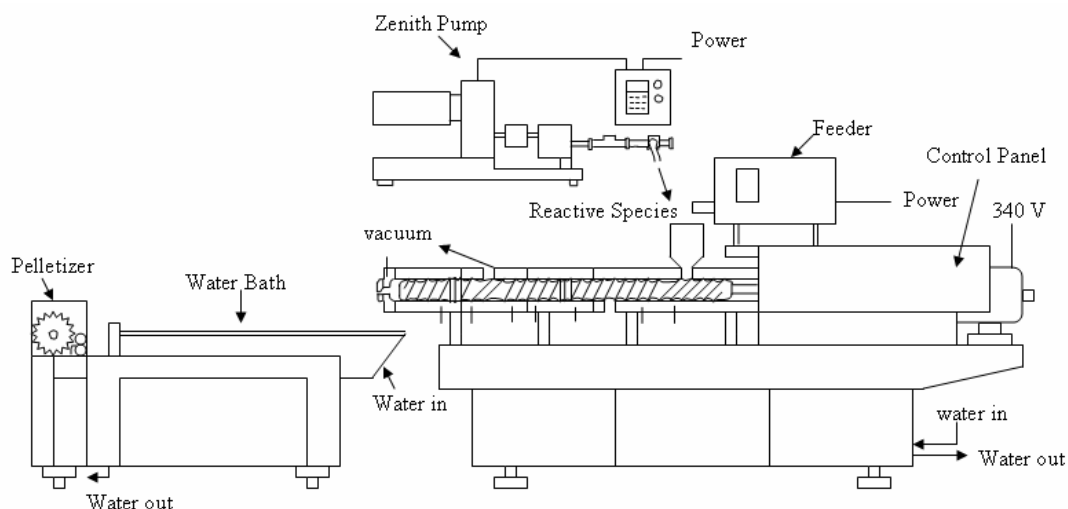
The initiator, 2,5dimethyl-2,5-di-(t-butylperoxy) hexane, was purchased from Atofina under the trade name Lupersol 101. Diethyleneglycol diacrylate (DEGDA), inhibited by 80ppm Hq and 120 ppm MEHQ, was graciously donated by Sartomer, an Atofina company.

7.2.2 Methods

7.2.2.1 Processing

All polymers were dried in an air circulating oven at 40°C for 24 hours prior to compounding. Before processing, the resins were premixed by hand for about 10 minutes. The monomers were passed through activated alumina columns to remove residual inhibitor. Monomer/initiator mixtures are magnetically stirred for 10 minutes before processing and a choice amount of the mixture was added to the dry polymer pellets before processing.

The blending was carried out in a 34 mm non-intermeshing, co-rotating twin screw extruder, APV Chemical Machinery (now B&P Process Systems) with an L/D ratio of 39. The temperature of the extruder was regulated by electrical resistance and water circulation in the barrels. The dried, pre-mixed resins were then introduced into the



Die	Zone 1	Zone 2	Zone 3	Zone 4	Zone 5	Zone 6	Zone 7 (Feed)
195°C	205°C	210°C	210°C	200°C	190°C	180°C	165°C

Figure 7-1: Schematic drawing of the reactive twin screw extruder and a common temperature profile.

extruder at 60 g/min through a screw dry material feeder, Accu Rate, Inc. A Zenith pump controlled the rate of monomer/initiator solution addition into the extruder. The screw

speed, unless otherwise noted was 150 rpm. Devolatilization was carried out by a vacuum pump, VPS-10A, Brooks Equipment Company. This was placed near the die and created a pressure of about 15 in Hg. The extruder was always starved to feed. Figure 7-1 is a schematic of the extruder, with a typical temperature profile. After compounding, the resulting strands which exit the die are quenched in a water bath, pelletized, and dried in a vacuum oven at 100°C, 28 in Hg for 24 hours.

7.2.2.2 Mechanical properties

In order to measure the strength of the material at very high testing rates, a notched Izod impact test was performed according to ASTM D256 standards. The pellets were placed in a mold with 6 slots, each measuring 0.5x0.5x2.5 in³. The mold was put in a Carver press (Fred S. Carver, Inc.) at 200°C and after the material melts, pressed up to 5000 psi. After waiting for 5-10 minutes, the pressure was slowly increased up to 10,000 psi. After another 5 minutes, the heat was turned off and the sample is let to cool down to room temperature at about 1.5°C/min. The bars were then taken out and notched with a Testing Machines, Inc. (TMI) notching machine. Before testing, they were conditioned at room temperature for 24 hours. A 30 ft-lb hammer was used with test method A on a TMI Izod impact tester. At least 5 bars were broken and impact strength is recorded as an average regardless of full or partial break.

For stress-strain measurements, dried pellets were placed in a mold measuring 15x15 cm²x1 mm thick. The mold is put into the Carver press at 200°C and after the material melts, pressed up to 5000 psi. After a 5-10 minute wait, the sample was slowly pressed to 10,000 psi. Five minutes later, the sample was quenched in a water bath. Specimens were tested according to ASTM D638 standards. Type V specimens were punched out of the compression molded sheet with a die, measuring 1 mm thick, 2.95

mm gauge width and 9.5 mm gauge length. Five samples were tested after conditioning at room temperature for 48 hours. The machine used to test the samples was an MTS Model 1120 Instron, using a 1000 lb load cell at a test speed of 12.7 mm/min.

7.2.2.3 Design of experiments

In a characterization experiment, we are usually interested in determining which process variables affect the response [438, 439]. Experiments done in Chapters 3 thru 6 have shown screw speed, temperature, and concentrations of additives (initiator, multifunctional monomer, styrene, and elastomer) have some effect on the mechanical properties of PP. These same process variables will be used to characterize the response of HDPE. Table 7-3 lists these factors and their corresponding codes and levels. The next logical step is to optimize – create a response surface using a factorial or central composite design. A fractional factorial design allows an experimenter to screen out factors that do not significantly affect the response variables by limiting the total

Table 7-3: Factors of interest, coded variables, and levels for the impact modification of HDPE

<u>Variable</u>	<u>Name</u>	<u>-1 Level</u>	<u>+1 Level</u>
A	% Initiator	0.3	1
B	% Styrene	4	8
C	PE:ENG8842	95:5	85:15
D	Screw Speed	100	200
E	% DEGDA	0.5	1
F	Temperature	190	210

number of experiments. The design of interest uses 6 factors at two levels each, for a total of 16 experiments. Tables 7-3 and 7-4 describe the experimental design of interest, including factors and levels. DesignExpert 6.0.11 from Stat-Ease, Inc. was used to generate the design and analyze the data.

Table 7-4: Basic fractional factorial design using coded variables from Table 7-3.

Fractional Factorial Design						
2 ⁶⁻² with 16 Runs Total						
Generated Variables = Temperature and % DEGDA						
Basic Design						
Run	A	B	C	D	E = ABC	F = BCD
1	-	-	-	-	-	-
2	+	-	-	-	+	-
3	-	+	-	-	+	+
4	+	+	-	-	-	+
5	-	-	+	-	+	+
6	+	-	+	-	-	+
7	-	+	+	-	-	-
8	+	+	+	-	+	-
9	-	-	-	+	-	+
10	+	-	-	+	+	+
11	-	+	-	+	+	-
12	+	+	-	+	-	-
13	-	-	+	+	+	-
14	+	-	+	+	-	-
15	-	+	+	+	-	+
16	+	+	+	+	+	+

7.3 Results and Discussion

7.3.1 Mechanical Properties

Table 7-5 includes all materials, levels, and resultant impact strength and stress-strain properties. The highest modulus, yield stress, and elongation at break are seen for pure HDPE, as expected, and the pure polymer also has the lowest impact strength. The good tensile performance is due to the high % crystallinity typically found in HDPE. The modulus and yield stress are not as high as those found for pure PP in Chapter 3, even though PP typically has lower % crystallinity than HDPE. HDPE is composed of radially oriented lamellar crystals which take shape in the spherulite, whereas PP is composed of cross-hatched spherulitic structures which are much stiffer [337, 370, 371, 375, 388]. The impact strength of pure HDPE is 2.2 ft-lbs/in, which is over two times greater than pure PP at 0.99 ft-lbs/in. This could be due to the less stiff crystalline state of HDPE, but

a more plausible explanation is that HDPE has low temperature relaxations (T_g is reported to be around -130°C) in which chains have the mobility to respond to high rate impact tests [100, 105, 107, 109, 304]. The T_g of PP has been reported to be about -10°C .

HDPE typically shows drastic increase in impact strength alongside a decrease in modulus with addition of a rubbery phase [125]. This trend is seen when blending HDPE with 8842 at both the 85:15 and 95:5 levels. The ENGAGE grade 8842 was chosen over 8407 because in a physical blend with HDPE it improved HDPE's impact strength to a greater extent. This may be attributed to better mixing of 8842 with HDPE and the existence of entangled high molar mass chains. Also, the density of 8842 is less than 8407.

There are many notable features in Table 7-3. Sample 16 has an impact strength of 16 ft-lbs/in, the highest value of all experiments in the Table and for all PP alloys. But its stress strain performance is poor compared to pure HDPE. The HDPE was originally thought to crosslink and form an entangled network with 8842, therefore reaping the benefits of high impact strength from the 8842 phase and high tensile strength from the HDPE phase via stress transfer mechanism. Initiator level does have to be above a certain level before any appreciable crosslinking can occur [7, 184, 187] and addition of monomer reduces the tendency to crosslink. Also, the grafting efficiency is believed to be lower for the HDPE-8842 system than PP-8407 system from bond dissociation energy considerations and the fact that HDPE is highly crystalline so it will have to be completely molten before any grafting will take place. For run 16, all variables are at

Table 7-5: Impact strength, elastic modulus, yield stress, and elongation at break results from the fractional factorial design created for the modification of HDPE.

Run	wt% Initiator	wt% Styrene	ENG8842	Screw Speed (rpm)	wt% DEGDA	Max Temp (°C)	Impact Strength (ft-lbs/in)	Std. Dev.	Elastic Modulus (MPa)	Std. Dev.	Stress at Yield (MPa)	Std. Dev.	Elongation at break (mm)	Std. Dev.
1	0.3	4	5	100	0.5	190	3.0	0.25	1279	101	24.3	1.2	52	8
2	1	4	5	100	1	190	8.3	0.80	908	66	21.1	0.8	25	5
3	0.3	8	5	100	1	210	1.5	0.25	1529	113	26.6	0.3	31	8
4	1	8	5	100	0.5	210	3.1	0.20	1133	98	23.2	0.6	17	3
5	0.3	4	15	100	1	210	7.6	0.30	809	33	19.7	0.8	61	10
6	1	4	15	100	0.5	210	14.8	0.40	634	47	18.6	0.5	33	14
7	0.3	8	15	100	0.5	190	7.0	0.30	864	68	20.0	0.6	49	8
8	1	8	15	100	1	190	14.7	0.90	693	35	18.2	0.3	29	5
9	0.3	4	5	200	0.5	210	2.8	0.20	1199	76	24.5	1.5	47	15
10	1	4	5	200	1	210	6.3	0.35	1033	78	22.7	1.1	31	2
11	0.3	8	5	200	1	190	2.6	0.10	1303	120	25.4	0.9	50	11
12	1	8	5	200	0.5	190	4.4	0.40	1000	48	22.4	0.8	31	5
13	0.3	4	15	200	1	190	7.7	0.30	832	120	20.0	1.3	60	7
14	1	4	15	200	0.5	190	15.0	0.60	646	24	17.0	2.0	26	6
15	0.3	8	15	200	0.5	210	7.7	0.40	845	71	19.8	0.5	63	12
16	1	8	15	200	1	210	16.0	0.60	690	41	18.2	1.0	48	3
Pure PE	-	-	-	100	-	190	2.2	0.10	1571	105	29.2	1.0	56	14
Physical Blend PE:8842 = (95:5)				100	-	190	3.3	0.10	1356	80	25.5	0.7	89	11

their high level, so a high amount of elastomer in conjunction with a high concentration of free radicals and monomer is beneficial to impact strength. This leads one to believe that the grafting of monomer is highest for this alloy. Also, notice that yield stress is highest for alloys at the low concentration of 8842 and initiator, so the crystal phase is not disrupted at these low levels. Between all alloys in this table, run 3 has the highest modulus and the lowest impact strength. The initiator and 8842 levels are low but all other levels are high so the grafting degree may be very low for this sample. In turn, the crystalline phase is not as drastically affected and so it retains its mechanical integrity.

7.3.2 Design of Experiments Results

The disadvantage of using a fractional factorial design is that each main-effect and interaction contrast will be confounded with one or more other main-effect and interaction contrasts and so cannot be estimated separately. Two factorial contrasts that are confounded are referred to as being aliased. The aliasing problem comes to the surface when a significant main effect is identified, but is not clear whether the observed effect is due to the main effect or to its interaction with other factors or to the combination of both. Because of the aliasing problem, fractional factorial designs are most often used as screening experiments. Appendix E lists the factorial effects aliases of interest.

7.3.2.1 Impact strength

When analyzing data from unreplicated factorial designs, occasionally real high-order interactions occur. A normal probability plot is thus used to estimate the effects. Figure 7-2 is a half normal plot of the significant effects on impact strength. The effects that are negligible are normally distributed, with a mean of zero and a variance of σ^2 and will tend to fall along a straight line in this plot. Significant effects will have nonzero

means and will not lie along the straight line. A diagnostic check indicates that the only significant effects are initiator, HDPE:8842 ratio, and the interaction between them.

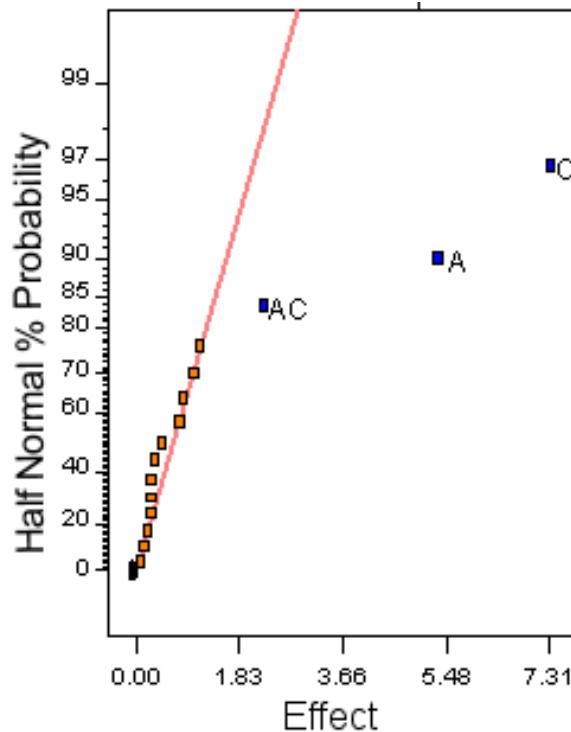


Figure 7-2: Half normal plot showing, in coded variables, the most significant effects on impact strength. A = initiator concentration and C = concentration of 8842.

Analysis of variance is derived from a partitioning of total variability into its component parts and is exemplified in Table 7-6. Sum of squares is a measure of the overall variability of the data. If the sum of squares is divided by the appropriate number of degrees of freedom, the sample variance would result. The number of degrees of freedom of a sum of squares is equal to the number of independent elements in that sum of squares. Each mean square is simply its sum of squares divided by its degrees of freedom. F is essentially a test statistic for the null hypothesis and the F ratio is the mean square of the treatment of interest divided by the mean square of the error within treatments. At an $\alpha = 0.05$, the F value is accepted, so the null hypothesis is rejected and both initiator and 8842 concentration significantly affect impact strength. The model F-

value of 76.6 implies the model is significant. There is only a 0.01% chance that a model F-value this large could occur due to noise. Values of "Prob > F" less than 0.05 indicate model terms are significant. In this case A, C, AC are significant model terms. Values greater than 0.10 indicate the model terms are not significant.

Table 7-6: Analysis of variance table (partial sum of squares) for impact strength.

Source	Sum of Squares	Degrees of Freedom	Mean Square	F Value	Prob > F
Model	348.8	3	116.3	76.6	< 0.0001
significant					
A (% initiator)	113.96	1	114	75.1	< 0.0001
C (% 8842)	213.89	1	214	141	< 0.0001
AC	20.93	1	21	13.8	0.003
Residual	18.20	12	1.5		
Cor Total	366.98	15			
Std. Dev. = 1.23	R-Squared = 0.95				
Mean = 7.7	Adj. R-Squared = 0.94				
C. V. = 16.1	Pred. R-Squared = 0.92				
PRESS = 32.4	Adeq. Precision = 20.5				

The "Pred R-Squared" of 0.92 is in reasonable agreement with the "Adj R-Squared" of 0.94. "Adeq Precision" measures the signal to noise ratio. A ratio greater than 4 is desirable, so the ratio of 20.5 indicates an adequate signal. This model can be used to navigate the design space. The final equation in terms of coded factors:

$$\text{Impact Strength} = +7.66 + (2.67 * A) + (3.66 * C) + (1.14 * A * C) \quad (7.1)$$

The final equation in terms of actual factors:

$$\text{Impact Strength} = -0.36 + (1.09 * \% \text{ Initiator}) + (0.31 * \text{Amt ENG8842}) + (0.65 * \% \text{ Initiator} * \text{Amt ENG8842}) \quad (7.2)$$

One more method to check for model adequacy is in Figure Figure 7-7(a), which is a normal probability plot of studentized residuals. Because of the linearity of this figure, the model is said to have a normal distribution about the mean. Figure 7-7(b) shows what, if any, outliers (i.e. influential values) are present. An outlier will have an

unusually high positive or negative value and are easy to detect from this plot. Outliers may be due to the error variables not being normally distributed, having different variances, or an incorrect specification of model. Run 2 is the only outlier but it also has a higher standard deviation than all other runs. This material has a high concentration of initiator and DEGDA but low levels of temperature, screw speed, and styrene. These each have typically opposite effects on grafting efficiency of PP from Chapter 5. A high

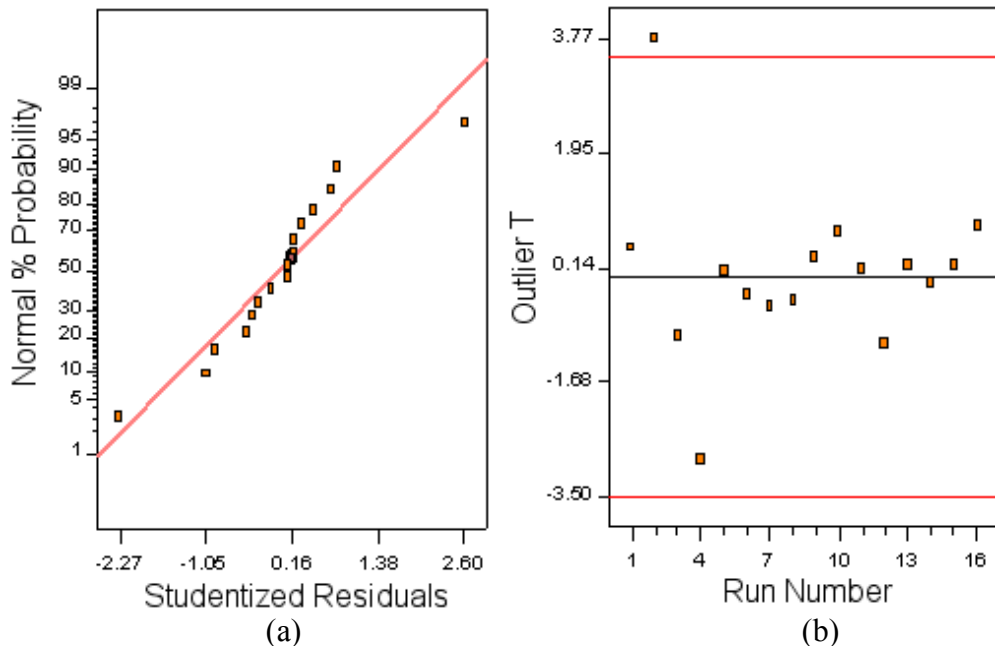


Figure 7-3: Normal plot of residuals (a) and outliers (b) show the diagnostic results of the model for impact strength.

initiator means more primary free radicals and hence higher grafting, high DEGDA content traps generated free radicals and creates more of a branched structure, low styrene means less homopolymerized material, low temperature leads to lower grafting efficiency, and lower screw speed has a tendency towards higher grafting efficiency.

Figure 7-4 is a cube graph of impact strength at various levels for each of these parameters. For high impact strength, initiator and 8842 concentration must be at their high levels, but all other variables will not have the same influential effects.

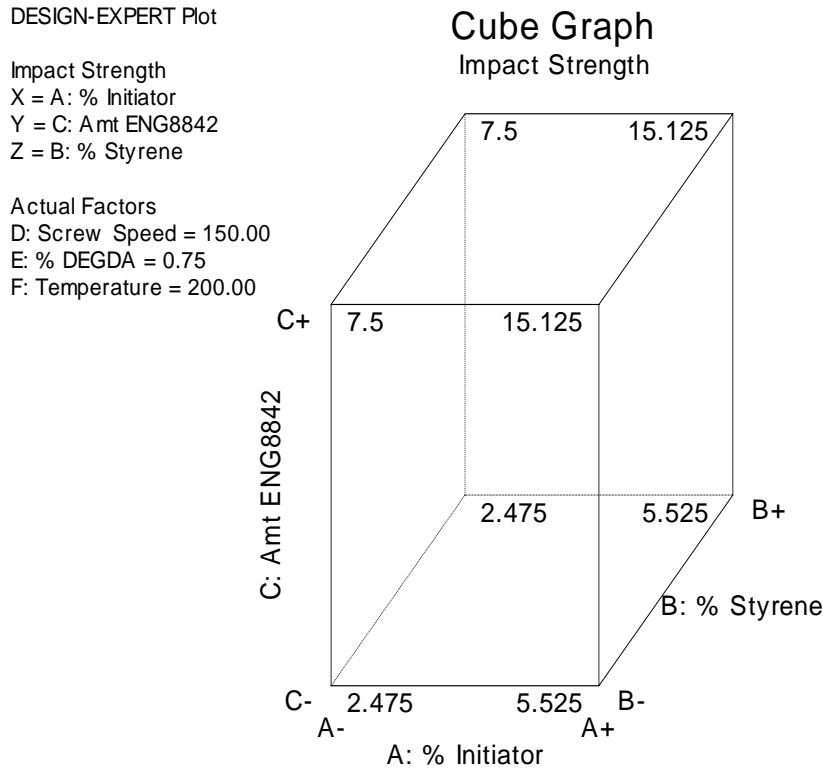


Figure 7-4: Cube graph of the effect of % initiator, 8842 content, and % styrene on impact strength at constant screw speed, % DEGDA, and temperature.

7.3.2.2 Elastic modulus

The half normal % probability plot in Figure 7-5 shows that only two variables (% initiator and 8842 content) significantly affect the response of elastic modulus. Analysis of variance in Table 7-7 gives a lot of information regarding the adequacy of the model and the ability to predict future outcomes. The model F-value of 56.1 implies the model is significant. There is only a 0.01% chance that a model F-value this large could occur due to noise. Values of "Prob > F" less than 0.05 indicate model terms are significant. In this case A, C, are significant model terms. Values greater than 0.10 indicate the model terms are not significant. The "Pred R-Squared" of 0.843 is in reasonable agreement with the "Adj R-Squared" of 0.88. "Adeq Precision" measures the signal to noise ratio. A

ratio greater than 4 is desirable. The ratio of 16.7 indicates an adequate signal. This model can be used to navigate the design space.

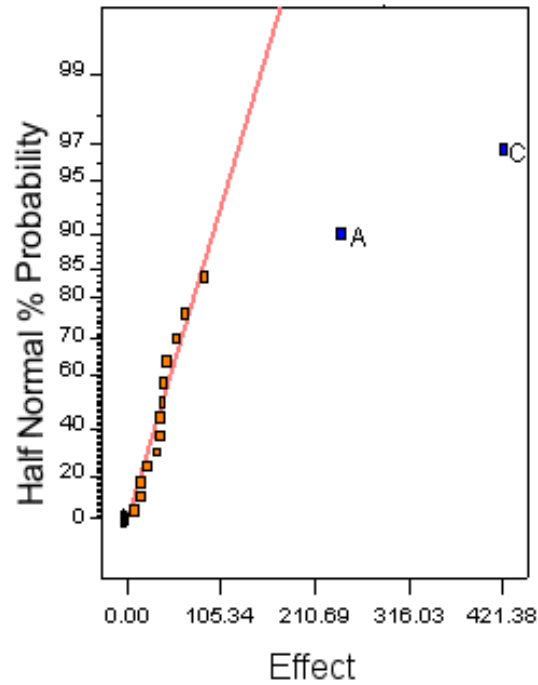


Figure 7-5: Half normal plot showing, in coded variables, the most significant effects on elastic modulus.

Table 7-7: Analysis of variance table (partial sum of squares) for elastic modulus.

Source	Sum of Squares	Degrees of Freedom	Mean Square	F Value	Prob > F
Model	9.4E+5	2	4.71E+5	56.1	< 0.0001
significant					
A	2.3E+5	1	2.31E+5	27.5	0.0002
C	7.1E+5	1	7.1E+5	84.6	< 0.0001
Residual	1.1E+5	13	8392.9		
Cor Total	1.05E+6	15			
Std. Dev. = 91.6		R-Squared = 0.90			
Mean = 962.3		Adj. R-Squared = 0.88			
C. V. = 9.5		Pred. R-Squared = 0.84			
PRESS = 1.6E+005		Adeq. Precision = 16.68			

The final equation in terms of coded factors:

$$\text{Elastic Modulus} = + 962 - (120 * A) - (211 * C) \quad (7.3)$$

The final equation in terms of actual factors:

$$\text{Elastic Modulus} = + 1607 - (343 * \% \text{ Initiator}) - (42 * \text{Amt ENG8842}) \quad (7.4)$$

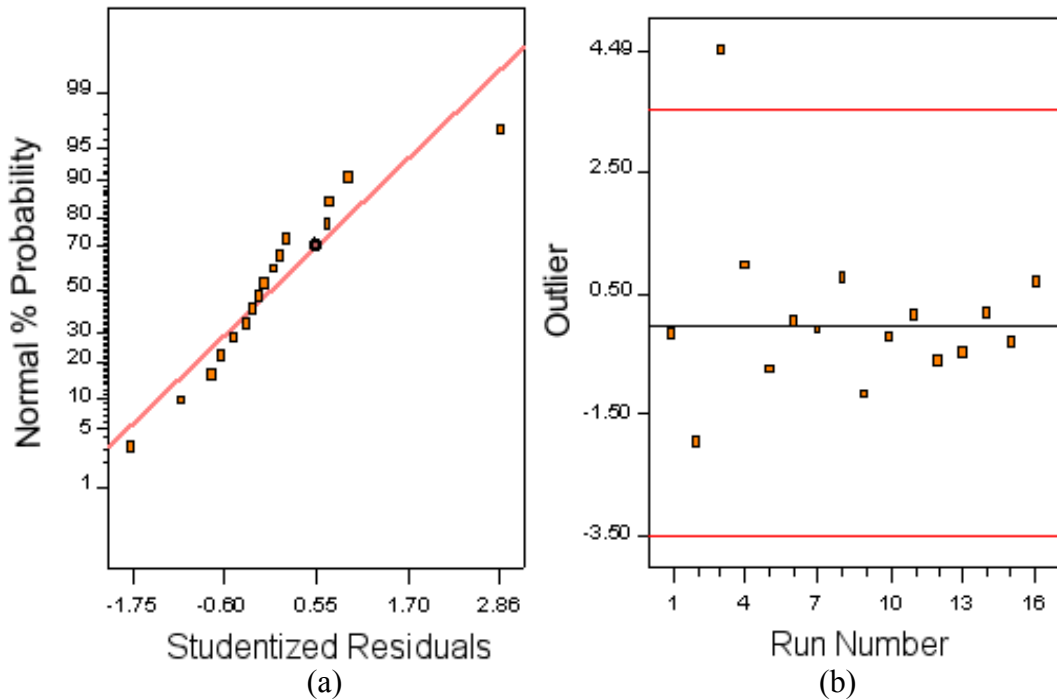


Figure 7-6: Normal plot of residuals (a) and outliers (b) show the diagnostic results of the model for elastic modulus.

Because of the linearity of this figure, the model is said to have a normal distribution about the mean. Figure 7-6(b) shows what, if any, outliers (i.e. influential values) are present. Run 3 is the only outlier, which has an extraordinarily high value. The material has a low initiator concentration and was extruded at a low temperature, but contains high monomer concentrations at the higher temperature. Elastic modulus is essentially the resistance of the non-crystalline phase of the plastic to deformation at low strains. A high initiator concentration may promote crosslinking of both PE and 8842, which should positively effect elastic modulus. The cube graph in Figure 7-7 shows the opposite trend. There may be pockets of insoluble gel which negatively effect stress-strain properties as a separate dispersed phase. More studies have to be conducted

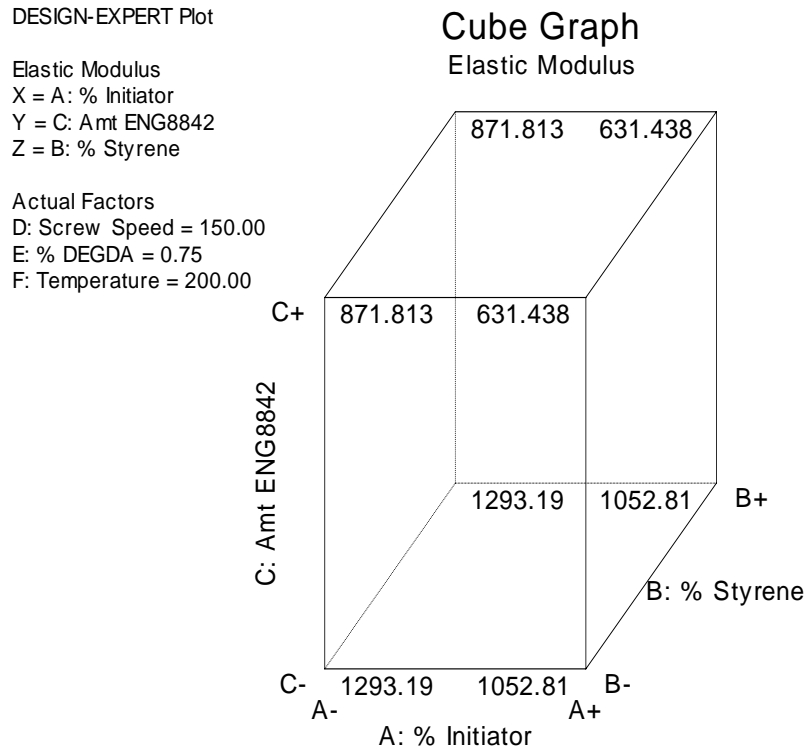


Figure 7-7: Cube graph of the effect of % initiator, 8842 content, and % styrene on elastic modulus at constant screw speed, % DEGDA, and temperature.

regarding gel content and grafting efficiency. Lower initiator concentrations presumably lead to lower levels of grafting in HDPE, but at high monomer concentrations, there is likely a high percentage of highly entangled, homopolymerized material within the amorphous phase. Further studies also need to be performed on the crystalline state of the alloys because lamellar crystals will essentially act as filler particles in the amorphous phase and thus stiffen the polymer. At high initiator concentrations, the crystalline state may be disrupted.

7.3.2.3 Yield strength

The half normal plot in Figure 7-8 indicates that, like elastic modulus, % initiator and 8842 concentration have the greatest effect on yield stress.

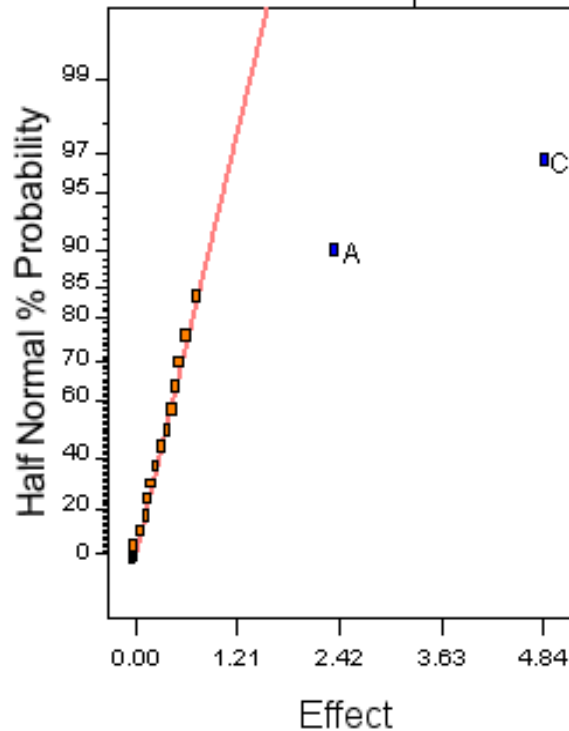


Figure 7-8: Half normal plot showing, in coded variables, the most significant effects.

From the analysis of variance (Table 7-8), the model F-value of 92.3 implies the model is significant. There is only a 0.01% chance that a model F-value this large could occur due to noise. In this case A and C are significant model terms. The "Pred R-Squared" of 0.90 is in reasonable agreement with the "Adj R-Squared" of 0.92. "Adeq Precision" measures the signal to noise ratio. A ratio greater than 4 is desirable. The ratio of 21 indicates an adequate signal. This model can be used to navigate the design space. The final equation in terms of coded factors is:

$$\text{Yield Strength} = + 21.4 - (1.2 * A) - (2.4 * C) \quad (7.5)$$

The final equation in terms of actual factors is:

$$\text{Yield Strength} = + 28.4 - (3.4 * \% \text{ Initiator}) - (0.5 * \text{Amt ENG8842}) \quad (7.6)$$

Figure 7-9(a) is linear with respect to studentized residuals, so the results from this design are normal about the mean. There are no outliers from Figure 7-9(b) and the

Table 7-8: Analysis of variance table (partial sum of squares) for yield stress.

Source	Sum of Squares	Degrees of Freedom	Mean Square	F Value	Prob > F
Model	115.9	2	58	92.3	< 0.0001
significant					
A	22.3	1	22.3	35.5	< 0.0001
C	93.6	1	93.6	149	< 0.0001
Residual	8.2	13	0.6		
Cor Total	124.1	15			
Std. Dev. = 0.79	R-Squared = 0.93				
Mean = 21.4	Adj. R-Squared = 0.93				
C. V. = 3.7	Pred. R-Squared = 0.90				
PRESS = 12.4	Adeq. Precision = 20.98				

distribution of is random about zero. The cube graph in Figure 7-10 indicates that 8842 and initiator level should be low in order to maximize yield stress. The crystalline state may be adversely affected at high initiator concentrations and insoluble gel may deleteriously affect yield stress, but more studies have to be conducted on this issue.

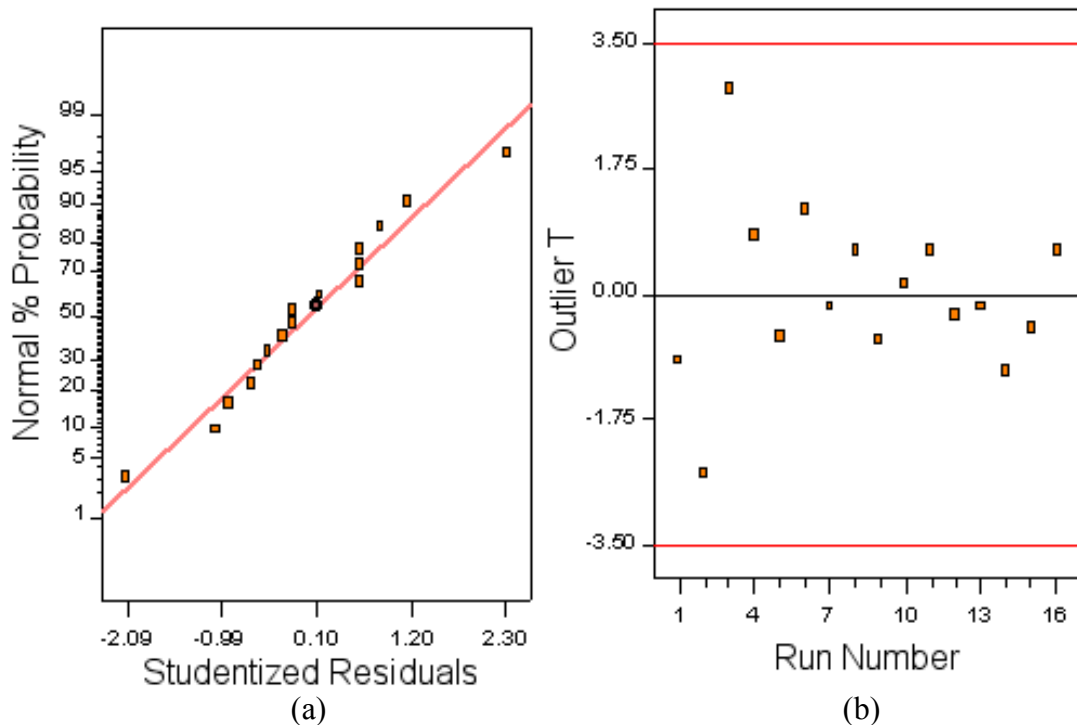


Figure 7-9: Normal plot of residuals (a) and outliers (b) show the diagnostic results of the model for yield stress.

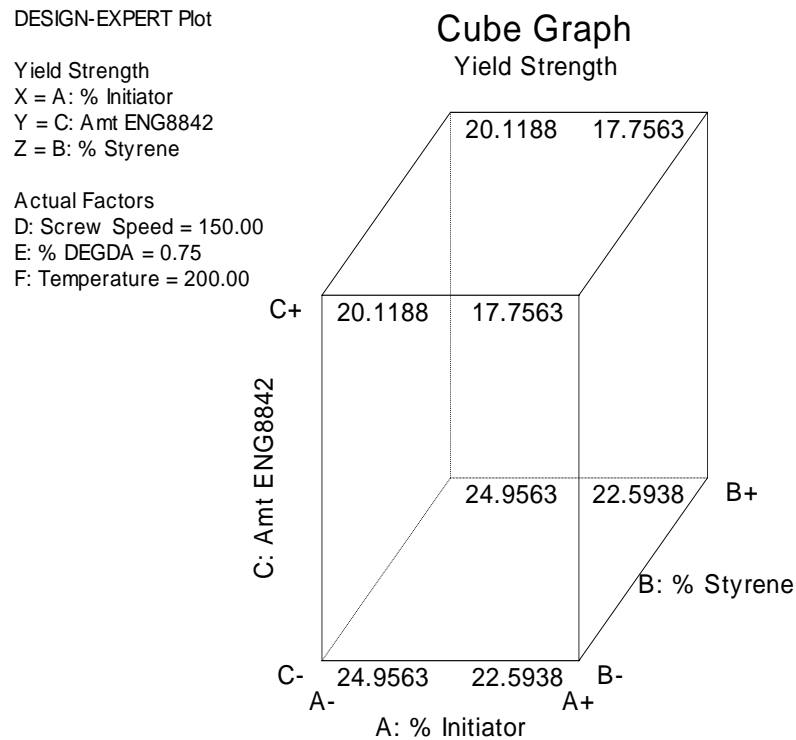


Figure 7-10: Cube graph of the effect of % initiator, 8842 content, and % styrene on yield stress at constant screw speed, % DEGDA, and temperature.

7.3.2.4 Elongation at break

Elongation (the ability to neck and draw) is more sensitive to defects and morphology than the other three mechanical properties studies thus far [271, 272]. This is evidenced by the greater number of significant effects from Figure 7-11. The initiator concentration has the greatest effect, followed by 8842 concentration, screw speed, and the interaction between screw speed and % styrene.

The ANOVA table (Table 7-8) gives direct analysis of these main effects. The model F-value of 27.5 implies the model is significant. There is only a 0.01% chance that a model F-value this large could occur due to noise. Values of "Prob > F" less than 0.05 indicate model terms are significant. In this case A, C, D, and BD are significant

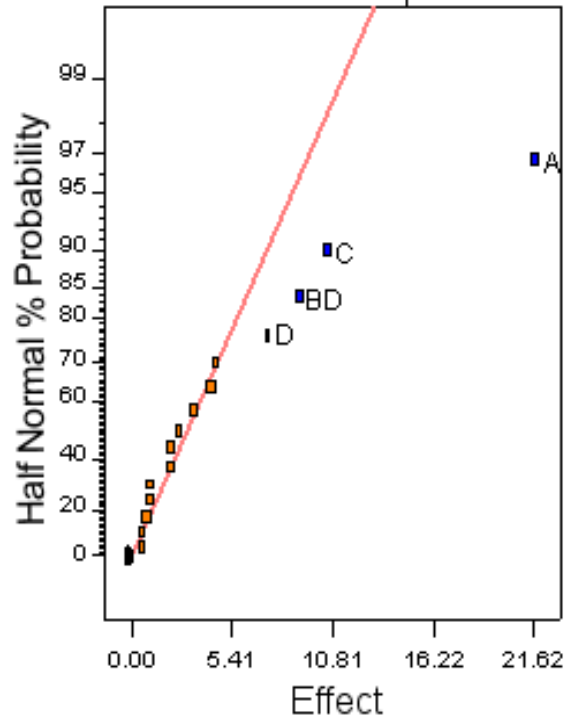


Figure 7-11: Half normal plot showing, in coded variables, the most significant effects.

model terms. Values greater than 0.10 indicate the model terms are not significant.

The "Pred R-Squared" of 0.81 is in reasonable agreement with the "Adj R-Squared" of 0.88. "Adeq Precision" measures the signal to noise ratio. A ratio greater

Table 7-9: Analysis of variance table (partial sum of squares) for elongation at break.

Source	Sum of Squares	Degrees of Freedom	Mean Square	F Value	Prob > F
Model	2872.8	4	718.2	27.5	< 0.0001
significant					
A	1870.6	1	1870.6	71.5	< 0.0001
C	451.6	1	451.6	17.3	0.002
D	72.7	1	72.7	2.8	0.124
BD	333.1	1	333.1	12.7	0.004
Residual	287.7	11	26.2		
Cor Total	3160.4	15			
Std. Dev. = 5.1		R-Squared = 0.9090			
Mean = 40.8		Adj. R-Squared = 0.88			
C. V. = 12.5		Pred. R-Squared = 0.81			
PRESS = 608.7		Adeq. Precision = 17.1			

than 4 is desirable. The ratio of 17.1 indicates an adequate signal. This model can be used to navigate the design space. The final equation in terms of coded factors is:

$$\text{Elongation} = + 40.8 - (10.8 * A) + (5.3 * C) - (4.3 * D) + (3.4 * B * D) \quad (7.7)$$

The normal probability plot in Figure 7-12 is linear, so the results are normal about the mean. There are no outliers from Figure 7-12(b) and the distribution is random about zero. The cube graph in Figure 7-13 shows that a high amount of 8842 along with a lower screw speed and initiator concentration will give the greatest elongation at break. This means that the amorphous 8842 may have a higher molar mass than HDPE or crosslinking may not be significant. A low initiator concentration means lower degree of grafting and side reactions like crosslinking. But a lower screw speed means longer residence time and less intensive mixing. From data gathered in Chapter 5 regarding PP, lower initiator concentration gives a high elongation at break but low screw speed results in low elongation.

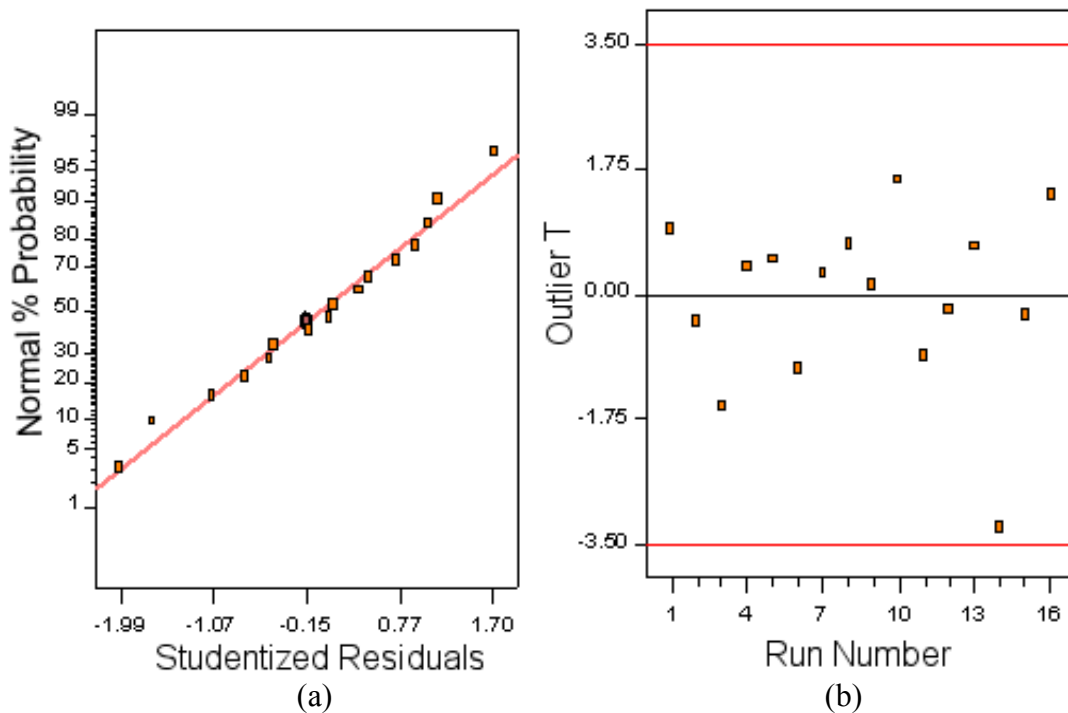


Figure 7-12: Normal plot of residuals (a) and outliers (b) show the diagnostic results of the model for elastic modulus.

DESIGN-EXPERT Plot

Elongation
 X = A: % Initiator
 Y = C: Amt ENG8842
 Z = D: Screw Speed

Actual Factors
 B: % Styrene = 4.00
 E: % DEGDA = 0.76
 F: Temperature = 193.78

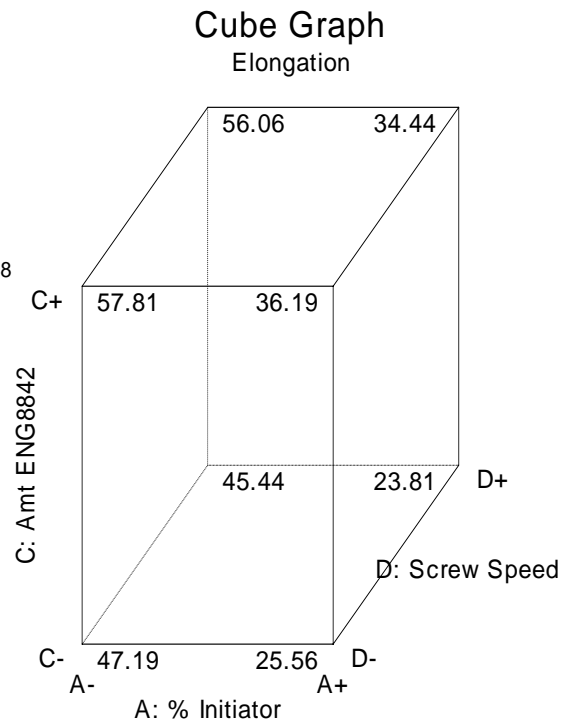


Figure 7-13: Cube graph of the effect of % initiator, 8842 content, and % styrene on elongation at break at constant % styrene, % DEGDA, and temperature.

7.4 Conclusions

The reactive extrusion of HDPE to increase its impact strength has been successful, but its stress-strain performance suffered, which is typical of rubber toughened thermoplastics. The grafting of the polymers was thought to increase the resistance to a tensile load, which it does in the Izod impact test. But at slow deformation rates, homopolymerized and non-polymerized monomer may affect the response of the alloy to a greater extent.

A design of experiments proved to be invaluable in deciding what variables significantly affected responses and the levels at which properties are maximized. The wt% initiator and amount of 8842 proved to be most important for overall property control. The initiator dictates when and to what extent the free radical grafting,

polymerization, and crosslinking events will take place. The content of 8842 has such a drastic effect on properties due to its non-crystalline state and low T_g characteristics. Also, 8842 is thought to be phase separated from HDPE, so its interfacial interactions will play a huge role in macroscopic properties.

CHAPTER 8 CONCLUSIONS AND FUTURE WORK

8.1 Summary and Conclusions

This work successfully described how to improve isotactic polypropylene's (PP) impact strength and why this occurs without compromising stress-strain performance. A novel ethylene-1-octene copolymer (EOC) was used as the impact modifier in the blends and alloys due to its outstanding low temperature toughness, limited defect distribution, excellent processability, and a fully saturated backbone. A low molecular weight grade has been shown to be an excellent candidate for modifying PP because it can be easily dispersed and distributed within the matrix.

By simply blending the impact modifier with PP, a modest jump in impact strength is seen but the all too common decrease in tensile strength, modulus, and elongation at break are experienced. So, a reactive extrusion process was employed to:

- Stabilize the phase separated domains within the matrix phase,
- Reduce average domain size, and
- Create an efficient stress transfer mechanism between phases.

This process used free radical chemistry to polymerize monomers using a so-called *in-situ* compatibilization technique as a one-step synthetic method to produce a polypropylene alloy. The combination of a peroxide initiator, styrene, and a multifunctional acrylate have proven to give a high grafting efficiency, low melt flow index, outstanding melt strength, and extremely high impact strength along with improved stress-strain behavior over the physical blend.

There are many types of reactions present in this complex reactive extrusion process. A key to controlling the microstructure of the alloys and the resulting macro-scale properties is to understand free radical grafting mechanisms. Figure 4-38 allows one to visualize the reactions likely occurring during the reactive extrusion process. As can be seen, initiator decomposition is the rate determining step, but once that

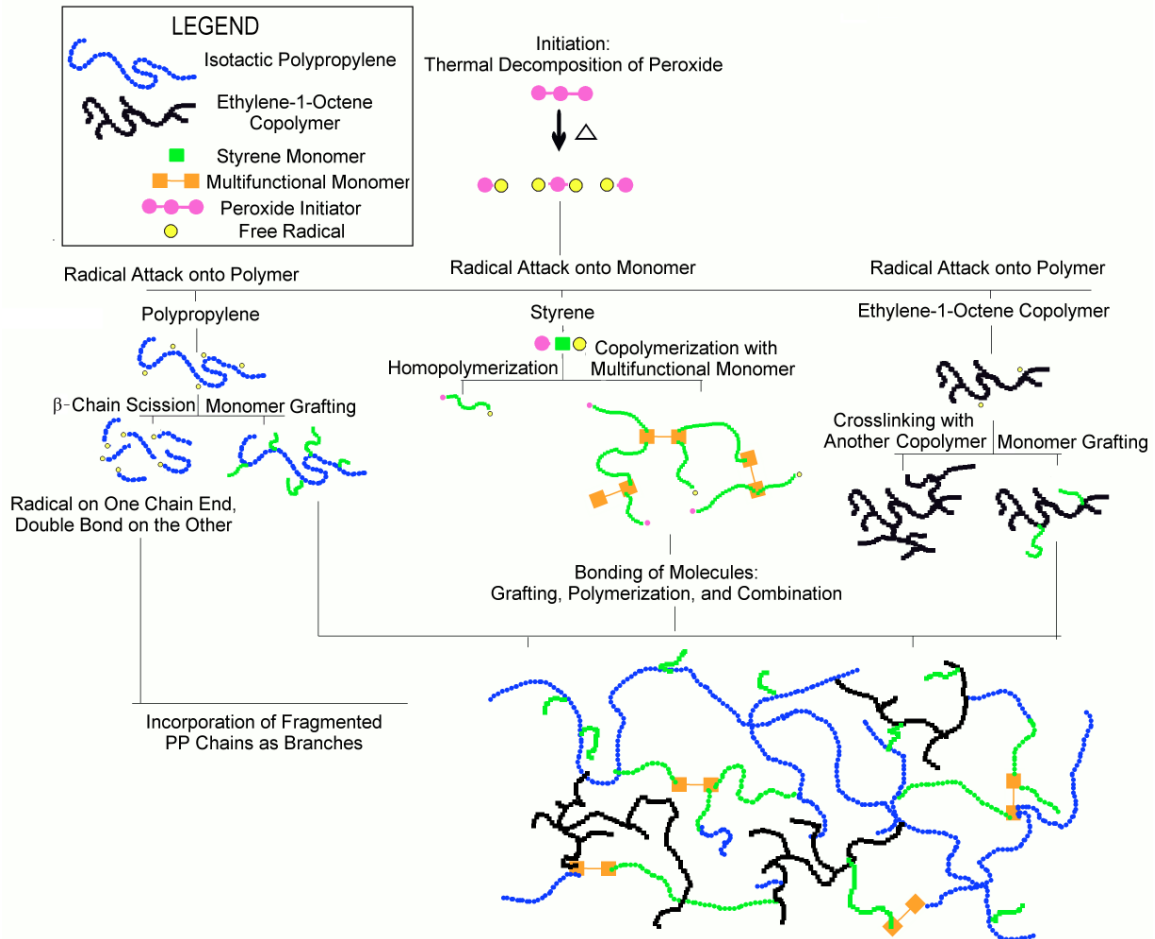


Figure 8-1: Schematic drawing of the likely free radical initiated processes during the reactive extrusion of PP, 8407, initiator, styrene, and multifunctional monomer.

energy barrier is overcome, several reactions happen at once. These include monomer polymerization, hydrogen abstraction from polymers, grafting of monomers onto polymers, and degradation of polymers. The end result is likely a diffusely

interconnected, branched collection of macromolecules with unique morphology, improved melt properties, and excellent mechanical properties.

Many interesting amorphous and crystalline features have been created through this reactive extrusion process. Using TEM for example, elastomer domains in the physical blends are distributed bimodally as spherical domains that range in size from 50 to 150 nm. For high impact samples, domains range in size from 10 nm (distributed throughout the sample) to oblong 300 nm domains having a variety of stained material dispersed throughout. SEM has shown that the physical blend's etched domains are roughly spherical, but the alloys have irregularly shaped domains which are much smaller in diameter and closer in proximity to each other. During an impact test, the extension of the amorphous phase and a rise temperature likely results in both a phase transformation and a highly elastic retractive force, thereby limiting chain breakage.

Figure 8-2 shows an interpretation of how grafted material locates in and around dispersed elastomer domains in a polypropylene-based alloy. For the high impact strength alloys, a high grafting efficiency coupled with small elastomer domains leads to a high degree of physical entanglements, covalent bonding, and an altered stress field at the interface of the particles. Also, grafting is thought to occur throughout these small domains. The mobility of the amorphous phase of PP is restricted in the presence of these branching components but dispersion of the elastomer on such a small scale may change the relaxation time distribution of PP. For the physical blends, large particles exist with a greater interparticle distance. This results in a low particle-matrix surface area and the ability to absorb energy through typical mechanisms like shear yielding, crazing, and cavitation is reduced.

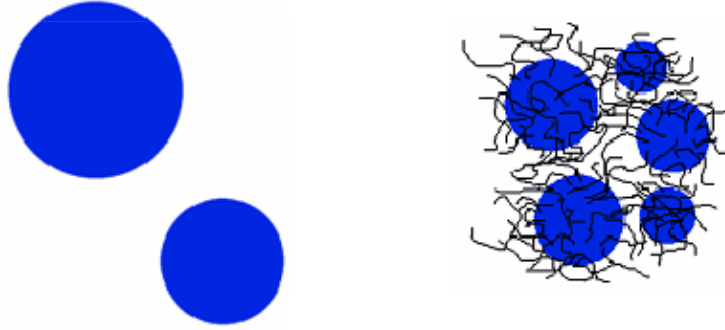


Figure 8-2: Interpretation of the effect of *in-situ* grafted polymeric chains at the PP-elastomer interface (blue circles = elastomer domains, black lines = grafted polymers). The physical blend (left) has no grafting and the alloy (right) has a high degree of grafting.

The crystalline state of the alloys is unique in that many small crystals with a high cross-hatch density are distributed throughout the sample. The high surface area leads to a higher energy state of the crystal, so the process of melt and recrystallization during deformation is facilitated. This enhances mechanical properties by absorbing and dissipating energy efficiently. Also, the β phase of PP is present in the alloys, which is known to have more energy absorption capability than the α phase due to its larger lattice structure and lower melting enthalpy. Polarized light microscopy coupled with DSC proved invaluable in the study of the crystallization of these materials. The high branching and interconnected network of the alloys drastically increases the crystallization temperature and decreases the spherulite size compared to its physical blend counterparts. The unique molecular architecture appears to promote the local ordering process known as the induction period before the well known nucleation and growth phenomenon.

Processing variables have a significant effect on overall properties of the alloys. Initiator concentration, which is the rate determining step in the grafting process, has a drastic effect on overall properties of the alloy. A high grafting efficiency does not

necessarily translate into high impact strength because of the degradation of PP through chain scission. Screw speed, barrel temperature, and monomer concentrations all play important roles in the performance of the alloy. Grafted material positively influences the overall mechanical properties of PP, but it is still not known whether this is due to a reduction in the amount of homopolymerized material, reduction in degradation of PP, and/or improvement of interfacial adhesion.

By controlling the properties of the impact modifier, both the blend and alloy's macro-scale performance can be dictated. A high density elastomer will give a high elastic modulus and yield strength, but poor impact strength. It will melt at a later point along the extruder barrel which results in a low grafting efficiency for the alloy. An elastomer with a very high MFI (low MW) will not give good impact properties because of its lack of molecular entanglements and tendency to coalesce. On the other hand, there is a sharp transition of elastomer molecular weight where all mechanical, rheological, and chemical properties drastically improve.

High density polyethylene, when modified using the reactive extrusion process with a high MW elastomer, gives an extremely high impact strength but at the expense of a low modulus and yield stress. A high degree of homopolymerized material as well as disturbance of the crystalline state of HDPE may be the cause for the imbalance of properties. A design of experiments approach allowed objective results to be obtained regarding which parameters affected impact strength, yield stress, modulus, and elongation at break.

8.2 Future Work

Reactive extrusion is such a diverse, versatile system that innumerable possibilities exist for the modification of polymers. One unique study that should be done is to use

fluorescent or deuterated monomers during the in-situ reactive extrusion process. One can then monitor and map out, either by confocal fluorescent microscopy, SANS, or NMR, the length of grafts, the placement of grafts, and the exact composition of grafts. The morphology of the alloys was so interesting that further studies must be done to clarify exactly what the deeply stained domains represent. Positron annihilation will give the free volume of the system, which is sure to change upon modification of polymers by grafting monomers. TEM coinciding with electron diffraction will elucidate the exact lamellar structure(s) present. Light scattering is another important technique when studying crystalline morphology. By annealing the high impact samples and comparing DSC and XRD results to pure PP, one should get a better idea of the limiting effect of branching on chain folding. Isothermal crystallization experiments will show the crystallization kinetics of the system and verify the belief that multifunctional monomer drastically increases crystallization rate. Also, *in-situ* small angle neutron scattering will allow one to explore the induction period before nucleation and growth, which should be unique to this alloy.

Studies should be conducted on the deformation and fracture mechanisms of this system. *In-situ* deformation experiments using TEM is vital to understand the structure of these alloys – will the stained regions cavitate, craze, or delaminate from the surrounding material? Stained TEM sections of the region surrounding the arrested crack tip in fractured impact bars may be very informative. Distinct ductile-to-brittle transitions should be found, even though it is already known that at high monomer and elastomer concentrations the materials changes its behavior from tough and ductile to brittle. The crack surfaces should be studied in more detail, as well as the notch

sensitivity. AFM or nanoindentation is valuable in polymer characterization because it should be able to pinpoint the modulus and viscoelasticity of the established nanometer-sized domains. Also, *in-situ* XRD/tensile deformation experiments should be done to determine exactly what phase transformations occur during deformation.

The processing conditions can further be varied to include an array of monomers with diverse viscosities and functionalities. The type and half life of initiator can be varied, powder instead of PP granules may be used, pellets could be imbibed with monomer mixtures before processing, and design should be created with a more complete set of experiments using supercritical carbon dioxide (scCO₂) as a processing/grafting aid. Supercritical CO₂ should be added at different ports along the extruder, it should be used with a variety of peroxides having lower half lives at 200°C, extruder screw speed should be lowered and barrel temperature should be increased when using scCO₂.

Adding high strength fillers to polymers is of great interest due to their ability to enhance mechanical, thermal, and rheological properties. Further studies should include the use of layered silicate clays (possibly montmorillonite), exfoliated graphite, carbon nanotubes, silica nanoparticles, and tungsten carbide whiskers, to name a few. A unique study may encompass surface functionalization of the particles to facilitate bonding between phases. Combining rigid fillers with thermoplastics is done through inexpensive, continuous processing routes, but a problem facing materials scientists is to efficiently disperse and distribute all types of particles having different surface chemistries. Alignment of high aspect ratio fillers may also be a desirable feature while melt processing to leverage their isotropic structures. Application of supercritical carbon dioxide is one method to do this. By functionalizing the surface of the nanoparticles with

scCO₂-philic functional groups, the shear forces in an extruder along with scCO₂ will facilitate the needed dispersion and distribution.

scCO₂ will also allow production of nano-elastomer domains in thermosets which will improve toughening to a greater extent than micron-sized elastomers. The RESS process (Rapid Expansion from a Supercritical Solution) has been modified recently to include Rapid Expansion of a supercritical solution into a solvent (RESolv). This shows promise in being able to dissolve polymers in scCO₂ and upon release of pressure shoot small polymeric particles into the matrix of choice.

APPENDIX A
CALIBRATION CURVE FOR ABSOLUTE STYRENE CONCENTRATIONS IN
REACTIVE BLENDS

For quantification of the grafted styrene, a calibration curve (Figure A-2) had to be established. This was done by extruding polypropylene/polystyrene blends of varying PS concentrations. By taking the ratio of the areas under the 700 cm^{-1} and 1376 cm^{-1} peaks and relating this to the amount of styrene added, absolute amounts of styrene present can be easily calculated. A ratio of areas is taken from Figure A-1 so that thickness variations will not affect the results.

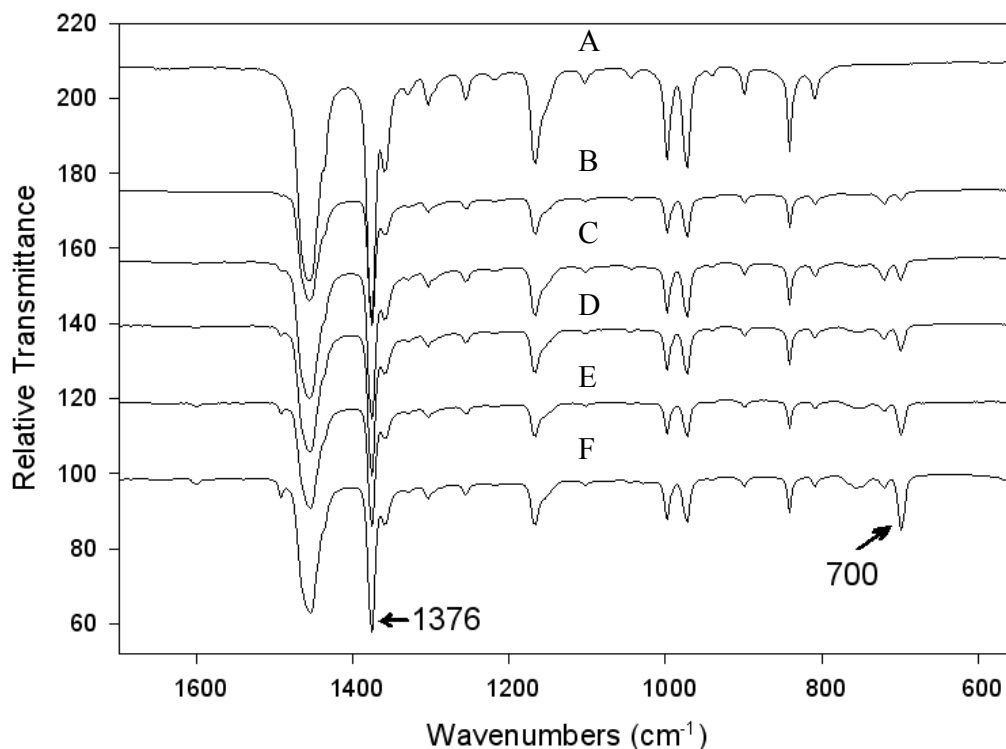


Figure A-1: FTIR calibration graphs of iPP/PS physical blends with varying PS content; A = 0%, B = 2%, C = 4%, D = 6%, E = 8%, F = 10%.

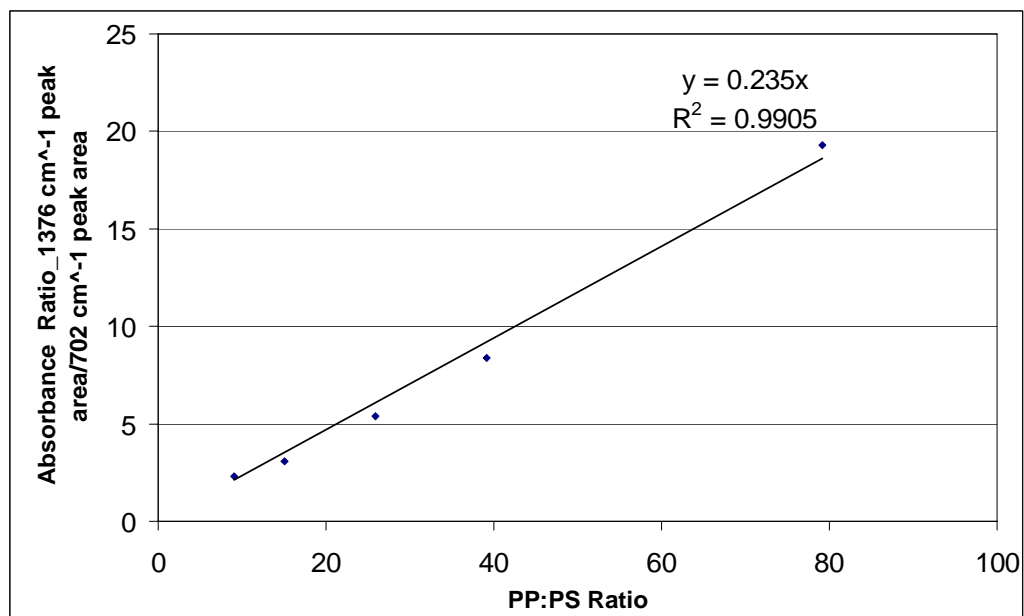


Figure A-2: Calibration curve for absolute styrene content determination

APPENDIX B
STRESS-STRAIN GRAPHS AND STATISTICS

This Appendix contains both graphs and statistical data for stress-strain behavior in Chapters 3, 4, 5, and 6.

Table B-1: Actual stress-strain values with standard deviations for Figures in Chapter 3 and Chapter 4.

Sample ID	Modulus (MPa)	σ_{Yield} (MPa)	Elongation at Break (mm)	σ_{Break} (MPa)	Energy to Break (N*mm)
Pure PP	1833 ± 57	36.8 ± 1.7	74 ± 2	49.4 ± 1.4	6000 ± 274
95:5_0	1707 ± 84	32.6 ± 0.3	70 ± 8	42.8 ± 2.5	5683 ± 943
95:5_A	1740 ± 36	33.4 ± 1.1	49 ± 8	38.3 ± 1	4254 ± 680
95:5_B	1858 ± 105	34.7 ± 1.6	54 ± 7	43.8 ± 5.2	5149 ± 1298
95:5_C	1761 ± 60	33.1 ± 0.9	53 ± 9	41.3 ± 4.2	4800 ± 1392
90:10_0	1450 ± 59	28.0 ± 1.9	58 ± 12	38.7 ± 4.8	4038 ± 825
90:10_A	1502 ± 74	28.3 ± 0.9	57 ± 4	37 ± 1.1	3840 ± 736
90:10_B	1695 ± 110	30.9 ± 1.5	60 ± 4	42.6 ± 1.5	4294 ± 155
90:10_C	1621 ± 47	29.9 ± 1	59 ± 4	41.8 ± 1.7	4458 ± 723
80:20_0	1125 ± 66	23.4 ± 1.1	39 ± 8	24.5 ± 3.5	3065 ± 1094
80:20_A	1275 ± 94	24.6 ± 1.8	35 ± 14	29 ± 4.8	2677 ± 896
80:20_B	1347 ± 77	24.8 ± 0.5	54 ± 10	35.8 ± 4.3	3635 ± 1269
80:20_C	1356 ± 110	25.3 ± 2	56 ± 10	35.9 ± 4.6	3488 ± 1208
70:30_0	928 ± 91	17.1 ± 1.1	6.1 ± 3	9.8 ± 1.1	179 ± 117
70:30_A	996 ± 37	18.1 ± 2.6	7 ± 3	15 ± 1.9	237 ± 79
70:30_B	1054 ± 33	18.5 ± 1	19 ± 7	19.8 ± 4.3	1308 ± 765
70:30_C	1109 ± 53	20.3 ± 1.6	11 ± 5	20.3 ± 1.5	768 ± 200

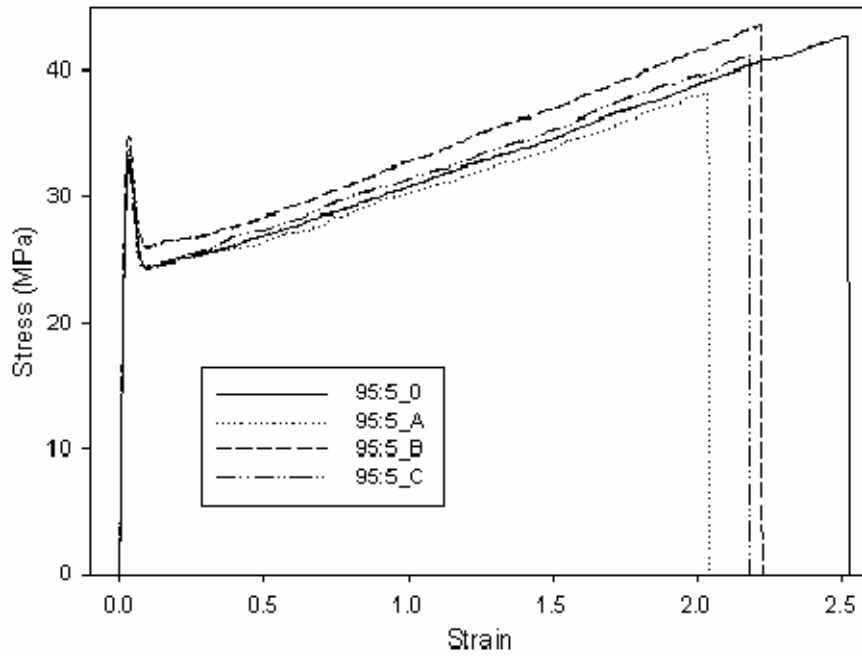


Figure B-1: Stress-strain graph comparison of 95:5 (PP:8407) physical blend and alloys.

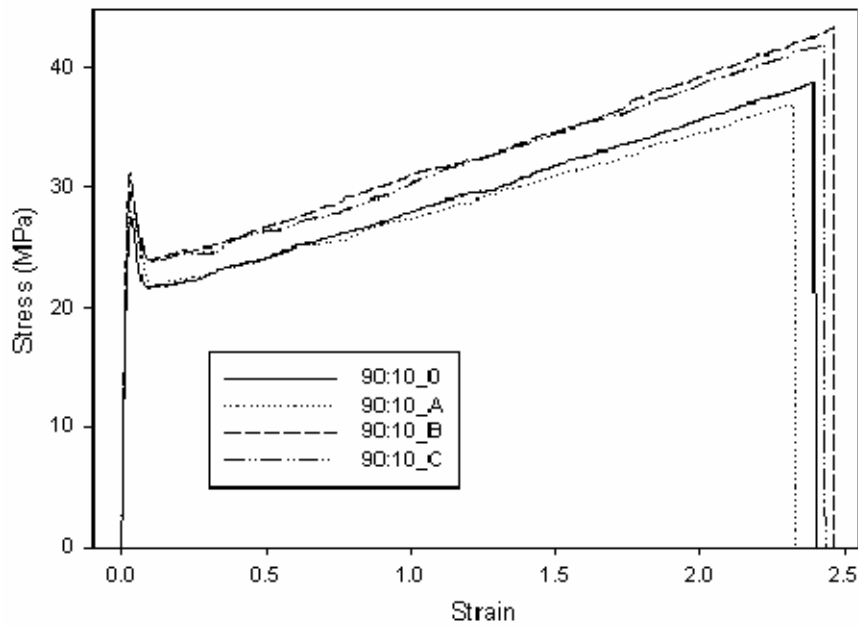


Figure B-2: Stress-strain graph comparison of 90:10 (PP:8407) physical blend and alloys.

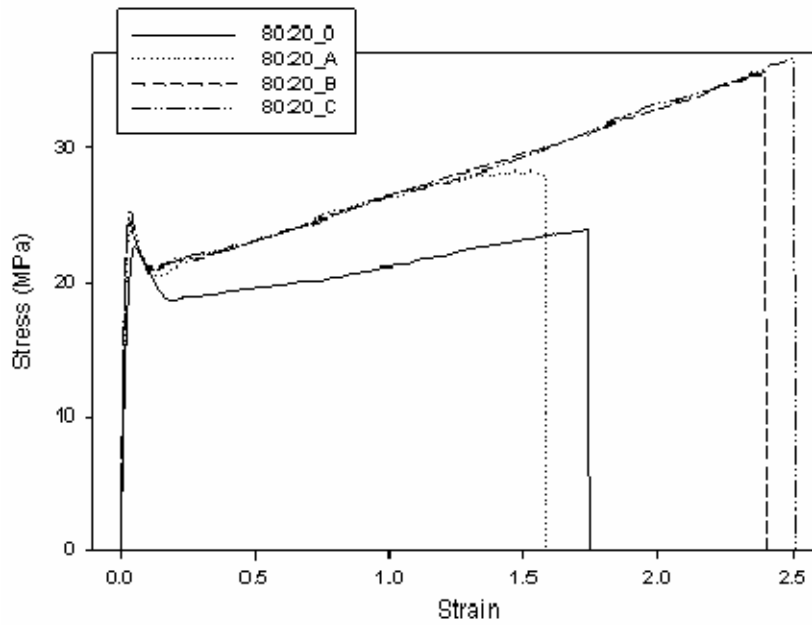


Figure B-3: Stress-strain graph comparison of 80:20 (PP:8407) physical blend and alloys.

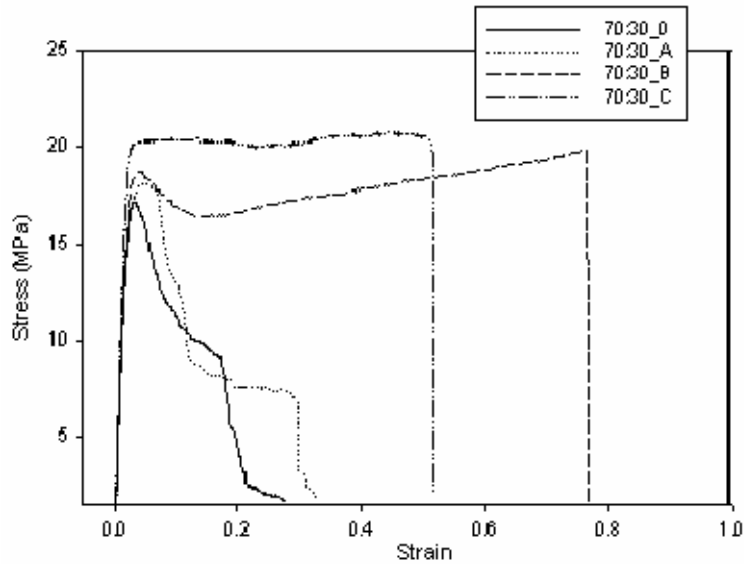


Figure B-4: Stress-strain graph comparison of 70:30 (PP:8407) physical blend and alloys.

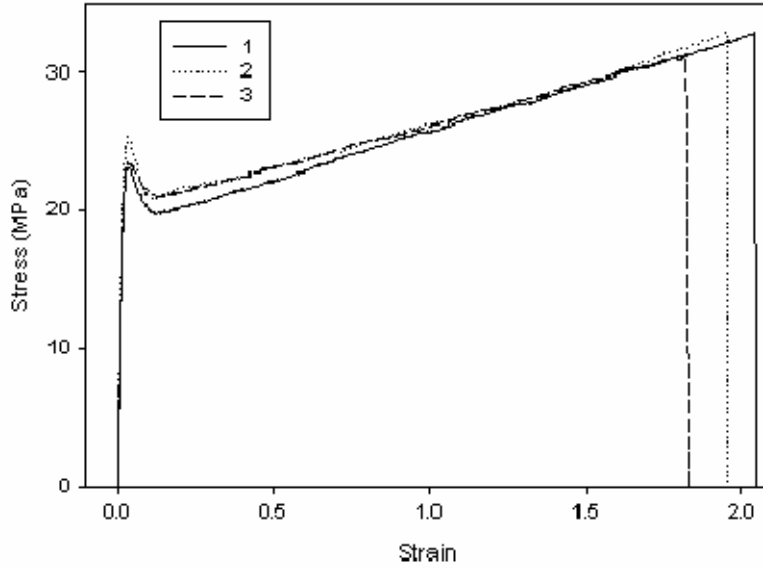


Figure B-5: Stress-strain graph comparison of the effect of extruder barrel temperature in relation to Figure 5-2 and Table 5-4. 1= low temperature, 2=middle temperature, 3=high temperature.

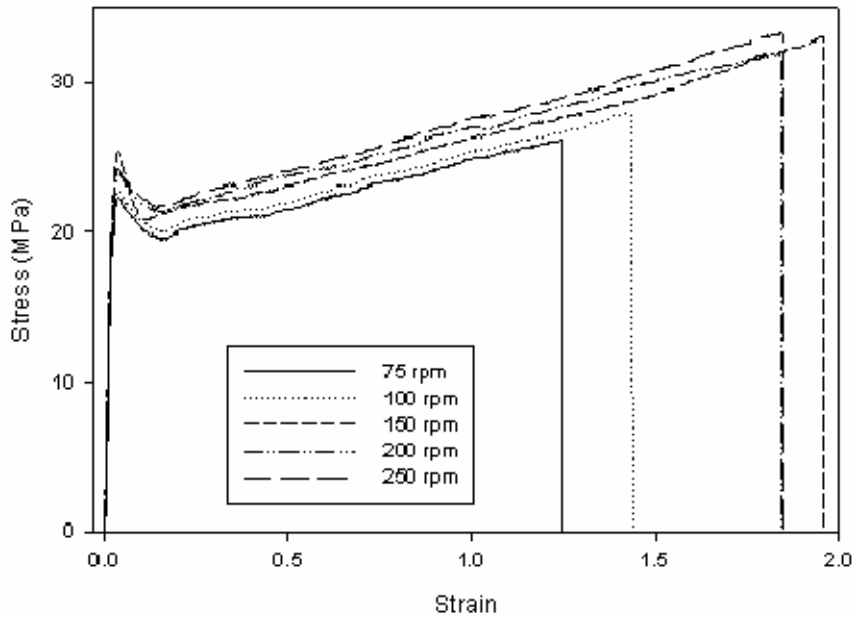


Figure B-6: Stress-strain graph comparison of the effect of extruder screw speed in relation to Table 5-6.

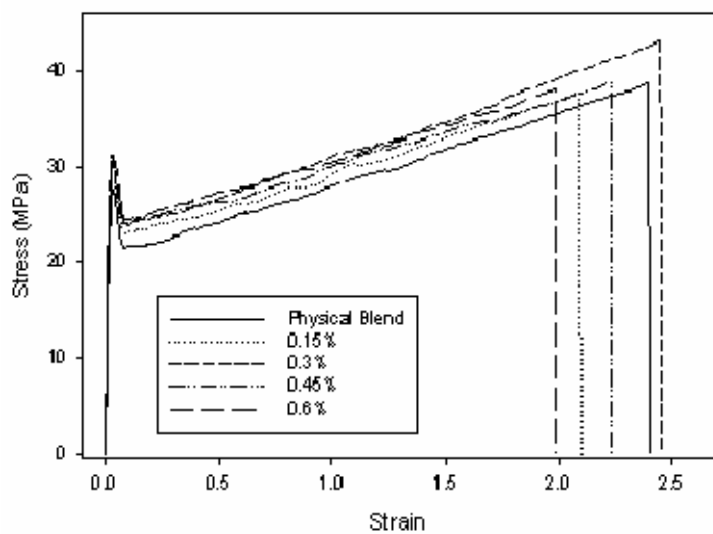


Figure B-7: Stress-strain graph comparison of the effect of initiator concentration in relation to Table 5-7.

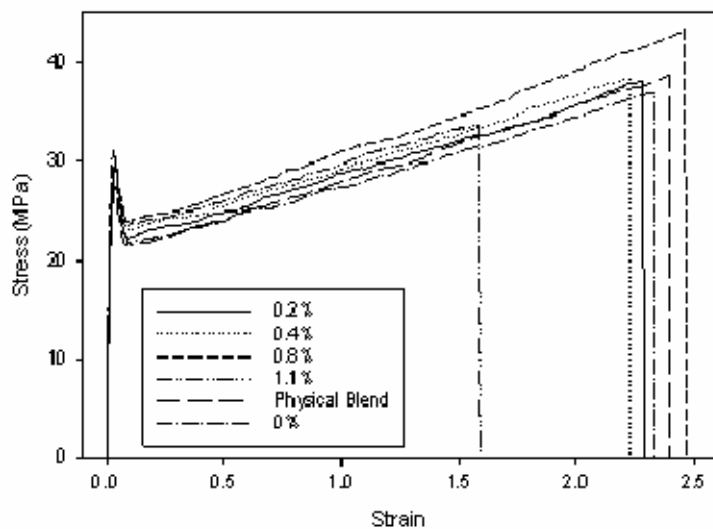


Figure B-8: Stress-strain graph comparison of the effect of DEGDA concentration in relation to Table 5-8.

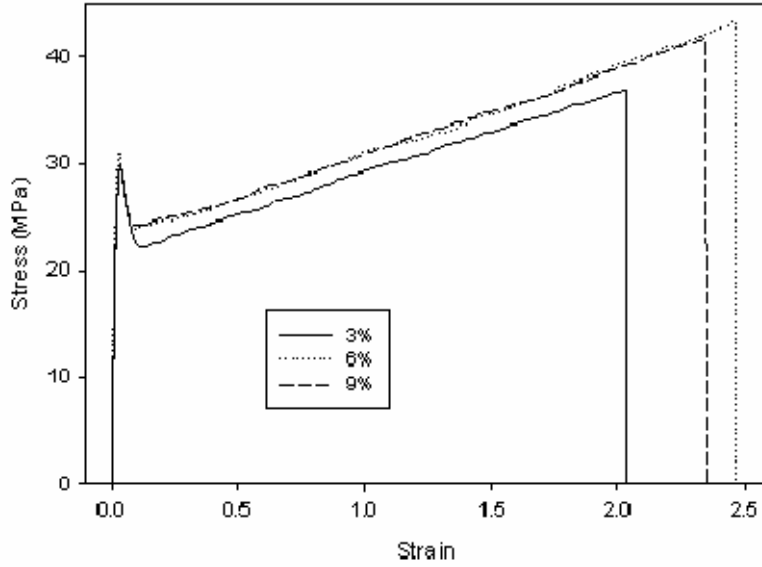


Figure B-9: Stress-strain graph comparison of the effect of styrene concentration in relation to Table 5-9.

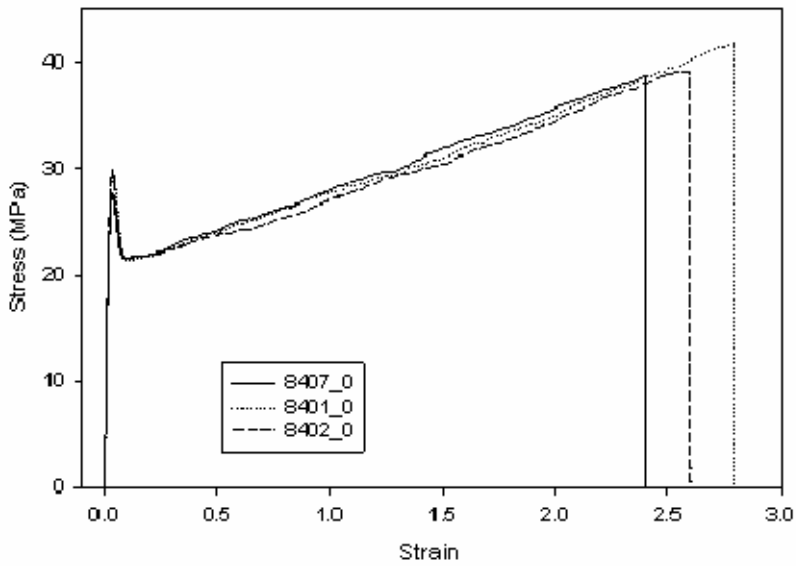


Figure B-10: Stress-strain graph comparison of the effect of elastomer density in relation to Table 6-5.

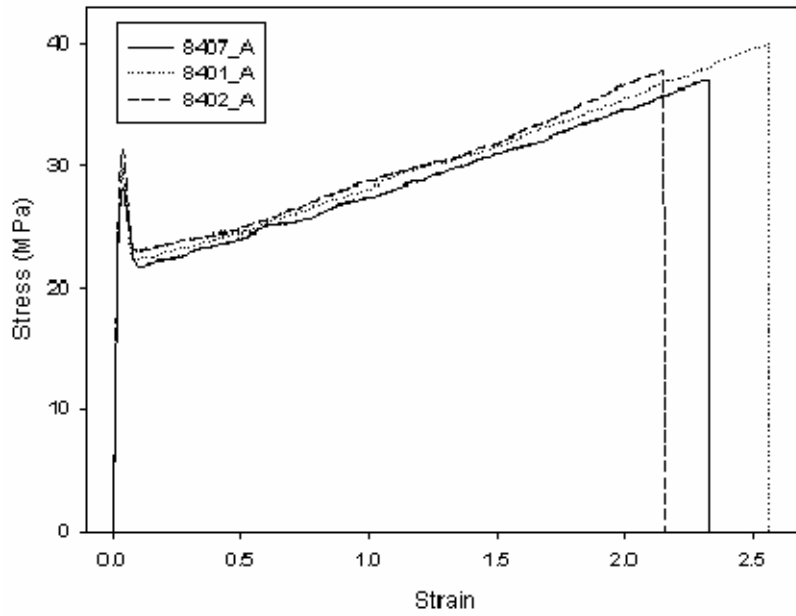


Figure B-11: Stress-strain graph comparison of the effect of elastomer density.

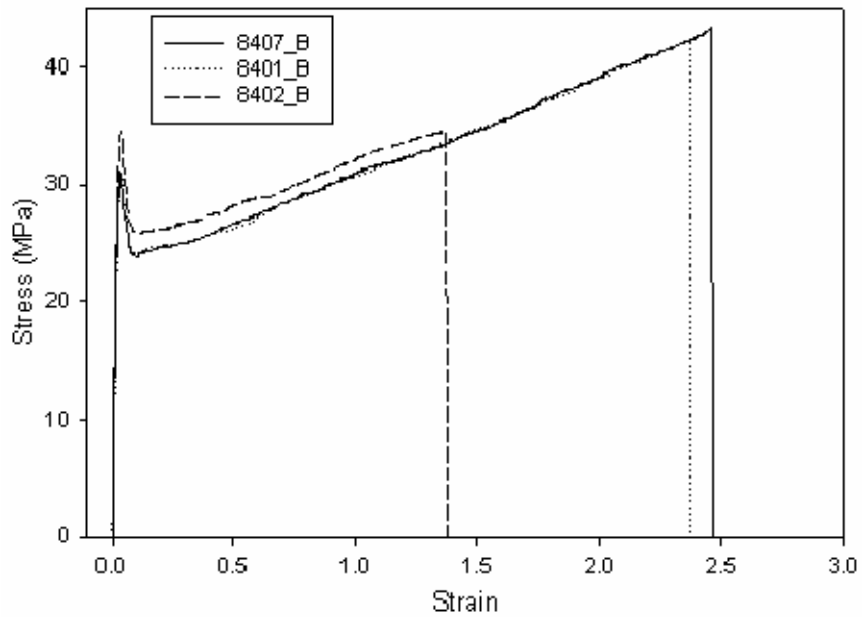


Figure B-12: Stress-strain graph comparison of the effect of elastomer density.

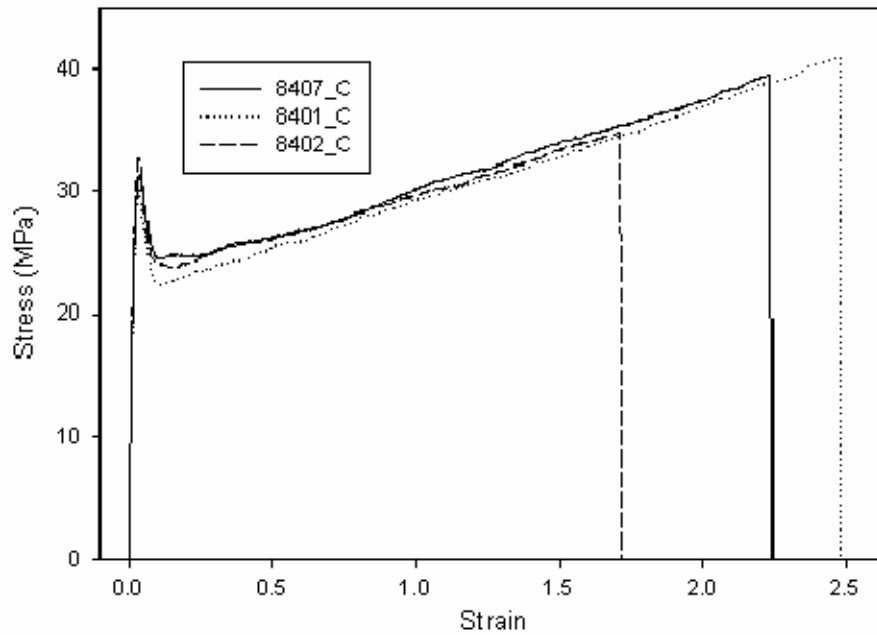


Figure B-13: Stress-strain graph comparison of the effect of elastomer density.

Table B-2: Stress-strain properties of PP:ENGAGE blends and alloys as a function of elastomer melt flow index.

Blend ID (MFI in g/10min)	Elastic Modulus (MPa)	σ_{Yield} (MPa)	Elongation at Break (mm)	σ_{Break} (MPa)	Energy to Break (N*mm)
002_0 (500)	1387 ± 72	28.3 ± 1.6	60 ± 9	38.7 ± 4.1	4636 ± 956
8407_0 (30)	1450 ± 59	28.5 ± 1.9	58 ± 12	38.7 ± 4.8	4038 ± 825
8200_0 (5)	1489 ± 49	28.8 ± 1.3	74 ± 4	45 ± 0.6	6543 ± 196
8842_0 (1)	1591 ± 54	30.5 ± 0.6	76 ± 8	49.5 ± 3.3	6814 ± 1426

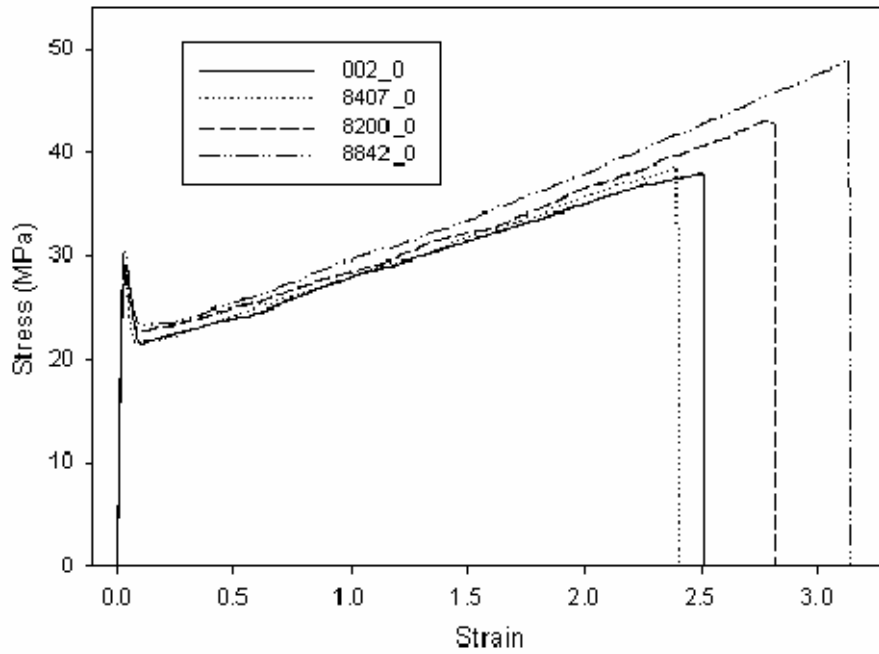


Figure B-14: Stress-strain graph of physical blends of ENGAGE elastomers with PP as a function of elastomer melt flow index.

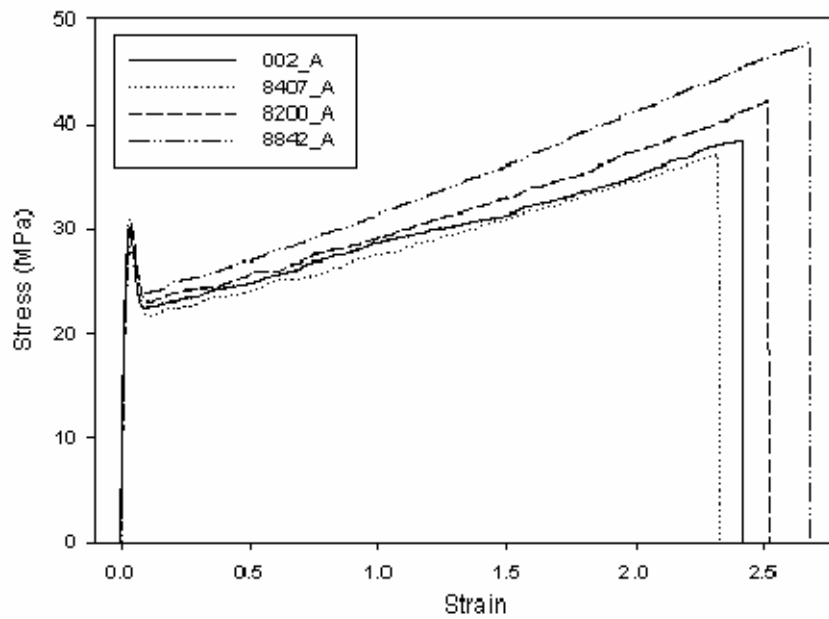


Figure B-15: Stress-strain graph comparison of the effect of elastomer MFI.

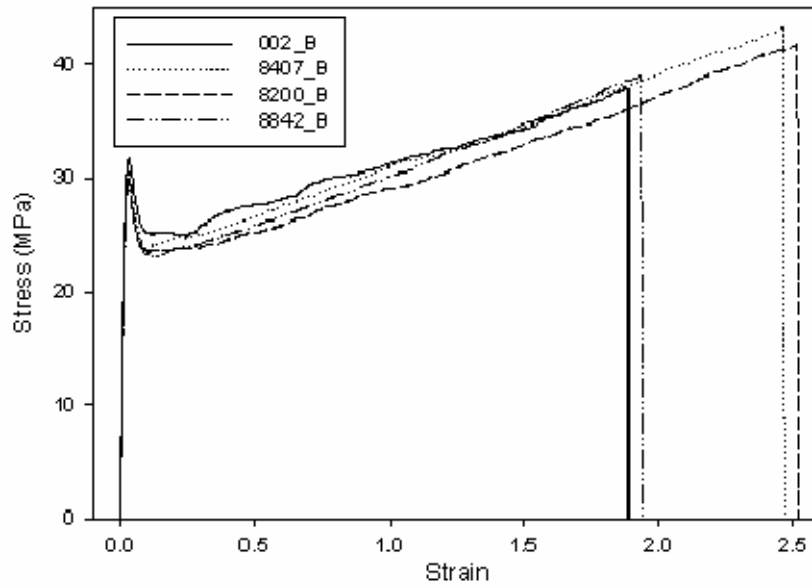


Figure B-16: Stress-strain graph comparison of the effect of elastomer MFI.

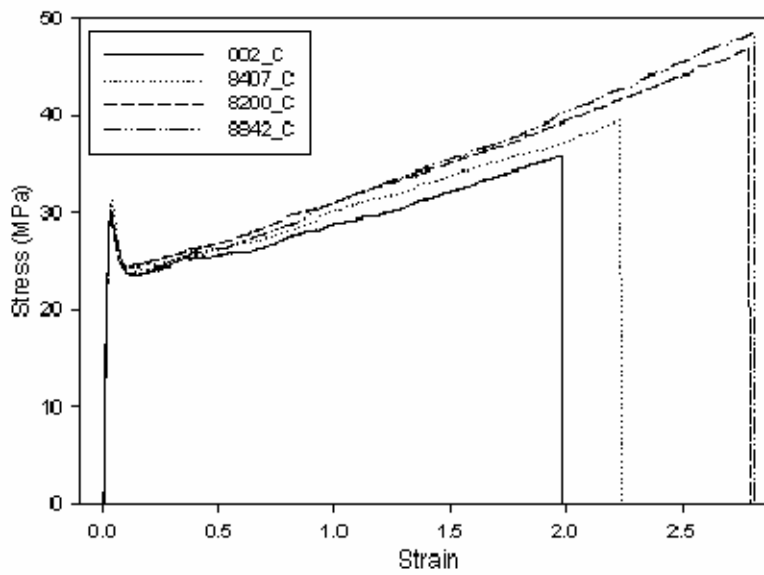


Figure B-17: Stress-strain graph comparison of the effect of elastomer MFI.

APPENDIX C FTIR GRAPHS

This Appendix lists representative graphs used to find grafting efficiency for many of the alloys found in Chapters 4 and 5.

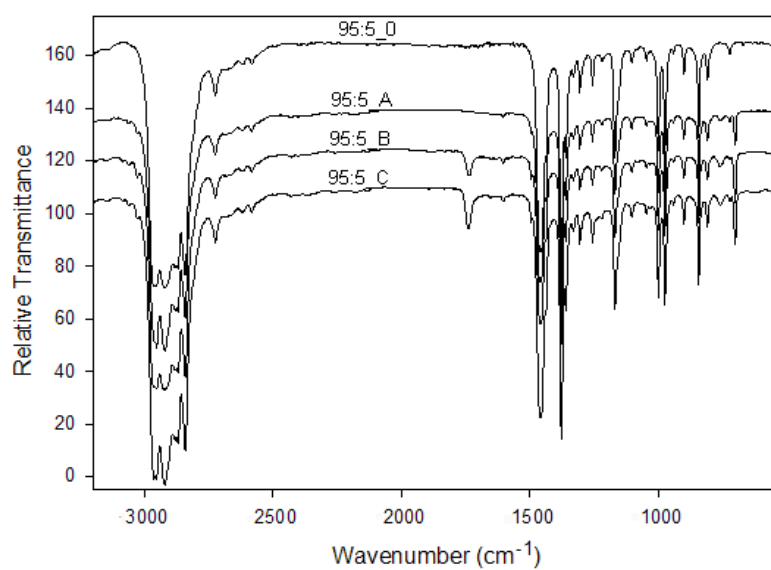


Figure C-1: FTIR graph comparison of 95:5_0, 95:5_A, 95:5_B, and 95:5_C.

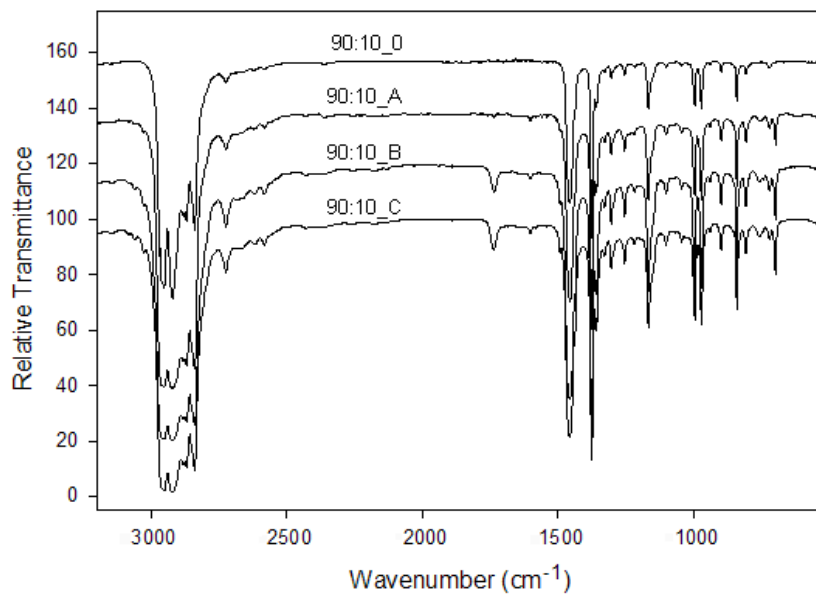


Figure C-2: FTIR graph comparison of 90:10_0, 90:10_A, 90:10_B, and 90:10_C.

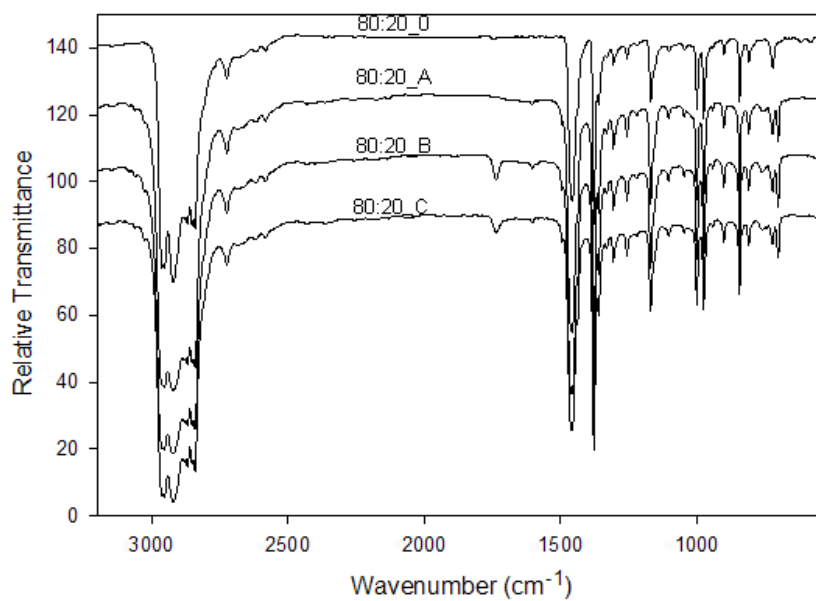


Figure C-3: FTIR graph comparison of 80:20_0, 80:20_A, 80:20_B, and 80:20_C.

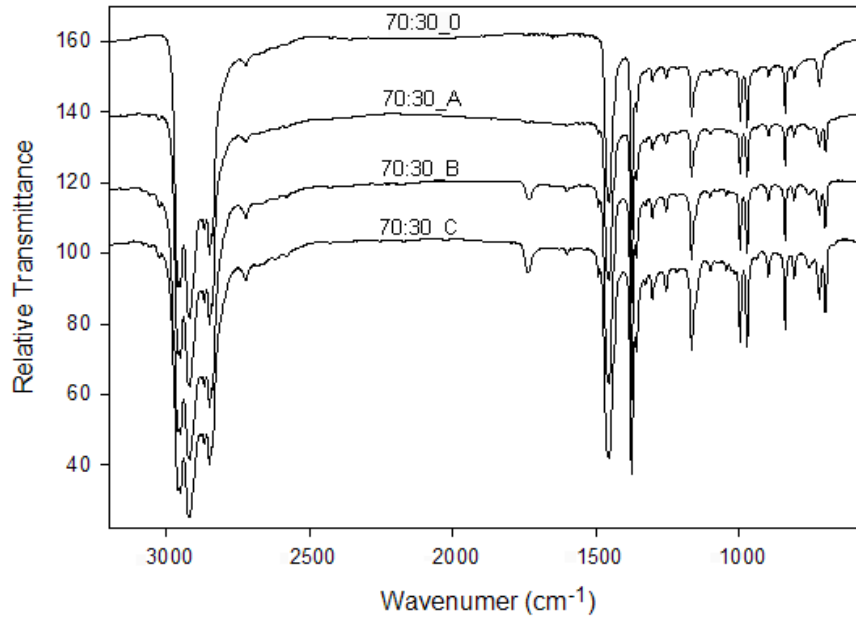


Figure C-4: FTIR graph comparison of 70:30_0, 70:30_A, 70:30_B, and 70:30_C.

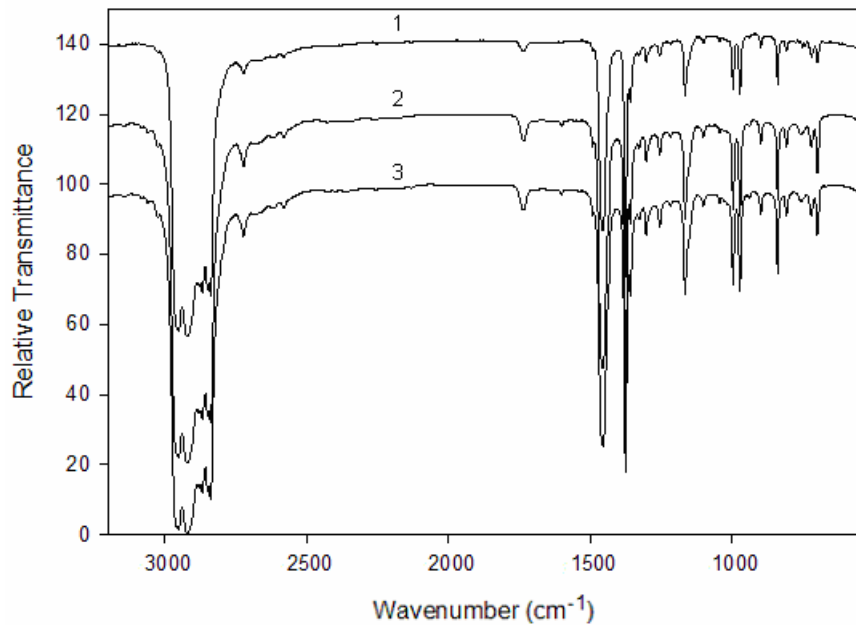


Figure C-5: FTIR graphs from Chapter 5 (Figure 5-2) of alloys processed at varying temperatures. 1 = low barrel temperature, 2 = middle barrel temperature, 3 = high barrel temperature.

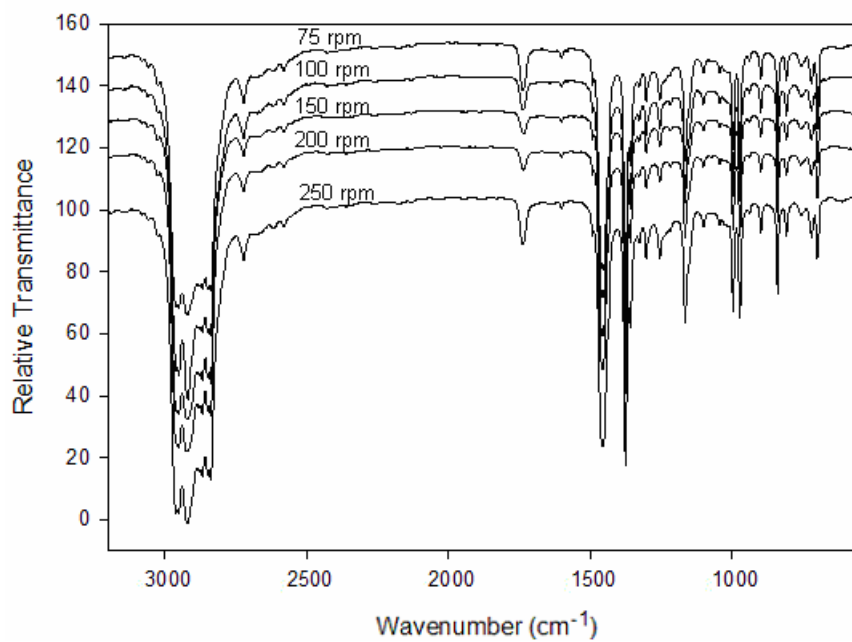


Figure C-6: FTIR graphs from Chapter 5 (Figure 5-3) of alloys processed at varying screw speeds.

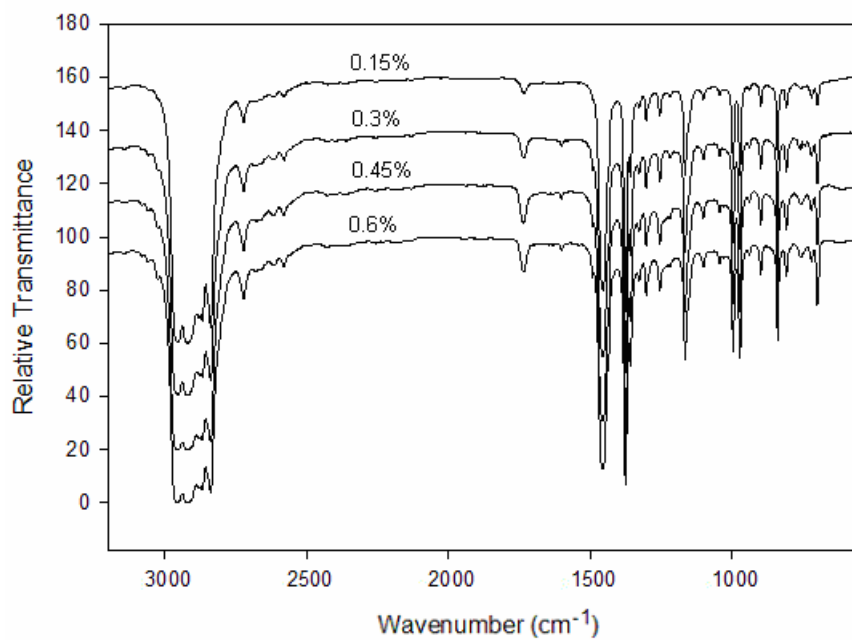


Figure C-7: FTIR graphs from Chapter 5 (Figure 5-4) of alloys processed at varying concentration of initiator.

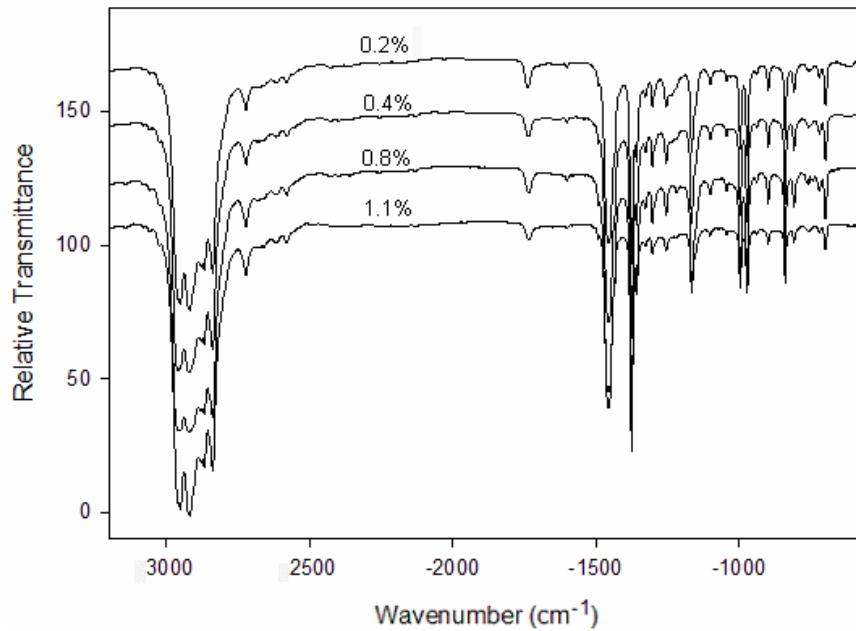


Figure C-8: FTIR graphs from Chapter 5 (Figure 5-5) of alloys processed at varying concentration of multifunctional monomer.

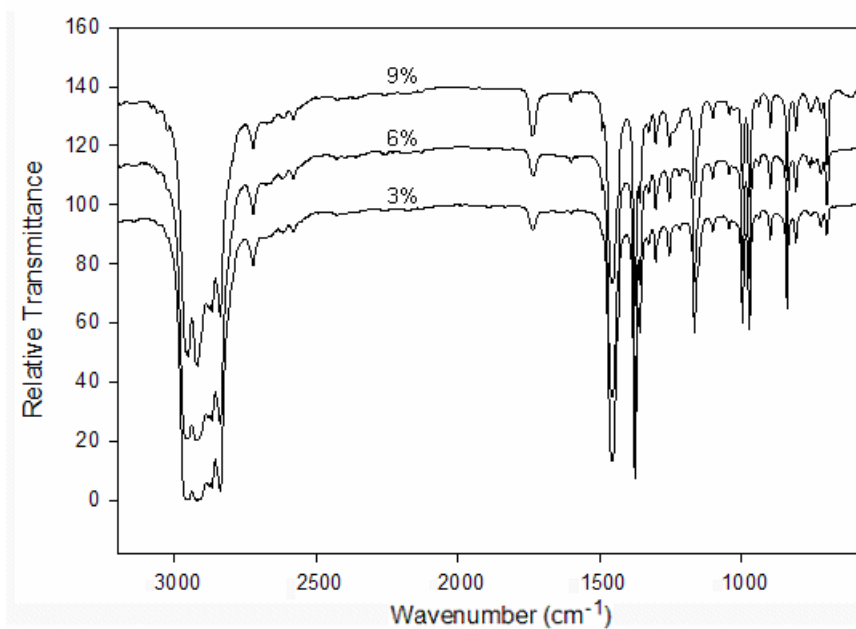


Figure C-9: FTIR graphs from Chapter 5 (Figure 5-6) of alloys processed at varying concentration of styrene, with DEGDA as multifunctional monomer.

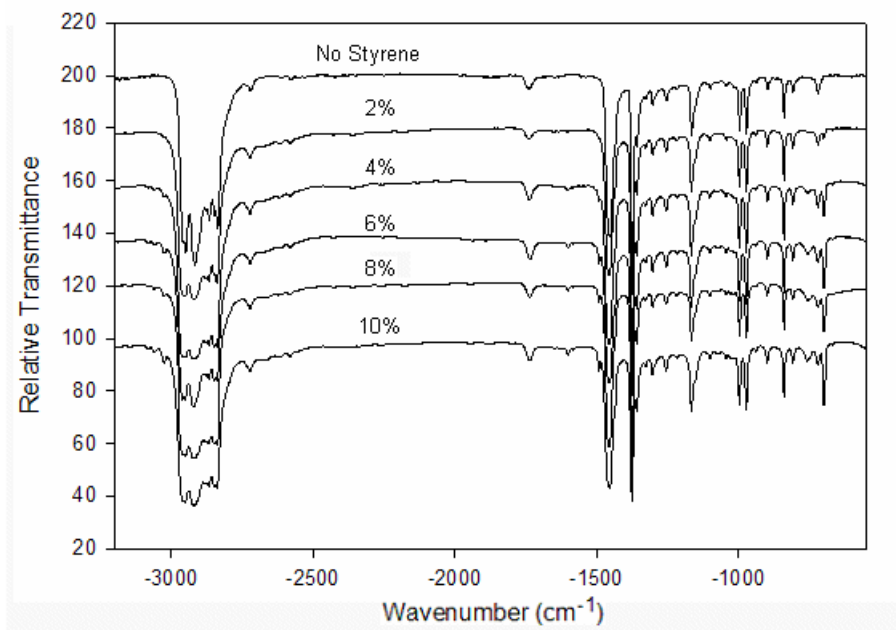


Figure C-10: FTIR graphs from Chapter 5 (Figure 5-7) of alloys processed at varying concentration of styrene, with TMPTA as multifunctional monomer.

APPENDIX D IMAGE ANALYSIS

This Appendix is a compilation of histograms representing image analysis of the SEM pictures from Chapters 3 and 4. It includes side-by-side comparisons of the mean diameter and roundness of physical blends vs. alloys at varying ratios of PP to 8407. The y axis is log scale for easier interpretation of results. These histograms are gathered from at least three different pictures taken from cryo-fractured, etched surfaces.

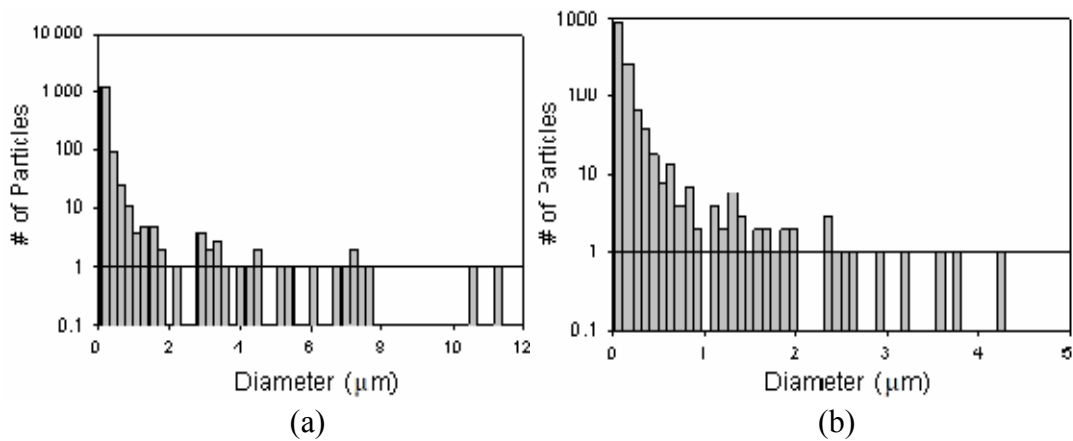


Figure D-1: Histogram of average particle diameters for (a) 70:30_0 and (b) 70:30_B.

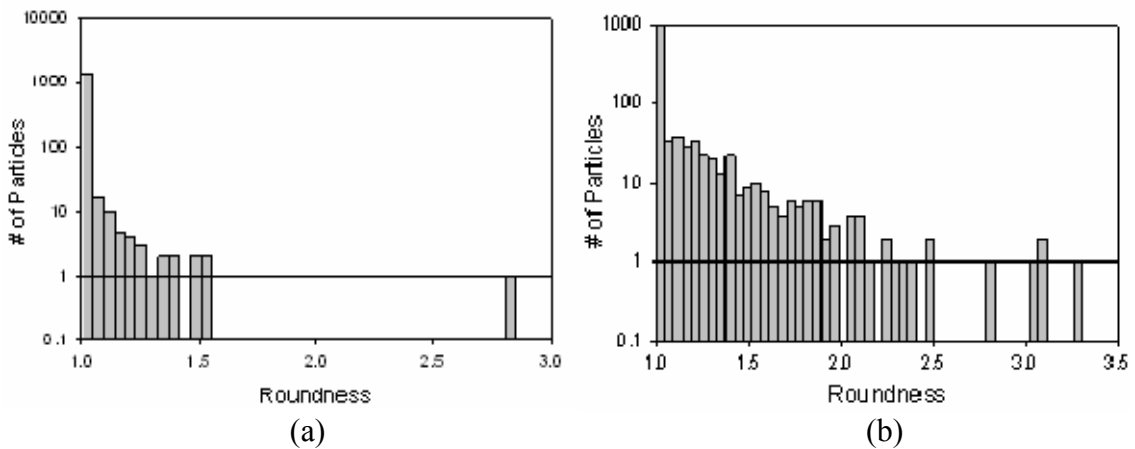


Figure D-2: Histograms of particle roundness for (a) 70:30_0 and (b) 70:30_B

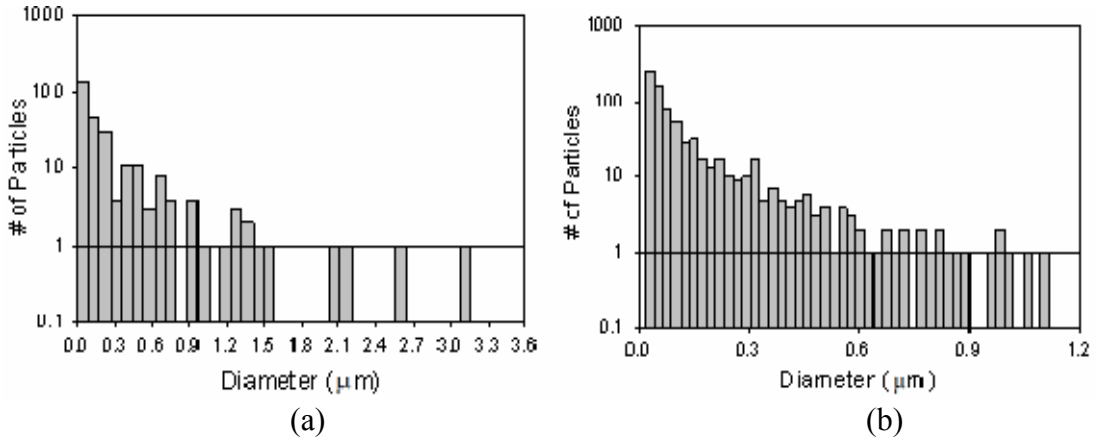


Figure D-3: Histogram of average particle diameters for (a) 80:20_0 and (b) 80:20_B

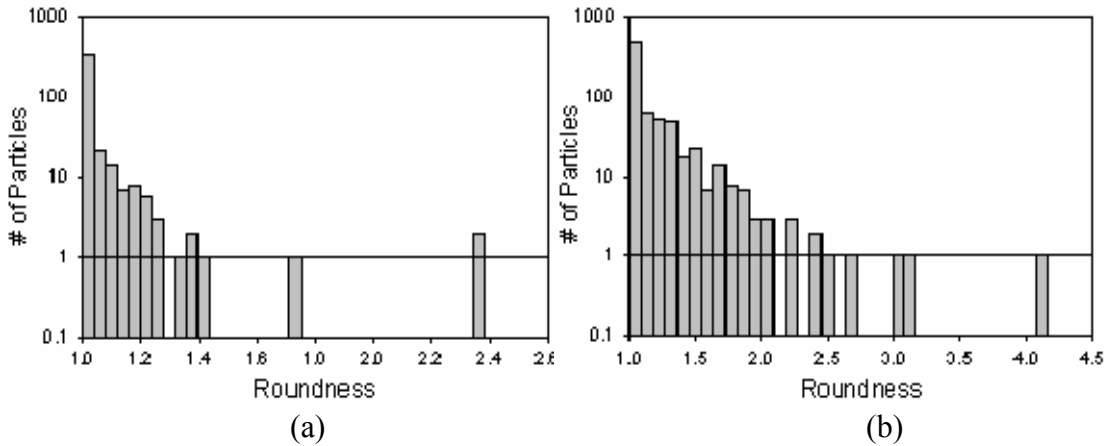


Figure D-4: Histograms of particle roundness for (a) 80:20_0 and (b) 80:20_B

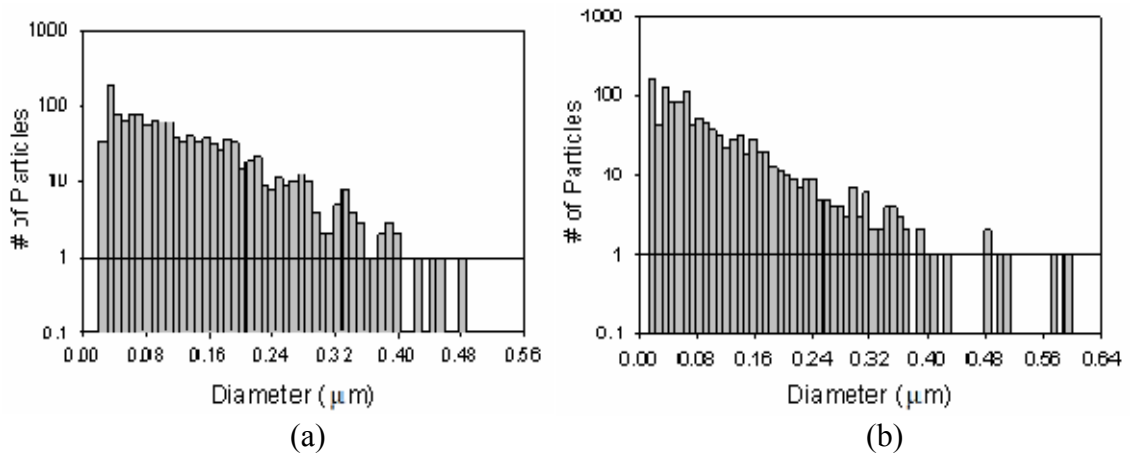


Figure D-5: Histogram of average particle diameters for (a) 90:10_0 and (b) 90:10_B

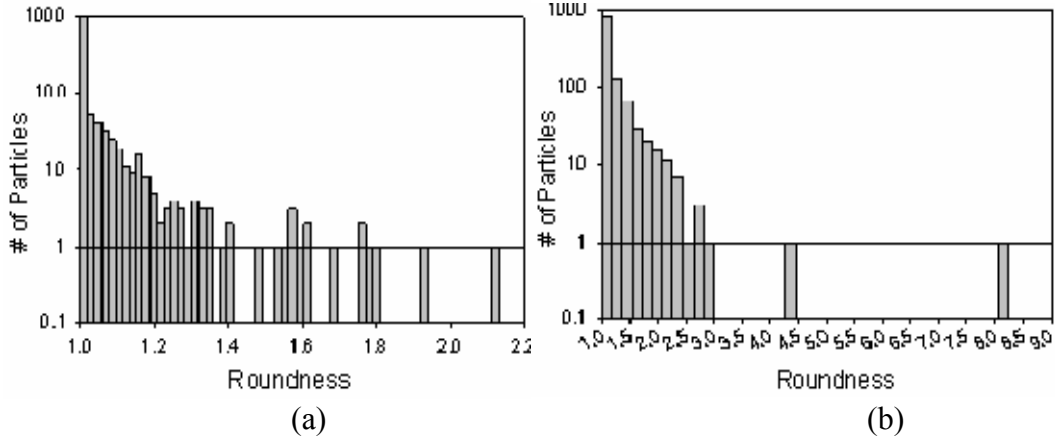


Figure D-6: Histograms of particle roundness for (a) 90:10_0 and (b) 90:10_B

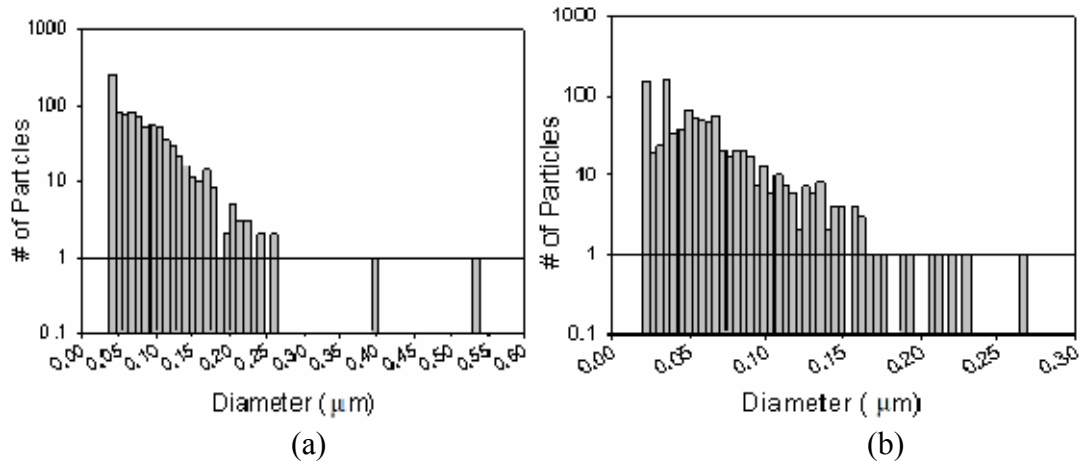


Figure D-7: Histogram of average particle diameters for (a) 95:5_0 and (b) 95:5_B

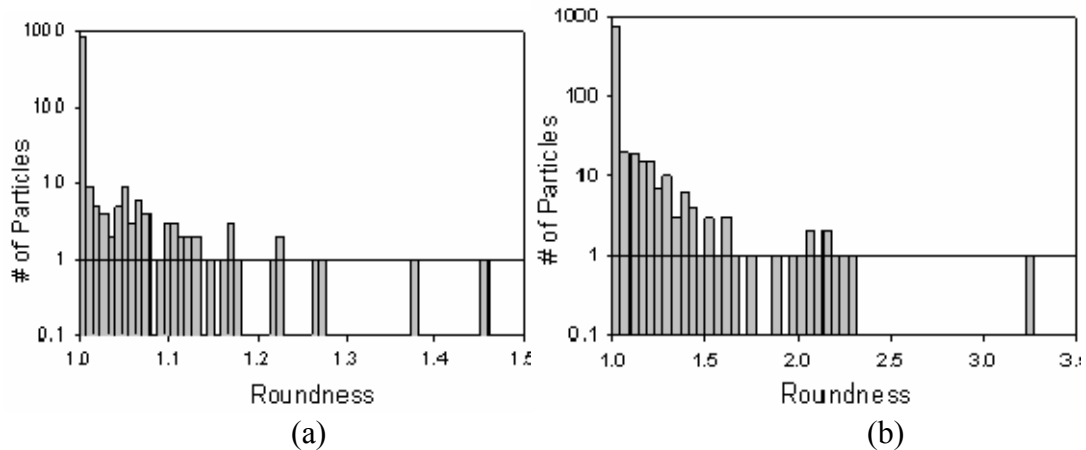


Figure D-8: Histograms of particle roundness for (a) 95:5_0 and (b) 95:5_B

APPENDIX E
ALIASED TERMS FROM CHAPTER 7

Table E-1: Aliased terms from the fractional factorial design given in Chapter 7

[Est. Terms]	Aliased Terms
[Intercept] =	Intercept - 1.75 * ACE - 1.75 * CDF
[A] =	A - 1.75 * CE - 2.75 * BCE + DEF
[B] =	B + 0.75 * ACE + 0.75 * CDF
[C] =	C + 2.33 * BC + 1.33 * ABE + 1.33 * BDF
[D] =	D - 1.75 * CF + AEF - 2.75 * BCF
[E] =	E + 2.33 * BE + 1.33 * ABC + ADF
[F] =	F - 1.75 * CD + ADE - 2.75 * BCD
[AB] =	AB + 0.75 * CE + 1.75 * BCE
[AC] =	AC + 1.33 * BE + 2.33 * ABC
[AD] =	AD + EF - 1.75 * ACF - 1.75 * CDE
[AE] =	AE + 1.33 * BC + DF + 2.33 * ABE + 2.33 * BDF
[AF] =	AF + DE - 1.75 * ACD - 1.75 * CEF
[BD] =	BD + 0.75 * CF + 1.75 * BCF
[BF] =	BF + 0.75 * CD + 1.75 * BCD
[ABD] =	ABD + 0.75 * ACF + BEF + 0.75 * CDE
[ABF] =	ABF + 0.75 * ACD + BDE + 0.75 * CEF

LIST OF REFERENCES

1. W. D., Calister Jr., *Materials Science and Engineering: An Introduction*, John Wiley and Sons, New York, (1997).
2. C. Rauwndaal, *Plastics Formulating and Compounding*, 15-26 (November/December, 1995).
3. D. B. Todd, *Plastics Compounding*, Hanser/Gardner Inc., Cincinnati, OH (1998).
4. M. Xanthos, *Reactive Extrusion – Principles and Practice*, Hanser/Gardner Inc., Cincinnati, OH (1992).
5. R. A. Pearson, *ACS Symp. Ser. 759, Toughening of Plastics*, American Chemical Society, Washington, DC, Chapters 1-10 (2000).
6. W. P. Benoit II, *SPE ANTEC*, **3**, 4298 (1995).
7. L. Yao, *The Functional Monomers Grafted Polyolefins and Their Applications in the Compatibilization of Polymer Blends*, Ph.D. Dissertation, University of Florida (1996).
8. D. R. Paul and C. B. Bucknall (Eds.), *Polymer Blends*, Volumes 1 and 2, John Wiley & Sons, Inc., New York (2000).
9. A. A. Collyer (Ed.), *Rubber Toughened Engineering Plastics*, Chapman & Hall, London (1994).
10. J. W. Barlow and D. R. Paul, *Polym. Eng. Sci.*, **21**, 985 (1981).
11. H. Tang, *Novel Polyolefin Elastomer-Based Blends and Their Applications*, Ph.D. Dissertation, University of Florida (2000).
12. I. S. Miles and S. Rostami, *Multicomponent Polymer Systems*, Longman Scientific & Technical, Essex, UK (1992).
13. C. W. Macosko, *Macromol. Symp.*, **149**, 171 (2000).
14. A. Aji and L. A. Utracki, *Polym. Eng. Sci.*, **36**, 1574 (1996).

15. L. H. Sperling, (Ed.), *Recent Advances in Polymer Blends, Grafts, and Blocks*, Plenum, New York (1974).
16. C. B. Bucknall, *Toughened Plastics*, Applied Science Publishers, London (1977).
17. K. J. Ganzeveld and L.P.B.M. Janssen, *Polym. Eng. Sci.*, **7**, 457 (1992).
18. M. Kontopoulou, W. Wang, T. G. Gopakumar, and C. Cheung, *Polymer*, **44**, 7495 (2003).
19. F. C. Stehling, T. Huff, C. S. Speed, and G. Wissler, *J. Appl. Polym. Sci.*, **26**, 2693 (1981).
20. C. Lotti, C. A. Correa, and S. V. Canevarolo, *Mater. Res.*, **3**, 37 (2000).
21. A. van der Wal, R. Nijhof, and R. J. Gaymans, *Polymer*, **40**, 6031 (1999).
22. B. Z. Jang, D. R. Uhlmann, and J. B. Vander Sande, *Polym. Eng. Sci.*, **25**, 643 (1985).
23. Y. Liu, X. Zhang, J. Gao, F. Huang, B. Tan, G. Wei, and J. Qiao, *Polymer*, **45**, 275 (2004).
24. F. O. M. S. Abreu, M. M. C. Forte, and S. A. Liberman, *J. Appl. Polym. Sci.*, **95**, 254 (2005).
25. T. Whelan, *Polymer Technology Dictionary*, Chapman & Hall London, UK (1994).
26. H. F. Guo, S. Packirisamy, N. V. Gvozdic, and D. J. Meier, *Polymer*, **38**, 785 (1997).
27. R. Potluri, C. G. Gogos, M. R. Libera, and S. S. Dagli, *SPE ANTEC*, **3**, 3172 (1995).
28. N. C. Liu, and W. E. Baker, *Polym. Eng. Sci.*, **32**, 1695 (1992).
29. N. C. Liu, and W. E. Baker, *Polymer*, **5**, 988 (1994).
30. J.-R. H. Schauder, U. S. Patent 6,303,688 (2001).
31. W. E. Baker, C. E. Scott, and G.-H. Hu, *Reactive Polymer Blending*, Hanser Gardner, Cincinnati, OH, Chapters 6 and 7 (2001).
32. U. Sundararaj, *Morphology Development During Polymer Blending*, Ph.D. Dissertation, University of Minnesota (1994).
33. D. Gersappe, D. Irvine, A. C. Balazs, Y. Liu, J. Sokolov, M. Rafailovich, S. Schwarz, and D. G. Peiffer, *Science*, **265**, 1072 (1994).

34. B. Z. Jang, D. R. Uhlmann, and J. B. van der Sande, *Rubb. Chem. Techn.*, **57**, 291 (1984).
35. S. Thomas, and R. E. Prudhomme, *Polymer*, **33**, 4260 (1992).
36. D. W. Park, and R. J. Roe, *Macromolecules*, **24**, 5324 (1991).
37. S. Datta, and D. J. Lohse, *Macromolecules*, **26**, 2064 (1993).
38. S. Endo, K. Min, J. L. White, and T. Kyu, *Polym. Eng. Sci.*, **26**, 45 (1986).
39. P. Pieroni, D. Ercoli, G. Goizueta, and N. Capiati, *Elast. Plast.*, **34**, 131 (2002).
40. L. F. Chen, B. Wong, and W. E. Baker, *Polym. Eng. Sci.*, **36**, 1594 (1996).
41. M. S. Lee, T. P. Lodge, and C. W. Macosko, *J. Polym. Sci. B: Polym. Phys.*, **35**, 2835 (1997).
42. H. K. Jeon, and J. K. Kim, *Macromolecules*, **33**, 8200 (2000).
43. G. H. Fredrickson and L. Leibler, *Macromolecules*, **29**, 2674 (1996).
44. J. Suhm, J. Heinmann, C. Worner, P. Muller, F. Stricker, J. Kressler, J. Okuda, and R. Mulhaupt, *Macromol. Symp.*, **129**, 1 (1998).
45. J. Karger-Kocsis, *Polypropylene: An A-Z Reference*, Kluwer Academic Publishers, Dordrecht, The Netherlands (1999). (a) R. Mulhaupt, "Metallocene catalysts and tailor-made polyolefins," pp. 455-475. (b) R. Mulhaupt, "Ziegler-Natta catalysis and propylene polymerization," pp. 896-920. (c) H. Ledwinka, and W. Neibl, "Industrial polymerization processes," pp. 314-319, (d) E. Andreassen, "Infrared and Raman spectroscopy of polypropylene," pp. 324-328, (e) A. Galeski, "Nucleation," pp. 545-553.
46. E. P. Moore, Jr., *Polypropylene Handbook*, Hanser, Munich (1996).
47. P. Walter, D. Mader, P. Reichert, and R. Mulhaupt, *J.M.S.-Pure Appl. Chem.*, **A36**, 1613 (1999).
48. DuPont Dow Elastomers, ENGAGE® Product Information, September 2001, <http://www.dupontdow.com/Products/Engage/engage.asp>. Last accessed June 4th, 2004.
49. J. Scheirs, and W. Kaminsky, *Metallocene-based Polyolefins*, Vol. 2, John Wiley & Sons, New York (2000).
50. F. J. Timmers, U. S. Patent 5,703,187, (1997).
51. J. Koivumaki, and J. Seppala, *Polymer*, **34**, 1958 (1993).

52. A. Bensason, J. Minick, A. Moet, S. Chum, A. Hiltner, and E. Baer, *J. Appl. Polym. Sci.*, **34**, 1301 (1996).
53. W. Kaminsky, *Macromol. Chem. Phys.*, **197**, 3907 (1996).
54. M. Arnold, J. Knorr, F. Koller, and S. Bornemann, *J.M.S. – Pure Appl. Chem.*, **A36**, 1655 (1999).
55. S. Lai and G. W. Knight, *SPE ANTEC*, **1**, 1188 (1993).
56. L. T. Kale, T. A. Plumley, R. M. Patel, and P. Jain, *SPE ANTEC*, **2**, 2249 (1993).
57. D. E. Turek and B. G. Landes, *SPE ANTEC*, **2**, 2270 (1995).
58. S. Bensason, V. Stepanov, S. Chum, A. Hiltner, and E. Baer, *Macromolecules*, **30**, 2436 (1997).
59. P. Thirion and T. Weil, *Polymer*, **25**, 609 (1984).
60. M. L. Cerrada, R. Benavente, and E. Perez, *J. Mater. Res.*, **16**, 1103 (2001).
61. M. Peeters, B. Goderis, H. Reynaers, and V. Mathot, *J. Polym. Sci. B: Polym. Phys.*, **37**, 83 (1999).
62. B. Goderis, H. Reynaers, and M. H. Koch, *Macromolecules*, **35**, 5840 (2002).
63. C. G. Vonk, *J. Polym. Sci. C: Polym. Lett.*, **24**, 305 (1986).
64. R. Androsch, *Polymer*, **40**, 2805 (1999).
65. R. Androsch, and W. Bernhard, *Macromolecules*, **33**, 9076 (2000).
66. C. I. Chung, *Extrusion of Polymers – Theory and Practice*, Hanser, Munich (2000).
67. W. Michaeli, A. Grefensten, and U. Berghaus, *Polym. Eng. Sci.*, **35**, 1485 (1995).
68. G. Moad, *Prog. Polym. Sci.*, **24**, 81 (1999) and all references therein.
69. S. Wu, *Polym. Eng. Sci.*, **27**, 335 (1987).
70. P Cheung, D. Suwanda, and S. T. Balke, *Polym. Eng. Sci.*, **30**, 1063 (1990).
71. I.-K. Yang and J. D. Lin, *Polym. Eng. Sci.*, **42**, 753 (2002).
72. G. Shearer and C. Tzoganakis, *Polym. Eng. Sci.*, **39**, 1584 (1999).
73. C. Tzoganakis, *Peroxide Degradation of Polypropylene During Reactive Extrusion*, Ph.D. Thesis, McMaster University, (1988).

74. A. V. Machado, J. A. Covas, and M. van Duin, *J. Appl. Polym. Sci.*, **71**, (1999), 135-141.
75. A. P. Plochocki, S. S. Dagli, and R. D. Andrews, *Polym. Eng. Sci.*, **30**, 741 (1990).
76. W. Huneault, M. F. Champagne, L. E. Daigneault, and M. M. Dumoulin, *SPE ANTEC*, **2**, 2020 (1995).
77. K. J. Ganzeveld and L. P. B. M. Janssen, *Polym. Eng. Sci.*, **32**, 457 (1992).
78. C.-K. Shih, *Polym. Eng. Sci.*, **35**, 1688 (1995).
79. C.-K. Shih, D. G. Tynan, and D. A. Denelsbeck, *Polym. Eng. Sci.*, **31**, 1670 (1991).
80. S. Tyagi, and A. K. Ghosh, *Polym. Eng. Sci.*, **42**, 1309 (2002).
81. C. Jordan, J. Y. Cavaille, and J. Perez, *J. Polym. Sci. B: Polym. Phys.*, **27**, 2361 (1989) and all references therein.
82. M. A. Huneault, M. F. Champagne, and A. Luciani, *Polym. Eng. Sci.*, **36**, 1694 (1996).
83. C. E. Scott and C. W. Macosko, *Polymer*, **36**, 461 (1995).
84. U. Sundararaj and C. W. Macosko, *Polym. Eng. Sci.*, **35**, 100 (1995).
85. M. H. Wilhelm and M. I. Felisberti, *J. Appl. Polym. Sci.*, **85**, 847 (2002).
86. H. K. Jeon and J. K. Kim, *Macromolecules*, **31**, 9273 (1998).
87. R. G. Cox, *J. Fluid Mech.*, **37**, 601 (1969).
88. D. Barthes-Biesel, D. and A. Acrivos, *J. Fluid Mech.*, **61**, 1 (1973).
89. B. D. Favis, C. Lavallee, and A. Derdouri, A., *J. Mater. Sci.*, **27**, 4211-4218 (1992).
90. H. Cartier and G. H. Hu, *Polym. Eng. Sci.*, **38**, 177 (1999).
91. A. V. Machado, J. A. Covas, and M. Van Duin, *Polymer*, **42**, 3649 (2001).
92. J. Cha and J. L. White, *Polym. Eng. Sci.*, **41**, 1238 (2001).
93. A. V. Machado, M. van Duin, and J. A. Covas, *J. Polym. Sci. A: Polym. Chem.*, **38**, 3919 (2000).
94. B. Wong, *Free Radical Melt Grafting of Glycidyl Methacrylate and Styrene onto Polypropylene: A Study of the Rheological and Chemical Properties*, Master's Thesis, Queen's University (1995).

95. Z. Song, and W. E. Baker, *Die Angew Makromol. Chem.*, **181**, 1, (1990).
96. H. F. Guo, S. Packirisamy, N. V. Gvozdic, and D. J. Meier, *Polymer*, **38**, 785 (1997).
97. G. I. Taylor, *Proc. R. Soc. London.*, **A138**, 41 (1932).
98. G. I. Taylor, *Proc. R. Soc. London.*, **A146**, 501 (1934).
99. A. Galeski and Z. Bartczak, *Macromol. Symp.*, **194**, 47 (2003).
100. L. H. Sperling, *Introduction to Physical Polymer Science*, 2nd Ed., John Wiley & Sons (1992).
101. X. Chen and Y. Mai, *Polym. Eng. Sci.*, **10**, 1763 (1998).
102. C. B. Bucknall, A. Karpodinis, and X. C. Zhang, *J. Mater. Sci.*, **29**, 3377 (1994).
103. C. J. Chou, K. Vijayan, D. Kirby, A. Hiltner, and E. Baer, *J. Mater. Sci.*, **23**, 2521 (1988).
104. K. Dijkstra, A. Van der wal, and R. J. Gaymans, *J. Mater. Sci.*, **29**, 3489 (1994).
105. A. Galeski, *Prog. Polym. Sci.*, **28**, 1643 (2001) and all references therein.
106. H. R. Brown, *Macromolecules*, **24**, 2752 (1991).
107. J. T. Lutz, Jr. and R. F. Grossman, *Polymer Modifiers and Additives*, Chapters 8 and 11, Marcel Dekker, New York (2001).
108. K. A. Mazich, M. A. Samus, C. A. Smith, and G. Rossi, *Macromolecules*, **24**, 2766 (1991).
109. S. H. Jafari and A. K. Gupta, *J. Appl. Polym. Sci.*, **78**, 962 (2000).
110. C. B. Bucknall and C. J. Page, *J. Mater. Sci.*, **17**, 808 (1982).
111. D. C. Clark, W. E. Baker, K. E. Russell, and R. A. Whitney, *J. Polym. Sci. A: Polym. Chem.*, **38**, 2456 (2000).
112. M. E. Fowler, H. Keskkula, and D. R. Paul, *Polymer*, **28**, 1703 (1987).
113. F. Stricker, Y. Thomann, and R. Mulhaupt, *J. Appl. Polym. Sci.*, **68**, 1891 (1998).
114. X. Wang, C. Tzoganakis, and G. L. Rempel, *J. Appl. Polym. Sci.*, **61**, 1395 (1996).
115. J. A. W. van Dommelen, W. A. M. Brekelmans, and F. P. T. Baaijens, *Mech. Mater.*, **35**, 845 (2003).

116. A. van der Wal, A. J. J. Verheul, and R. J. Gaymans, *Polymer*, **40**, 6057 (1999).
117. M. Ishikawa, M. Sugimoto, and T. Inoune, *J. Appl. Polym. Sci.*, **62**, 1495 (1996).
118. M. Zhang, Y. Liu, X. Zhang, J. Gao, F. Huang, Z. Song, G. Wei, and J. Qiao, *Polymer*, **43**, 5133 (2002).
119. S. Wu, *Polymer*, **26**, 1855 (1985).
120. S. Wu, *J. Appl. Polym. Sci.*, **35**, 549 (1988).
121. S. Wu, *J. Polym. Sci. B.: Polym. Phys.*, **21**, 699 (1983).
122. M. H. Ha, B. K. Kim, and E. Y. Kim, *J. Appl. Polym. Sci.*, **93**, 179 (2004).
123. F. C. Stehling, T. Huff, C. S. Speed, and G. Wissler, *J. Appl. Polym. Sci.*, **26**, 2693 (1981).
124. W. Grellmann, S. Seidler, K. Jung, and I. Kotter, *J. Appl. Polym. Sci.*, **79**, 2317 (2001).
125. Z. Bartczak, *J. Macromol. Sci.*, **B41**, 1205 (2002).
126. O. K. Muratoglu, A. S. Argon, and R. E. Cohen, *Polymer*, **36**, 921 (1995).
127. B. Z. Jang, D. R. Uhlmann, and J. B. Vander Sande, *J. Appl. Polym. Sci.*, **30**, 2485 (1985).
128. W. Wang, Q. Wu, and B. Qu, *Polym. Eng. Sci.*, **43**, 1798 (2003).
129. S. Hillmansen and R. N. Haward, *Polymer*, **42**, 9301 (2001).
130. A. van der Wal, and R. J. Gaymans, *Polymer*, **40**, 6045 (1999).
131. I. Brough, R. N. Haward, G. Healey, and A. Wood, *Polymer*, **45**, 3115 (2004).
132. R. Segula, E. Staniek, B. Escaig, and B. Fillon, *J. Appl. Polym. Sci.*, **71**, 1873 (1999).
133. A. C. Steenbrink, H. Janik, and R. J. Gaymans, *J. Mater. Sci.*, **32**, 5505 (1997).
134. J. Karger-Kocsis, *Polym. Eng. Sci.*, **36**, 203 (1996).
135. J. T. Dickenson, L. C. Jensen, S. C. Langford, and R. P. Dion, *J. Polym. Sci. B: Polym. Phys.*, **32**, 779 (1994).
136. T. Inoue, *J. Appl. Polym. Sci.*, **54**, 723 (1994).

137. E. Borsig, A. Fiedlerova, and M. Lazar, *J. Macromol. Sci.- Chem.*, **A16**, 513 (1981).
138. E. Niki and Y. Kamiya, *J. Org. Chem.*, **38**, 1403 (1973).
139. N.-J. Huang and D. C. Sundberg, *J. Polym. Sci. A: Polym. Chem.*, **33**, 2533 (1995).
140. N.-J. Huang and D. C. Sundberg, *J. Polym. Sci. A: Polym. Chem.*, **33**, 2551 (1995).
141. N.-J. Huang and D. C. Sundberg, *J. Polym. Sci. A: Polym. Chem.*, **33**, 2571 (1995).
142. N.-J. Huang and D. C. Sundberg, *J. Polym. Sci. A: Polym. Chem.*, **33**, 2587 (1995).
143. X. Zhang and W. E. Baker, *J. Appl. Polym. Sci.*, **67**, 427 (1998).
144. P. A. Callais and R. T. Kazmierczak, *SPE ANTEC*, **1**, 1368 (1989).
145. Atofina Chemicals, Inc., "Organic Peroxides Product Bulletin - Dialkyl Peroxides," March 2001, <http://www.atofinchemicals.com>. Last accessed January 6th, 2004.
146. C. E. Carraher, Jr., *Polymer Chemistry*, 5th Ed., Marcel Dekker, New York (2000).
147. P. A. Callais and R. T. Kazmierczak, *SPE ANTEC*, **1**, 1921 (1990).
148. J. Cha and J. L. White, *Polym. Eng. Sci.*, **41**, 1238 (2001).
149. M. Lazar, A. Kleinova, A., Fiedlerova, I. Janigova, and E. Borsig, *J. Polym. Sci.: A: Polym. Chem.*, **42**, 675 (2004).
150. P. Dokolas, M. Looney, S. Musgrave, S. Poon, and D. H. Solomon, *Polymer*, **41**, 3137 (2000).
151. G. H. Hu, Y. J. Sun, and M. Lambla, *Polym. Eng. Sci.*, **36**, 676 (1996).
152. W. Zhou and S. Zhu, *Ind. Eng. Chem. Res.*, **36**, 1130 (1997).
153. J. Fossey, D. Lefort, and J. Sorba, (Eds.), *Free Radicals in Organic Chemistry*, John Wiley & Sons. New York (1995).
154. D. W. Mead, *J. Appl. Polym. Sci.*, **57**, 151, (1995).
155. K. E. Russell, *Prog. Polym. Sci.*, **27**, 1007 (2002) and all references therein.
156. S. Camara, B. C. Gilbert, R. J. Meier, M. van Duin, and A. C. Whitwood, *Org. Biomol. Chem.*, **1**, 1181 (2003).
157. M. P. Stevens, *Polymer Chemistry: An Introduction*, 3rd Ed., Oxford, New York (1999).

158. W. A. Pryor, *Free Radicals*, McGraw-Hill, New York (1966).
159. F. M. Lewis, C. Walling, W. Cummings, E. R. Briggs, and F. R. Mayo, *J. Am. Chem. Soc.*, **70**, 1515 (1948).
160. F. M. Lewis, C. Walling, W. Cummings, E. R. Briggs, and F. R. Mayo, *J. Am. Chem. Soc.*, **70**, 1529 (1948).
161. P. J. Flory, *Principles of Polymer Chemistry*, Cornell University Press, Inc., New York (1953).
162. J. Bandrup and E. H. Immergut (Eds.), *Polymer Handbook*, 3rd Ed., Wiley-Interscience, New York, (1989); (a) K. C. Berger and G. Brandrup, pp. 81II, (b) R. Z. Greenley, pp. 153, (c) R. Z. Greenley, pp.267.
163. A. Kannurpatti, J. W. Anseth, and C. N. Bowman, *Polymer*, **39**, 2507 (1998).
164. S. W. Benson and A. M. North, *J. Am. Chem. Soc.*, **84**, 935 (1962).
165. G. T. Russell, D. H. Napper, and R. G. Gilbert, *Macromolecules*, **21**, 2133 (1988).
166. K. E. Oliphant, K. E., Russell, and W. E. Baker, *Polymer*, **36**, 1597 (1995).
167. C. Kiparissides and D. Achilias, *J. Appl. Polym. Sci.*, **35**, 1303 (1988).
168. A. Husain and A. E. Hamielec, *J. Appl. Polym. Sci.*, **22**, 1207 (1978).
169. G. Moad, E. Rizzardo, and D. H. Solomon, *Macromolecules*, **15**, 909 (1982).
170. N. Sahloul and A. Penlidis, *Adv. Polym. Tech.*, **23**, 186 (2004).
171. E. J. Dietz and N. A. Peppas, *Polymer*, **38**, 3767 (1997).
172. J. S. Young, A. Kannuroatti, and C. N. Bowman, *Macromol. Chem. Phys.*, **199**, 1043 (1998).
173. A. Thakur, K. Banthia, and B. R. Maiti, *J. Appl. Polym. Sci.*, **58**, 959 (1995).
174. Y. R. Luo, *Handbook of Bond Dissociation Energies in Organic Compounds*, CRC Press, Boca Raton, FL (2003).
175. S. Fliszar, *Atoms, Chemical Bonds, and Bond Dissociation Energies*, Springer-Verlag, New York (1994).
176. A. A. Zavitsas, *J. Chem. Education*, (78) 417 (2001).
177. M. Ratzsch, H. Bucka, A. Hesse, and M. Arnold, *J.M.S. – Pure Appl. Chem.*, **A33**, 913 (1996).

178. G. G. Cameron and M. Y. Qureshi, *J. Polym. Sci. A: Polym. Chem.*, **18**, 2143 (1980).
179. M. Ratzsch, M. Arnold, E. Borsig, H. Bucka, and N. Reichelt, *Prog. Polym. Sci.*, **27**, 1195 (2002) and all references therein.
180. J. B. Wong Shing, W. E. Baker, K. E. Russell, and R. A. Whitney, *J. Polym. Sci. A: Polym. Chem.*, **32**, 1691 (1994).
181. Q. Yu and S. Zhu, *Polymer*, **40**, 2961 (1999)
182. M. Saule, S. Navarre, O. Babot, W. Maslow, L. Vartommen, and B. Maillard, *Macromolecules*, **36**, 7469 (2003).
183. P. Dokolas, Q. G. Guanghua, and D. H. Solomon, *J. Appl. Polym. Sci.*, **83**, 898 (2002).
184. K. Siriinha and D. Meksawat, *J. Appl. Polym. Sci.*, **93**, 1179 (2004).
185. L. H. U. Andersson, B. Gustafsson, and T. Hjertberg, *Polymer*, **45**, 2577 (2004).
186. G. Odian and B. S. Bernstein, *J. Polym. Sci. A: Polym. Chem.*, **2**, 2835 (1964).
187. J. Yang, Z. Yao, D. Shi, H. Huang, Y. Wang, and J. Yin, *J. Appl. Polym. Sci.*, **79**, 535 (2001).
188. V. R. Landi and E. K. Easterbrook, *Polym. Eng. Sci.*, **18**, 1135 (1978).
189. C. Tzoganakis, J. Vlachopoulos, and A. E. Hamielec, *Polym. Eng. Sci.*, **28**, 170 (1988).
190. G. H. Hu, J. J. Flat, and M. Lambla, *SPE ANTEC*, **1**, 2775 (1994).
191. D. Suwanda, R. Lew, and S. T. Balke, *J. Appl. Polym. Sci.*, **35**, 1019 (1988).
192. D. Suwanda, R. Lew, and S. T. Balke, *J. Appl. Polym. Sci.*, **35**, 1033 (1988).
193. F. Berzin and B. Vergnes, *Polym. Eng. Sci.*, **40**, 344 (2000).
194. V. J. Triacca, P. E. Gloor, S. Zhu, A. N. Hrymak, and A. E. Hamielec, *Polym. Eng. Sci.*, **33**, 445 (1993).
195. P. V. Krishna and R. H. Boyd, *Macromolecules*, **26**, 679 (1993).
196. C. Rosales, R. Perera, M. Ichazo, J. Gonzales, H. Rojas, A. Sanchez, and A. D. Barrios, *J. Appl. Polym. Sci.*, **70**, 161 (1998).
197. H. G. Fritz, *J.M.S. – Pure Appl. Chem.*, **A36**, 1683 (1999).

198. W. Heinen, S. W. Erkens, M. van Duin, and J. Lugtenburg, *J. Polym. Sci. A: Polym. Chem.*, **37**, 4368 (1999).
199. R. S. Auda, W. M. Davis, D. Y.-L. Chung, L. W. Flatley, Jr., B. G. Jones, D. A. White, and H. G. Woudboer, U. S. Patent 5,651,927 (1997).
200. S. K. Singh, S. P. Tambe, A. B. Samui, and D. Kumar, *J. Appl. Polym. Sci.*, **93**, 2802 (2004).
201. Y. Qing and X. Wenying, *Polym. Eng. Sci.*, **34**, 446 (1994).
202. J. Martinez, R. Benavides, C. Guerrero, and B. E. Reyes, *Polym. Degrad. Stabil.*, **86**, 129 (2004).
203. J. Yamauchi, A. Yamaoka, K. Ikemoto, and T. Matsui, *J. Appl. Polym. Sci.*, **43**, 1197 (1991).
204. B. Boutevin, J. J. Robin, N. Torres, and J. Casteil, *Macromol. Chem. Phys.*, **203**, 245 (2002).
205. G.-H. Hu, H. Li, L.-F. Feng, and L. A. Pessan, *J. Appl. Polym. Sci.*, **88**, 1799 (2003).
206. R. Rengarajan, M. Vicic, and S. Lee, *Polymer*, **30**, 834 (1989).
207. L. Wild, J. A. Hinnenkamp, B.-H. Chang, B.-H., and W. W. Kiang, U. S. Patent 5,344,888 (1994).
208. S. W. Coe, U. S. Patent 6,426,389 (2002).
209. M. S. Rodriguez, P. N. Tutunjian, C. L. Edwards, P. K. Casey, C. E. Ash, C. C. Hwo, and P. K. Wong, U. S. Patent 6,448,333 (2002).
210. L. Wild, J. A. Hinnenkamp, B. H. Chang, and W. W. Kiang, U. S. Patent 2,344,888, (1994).
211. K. Nakashima, R. Muroi, M. Imai, and K. Sato, U. S. Patent 3,981,958 (1976).
212. F. Picchioni, J. G. P. Goossens, M. van Duin, and P. Magusin, *J. Appl. Polym. Sci.*, **89**, 3279 (2003).
213. S. A. Michaels and H. J. Bixler, *J. Polym. Sci.*, **50**, 393-409 (1961).
214. F. Yoshii, K. Makuuchi, S. Kikukawa, T. Tanaka, J. Saitoh, and K. Koyama, *J. Appl. Polym. Sci.*, **60**, 617 (1996).
215. X. Yunshu, F. Yoshii, and K. Makuuchi, *J. Macromol. Chem.*, **A32**, 1803 (1995).

216. M. Lazar, L. Hrcckova, E. Borsig, A. Marcincin, and N. Reichelt, *J. Appl. Polym. Sci.*, **78**, 886 (2000).
217. I. Chodak, M. Lazar, and M. Capla, *J. Polym. Sci. A: Polym. Chem.*, **29**, 581 (1991).
218. I. Chodak and E. Zimanyova, *Eur. Polym. J.*, **20**, 81 (1984).
219. E. Borsig, L. Hrchova, A. Fiedlerova, and M. Lazar, *J.M.S.-Pure Appl. Chem.*, **A35**, 1313 (1998).
220. K. N. Ludwig and R. B. Moore, *SPE ANTEC*, **1**, 1844 (1999).
221. D. Graebing, *Macromolecules*, **35**, 4602 (2002).
222. L. K. Yoon, C. H. Choi, and B. K. Kim, *J. Appl. Polym. Sci.*, **56**, 239 (1995).
223. R. Greco, G. Maglio, and P. V. Musto, *J. Appl. Polym. Sci.*, **33**, 2513 (1987).
224. A. Brydon, G. M. Burnett, and G. G. Cameron, *J. Polym. Sci.*, **11**, 3255 (1973).
225. A. Brydon, G. M. Burnett, and G. G. Cameron, *J. Polym. Sci.*, **12**, 1011 (1974).
226. N. G. Gaylord and M. K. Mishra, *J. Polym. Sci. C: Polym. Lett.*, **21**, 23 (1983).
227. G. Doney and K. Salsman, U. S. Patent 6,855,771 (2005).
228. Y. Li, X. M. Xie, and B. H. Guo, *Polymer*, **42**, 3419 (2001).
229. D. Braun, S. Richter, G. P. Hellmann, and M. Ratzch, *J. Appl. Polym. Sci.*, **68**, 2019 (1998).
230. I. H. Do, L. K. Yoon, B. K. Kim, and H. M. Jeong, *Eur. Polym. J.*, **32**, 1387 (1996).
231. J. C. Randall, Jr. and T. Huff, U. S. Patent 5,066,723 (1991).
232. B. I. Chaudhary, T. H. Ho, T. Oswald, and J. DellaMea, U. S. Patent Application 20020151609 (2002).
233. W. Y. Chiu and S. J. Fang, *J. Appl. Polym. Sci.*, **30**, 1473 (1985).
234. J. W. Teh, A. Rudin, and J. C. Keung, *Adv. Polym. Techn.*, **13**, 1 (1994).
235. T. Murayama, *Dynamic Mechanical Analysis of Polymeric Material*, Materials Science monographs; **1**, Elsevier, The Netherlands (1978).
236. C. D. Lee, *SPE ANTEC*, **1**, 2035 (2005).

237. H. G. Heck, D. R. Parikh, L. B. Weaver, J. R. Bethea, L. A. Meiske, and M. F. Martin, U. S. Patent 6,506,842 (2003).
238. D. Graebbling, M. Lambla, and H. Wautier, *J. Appl. Polym. Sci.*, **66**, 809 (1997).
239. K. L. Walton, U. S. Patent 6,548,600 (2003).
240. E. Borsig, A. Fiedlerova, L. Rychla, M. Lazar, M Ratzsch, and G. Haudel, *J. Appl. Polym. Sci.*, **37**, 467 (1989).
241. T. Inoue and T. Suzuki, *J. Appl. Polym. Sci.*, **56**, 1113 (1995).
242. T. Inoue and T. Suzuki, *J. Appl. Polym. Sci.*, **59**, 1443 (1996).
243. J. Yun, R. Patel, and D. C. Worley, *SPE ANTEC*, **3**, 4172 (2004).
244. J. Teng, J. U. Otaigbe, and E. Taylor, *SPE ANTEC*, **1**, 1362 (2003).
245. J. Teng, J. U. Otaigbe, and E. P. Taylor, *Polym. Eng. Sci.*, **4**, 648 (2004).
246. G.-H. Hu, H. Carteir, and C. Plummer, *Macromolecules*, **32**, 4713 (1999).
247. V. Flaris and W. E. Baker, *SPE ANTEC*, 3164 (1995).
248. P. Lagardere and W. E. Baker, *SPE ANTEC*, **2**, 2433 (1998).
249. B. S. Kim and S. C. Kim, *J. Appl. Polym. Sci.*, **69**, 1307 (1998).
250. J. W. Teh and A. Rudin, *Polym. Eng. Sci.*, **22**, 1678 (1992).
251. T. Vestberg, V. Lonnberg, T. Vainio, K. Hanhi, and H. Jukarainen, U. S. Patent 5,981,665 (1999).
252. A. van der Wal and R. J. Gaymans, *Polymer*, **40**, 6067 (1999).
253. S. Havriliak, C. A. Cruz, and S. E. Slavin, *Polym. Eng. Sci.*, **36**, 2327 (1996).
254. S. Jose, A. S. Aprem, B. Francis, M. C. Chandy, P. Werner, V. Alstaedt, and S. Thomas, *Eur. Polym. J.*, **40**, 2105 (2004).
255. J. Karger-Kocsis, A. Kallo, A. Szafner, G. Bodor, and Z. Senyei, *Polymer*, **20**, 37 (1979).
256. P. Phinyocheep, F. H. Axtell, and T. Laosee, *J. Appl. Polym. Sci.*, **86**, 148 (2002).
257. E. Martuscelli, C. Silvestre, and G. Abate, *Polymer*, **23**, 229 (1984).
258. H.-W. Xiao, S.-Q. Huang, T. Jiang, and S.-Y. Cheng, *J. Appl. Polym. Sci.*, **83**, 315 (2002).

259. A. Galeski and E. Piorkowska, *J. Polym. Sci. B: Polym. Phys.*, **21**, 1313 (1983).
260. M. M. Winram, D. Grubb, and A. Keller, *J. Mater. Sci.*, **13**, 791 (1978)
261. X.-Q. Zhou and J. N. Hay, *Polymer*, **34**, 4710 (1993).
262. R. E. Robertson and D. R. Paul, *J. Polym. Sci.*, **17**, 2579 (1973).
263. Z. Bartczak, A. Galeski, and M. Pracella, *Polymer*, **27**, 537 (1986).
264. S. George, K. T. Varughese, and S. Thomas, *Polymer*, **41**, 5485 (2000).
265. M. Gahleitner, J. Wolfschwenger, C. Bachner, K. Bernreitner, and W. Neibl, *J. Appl. Polym. Sci.*, **61**, 649 (1996).
266. D. S. Li, H. Garmestani, R. G. Alamo, and S. R. Kalidindi, *Polymer*, **44**, 5355 (2003).
267. G. Machado, E. L. G. Denardin, E. J. Kinast, M. C. Goncalves, M. A. de Luca, S. R. Teixeira, and D. Samios, *Eur. Polym. J.*, **41**, 129 (2005).
268. P. J. Flory and D. Y. Yoon, *Nature*, **272**, 226 (1978).
269. M. A. Kennedy, A. J. Peacock, and L. Mandelkern, *Macromolecules*, **27**, 5297 (1994).
270. V. Petraccone, I. C. Sanchez, and R. S. Stein, *J. Polym. Sci. B: Polym. Phys.*, **13**, 1991 (1975).
271. L. E. Nielsen and F. E. Stockton, *J. Polym. Sci. A: Polym. Chem.*, **1**, 1995 (1963).
272. B. A. G. Schrauwen, R. P. Janssen, L. E. Govaert, and H. E. H. Meijer, *Macromolecules*, **37**, 6069 (2004).
273. P. T. S. Dijkstra, D. J. Van Dijk, and J. Huetink, *Polym. Eng. Sci.*, **42**, 152 (2002).
274. K. Premphet and W. Paecharoenchai, *J. Appl. Polym. Sci.*, **82**, 2140 (2001).
275. K. Premphet and W. Paecharoenchai, *J. Appl. Polym. Sci.*, **85**, 2412 (2002).
276. D. W. van der Meer, B. Pukanszky, B., and G. J. Vancso, *J. Macomol. Sci.*, **B41**, 1105 (2002).
277. R. Seguela and F. Rietsch, *Polymer*, **27**, 532 (1986).
278. T. A. Huy, R. Adhikari, T. Lupke, S. Henning, and G. H. Michler, *J. Polym. Sci. B: Polym. Phys.*, **42**, 4478 (2004).

279. C. Passingham, P. J. Hendra, M. E. A. Cudby, V. Zichy, and M. Weller, *Eur. Polym. J.*, **26**, 631 (1990).
280. S. Thomas and G. Groeninckx, *Polymer*, **40**, 5799 (1999).
281. C. Grein, K. Bernreitner, and M. Gahleitner, *J. Appl. Polym. Sci.*, **93**, 1854 (2004).
282. C. Jourdan, C., Cavaille, and J. Perez, *J. Polym. Sci. B, Polym. Phys.*, **27**, 2361 (1989).
283. M. L. Cerrada, O. Prieto, J. M. Perena, R. Benavente, and E. Perez, *Macromol. Symp.*, **198**, 91 (2003).
284. Y. P. Khanna, E. A. Turi, T. J. Taylor, V. V. Vickroy, and R. F. Abbott, *Macromolecules*, **18**, 1302 (1985).
285. J. Stepek and H. Daoust, *Additives for Plastics*, Springer-Verlag, New York (1983).
286. N. McCrum, *J. Polym. Sci. B: Polym. Phys.*, **2**, 495 (1964).
287. P. Jacoby, B. H. Bersted, W. J. Kissel, and C. E. Smith, *J. Polym. Sci. B: Polym. Phys.* **24**, 461 (1986).
288. R. Popli, M. Glotin, and L. Mandelkern, *J. Polym. Sci. B: Polym. Phys.*, **22**, 407 (1984) and all references therein.
289. Z. Liang and H. L. Williams, *J. Appl. Polym. Sci.*, **44**, 699 (1992).
290. J. Li, R. A. Shanks, and Y. Long, *Polymer*, **42**, 1941 (2001).
291. J. Li, R. A. Shanks, R. H. Olley, and G. R. Greenway, *Polymer*, **42**, 7685 (2001).
292. M. Yamaguchi, H. Miyata, and K.-H. Nitta, *J. Appl. Polym. Sci.*, **62**, 87 (1996).
293. J. J. Rajasekaran, J. G. Curro, and J. D. Honeycutt, *Macromolecules*, **28**, 6843 (1995).
294. J. Gao, D. Wang, M. Yu, and Z. Yao, *J. Appl. Polym. Sci.*, **93**, 1203 (2004).
295. A. L. N. D. Silva, M. C. G. Rocha, F. M. B. Coutinho, R. E. S. Bretas, and C. Scuracchio, *J. Appl. Polym. Sci.*, **79**, 1634 (2001).
296. M. Yamaguchi, H. Miyata, and K. H. Nitta, *J. Polym. Sci. B: Polym. Phys.*, **35**, 953 (1997).
297. W. Wenig and K. Meyer, *Coll. Polym. Sci.*, **258**, 1009 (1980).
298. Z. Bartczak and A. Galeski, *Polymer*, **27**, 544 (1986).

299. N. Kukaleva, F. Cser, M. Jollands, and E. Kosior, *J. Appl. Polym. Sci.*, **77**, 1591 (2000).
300. T. McNally, P. McShane, G. M. Nally, W. R. Murphy, M. Cook, and A. Miller, *Polymer*, **43**, 3785 (2002).
301. A. Romankiewicz, J. Jurga, and T. Sterzynski, *Macromol. Symp.*, **202**, 281 (2003).
302. S. George, N. R. Neelakantan, K. T. Varughese, and S. Thomas, *J. Polym. Sci. B: Polym. Phys.*, **35**, 2309 (1997).
303. J. Heijboer, *J. Polym. Sci. C: Polym. Lett.*, **16**, 3755 (1968).
304. L. Woo, S. Westphal, and M. T. K. King, *Polym. Eng. Sci.*, **34**, 420 (1994).
305. W. G. Oakes and D. W. Robinson, *J. Polym. Sci.*, **14**, 505 (1954).
306. J. A. Roetling, *J. Polym. Sci.*, **7**, 303 (1966).
307. F. Avalos, M. A. Lopez-Machado, and M. Arroyo, *Polymer*, **25**, 5681 (1996).
308. W. Wenig and M. Asresahegn, *Polym. Eng. Sci.*, **33**, 877 (1993).
309. A. K. Gupta, S. K. Rana, and B. L. Deopura, *J. Appl. Polym. Sci.*, **44**, 719 (1992).
310. V. Choudhary, H. S. Varma, and I. K. Varma, *Polymer*, **32**, 2534 (1991).
311. S. Laihonen, U. W. Gedde, P.-E. Werner, M. Westdahlo, P. Jaaskelainen, and J. Martinez-Salazar, *Polymer*, **38**, 371 (1997).
312. S. Hoshino, E. Meinecke, J. Powers, R. S. Stein, and S. Newman, *J. Polym. Sci. A.: Polym. Chem.*, **3**, 3041 (1965).
313. R. Mehta and T. Kyu, *J. Polym. Sci. B.: Polym. Phys.*, **42**, 2892 (2004).
314. R. H. Olley, D. C. Bassett, *Polymer*, **23**, 1707 (1982).
315. K. L. Naylor and P. J. Phillips, *J. Polym. Sci. B: Polym. Phys.*, **21**, 2011 (1983).
316. R. H. Olley and D. C. Bassett, *Polymer*, **30**, 399 (1989).
317. M. Aboulfaraj, B. Ulrich, A. Dahoun, and C. G'Sell, *Polymer*, **34**, 4817 (1993).
318. L. C. Sawyer and D. T. Grubb, *Polymer Microscopy*, 2nd Ed., Chapman & Hall, London, Chapter 4 (1996).
319. G. Socrates, *Infrared and Raman Characteristic Group Frequencies*, 3rd Ed., John Wiley & Sons, London (2001).

320. J. Coates, "Interpretation of Infrared Spectra, A Practical Approach," in *Encyclopedia of Analytical Chemistry*, R. A. Meyers (Ed.), John Wiley & Sons Ltd., Chichester, pp. 10815-10837 (2000).
321. B. D. Favis, C. Lavalley, and A. Derdouri, *J. Mater. Sci.*, **27**, 4211 (1992).
322. B. Fillon, A. Thierry, J. C. Wittmann, and B. Lotz, *J. Polym. Sci. B: Polym. Phys.*, **31**, 1407 (1993).
323. Q. Yuan, W. Jiang, and L. An, *Coll. Polym. Sci.*, **282**, 1236 (2004).
324. S. Vleeshouwers, *Polymer*, **38**, 3213 (1997).
325. A. J. Lovinger, J. O. Chua, and C. G. Gryte, *J. Polym. Sci. B: Polym. Phys.*, **15**, 641 (1977).
326. K. Cho, D. N. Saheb, H. Tang, B.-I. Kang, J. Kim, and S.-S. Lee, *Polymer*, **44**, 4053 (2003).
327. J. Garbarczyk, D. Paukszta, and S. Borysiak, *J. Macromol. Sci.*, **B41**, 1267 (2002).
328. T. Pressly, N. Jivraj, C. Bosnyak, G. Young, and V. Tharp, *SPE ANTEC*, **1**, 2020 (2004).
329. G.-X. Wei and H.-J. Sue, *Polym. Eng. Sci.*, **40**, 1979 (2000).
330. L. E. Nielsen and F. D. Stockton, *J. Polym. Sci. A: Polym. Chem.*, **1**, 1995 (1963).
331. F. J. B. Calleja, J. C. G. Ortega, and J. Martinez de Salazar, *Polymer*, **19**, 1094 (1978).
332. T. Labour, G. Vigier, R. Seguela, C. Gauthier, G. Orange, and Y. Bomal, *J. Polym. Sci. B: Polym. Phys.*, **40**, 31 (2002).
333. J. Varga, *J. Macromol. Sci.*, **B41**, 1121 (2002) and all references therein .
334. Y. Cohen, and R. F. Saraf, *Polymer*, **42**, 5865 (2001).
335. C. Grein, C. J. G. Plummer, H.-H. Kausch, Y. Germain, and P. Beguelin, *Polymer*, **43**, 3279 (2002).
336. M. Raab, J. Kotek, J. Baldrian, and W. Grellmann, *J. Appl. Polym. Sci.*, **69**, 2255 (1998).
337. T. Labour, C. Gauthier, R. Segula, G. Vigier, Y. Bomal, and G. Orange, *Polymer*, **42**, 7127 (2001).
338. T. Sterzynski, P. Calo, M. Lambla, and M. Thomas, *Polym. Eng. Sci.*, **37**, 1917 (1997).

339. J. Kotek, M. Raab, J. Baldrian, and W. Grellmann, *J. Appl. Polym. Sci.*, **85**, 1174 (2002).
340. T. Labour, L. Ferry, C. Gauthier, P. Hajji, and G. Vigier, *J. Appl. Polym. Sci.*, **74**, 195 (1999).
341. K. J. Kim, Y. S. Ok, and B. K. Kim, *Eur. Polym. J.*, **28**, 1487 (1992).
342. R. A. Ozzetti, A. P. D. O. Filho, U. Schuchardt, and D. Mandelli, *J. Appl. Polym. Sci.*, **85**, 734 (2002).
343. A. Kotschkina and M. Grell, *J. Polym. Sci. Part. C*, **16**, 3731 (1968).
344. D. Montezinos, B. G. Wells, and J. L. Burns, *J. Appl. Polym. Sci.*, **23**, 421 (1985).
345. S. Hosoda, and K. Kojima, *Polym. Comm.*, **30**, 83 (1989).
346. J. M. Kim, M. Lee, S. Kim, and S. Y. Kang, *SPE ANTEC*, **1**, 1931 (2003).
347. J. X. Li and W. L. Cheung, *J. Appl. Polym. Sci.*, **72**, 1529 (1999).
348. G. M. Brown and J. H. Butler, *Polymer*, **38**, 3937 (1997).
349. H. G. Haubruge, A. M. Jonas, and R. Legras, *Polymer*, **44**, 3229 (2003).
350. A. Smit and A. Bezjak, *Polymer*, **22**, 590 (1981).
351. Y. Kodera and B. J. McCoy, *Energy & Fuels*, **16**, 119 (2002).
352. D. Dudic, D. Kostoski, V. Djokovic, and Z. Stojanovic, *Polym. Deg. Stab.*, **67**, 233 (2000).
353. H. C. Lau, S. N. Bhattacharya, and G. J. Field, *Polym. Eng. Sci.*, **38**, 1915 (1998).
354. S. Muke, I. Ivanov, N. Kao, and S. N. Bhattacharya, *Polym. Int.*, **50**, 515 (2001).
355. H. M. Laun and H. Schuch, *J. Rheol.* **33**, 119 (1989).
356. J. J. Morad, *SPE ANTEC*, **1**, 783 (1995).
357. A. Dharia and R. Folland, *SPE ANTEC*, **1**, 2156 (2005).
358. M. Ratzsch, *J.M.S. – Pure Appl. Chem.*, **A36**, 1759 (1999).
359. C. He, S. Costeux, P. Wood-Adams, and J. M. Dealy, *Polymer*, **44**, 7181 (2003).
360. P. Micic and S. N. Bhattacharya, *Polym. Eng. Sci.*, **40**, 1571 (2000).
361. M. Obadal, R. Cermak, and K. Stoklasa, *SPE ANTEC*, **1**, 2151 (2005).

362. J. M. Schultz, *Polymer Crystallization*, Oxford University Press, New York (2001).
363. S. V. Meille, D. R. Ferro, S. Bruckner, A. Lovinger, and F. J. Padden, *Macromolecules*, **27**, 2615 (1994).
364. B. Lotz, J. C. Wittmann, and A. J. Lovinger, *Polymer*, **37**, 4979 (1996).
365. J. Varga, *J. Macromol. Sci.*, **B41**, 1121 (2002) and all references therein .
366. F. J. Padden and H. D. Keith, *J. Appl. Phys.*, **30**, 1479 (1959).
367. A. Zambelli, P. Ammendola, A. Grassi, P. Longo, and A. Proto, *Macromolecules*, **19**, 2703 (1986).
368. B. Wunderlich, *Macromolecular Physics*, **3**, Academic Press, New York (1980).
369. Y. Jin, M. Rogunova, A. Hiltner, E. Baer, R. Nowacki, A. Galeski, and E. Piorkowska, *J. Polym. Sci. B: Polym. Phys.*, **42**, 3380 (2004).
370. F. L. Binsbergen and B. G. M. de Lange, *Polymer*, **9**, 23 (1968).
371. A. J. Lovinger, *J. Polym. Sci. B: Polym. Phys.*, **21**, 97 (1983).
372. B. Lotz, and J. C. Wittmann, *J. Polym. Sci. B: Polym. Phys.*, **24**, 1541 (1986).
373. C. Mathieu, A. Thierry, J. C. Wittmann, and B. Lotz, *J. Polym. Sci. B: Polym. Phys.*, **40**, 2504 (2002).
374. J. J. Janimak, S. Z. D. Cheng, P. A. Giusti, and E. T. Hsieh, *Macromolecules*, **24**, 2253 (1991).
375. V. Petraccone, B. Pirozzi, and S. V. Meille, *Polymer*, **27**, 1665 (1986).
376. P. S. Dai, P. Cebe, M. Capel, R. G. Alamo, and L. Mandelkern, *Macromolecules*, **36**, 4042 (2003).
377. J. X. Li and W. L. Cheung, *Polymer*, **39**, 6935 (1998).
378. J. Varga, I. Mudra, and G. W. Ehrenstein, *J. Appl. Polym. Sci.*, **74**, 2357 (1999).
379. I. A. Al-Raheil, A. M. Qudah, and M. Al-Share, *J. Appl. Polym. Sci.*, **67**, 1259 (1998).
380. A. Turner-Jones, J. M. Aizlewood, and D. R. Beckett, *Makromol. Chem.*, **75**, 134 (1964).
381. J. Varga, *Angew. Makromol. Chem.*, **104**, 79 (1982).

382. B. Fillon, B. Lotz, J. Thierry, and J. C. Wittmann, *J. Polym. Sci. B: Polym. Phys.*, **31**, 1395 (1993).
383. J. Karger-Kocsis, A. Kallo, A. Szafner, and G. Bodor, *Polymer*, **20**, 37 (1979).
384. C. S. Ha and S. C. Kim, *J. Appl. Polym. Sci.*, **35**, 2211 (1988).
385. J. Garbarczyk and D. Paukszta, *Coll. Polym. Sci.*, **263**, 985 (1985).
386. L. D'Orazio, R. Guarino, C. Mancarella, E. Martuscelli, and G. Cecchin, *J. Appl. Polym. Sci.*, **75**, 553 (2000).
387. R. H. Olley, A. M. Hodge, and D. C. Bassett, *J. Polym. Sci. B: Polym. Phys.*, **17**, 627 (1979).
388. F. Rybnikar, *J. Appl. Polym. Sci.*, **27**, 1479 (1982).
389. R. M. Gohil and P. J. Phillips, *Polymer*, **27**, 1687 (1986).
390. H. F. Mark, N. Bikales, C. G. Overberger, and G. Merges, *Encyclopedia of Polymer Science and Engineering*, 2nd Ed., John Wiley & Sons Inc., New York, 482 (1986).
391. P. J. Flory, *Trans. Faraday Soc.*, **51**, 848 (1955).
392. M. J. Richardson, P. J. Flory, and J. B. Jackson, *Polymer*, **4**, 221 (1963).
393. Y. H. Kao and P. J. Phillips, *Polymer*, **27**, 1669 (1986).
394. P. J. Phillips and Y. H. Kao, *Polymer*, **27**, 1679 (1986).
395. R. M. Gohil and P. J. Phillips, *Polymer*, **27**, 1699 (1986).
396. G. Teramoto, T. Oda, H. Saito, H. Sano, and Y. Fujita, *J. Polym. Sci. B: Polym. Phys.*, **42**, 2738 (2004).
397. M. Iijima and G. Strobl, *Macromolecules*, **33**, 5204 (2000).
398. F. L. Binsbergen, *J. Polym. Sci. B: Polym. Phys.*, **11**, 117 (1973).
399. S. Yamazaki, M. Hikosaka, A. Toda, I. Wataoka, and F. Gu, *Polymer*, **43**, 6585 (2002).
400. X. Zhu, D. Yan, and Y. Fang, *J. Phys. Chem. B.*, **105**, 12461 (2001).
401. D. R. Burfield, P. S. T. Loi, Y. Doi, and J. Mejjik, *J. Appl. Polym. Sci.*, **41**, 1095 (1990).
402. X. Wang, C. Tzoganakis, and G. L. Rempel, *J. Appl. Polym. Sci.*, **61**, 1395 (1996).

403. D. A. Hemsley (Ed.), *Applied Polymer Light Microscopy*, Elsevier, New York (1989).
404. Z.-G. Wang, B. S. Hsiao, E. B. Sirota, P. Agarwal, and S. Srinivas, *Macromolecules*, **33**, 978 (2000).
405. M. Imai, K. Mori, T. Mizukami, K. Kaji, and T. Kanaya, *Polymer*, **33**, 4451 (1992).
406. N. V. Pogodina, S. K. Siddiquee, J. W. van Egmond, and H. H. Winter, *Macromolecules*, **32**, 1167 (1999).
407. N. V. Pogodina and H. H. Winter, *Macromolecules*, **31**, 8164 (1998).
408. F. L. Binsbergen, *Polymer*, **11**, 253 (1970).
409. C. E. Locke and D. R. Paul, *J. Appl. Polym. Sci.*, **17**, 2597 (1973).
410. J. A. Sauer, L. J. Merrill, and A. E. Woodward, *J. Appl. Polym. Sci.*, **58**, 19 (1962).
411. S. Filipe, M. T. Cidade, M. Wilhelm, and J. M. Maia, *Polymer*, **45**, 2367 (2004).
412. G.-H. Hu and H. Cartier, *J. Appl. Polym. Sci.*, **71**, 125 (1999).
413. K. Sirsinha and D. Meksawat, *J. Appl. Polym. Sci.*, **93**, 1179 (2004).
414. O. Darras and R. Seguela, *J. Polym. Sci.: B, Polym. Phys.*, **31**, 759 (1993).
415. P. Starck, *Eur. Polym. J.*, **3**, 339 (1997).
416. X. Guan and P. J. Phillips, *SPE ANTEC*, **2**, 2076 (2004).
417. U. W. Gedde, *Polymer Physics*, Chapman and Hall, London, pp. 106 (1995).
418. J. M. Schultz, *Polym. Eng. Sci.*, **24**, 770 (1982).
419. A. Lustiger, C. N. Marzinsky, and R. R. Mueller, *J. Polym. Sci. B: Polym. Phys.*, **36**, 2047 (1998).
420. A. Smedberg, T. Hjertberg, and B. Gustafsson, *Polymer*, 3395 (2003).
421. M. D. Elkovitch, L. J. Lee, and D. L. Tomasko, *Polym. Eng. Sci.*, **41**, 2108 (2001).
422. V. Khan, C. Kwag, C. W. Manke, and E. Gulari, *SPE ANTEC*, **1**, 1418 (1998).
423. A. Xue and C. Tzoganakis, *SPE ANTEC*, **1**, 2276 (2003).
424. H. Li, L. J. Lee, and D. L. Tomasko, *Ind. Eng. Chem. Res.*, **43**, 509-514 (2004).

425. Y.-P. Sun, *Supercritical Fluid Technology in Materials Science and Engineering*, Marcel Dekker, Inc., New York (2002).
426. A. I. Cooper, *J. Mater. Chem.*, **10**, 207 (2000).
427. J. J. Watkins and T. J. McCarthy, *Macromolecules*, **27**, 4845 (1994).
428. J. A. Hyatt, *J. Org. Chem.*, **49**, 5097 (1984).
429. S. Lee, K. Soonjong, and A. Fouad, U. S. Patent 5,663,237 (1997).
430. B. M. Dorscht and C. Tzoganakis, *J. Appl. Polym. Sci.*, **87**, 1116 (2003).
431. Z. Dong, Z. Liu, B. Han, J. He, T. Jiang, and G. Yang, *J. Mater. Chem.*, **12**, 3565 (2002).
432. S. Beuermann, M. Buback, C. Isemer, I. Lacik, and A. Wahl, *Macromolecules*, **35**, 3866 (2002).
433. Q. Dong and Y. Liu, *J. Appl. Polym. Sci.*, **90**, 853 (2003).
434. A. I. Cooper, *Adv. Mater.*, **15**, 1049 (2003).
435. S. Sicardi, L. Manna, and M. Banchero, *J. Supercrit. Fluids*, **17**, 187 (2000).
436. S.-J. Park and S.-D. Yeo, *Sep. Sci. Tech.*, **34**, 101 (1999).
437. Univation Technologies, "News and Information – PE Markets," January 2003, <http://www.univation.com>. Last accessed July 13th, 2005.
438. D. C. Montgomery, *Design and Analysis of Experiments*, John Wiley & Sons, Inc., New York (2001).
439. A. Dean and D. Voss, *Design and Analysis of Experiments*, Springer-Verlag, New York (1999).

BIOGRAPHICAL SKETCH

Nathan Fraser Tortorella was born on January 9, 1979, in Attleboro, MA. He spent most of his childhood in Massachusetts but attended high school in Kinnelon, NJ. His family moved to Florida during the summer of 1997, the same year he would start school at the University of Florida. He declared materials science and engineering as his major not long after entering the University and has flourished ever since. A Bachelor of Science degree in May 2002, Master of Science degree in May 2005, and Ph.D. in December 2005 within the department soon followed.

The author enjoys Gator Athletics, fishing, mountain biking and hiking. He also likes to play an occasional pickup game of basketball. He married his wife, Michelle, on April 24, 2004, and they had their daughter, Katelynn Victoria, on June 2, 2005.